# 3D-Printed Coupling Elements for Photonic and Terahertz Assemblies

Zur Erlangung des akademischen Grades eines

**DOKTORS DER INGENIEURWISSENSCHAFTEN (Dr.-Ing.)**

von der KIT-Fakultät für
Elektrotechnik und Informationstechnik
des Karlsruher Instituts für Technologie (KIT)

angenommene

**DISSERTATION**

von

**Pascal Maier, M.Sc.**
geb. in Lörrach

| | |
|---|---|
| Tag der mündlichen Prüfung: | 20.03.2024 |
| Hauptreferent: | Prof. Dr.-Ing. Christian Koos |
| Korreferent: | Prof. Dr.-Ing. Dr. h. c. Thomas Zwick |
| Korreferent: | Prof. Dr.-Ing. Dr. h. c. Wolfgang Freude |

# Table of contents

# Kurzfassung

Die Fortschritte in der Halbleitertechnologie und dieser zugrundeliegenden lithografischen Verfahren haben unsere digitale Welt seit über einem halben Jahrhundert geprägt. Heute tragen die zunehmende Zahl miteinander verbundener Geräte sowie zahlreiche Dienste wie z.B. Videostreaming oder die industrielle Automatisierung erheblich zum Wachstum des Internetverkehrs bei. Optische Kommunikation wird aufgrund der hohen Bandbreite eingesetzt, um die hiermit verbundenen gewaltigen Datenmengen effizient zu übertragen. Dies betrifft sowohl globale Kommunikationsnetze als auch Datenzentren, in denen die Vernetzung von typischerweise hunderttausenden von Servern eine große technische Herausforderung darstellt. Die Integration elektronischer sowie optischer Bauteile ist daher der Schlüssel zur Schaffung schneller, effizienter und skalierbarer Kommunikationssysteme.

Vor diesem Hintergrund hat sich die integrierte Optik in den letzten Jahren als einer der wichtigsten Technologietreiber der Informations- und Kommunikationstechnik entwickelt. Hiermit einhergehende photonische integrierte Schaltkreise (engl. photonic integrated circuits, PIC) enthalten analog zu elektronischen integrierten Schaltkreisen eine große Anzahl dicht integrierter Bauelemente und können auf Waferebene hergestellt werden. Die Photonik umfasst jedoch ein breites Spektrum an Materialien, die jeweils auf spezifische Bedürfnisse zugeschnitten sind. Die Silizium-Photonik (SiP) beispielsweise ist im Telekommunikationssektor aufgrund ihrer Kompatibilität mit der ausgereiften CMOS-Fertigungstechnologie (engl. complementary metal-oxide-semiconductor) sehr erfolgreich und ermöglicht eine kostengünstige und dichte Integration von Bauelementen mit hoher Zuverlässigkeit und Ausbeute. Allerdings verhindert die indirekte Bandlücke von Silizium eine effiziente Lichtemission, weshalb Lichtquellen und Verstärker auf III-V-Verbindungshalbleitern wie Indium-Gallium-Arsenid-Phosphid (InGaAsP)

basieren. Auch die Siliziumnitrid-Plattform ($Si_3N_4$) findet zunehmend Beachtung, da diese sich durch ein breitbandiges Transparenzfenster und einen niedrigen Indexkontrast auszeichnet, was verlustarme Wellenleiter und Resonatoren mit hoher Güte ermöglicht. Folglich beruht die photonische Integration entscheidend auf der Kombination verschiedenartiger Materialien, um leistungsfähige Systeme zu schaffen. Insbesondere hybride Integrationsprozesse auf Package-Ebene, bei denen fertig prozessierte Chips verschiedener Materialsysteme durch Co-Packaging in sogenannten Multi-Chip-Modulen kombiniert werden, bieten zahlreiche Vorteile. Hierzu gehören die Nutzung etablierter Fertigungsverfahren sowie ein hohes Maß an Flexibilität und damit eine gute Anpassungsfähigkeit an die Anforderungen des stark fragmentierten Photonikmarktes. Die verlustarme Verbindung von PIC sowie die Anbindung an die Außenwelt über Fasern stellen allerdings große Herausforderungen dar. Selbst bei einer perfekten Überlappung der Modenfelder zwischen den verschiedenen zu verbindenden Komponenten sind die Durchmesser der Modenfelder im Allgemeinen sehr klein. Daraus ergeben sich stringente Anforderungen an die mechanische Ausrichtung, die häufig den Einsatz langsamer und teurer aktiver Ausrichtungsverfahren erfordert, bei denen die Kopplungseffizienz während der Platzierung jedes einzelnen Bauteils kontinuierlich überwacht wird. Solche Verfahren tragen erheblich zu den Kosten photonisch integrierter Baugruppen bei und stellen daher einen limitierenden Faktor für die Skalierbarkeit der entsprechenden Systeme dar — wenngleich die Massenproduktion der Chips auf Waferebene bereits ausgereift ist.

Der Millimeterwellen- (mmW) und Terahertz-Frequenzbereich (THz) bietet ebenfalls großes Potenzial in der Kommunikationstechnik. Die Datenübertragung bei Trägerfrequenzen von Hunderten von GHz eröffnet hier wegen der hohen Trägerfrequenzen die Möglichkeit, derzeitig vorherrschende Bandbreitenlimitierungen drahtloser Netzwerke zu überwinden. Im Gegensatz zur optischen Freiraumkommunikation sind Übertragungen bei Trägerfrequenzen im mmW- und THz-Frequenzbereich in der Regel weniger anfällig für Dämpfung durch Nebel, Szintillation und Fehlausrichtung. Dies ermöglicht es, einen attraktiven Kompromiss zwischen Übertragungskapazität und Resilienz gegenüber Witterungseinflüssen zu finden. In der Vergangenheit basierten THz-Baugruppen häufig auf

präzisionsgefrästen metallischen Aufbauten (engl. split-block), die zwar eine effiziente Signalführung und Kopplung mittels Hohlleitern ermöglichen, gleichzeitig allerdings signifikant zu den Kosten und dem Gewicht des Gesamtsystems beitragen. In Analogie zur photonischen Integration spielen daher hybride Multi-Chip-Module, die Verstärker auf der Grundlage von MMIC (engl. monolithic microwave integrated circuits) mit z.B. THz-Signalquellen, Detektoren und Antennen kombinieren, eine entscheidende Rolle bei der Bereitstellung einer vielseitigen Plattform zur Adressierung der entsprechenden Frequenzbereiche. Heutzutage werden elektrische Verbindungen in der Regel durch metallische Bändchen (engl. ribbon bonds) oder Flip-Chip Verbindungen realisiert. Aufgrund der begrenzten Kontrolle über die dreidimensionale (3D) Geometrie der elektrischen Leiter ist jedoch eine Fehlanpassung der charakteristischen Impedanzen am Übergang der miteinander verbundenen Übertragungsleitungen kaum zu vermeiden. Die erreichbaren Betriebsbandbreiten zugehöriger Multi-Chip-Module sind daher aufgrund zunehmender Reflexions- und Strahlungsverluste bei hohen Frequenzen zunehmend limitiert. Dies unterstreicht den Bedarf einer kostengünstigen, kompakten und effizienten Aufbau- und Verbindungstechnik für THz-Baugruppen.

Die additive Mikrofabrikation von 3D-Freiform-Kopplungsstrukturen stellt einen vielversprechenden Weg zur Überwindung dieser Technologielücke sowohl für photonische als auch für THz-Baugruppen dar. Die vorliegende Dissertation baut auf früheren Arbeiten [1–3] auf und nutzt die Multiphotonenlithographie (MPL) zur Herstellung einer Vielzahl an 3D-gedruckten Kopplungsstrukturen. Dies umfasst zum einen etablierte optische Kopplungsstrukturen wie dielektrische Wellenleiter, sogenannte photonische Wirebonds (PWB), sowie Mikrolinsen an Bauteilfacetten (engl. facet-attached microlenses, FaML). Ausgehend von den einzigartigen Möglichkeiten, die PWB und FaML in der optischen Aufbau- und Verbindungstechnik bieten, wird das bestehende Portfolio an Demonstrationen und Anwendungen erheblich erweitert — insbesondere im Hinblick auf hybrid integrierte Lichtquellen und optische Transceiver-Baugruppen, die das Konzept des räumlichen Multiplexings (engl. space-division multiplexing, SDM) zur parallelen Übertragung großer Datenströme nutzen. Zum anderen wird das Konzept 3D-gedruckter Kopplungsstrukturen auf THz-Baugruppen ausgedehnt. Hierbei ermöglicht die lokalisierte

Metallbeschichtung von 3D-gedruckten Polymer-Trägerstrukturen die Herstellung von mmW- und THz-Strukturen mit präzise definierten 3D-Freiformgeometrien. Dieser bislang unerreichte Designfreiraum wird für eine Reihe von THz-Bauteilen genutzt: Chip-Chip-Verbindungen, Tastspitzen und Antennen. Die einzelnen Kapitel dieser Arbeit behandeln die folgenden Themen:

*Kapitel 1* erörtert die Bedeutung von PIC und MMIC für die Informations- und Kommunikationstechnik und unterstreicht die Notwendigkeit effizienter Aufbau- und Verbindungstechniken für die jeweiligen photonischen und THz-Baugruppen. Die Multiphotonenlithographie wird als praktikables Werkzeug für die Bewältigung der hiermit verbundenen Herausforderungen bei der Montage von Multi-Chip-Modulen eingeführt.

*Kapitel 2* legt die theoretischen und technologischen Grundlagen für die folgenden Kapitel. Die Prinzipien der Multiphotonenlithographie werden erläutert, und die verschiedenen Anwendungen sowie Vorteile von 3D-gedruckten Kopplungsstrukturen für photonische und THz-Baugruppen werden diskutiert.

*Kapitel 3* beschreibt die Anwendung von 3D-gedruckten Wellenleitern, sog. PWB, in hybrid integrierten Diodenlasern mit breitbandig abstimmbaren externen Resonatoren (engl. external-cavity laser, ECL). Ein PWB verbindet hierbei einen Halbleiterverstärkerchip mit einer auf $Si_3N_4$ aufgebauten externen Rückkopplungsstruktur hoher Güte und ermöglicht so den Betrieb mit besonders geringem Phasenrauschen. Zum ersten Mal wird ein durch ein einzelnes im Resonator umlaufendes Soliton erzeugter Kerr-Frequenzkamm mit einem Pumplaser erzeugt, dessen Signal von solch einem hybrid-integrierten ECL abgeleitet wurde.

*Kapitel 4* führt aus, wie 3D-gedruckte Mikrolinsen eine verlustarme Kopplung mit weniger stringenten Anforderungen an die mechanische Ausrichtungsgenauigkeit in Transceiver-Baugruppen ermöglichen, die SDM zur parallelen Übertragung großer Datenströme nutzen. Sowohl die einzelnen Kerne von Multimoden-Mehrkernfasern als auch Multimoden-Faseranordnungen werden hierbei mit standardisierten Anordnungen von oberflächenemittierenden Lasern (engl. vertical-cavity surface-emitting laser, VCSEL) oder Photodioden (PD) verbunden. Dies ist die erste Demonstration einer Kopplungsschnittstelle, die einzelne Kerne einer

Mehrkernfaser mit linear angeordneten VCSEL / PD verbindet, ohne dass zusätzliche Fan-out-Strukturen erforderlich sind. Es wird ein passiver Montageprozess vorgestellt sowie ein Datenübertragungsexperiment über drei räumlich getrennte Kanäle durchgeführt.

*Kapitel 5* erweitert das Konzept 3D-gedruckter Kopplungsstrukturen auf mmW- und THz-Baugruppen. Es wird ein neuartiges Konzept zur Herstellung präzise definierter mmW- und THz-Strukturen vorgestellt, das verlustarme Dielektrika und hochleitfähige Metallelemente in einer wohldefinierten 3D-Freiformgeometrie kombiniert. Das Konzept nutzt 3D-gedruckte Polymer-Trägerstrukturen, die durch hochdirektionale Metallabscheidungstechniken in Kombination mit präzise ausgerichteten 3D-gedruckten Abschattungsstrukturen selektiv beschichtet werden. Die Tragfähigkeit dieser Idee wird mittels einer Auswahl funktionaler THz-Strukturen demonstriert: Ultra-breitbandige Chip-Chip-Verbindungen zur Überbrückung von Unterbrechungen zwischen elektrischen Leitungen auf verschiedenen planaren Substraten, Tastspitzen mit beispielloser Formtreue, die sich für die Prüfung von integrierten mmW- und THz-Schaltungen eignen, sowie Antennen, die zur Erhöhung der Strahlungseffizienz vom darunter liegenden hochbrechenden Substrat abgehoben sind.

*Kapitel 6* fasst die vorliegende Arbeit zusammen und skizziert weiterführende Verbesserungen, Anwendungen und Forschungsrichtungen im Hinblick auf 3D-gedruckte Kopplungsstrukturen in photonischen und THz-Baugruppen.

# Preface

Advances in semiconductor technology and of the underlying lithographic processing techniques have shaped our digital world for over half a century. Today, the increasing amount of interconnected devices as well as services like video streaming or industrial automation contribute significantly to the ever-increasing internet traffic. Optical communications is used due to its high bandwidth to efficiently transmit the huge amounts of data involved. This applies both to global communication networks as well as to datacenters, where interconnecting hundreds of thousands of servers represents a major technical challenge. Electrical as well as optical device integration has thus become key to create fast, efficient, and scalable communication systems.

Against this backdrop, integrated optics has become one of the most important technology drivers in information and communication technology in recent years. The associated photonic integrated circuits (PIC), much like electronic integrated circuits, contain a vast amount of densely integrated devices which can be fabricated on a wafer-scale. However, photonics spans a wide spectrum of materials, each serving specific needs. Silicon photonics (SiP), for example, thrives in the telecom sector due to its compatibility with mature complementary metal-oxide-semiconductor (CMOS) technology, allowing cost-effective and dense device integration with high reliability and yield. However, the indirect band gap of silicon prevents efficient light emission. Therefore, light sources and amplifiers are based on III-V compound semiconductors such as indium gallium arsenide phosphide (InGaAsP). The silicon nitride ($Si_3N_4$) platform has also gained increasing attention, boasting a broadband transparency window and low index-contrast, which enables low-loss waveguides and resonators with ultra-high $Q$-factors. Therefore, photonic integration crucially relies on the combination of

different materials to create high-performance systems. Especially package-level hybrid integration processes, which combine fully processed dies of different material systems by co-packaging in so-called multi-chip modules, offer numerous advantages. These include the use of established manufacturing processes as well as a high degree of flexibility and thus good adaptability to the requirements of the highly fragmented photonics market. However, low-loss coupling among PIC and the connection to the outside world via fibers represent major challenges. A perfect mode-field overlap between the various components to be interconnected is difficult to achieve, because the mode-field diameters are generally very small. This results in stringent requirements for mechanical alignment, often requiring the use of slow and expensive active alignment techniques where the coupling efficiency is continuously monitored during the placement of each component. Such techniques add significantly to the cost of photonic assemblies and are therefore a limiting factor for the scalability of the corresponding systems — despite the mature wafer-level production of the chips themselves.

The millimeter-wave (mmW) and terahertz (THz) frequency range has likewise opened up new frontiers in communications, where data transmission at carrier-frequencies of hundreds of GHz has the potential to overcome bandwidth limitations of current wireless networks. In contrast to free-space optical links, transmission at carrier frequencies in the mmW and THz frequency range are typically less susceptible to attenuation by fog, scintillation, and misalignment. This enables an attractive trade-off between transmission capacity and resilience to weather influences. In the past, THz assemblies were often based on precision-milled metallic split-blocks, which enable efficient signal routing and coupling by means of hollow waveguides, but at the same time contribute significantly to the cost and weight of the overall system. In close analogy to photonic integration, hybrid multi-chip modules combining amplifiers based on monolithic microwave integrated circuits (MMIC) with, e.g., THz signal sources, detectors and antennas hence play a pivotal role in providing a versatile technology platform for addressing the associated frequency range. Nowadays, electrical connections are usually realized by thermosonic ribbon bonding or flip-chip interconnects. However, due to limited control over the three-dimensional (3D) geometry of the electrical conductors, a mismatch of the characteristic impedances at the transition

of interconnected transmission lines is hardly avoidable. The achievable operational bandwidths of associated multi-chip modules are hence limited to a narrow band due to increasing reflection and radiation losses at high frequencies. These challenges underpin the need for cost-effective, compact, and efficient packaging solutions of THz assemblies.

Additive micro-fabrication of 3D freeform coupling elements represents a promising path to overcome this technology gap for both photonic and THz assemblies. This thesis builds upon previous work [1–3] and uses direct-write multi-photon lithography (MPL) for the fabrication of various 3D-printed coupling elements. This includes well-established optical coupling elements such as dielectric waveguides, so-called photonic wire bonds (PWB), as well as facet-attached microlenses (FaML). Building upon the unique capabilities offered by PWB and FaML in photonic assemblies, the existing portfolio of demonstrators and applications has significantly advanced — especially with regard to hybrid integrated light sources and optical transceiver assemblies that use the concept of space-division multiplexing (SDM) for the parallel transmission of large data streams. Furthermore, the concept of 3D-printed coupling elements is expanded to THz assemblies. Here, the localized metal-coating of 3D-printed polymer templates enables the fabrication of mmW and THz structures with precisely defined 3D freeform geometries. This unprecedented design freedom is used for demonstrating a range of THz devices: chip-chip interconnects, probe tips and antennas. The individual chapters of this work cover the following subjects:

*Chapter 1* discusses the relevance of PIC as well as MMIC for information and communication technology, and highlights the importance of efficient packaging solutions for the respective photonic and THz assemblies. Multi-photon lithography is introduced as a viable tool for tackling the associated challenges of multi-chip assemblies.

*Chapter 2* lays the theoretical and technological foundation for the following chapters. The principles of direct-write multi-photon lithography are reviewed, and the various applications and advantages of 3D-printed coupling elements for photonic and THz assemblies are discussed.

*Chapter 3* describes the application of 3D-printed waveguides, so-called PWB, in hybrid external-cavity lasers (ECL). The PWB connects a semiconductor optical amplifier chip with a low-loss $Si_3N_4$-based external feedback circuit, thereby enabling operation with particularly low phase noise performance. For the first time, a single-soliton Kerr comb is generated with a pump that is derived from such a hybrid-integrated ECL.

*Chapter 4* explains how 3D-printed microlenses enable low-loss and alignment-tolerant coupling in transceiver assemblies that use SDM for the parallel transmission of large data streams. Both individual cores of multimode multicore fibers (MCF) as well as multimode fiber arrays are connected to standard arrays of vertical-cavity surface-emitting lasers (VCSEL) or photodiodes (PD). This represents the first demonstration of a coupling interface that connects individual cores of an MCF to VCSEL / PD arranged in a standard linear array without the need of additional fan-out structures. A passive assembly process is presented, and a data-transmission experiment over three spatially separated channels is performed.

*Chapter 5* extends the concept of 3D-printed coupling elements to mmW and THz assemblies. A novel concept for fabricating precisely defined mmW and THz structures is introduced, combining low-loss dielectrics and highly conductive metal elements in a well-defined 3D freeform geometry. The concept exploits *in-situ* printed polymer support structures that are selectively coated through highly directional metal deposition techniques in combination with precisely aligned 3D-printed shadowing structures. The viability of this concept is demonstrated by a selection of functional THz structures: ultra-broadband chip-chip interconnects, bridging the gap between electrical transmission lines on different planar substrates, probe tips of unprecedented shape fidelity that lend themselves to testing of mmW and THz integrated circuits, and suspended antennas that are raised above the underlying high-index substrate for increased radiation efficiency.

*Chapter 6* summarizes the work in this thesis and outlines further improvements, applications and research directions with regards to 3D-printed coupling elements in photonic and THz assemblies.

# Achievements of the present work

In this thesis, 3D-printed coupling elements are used for both photonic and terahertz (THz) assemblies. Existing tools and methods [1, 2] for the design and fabrication of optical coupling elements such as photonic wire bonds (PWB) and facet-attached microlenses (FaML) are adapted to enable various novel applications. In particular, the concept of hybrid external-cavity lasers (ECL) based on 3D-printed intra-cavity coupling elements is expanded by replacing previously used silicon photonic feedback circuits [J1] with their silicon-nitride-($Si_3N_4$)-based counterparts. As a result of the lower linear and nonlinear losses, intrinsic $Q$-factors of the underlying resonators are greatly increased and two-photon absorption is eliminated as a critical impairment at high power levels, thereby facilitating greatly reduced phase noise and small linewidths [J2]. In a second area of research, the advantages offered by the FaML-based concept are demonstrated for low-loss coupling with relaxed alignment tolerances in optical transceiver assemblies that use space-division multiplexing (SDM) for parallel transmission of large data streams. Coupling of both individual cores of multimode multicore fibers (MM-MCF) as well as conventional multimode fiber arrays (MM-FA) to standard arrays of vertical-cavity surface-emitting lasers (VCSEL) or photodiodes (PD) is demonstrated [J3]. Finally, the concept of 3D-printed coupling elements is extended to the field of millimeter-wave (mmW) and THz assemblies. Here, the localized metal-coating of 3D-printed polymer templates enables the fabrication of mmW and THz structures with precisely defined 3D freeform geometries. This unprecedented design freedom is used for demonstrating a range of THz devices: chip-chip interconnects, probe tips and antennas [J4].

A concise overview of the major achievements is given in the following list:

**Demonstration of hybrid ECL that combine low-loss $Si_3N_4$-based feedback circuits with PWB as intra-cavity coupling element:** A proof-of-concept device using a PWB as intra-cavity coupling element between the InP-based gain chip and a $Si_3N_4$-based feedback circuit offers much improved performance compared to its silicon photonics counterpart [J1]. We demonstrate a 90 nm tuning range (1480 nm – 1570 nm) with on-chip output powers of more than 12 dBm and side-mode suppression ratios of up to 59 dB in the center of the tuning range. The devices exhibit intrinsic linewidths of less than 1 kHz, which is one of the lowest values reported for comparable feedback architectures, see Section 3.2 and journal publication [J2] for details.

**First demonstration of a single-soliton Kerr comb generated with a pump that is derived from a hybrid ECL:** The versatility of the $Si_3N_4$-based hybrid ECL is demonstrated by using the device as a precisely tunable pump laser to generate dissipative Kerr soliton frequency combs in high-$Q$ $Si_3N_4$ microresonators, see Section 3.3 and journal publication [J2] for details.

**Low-loss and alignment-tolerant coupling between MM-FA and standard linear arrays of VCSEL / PD:** Using FaML, low-loss and alignment-tolerant connections between MM-FA and standard linear arrays of VCSEL / PD are demonstrated in transceiver assemblies that use SDM for parallel transmission of large data streams. Average optical coupling losses as low as 0.35 dB for the transmitter (Tx) and 0.70 dB for the receiver (Rx) are achieved, along with lateral 1 dB alignment tolerances of $\pm 17$ µm (Tx) and $\pm 62$ µm (Rx), respectively. Using a machine-vision based passive alignment process on a custom pick-and-place machine, average coupling losses of 0.50 dB (Tx) and 0.70 dB (Rx) are shown, see Section 4.3 and journal publication [J3] for details.

**First demonstration of a coupling interface connecting individual cores of MCF to VCSEL / PD arranged in standard linear arrays:** Using FaML, low-loss and alignment-tolerant connections between individual cores of an MM-MCF and standard linear arrays of VCSEL / PD are demonstrated in transceiver assemblies that use SDM for parallel transmission of large data streams. The presented scheme does not require any additional fiber-based or waveguide-based fan-out

structures. Average coupling losses of $0.67$ dB (Tx) and $0.63$ dB (Rx) are achieved, along with lateral $1$ dB alignment tolerances of $\pm 18$ µm (Tx) and $\pm 25$ µm (Rx), respectively. Using a machine-vision based passive alignment process, average coupling losses of $1.0$ dB (Tx) and $0.63$ dB (Rx) are shown. Using this approach, a $3 \times 25$ Gbit/s datacenter transceiver assembly which fits into a small form-factor pluggable module is built, fulfilling many of the performance metrics specified in the IEEE 802.3 standard, see Section 4.4 and journal publication [J3].

**Development of a novel manufacturing process for fabricating freeform mmW and THz structures:** A novel concept for fabricating precisely defined mmW and THz structures is introduced and experimentally verified, combining low-loss dielectrics and highly conductive metal elements in a well-defined 3D freeform geometry. The concept exploits *in-situ* printed polymer support structures that are selectively coated through highly directional metal deposition techniques in combination with precisely aligned 3D-printed shadowing structures. The resulting metal-coated freeform structures (MCFS) offer high surface quality in combination with conductivities comparable to bulk material values and do not require any manual assembly steps, see Section 5.2 and the preprint [J4] of a submitted journal contribution for details.

**Demonstration of chip-chip interconnects offering record-high bandwidths of $0.33$ THz and beyond:** The concept of MCFS is used for demonstrating THz interconnects that bridge the gap between electrical transmission lines located on different planar substrates. The demonstrated $3$ dB-bandwidths in excess of $0.33$ THz represent a record for in-plane chip-chip connections, see Section 5.3.1 and the preprint [J4] of a submitted journal contribution for details.

**First demonstration of additively manufactured electrical probes with operating frequencies above $110$ GHz:** The concept of MCFS is further used for demonstrating THz probes offering unprecedented shape fidelity that lend themselves to testing of mmW and THz integrated circuits. Highly repeatable contacting over many probing cycles with $3$ dB-bandwidths in excess of $0.19$ THz and with $6$ dB-bandwidths far beyond the $0.33$ THz range of our measurement system are demonstrated, see Section 5.3.2 and the preprint [J4] of a submitted journal contribution for details.

**First demonstration of additively manufactured 3D freeform mmW / THz antennas without the requirement of manual assembly:** The concept of MCFS is finally used for demonstrating THz antennas which are raised above the underlying high-index substrate for better radiation efficiency. No manual assembly steps are required. At a frequency of $0.27\,\mathrm{THz}$, a maximum gain of $5.5\,\mathrm{dBi}$ over an isotropic radiator is measured in the surface-normal direction, see Section 5.3.3 and the preprint [J4] of a submitted journal contribution for details.

# 1 Introduction

In the evolving landscape of modern technology, the fusion of electronics and photonics has progressed for over half a century owing to advances in semiconductor technology and of the underlying lithographic processing techniques [4]. This convergence has been the technical foundation of modern information and communication technology [5], shaping a world where digital devices, from personal computers to smartphones, have seamlessly integrated into our daily lives. These devices have consequently given rise to a vast amount of services and applications, including cloud-based services such as video streaming, the internet of things, remote work or industrial automation. As a result, global internet traffic was already predicted to surpass $4.8$ zettabytes per year by 2022 [6], which corresponds to more data traffic per day as ten years ago within about two weeks. Herein, mobile and wireless devices contribute $20$ % of the total traffic, and are expected to exceed a staggering $7$ zettabytes per year by 2030 [7]. Optical communications is used due to its high bandwidth to efficiently transmit the huge amounts of data involved. This applies both to global communication networks as well as to datacenters, where interconnecting hundreds of thousands of servers represents a major technical challenge. Yet, data are primarily generated and processed in electronic form, thus requiring devices for electro-optic and opto-electronic conversion, i.e., modulators and photodiodes (PD). Electrical as well as optical device integration has thus become key to create fast, efficient, and scalable communication systems.

### Challenges and approaches for photonic assemblies

Against this backdrop, integrated optics has become one of the most important technology drivers in information and communication technology in recent years. Unlike electronics, where silicon has dominated as the principal material of choice

for fabricating circuits [4], photonics spans a wide spectrum of material systems and associated integration platforms, each tailored to specific needs. Among these integration platforms, silicon photonics (SiP) [8] thrives in the telecom sector, leveraging mature complementary metal-oxide-semiconductor (CMOS) technology to achieve high yield and high-density device integration at low cost. With silicon being optically transparent at the important optical communication wavelength bands around $1.31\,\mu\text{m}$ and $1.55\,\mu\text{m}$, this platform offers a variety of passive components such as waveguides [9] and passive devices such as power splitters [10], resonators [11], or filters [12] along with active devices, such as electro-optic modulators based on the plasma-dispersion effect [13] or highly-efficient waveguide-coupled germanium (Ge) PD [14]. However, the indirect band gap of silicon impedes efficient light emission. For applications requiring light sources or optical amplifiers, III-V compound semiconductors such as indium gallium arsenide phosphide (InGaAsP) are key [15]. However, despite its potential for efficient light generation and detection, the InP platform also suffers from drawbacks such as comparatively high raw-material and processing costs in conjunction with small substrate areas and comparatively low yield — facts which ultimately limit the scalability of the associated PIC. In addition to SiP and InP, several other material platforms have received attention over the previous years, comprising also different variations of silicon-nitride-($Si_3N_4$)-based PIC [11, 16, 17]. The main reasons are the broadband transparency window of $Si_3N_4$, which reaches from the ultraviolet (UV) to the mid-infrared (mid-IR) as a result of the large band gap of the order of $(3\ldots4)\,\text{eV}$. Two-photon absorption (TPA) is thus eliminated as a critical impairment at high power levels as the photon energies of $0.95\,\text{eV}$ and $0.8\,\text{eV}$ associated with the telecom wavelengths of $1.31\,\mu\text{m}$ and $1.55\,\mu\text{m}$, respectively, are below half the band gap energy of $Si_3N_4$ [18]. Furthermore, the refractive-index-contrast between the $Si_3N_4$ waveguide core and the surrounding silicon dioxide ($SiO_2$) cladding is smaller than that for SiP circuits, which is key to ultra-low-loss waveguides [19]. Consequently, intrinsic $Q$-factors of resonator-based feedback circuits can be largely increased. These features are particularly important for high-performance chip-scale lasers, which crucially rely on high intra-cavity power levels and on low-loss frequency-selective feedback circuits for achieving low phase noise performance [20, 21]. Furthermore, $Si_3N_4$ shows

a Kerr-nonlinearity which, in combination with the possibility of engineering the waveguide cross-section to achieve anomalous dispersion [16, 22], can be leveraged for generating so-called Kerr-soliton frequency-combs in high-$Q$ $Si_3N_4$ ring resonators [23–26]. However, silicon nitride is still limited to purely passive functionalities and is unsuited for implementing PD, high-speed electro-optic modulators, or light-emitting devices such as lasers or optical amplifiers.

As these examples illustrate, there is no universally applicable optical integration platform that can offer all functionalities to build high-performance systems. As a consequence, photonic integration crucially relies on the combination of different materials in a common system, and the associated approaches can be largely subdivided into two fields: Chip-level hybrid integration, where different material systems are combined in the front-end of the fabrication line, and package-level hybrid integration processes, which combine fully processed dies of different material systems by co-packaging in so-called multi-chip modules at the back-end of the line. Chip-level hybrid integration comprises so-called heterogeneous integration, which combines different materials based on transfer of InGaAsP epitaxial layers to pre-processed passive silicon or silicon nitride PIC using wafer bonding techniques [27–29]. While such concepts pave a path towards high-density monolithic integration, the underlying processes are still comparatively complex [30] and hence mainly suited for high-volume applications that justify the associated technological overhead. Alternatively, individual dies can first be processed on separate substrates and then be combined in a compact multi-chip module using package-level hybrid integration. This concept comes with a number of advantages, including the use of established manufacturing processes for the respective dies as well as the possibility to optimize and test individual components. This high degree of flexibility is furthermore beneficial for coping with the requirements of a highly fragmented photonics market. However, coupling of light among PIC and the connection to the outside world via fibers represent major challenges due to a possible mismatch of the mode-field diameters (MFD) of the underlying components as well as stringent requirements on the mechanical alignment. Since the associated MFD might range from $10\,\mu m$ for standard single-mode fibers (SMF) at $1.55\,\mu m$ to hardly $0.5\,\mu m$ for SiP waveguides, most PIC employ mode-expanding spot-size converters (SSC) [31, 32] or

inverse tapers [33, 34]. Nevertheless, even if the MFD of the components can be sufficiently matched, they are generally still tiny — bringing the chips in physical contact in spite of similarly small alignment tolerances hence remains a laborious task [35]. Achieving low-loss coupling is therefore usually not possible with passive alignment procedures. Instead, slow and expensive active alignment techniques must be pursued, where the coupling efficiency is continuously monitored during the placement of each component. Such techniques add significantly to the cost of photonic assemblies and are therefore a limiting factor for the scalability of the corresponding systems [36, 37] — despite the mature wafer-level production of the chips themselves.

Additive manufacturing of three-dimensional (3D) freeform coupling elements has emerged as a promising concept to overcome this technological gap for photonic assemblies. In this context, multi-photon lithography (MPL) [38] allows the fabrication of nearly arbitrary 3D structures with tiny features on the nanoscale and superior surface finish [39]. In MPL systems, the localized polymerization of a photoresist material is initiated by irradiating the initially liquid material with a focused femtosecond laser beam. Importantly, conventional microscopic imaging techniques such as nonlinear fluorescence imaging or confocal laser scanning can be employed for the detection of on-chip structures in the coordinate system of the lithography tool. This allows for the precise alignment of the 3D-printed structures with respect to optical interfaces or markers on the underlying PIC. Alignment accuracies of the order of 100 nm can be achieved with such strategies [40], thereby alleviating the need for costly high-precision assembly. Previous work has explored hybrid optical multi-chip or fiber-chip assemblies using 3D-printed dielectric waveguides, so-called photonic wire bonds (PWB) [J1, 40–42], as well as facet-attached microlenses (FaML) [3, J5, J6, 43]. In the first approach, PWB are used in analogy to electrical wire bonds, therefore requiring only moderate accuracy in the initial positioning of PIC and fibers. The precise positions and directions of the optical coupling interfaces are detected in a second step, once the glued assembly is temporarily fixed within the MPL system. A suitable 3D freeform trajectory of the PWB can be found, and the associated waveguide cross-section along this path is adapted to match the MFD of the coupling interfaces on either end of the PWB. Care must be taken such that all interfaces in the package

remain accessible to the lithography tool during the writing process. Typical dimensions of PWB are therefore limited to a single write field of the MPL system, which corresponds approximately to a circle with a diameter of $400\,\mu m$. For bridging larger coupling distances up to the millimeter range, MPL can be used for 3D-printing of individually optimized beam-expanding microlenses on the facets of PIC or fibers prior to final assembly. In this FaML-based approach, the lensed components are then aligned with respect to each other in a second step. As a result of the enlarged beams, alignment is greatly simplified and passive assembly, e.g., based on industry-standard machine vision, becomes feasible. With respect to PWB, this thesis focuses on demonstrating a chip-scale hybrid external-cavity laser (ECL) that is based on low-loss $Si_3N_4$ feedback circuits, and that comprises a PWB as intra-cavity coupling element to connect the InP-based optical amplifier chip with the PIC providing frequency-selective feedback. Regarding FaML, low-loss and alignment-tolerant coupling of individual cores of multimode multicore fibers as well as multimode fiber arrays to standard arrays of vertical-cavity surface-emitting lasers (VCSEL) or PD are demonstrated within transceiver assemblies, that use the concept of space-division multiplexing (SDM) for the parallel transmission of large data streams.

### Challenges and approaches for terahertz assemblies

While photonics has revolutionized fiber-bound communication links, the millimeter-wave (mmW) and terahertz (THz) frequency range likewise opened up new frontiers in wireless communications within the realm of future sixth-generation (6G) networks [44]. Specifically, data transmission at carrier-frequencies of hundreds of GHz has the potential to overcome bandwidth limitations of current wireless networks, thereby enabling for example high-speed wireless backhaul applications [45, 46]. In contrast to free-space optical links, transmission at carrier frequencies in the mmW and THz frequency range are typically less susceptible to attenuation by fog, scintillation, and misalignment [45]. This enables an attractive trade-off between transmission capacity and resilience to weather influences. However, this challenging territory, often referred to as the "THz gap" [47], remained inaccessible for years due to the scarcity of efficient

sources and detectors. Recent advancements in solid-state devices have made THz signal generation and processing possible [48], but the need for packaging solutions that facilitate efficient and broadband connections has become evident as the electrical technologies prevalent at lower carrier frequencies are not arbitrarily scalable to shorter and shorter wavelengths.

Historically, mmW and THz assemblies were based on precision-milled metallic split-blocks [48, 49], facilitating highly efficient signal guidance and coupling through hollow waveguides. However, the evolving need for weight and cost reduction drove the demand for new packaging and assembly concepts for THz circuits. In close analogy to photonic integration involving PIC, hybrid multi-chip modules combining amplifiers based on monolithic microwave integrated circuits (MMIC) with, e.g., THz signal sources, detectors and antennas hence play a pivotal role in providing a versatile platform addressing the associated frequency range. THz signals can for example be generated by means of opto-electronic conversion, where the signal is first modulated onto an optical carrier which is then downconverted to the THz domain in a second step. Hereby, photomixers such as PD are commonly used for mixing of the two optical signals, which leads to a beat note in the photocurrent centered about the difference frequency. In this context, uni-traveling-carrier (UTC) PD coupled to optical waveguides on the InP platform are particularly interesting due to their capability for high-speed operation as a result of the large operating bandwidths [50]. The reverse operation, namely the conversion of THz signals into the optical domain, can be achieved with the help of fast photoconductors [51], ultra-broadband modulators [52] or plasmonic internal-photoemission detectors (PIPED) [53], which could potentially be co-integrated on the SiP platform. On the other hand, state-of-the-art MMIC-based power amplifiers achieving operating bandwidths of more than 200 GHz are commonly based on InP heterojunction bipolar transistors (HBT) or indium gallium arsenide (InGaAs) high-electron-mobility transistors (HEMT) [54]. In the associated multi-chip modules, electrical chip-to-chip and chip-to-board interconnects between the various MMIC and the underlying packaging substrate are usually realized by thermosonic ribbon bonding [49]. However, due to limited control over the 3D geometry of the electrical conductors, a significant mismatch of the characteristic impedances at the transition of interconnected transmission

lines is hardly avoidable. A sizable parasitic inductance is furthermore introduced if the electrical bond wires are getting extensively long [55]. Flip-chip interconnects on the other hand suffer from a parasitic capacitance of the associated bond pads or balls. Improving the performance thus crucially relies on the optimization of the interconnect geometry [56]. In all these cases, however, the design freedom and precision of the underlying manufacturing processes are limited and do in particular not allow for a versatile adaption of the 3D geometry to the extent that the characteristic impedance of the interconnect can be precisely controlled. The achievable operational bandwidths of associated multi-chip modules are hence limited to a narrow band due to increasing reflection and radiation losses at high frequencies [49]. Other prevailing solutions that exploit on-chip antennas for radiating into, e.g., hollow waveguides have the drawback of a limited antenna efficiency and directivity. Although antennas that are suspended from the underlying substrate can be used for improved performance, the associated complex fabrication and assembly still remain laborious tasks [49]. These challenges underpin the urgency for innovative packaging solutions of THz assemblies that address the specific demands while remaining cost-effective, compact, and efficient.

Within this thesis, the concept of 3D-printed coupling elements using MPL is further extended to the field of mmW and THz assemblies. A novel approach is introduced and experimentally demonstrated that exploits precisely localized conductive coatings of *in-situ* printed polymer templates, obtained through highly directional metal deposition techniques in combination with 3D-printed shadowing structures. The resulting metal-coated freeform structures (MCFS) offer high surface quality, low dielectric losses in the polymer base structure, and high coating conductivities close to those of bulk metal, while alleviating the need for additional mechanical assembly steps. Owing to the unprecedented design freedom offered by this concept, the fabricated 3D-freeform mmW and THz structures overcome the limitations of conventional planar architectures and offer hitherto unachieved precision and functionality. The presented experimental demonstrations comprise ultra-broadband chip-chip interconnects, THz probe tips, and suspended THz antennas that are raised above the underlying substrate, offering bandwidths in excess of $0.3\,\mathrm{THz}$.

# 2 Theoretical and technological background

This chapter introduces the theoretical and technological background which is relevant for this work. Section 2.1 gives a general introduction to direct-write multi-photon laser lithography (MPL), followed by a brief description of the MPL system used within this work. In Section 2.2, key metrics of laser frequency noise are presented and applied to the case of hybrid integrated external-cavity lasers (ECL). Section 2.3 summarizes multiplexing techniques in optical fiber communications with an emphasis on space-division multiplexing (SDM) in short-reach systems. Finally, Section 2.4 outlines the fundamentals of millimeter-wave (mmW) and terahertz (THz) technology including electrical transmission lines and antennas.

## 2.1 Direct-write multi-photon laser lithography

Over the previous two decades, multi-photon lithography (MPL) has emerged as a powerful laser-based additive micro- and nanofabrication technique, enabling precise fabrication of three-dimensional structures with unparalleled design freedom and highest resolution [38, 57]. The technology has been used in various application fields, including (but not limited to) micromechanics [58], material sciences [59], microfluidics [60], life sciences [61], microelectronics [62] as well as photonics [3, 39, 42, 63], where *in-situ* printed optical coupling elements offer new perspectives for package-level system integration [40, J5].

### 2.1.1 Fundamentals of multi-photon lithography

In essence, multi-photon lithography relies on the simultaneous absorption of two or more photons in the focal spot of a high-intensity laser. Interestingly, the process of two-photon absorption was first postulated by Maria Göppert-Mayer[1] in her 1930 doctoral thesis and one year later in a publication [64], although its experimental demonstration was considered unfeasible at the time. It was only after the advent of Theodore Maiman's laser in 1960 that access to the necessary high optical intensities became possible, leading to the first experimental verification of two-photon absorption by Kaiser and Garrett in 1961 [65]. Despite this achievement, it was not until three decades later, in the 1990s, that two-photon absorption found practical applications, particularly in biological microscopy, where two-photon-induced fluorescence microscopy is now widely used [66]. In 1997, Maruo and coworkers played a pivotal role in advancing the field by pioneering two-photon polymerization using a photo-sensitive polymer material [67]. The evolution of MPL was further facilitated by the development of cost-effective and compact fiber-based femtosecond (fs) lasers, replacing significantly more expensive mode-locked titanium-sapphire lasers. Today, commercial lithography systems have become readily available, leading to widespread adoption of MPL as a tool of choice for high-resolution 3D lithography [68].

In MPL systems, negative-tone photoresists are commonly used, for which molecular moieties in exposed regions are cross-linked and hence become insoluble in a subsequent solvent-based development process. These photoresists usually consist of soluble organic monomers[2] and a photoactive substance, often referred to as a photoinitiator. In most commonly used photoresists, the photoinitiator generates free radicals upon exposure to light, thereby initiating a radical-polymerization chain reaction. This process cross-links the monomers, each possessing one or

[1] The two-photon absorption cross-section is typically given in the non-SI unit Göppert-Mayer (GM), $1\,\mathrm{GM} = 1 \times 10^{-50}\,\mathrm{cm}^4\,\mathrm{s}$ per photon and molecule.

[2] Various chemical systems have been employed for MPL photoresists, including epoxies [69], thiol-ene chemistry [70] or (meth)acrylates [71]. Among these, multi-functional acrylates are widely used due to their cost-effectiveness, availability, and rapid polymerization rates [72].

more functional groups, and leads to the formation of a polymer chain or network. Once a certain polymerization level is reached, the polymer network becomes insoluble to the developer. To avoid unrestrained chain growth, which could cause the entire material to be cross-linked and would hence impede localized solidification as needed for defining 3D features with high spatial resolution, termination of this chain reaction is crucial. Termination can either occur through reaction with other radicals or through the presence of inhibitors like dissolved molecular oxygen [72] or deliberately added quenchers [73]. Photoresist materials are therefore carefully engineered such that these termination effects are strong enough to not negatively impact the achievable resolution. As a consequence, the size of the polymerized volume element (voxel) is predominantly determined by the level of exposure to the lithography radiation [74]. To model the influence of the lithography system and the beam shape on the locally achieved degree of polymerization within one such volume element, a common assumption is that the amount of generated radicals is directly proportional to the deposited lithography dose $D$ [71]. The number of simultaneously absorbed photons which are required to generate one radical is commonly referred to as the nonlinearity order $N$. With the exposure time $\tau_{\mathrm{exp}}$ and a local photon flux $\phi$ proportional to the incident laser power $P$, the accumulated exposure dose $D$ can be expressed as

$$D \propto \tau_{\mathrm{exp}}\, \phi^N \propto \tau_{\mathrm{exp}}\, P^N. \tag{2.1}$$

The nonlinearity order $N$ depends on the photoinitiator as well as on the lithography wavelength. A significant number of photoinitiators known from traditional photolithography using ultraviolet (UV) light also exhibit two-photon absorption ($N = 2$) when exposed to near-infrared (NIR) light at approximately $800\,\mathrm{nm}$, i.e., at half the UV photon energy. Nevertheless, it is also known that when using these photoinitiators, more intricate absorption processes such as cascaded absorption

via a triplet state arise, therefore resulting in higher nonlinearity orders ($N > 2$) in many situations[3] [71].

Despite the complex and hitherto not fully understood reaction kinetics of the photoresists, the creation of micro-structures by MPL can generally be modeled by two simplifying assumptions [75, 76]:

- **Threshold behavior:** According to the threshold model, the highly-nonlinear dependence of the photoresist solubility on the exposure dose can be approximated by a step-like behavior. The material is only sufficiently cross-linked if a certain local threshold dose $D_{\mathrm{th}}$ is exceeded, whereas all regions with $D < D_{\mathrm{th}}$ are not polymerized and do not remain after the development process.
- **Dose accumulation:** According to the accumulation model, a photoresist "integrates" exposure doses over time[4]. The total locally deposited dose is therefore given by $D \propto \int P^N(t)\,\mathrm{d}t$, where $P^N(t)$ is the time-dependent local incident laser power. Note that the validity of the accumulation model is subject to some limitations[5].

Figure 2.1 shows the simulated dose distributions $D$ for different lithography laser wavelengths $\lambda$ (measured in vacuum) and nonlinearity orders $N$. The depicted normalized distributions are based on calculations of the optical point-spread

[3] Experimental studies of the nonlinearity order have been performed by varying the repetition rate and the pulse energy of the lithography laser when exposing lines with a constant velocity [71]. It was found that, for repetition rates above 100 kHz and depending on the chemical composition of the specific photoresist, the nonlinearity order for the polymerization threshold lies in the range $N = 2 \ldots 3$, whereas the damage threshold indicated by micro explosions rather follows a $N = 5 \ldots 7$ dependency. This discrepancy arises, e.g., from heat accumulation in the photoresist when using large pulse energies and/or high repetition rates, thus necessitating careful optimization of the parameters for maintaining a wide process window.

[4] The opposite of the accumulation model would be the forgetting photoresist, which completely ignores all below-threshold exposures. So far, however, no practical viable forgetting photoresist has been demonstrated.

[5] For instance, photoresin diffusion processes or the decay of radicals are neglected. The model also breaks down in cases where the laser power is chosen so low that the rate of oxygen diffusion from the surrounding exceeds the rate of radical generation, thereby preventing polymerization even for infinitely long exposure times. In analogy to similar effects in analog photography, this is referred to as the Schwarzschild-effect [77].

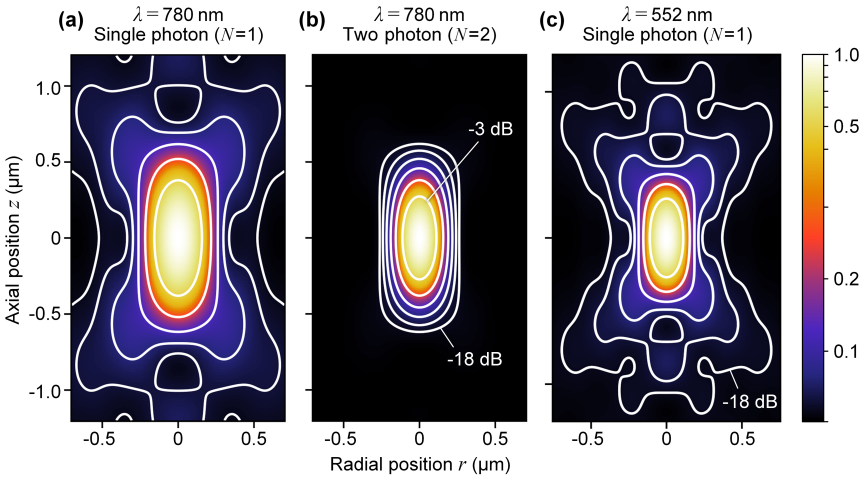


**Fig. 2.1:** Simulated normalized distributions of deposited lithography dose $D$ in a photoresist ($n = 1.52$) for different vacuum wavelengths $\lambda$ of the lithography laser and for different nonlinearity orders $N$. The depicted distributions are based on calculations of the optical point-spread function (PSF) assuming an immersion-objective with a numerical aperture of NA $= 1.4$. White contour lines depict 3 dB steps of deposited dose. **(a)** Dose distribution for single-photon absorption ($N = 1$) at $\lambda = 780$ nm, indicating a low resolution and significant axial side lobes. Hence, exposing adjacent positions results in dose accumulation in all three dimensions, see Fig. 2.2. **(b)** Dose distribution for two-photon absorption ($N = 2$) at $\lambda = 780$ nm, revealing an improvement in resolution and largely suppressed side lobes. **(c)** Dose distribution for single-photon absorption ($N = 1$) at $\lambda = 780\,\text{nm}/\sqrt{2} \approx 552$ nm, providing nominally identical resolution as in Subfigure (b). However, the influence of the axial side lobes remains much more pronounced.

function (PSF)[6] assuming an immersion objective with a numerical aperture of NA $= 1.4$ [38]. The refractive index of the photoresist, which simultaneously acts as an index-matched immersion fluid between the substrate and the lithography objective, is set to $n = 1.52$. White contour lines depict 3 dB steps of deposited dose, taken with respect to the highest dose close to the center of the voxel. When comparing Fig. 2.1(a) and (b), one can clearly see that for a fixed lithography wavelength of, e.g., $\lambda = 780$ nm the dose distribution for two-photon absorption ($N = 2$) is more confined than in the case of single-photon

[6] The depicted optical PSF can be numerically calculated using the vectorial Debye approximation [38, 78].

absorption ($N = 1$). Consequently, the resolution is enhanced as can be inferred from the denser contour spacing. Generally speaking, by using an $N$-th order absorption process, the achievable resolution improves by roughly a factor of $\sqrt{N}$ [75]. It is therefore often wrongly claimed that the enhanced optical resolution is the main advantage of multi-photon lithography. However, as can be seen in Fig. 2.1(c), the nominally identical resolution as in the depicted two-photon absorption case can also be achieved by a single-photon absorption process using a green laser at $\lambda = 780\,\mathrm{nm}/\sqrt{2} \approx 552\,\mathrm{nm}$. In fact, by virtue of the threshold model, arbitrarily small voxels could theoretically be solidified irrespective of the nonlinearity order $N$ or laser wavelength $\lambda$, given that the laser power $P$ can be adjusted such that only a small portion of the illustrated dose distribution $D$ is just above the threshold dose $D_{\mathrm{th}}$. Therefore, any of the contour lines in Fig. 2.1 could depict a region where a polymerized voxel is formed — the size is especially not limited to the optical resolution according to the Abbe diffraction limit [75].

The key advantage of using multi-photon lithography is only revealed when fabricating complex three-dimensional bulk structures. In traditional single-photon absorption ($N = 1$), the PSF exhibits significant side lobes as seen in Fig. 2.1(a) and (c). The deposited doses for each focus therefore overlap in the entire volume and are integrated according to the accumulation model. This leads to unintentional dose accumulation and thereby polymerization outside of the desired 3D-geometry if $D_{\mathrm{th}}$ is exceeded — a phenomenon known as the proximity effect [1, 76]. This issue becomes especially pronounced when structuring large thin areas oriented perpendicular to the axial direction of the lithography beam. On the contrary, for multi-photon absorption ($N \geq 2$) the axial lobes of the PSF are suppressed significantly as seen in Fig. 2.1(b) for $N = 2$. Dose contributions located at a larger distance to the voxel center therefore fail to add up to a significant degree. This phenomenon can be more intuitively understood with the help of a simple model, illustrated in Fig. 2.2 [1]. For a first exposure at a point $P_0$ within the focal plane, a focal area $A_0$ with a uniform intensity $I_0$ and consequently a uniform dose $D_0$ within are considered. The unintentionally accumulated dose $D_1$ at a second point $P_1$, which is located outside the writing plane at an axial distance $\Delta z$ from $P_0$, can then be estimated. Owing to the $s$-fold increase of the lithography

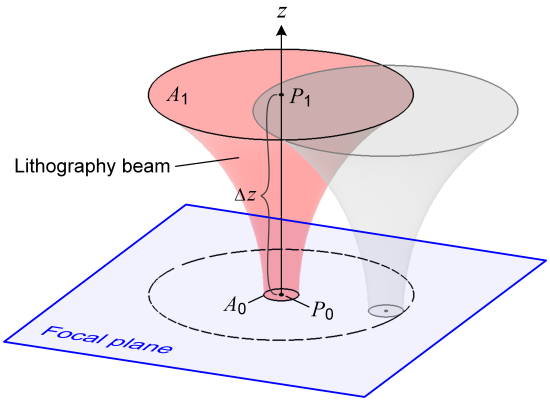


**Fig. 2.2:** Simplified model for visualizing the impact of dose accumulation outside the writing plane when structuring extended areas within a focal plane of the lithography laser (blue rectangle). For a first exposure at a point $P_0$ inside the focal plane, a focal area $A_0$ with a uniform intensity $I_0$ is considered. For this illumination of $A_0$, the unintentionally accumulated dose $D_1$ at a second point $P_1$, which is located outside the writing plane at an axial distance $\Delta z$ from $P_0$, can then be estimated. Owing to the $s$-fold increase of the lithography beam cross-section in the plane of $P_1$, the intensity $I_1$ at $P_1$ is $s$-fold smaller, i.e., $I_1 = I_0/s$. However, scanning the laser beam within the projected area of $A_1$ in the focal plane of $P_0$ (indicated by the dashed circle) will lead to an unintentional dose accumulation at $P_1$. This $z$-independent dose accumulation essentially impedes 3D structuring for $N = 1$, but may be significantly reduced by utilizing an absorption process with a nonlinearity order $N \geq 2$.

beam cross-section in the plane of $P_1$, $A_1 = sA_0$, the intensity $I_1$ at $P_1$ is $s$-fold smaller, i.e., $I_1 = I_0/s$. However, when the laser beam is laterally scanned within the projected area of $A_1$ in the focal plane of $P_0$ (indicated by the dashed circle), the dose at $P_1$ will accumulate for the $s$ non-overlapping point exposures required to fill this area. For single-photon absorption ($D \propto I$), we hence find that the unintentionally accumulated dose is given by $D_1 \propto s \times I_0/s = I_0$, which is constant[7] and in particular independent of the axial distance $\Delta z$. On the other hand, for the case of an $N$-th order absorption process ($D \propto I^N$), the relation becomes $D_1 \propto s \times I_0/s^N = I_0/s^{N-1}$, such that the reduced dose accumulation

[7] Strictly speaking, this is only correct if the absorbance of the input light in the photoresist can be neglected between the two considered planes with separation $\Delta z$. Nevertheless, printing of 3D-structures is possible even when using linear absorption processes ($N = 1$) in practice, since the accumulation model does not consider the case of very low exposure doses for which practically no polymerization is observable independently of the exposure time, see also [5].

leads to a drastically improved shape-fidelity. Nevertheless, the resolution of the lithography system will ultimately be limited if two voxels are placed very close to one another as a result of the overlapping dose distributions. The minimum separation between the two voxels for which two adjacent features can still be distinguished is determined by the multi-photon Sparrow criterion[8] [75], and is often referred to as the "resolution of the lithography system".

Another essential metric of an MPL system is the attainable aspect ratio of a polymerized voxel. While the ideal voxel would be spherical, it becomes evident from Fig. 2.1(b) that the voxel shape is typically elongated along the axial coordinate $z$ and further dependent on the exposure dose $D$. Assuming that the tails of the dose distribution are sufficiently suppressed, we can make the simplified assumption that the relevant center part of the distribution can be well approximated by a 3D Gaussian distribution with standard deviations $\sigma_r$ and $\sigma_z$ in the radial direction $r$ and in the axial direction $z$, respectively,

$$D(r,z) \propto \mathrm{e}^{-\frac{r^2}{2\sigma_r^2}} \, \mathrm{e}^{-\frac{z^2}{2\sigma_z^2}}. \tag{2.2}$$

As can be seen from Eq. 2.2, the dose distribution $D(r,z)$ is rotationally symmetric with respect to the axis of the lithography beam and drops off from its on-axis maximum value depending on the radial distance $r$. In the case of a low-NA objective, the lateral and axial optical resolution lead to $\sigma_r \propto \frac{\lambda/n}{\mathrm{NA}/n}$ and $\sigma_z \propto \frac{\lambda/n}{(\mathrm{NA}/n)^2}$, respectively [79]. The dose distribution in the radial direction hence scales roughly linearly, while the size in the axial direction scales approximately quadratically with the NA. For the aspect ratio of the voxel we consequently find $\sigma_z/\sigma_r \propto n/\mathrm{NA} = 1/\sin(\theta_{\max})$ with the objective acceptance angle $\theta_{\max}$. The need for high-NA objectives therefore becomes immediately apparent when considering the fabrication of 3D-structures with fine details, in particular in the axial direction. Note that for high-NA objectives there does not exist a closed form expression for the PSF. Thus, numerical simulations as shown in Fig. 2.1

[8] For conventional optical instruments, the Sparrow limit is defined as the distance between two point objects of equal intensity at which a dip half way between them ceases to be visible in the joint intensity distribution.

are used to approximate the expected lithography resolution as well as the exact aspect ratio of the voxel. Empirical approximations for $\sigma_r$ and $\sigma_z$ for $\mathrm{NA} > 0.7$ are given as[9] [66]

$$\begin{aligned} \sigma_r &= \frac{0.230}{\sqrt{N}} \times \frac{\lambda}{\mathrm{NA}^{0.91}}, \\ \sigma_z &= \frac{0.376}{\sqrt{N}} \times \frac{\lambda}{n - \sqrt{n^2 - \mathrm{NA}^2}}. \end{aligned} \tag{2.3}$$

When using identical values as for the dose simulations in Fig. 2.1, namely an objective with $\mathrm{NA} = 1.4$ immersed in a photoresist with $n = 1.52$ at a lithography wavelength of $\lambda = 780\,\mathrm{nm}$, we find from Eq. 2.3 $\sigma_r \approx 93\,\mathrm{nm}$ and $\sigma_z \approx 230\,\mathrm{nm}$ for a two-photon process ($N = 2$). The aspect ratio of the voxel is given as $\sigma_z/\sigma_r \approx 2.5$. These values correspond to full-width at half maximum (FWHM) beam widths of $w_{r,\mathrm{FWHM}} = 220\,\mathrm{nm}$ and $w_{z,\mathrm{FWHM}} = 526\,\mathrm{nm}$, which can be directly interpreted as the voxel size in the lateral and the axial direction, respectively, if the threshold dose $D_{\mathrm{th}}$ lies at half of the peak dose. The corresponding region is depicted in Fig. 2.1(b) by the contour line at $-3\,\mathrm{dB}$.

### 2.1.2 Lithography system

The fabrication of 3D-printed coupling structures for photonic and terahertz assemblies does not only require highest resolution on the sub-micrometer scale, but also precise alignment of the fabricated structures with respect to existing circuitry or alignment markers on the underlying substrates. Within this thesis, a lithography machine from preceding work [2] was used, see Fig. 2.3. Only minor modifications in the respective processes and machine software were required for the experimental demonstrations presented in Chapter 3, 4 and 5.

[9] Note that among various literature sources, the widths of a Gaussian distribution with given standard deviation $\sigma$ may be defined differently. The width could be referred to as 1/e half-width $w_{1/\mathrm{e}} = \sqrt{2}\,\sigma \approx 1.41\,\sigma$, as $1/\mathrm{e}^2$ half-width $w_{1/\mathrm{e}^2} = 2\,\sigma$ or as full-width at half maximum (FWHM) $w_{\mathrm{FWHM}} = 2\sqrt{2\ln 2}\,\sigma \approx 2.35\,\sigma$.

The MPL system is implemented as a versatile setup designed to combine high-resolution nanolithography and advanced imaging capabilities. The core of the system is a fs-laser source emitting $58\,\text{fs}$ pulses at a repetition rate of $100\,\text{MHz}$ at $\lambda = 780\,\text{nm}$. A pulse compressor pre-chirps the pulses to compensate the group delay dispersion (GDD) introduced by various optical components in the system. The optical power of the laser beam is modulated using an acousto-optic modulator (AOM). The beam then passes the optical setup until it reaches an inverted microscope[10], where a high-NA objective[11] focuses the laser beam into the liquid photoresist, which concurrently serves as an index-matched immersion medium. The AOM allows for precise control of the laser intensity, enabling the deposition of specific exposure doses in the photoresist. Galvanometric mirrors are used for fast scanning of the beam in the $(x, y)$-plane, allowing the layer-by-layer fabrication of complex 3D structures at manageable fabrication times. For controlling the $z$-position, a piezoelectric actuator moves the microscope objective accordingly. The high NA of the objective ensures a small focal spot, resulting in sub-micron resolution during the fabrication process. To achieve the highest possible NA and thus the smallest possible voxel size, a variable beam expander is integrated into the system. The beam expander ensures that the rear aperture of the objective is fully illuminated, thereby maximizing the effective NA.

The lithography system also offers two advanced imaging modalities: confocal laser imaging and fluorescence imaging, both operated at laser powers far below the polymerization threshold. For confocal imaging, the lithography focus is scanned throughout the sample, and the recorded signal levels of the back-scattered light can be used for reconstruction of a volumetric image based on the known focus locations. This proves especially useful for the detection of strongly reflective surfaces within the sample, where the large amount of reflected light leads to a high signal-to-noise ratio (SNR). The acquired images are furthermore inherently aligned to the coordinate system of the lithography system, and fabricated structures

[10] In such a configuration, the microscope objective in fact points upwards and the sample is mounted inside the MPL system upside-down.

[11] The depicted MPL system can be operated with different objectives. Within the scope of this thesis, the 3D-printed coupling structures presented in Chapter 3 have been fabricated using a $63\times\,/\,1.4$ objective. All other samples have been printed with a $40\times\,/\,1.4$ objective.

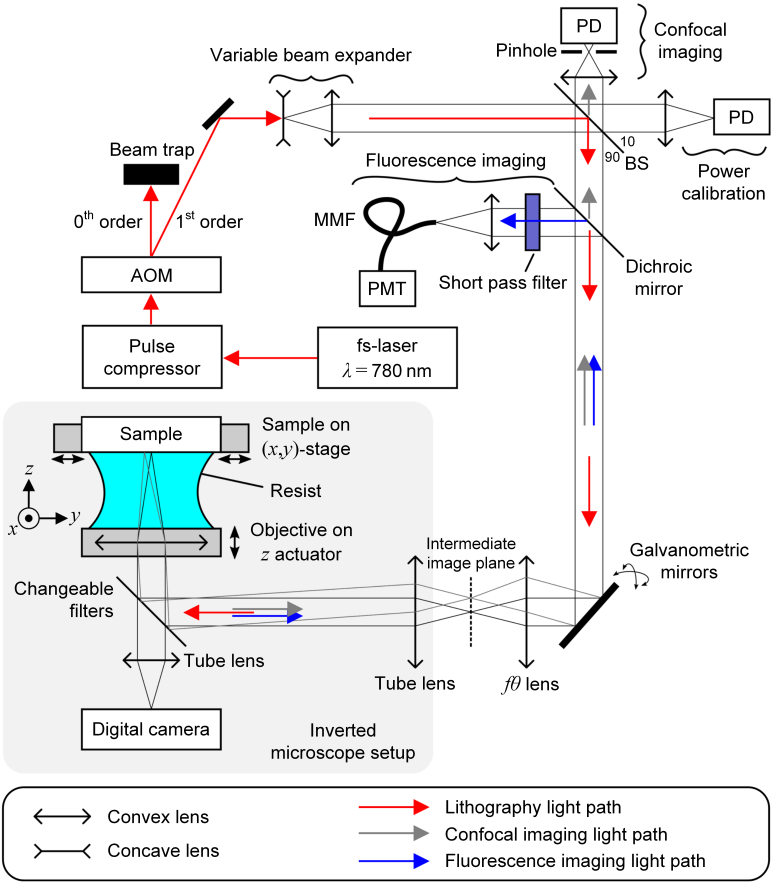


**Fig. 2.3:** Schematic of the MPL system [2] used for this work. Abbreviations: AOM – acousto-optic modulator; BS – beam splitter; PD – photodetector; MMF – multimode fiber; PMT – photo multiplier tube. The lithography system utilizes a femtosecond (fs) laser emitting around a vacuum wavelength of $\lambda = 780\,\mathrm{nm}$, the power of which can be modulated by an acousto-optic modulator (AOM). After the modulator, the beam passes through the optical setup and reaches an inverted microscope, where a high-NA objective focuses the laser beam into the liquid photoresist which concurrently serves as an index-matched immersion medium. Galvanometric mirrors are used for fast scanning of the beam in the $(x, y)$-plane. For controlling the $z$-position, a piezoelectric actuator moves the microscope objective accordingly. The MPL system is equipped both with a confocal as well as a fluorescence imaging path for precise detection and alignment of the fabricated structures with respect to existing features on the sample. The illumination for standard bright-field microscopic imaging has been omitted for simplicity. *Adapted and reproduced with permission from [1, 2].*

can thereby be precisely aligned with respect to existing circuitry or alignment markers on the underlying substrates. Note that finding the desired sample position based on a maximum of the confocal signal requires precise axial alignment of the confocal pinhole, which can be done using a suitable test target. As a complementary modality, fluorescence imaging relies on multi-photon excitation of the photoinitiator and a parasitic decay path present in the photoresist [80], which leads to the emission of fluorescent light only if the focal spot is within the material. Since this highly localized fluorescence emission occurs specifically at the focal spot of the laser beam, no additional spatial filtering is required due to its confined nature. Fluorescence imaging proves particularly valuable for weakly reflecting interfaces, such as resist-glass interfaces and hence allows for accurate determination of interface height and monitoring of the optical resolution of the MPL system without relying on the alignment of specific optical components such as pinholes, see Appendix D of [2] for more details.

One critical aspect of any MPL system is the achievable peak printing rate (in voxels/s), which is loosely determined by the scanning speed of the laser focus $v_{\mathrm{scan}}$ for a specific lateral voxel size[12]. Typical scanning speeds used within the framework of this thesis are of the order of $50\,\mathrm{mm/s}$, resulting in peak printing rates of approximately $2 \times 10^5$ voxels/s when considering the simulated lateral voxel size of $w_{r,\mathrm{FWHM}} = 220\,\mathrm{nm}$. The scanning speed $v_{\mathrm{scan}} \propto 1/\tau_{\mathrm{exp}}$ could be further increased by appropriately scaling the laser power $P$ in proportion to $\sqrt[N]{v_{\mathrm{scan}}}$ as to maintain the effective dose for a given nonlinearity order $N$, see Eq. 2.1. Peak printing rates of up to $10^7$ voxels/s have already been demonstrated with an AOM-based scanning system [81]. Further parallelization of the printing process can be achieved through the use of multiple voxels in conjunction with a digital phase mask, which can lead to printing rates of up to $10^8$ voxels/s [81]. Typical volume printing rates for MPL[13] lie in the range $(10^{-9} \ldots 10^{-2})\,\mathrm{mm^3/s}$.

[12] In practice, the maximum focal scanning speed can only be reached for large structures with a high fill factor, for which the scanning direction does not change too often within a single writing field. The overall volume printing rate is often additionally limited by the settling time of the piezoelectric drive which is used to move the comparatively heavy objective lens.

[13] An up to date overview of the performance parameters for various printing techniques can be found here: `https://3dprintingspeed.aph.kit.edu`.

It is also worth mentioning, that significant efforts have recently been spent to replace expensive fs-lasers in conventional MPL setups by cheap continuous-wave (CW) lasers through the use of so-called two-step absorption as the primary excitation mechanism [82–84]. In this concept, a special photoinitiator is added to the photoresist to permit the excitation of electrons into a real idle state via a first single-photon absorption step. Absorption of a second photon via another single-photon process then allows the electron in the idle state to reach an energetic level from which the polymerization reaction is started[14]. This successive two-step excitation can take place, e.g., using a single $405\,\mathrm{nm}$ CW laser if the absorption spectra of the ground and intermediate state overlap sufficiently[15] [82]. Importantly, the same quadratic dependency on the incident power as for two-photon absorption ($N = 2$) is achieved, permitting a similar resolution. However, the achievable printing rates of the order of $10^4$ voxels/s are currently still limited by the lifetime associated with the intermediate state [82]. Alternatively, the photoresist is engineered such that the absorption spectrum of the ground state is maximum at the emission wavelength of a first laser, whereas the intermediate state is only sensitive to an exposure at the wavelength of a second laser. This so-called two-color two-step absorption can be used to reach improved volume printing rates of $(10^{-2} \ldots 10^{2})\,\mathrm{mm}^3/\mathrm{s}$ at the expense of larger voxel sizes in a light-sheet-type printing configuration [83]: In this approach, the beam of a CW laser emitting at $660\,\mathrm{nm}$ is shaped into a flat sheet of light parallel to the substrate. A $440\,\mathrm{nm}$ CW laser then projects a high-resolution image into a focal plane coinciding with the light sheet. Polymerization can thus only occur in the regions where both beams overlap. Although this technique could in principle be beneficial for reducing the fabrication time — especially for mmW and THz structures with dimensions up to the mm-range — the concept can neither be readily applied to photonic nor THz multi-chip assemblies since the various dies on the submount severely restrict the accessibly of the coupling interfaces to the light sheet.

[14] Suitable photoinitiators for such chemical systems are known as reluctant Norrish type-I compounds [38] and comprise, e.g., benzil or biacetyl. Quenchers and scavengers are commonly added to ensure that no chemical reaction is triggered from the intermediate state [82, 83].

[15] An additional laser at $532\,\mathrm{nm}$ may be used for promoting transitions from the intermediate state, thereby increasing the polymerization rate and consequently the achievable printing speed [84].

## 2.2 Laser frequency noise and linewidth

Lasers with high spectral purity are important in various fields, including precise frequency measurement [85], advanced spectroscopy [86], high-speed coherent optical communications [31], or quantum photonic applications [87], just to name a few. Even for a single-frequency laser, where essentially all power is confined in a single resonator mode, the emitted light is never perfectly monochromatic as the amplitude and phase will undergo random fluctuations which are, e.g., triggered by spontaneous emission in the laser gain medium. While amplitude fluctuations lead to laser intensity noise[16], phase fluctuations and associated phase and frequency noise lead to a non-zero spectral width $\delta f$ of the emitted laser line or, equivalently, to a limited temporal coherence. Note that frequency and phase noise are often used interchangeably, in essence describing the same phenomenon in different ways[17].

### 2.2.1 Metrics of laser frequency noise

Historically, there exist two interrelated yet different definitions which are commonly used when referring to the frequency noise of a laser as illustrated in Fig. 2.4. The spectral characteristics can be described either in terms of the power spectral density (PSD) of the instantaneous optical frequency fluctuations $S_{\mathrm{F}}(f)$, often simply called the frequency-noise spectrum, Fig. 2.4(a), or by means of the optical

[16] In this context, the frequency-dependent so-called relative intensity noise $\mathrm{RIN}(f)$ is commonly used as a metric. The quantitiy $\mathrm{RIN}(f)\,\mathrm{d}f$ indicates the relative power fluctuations within an infinitesimally small frequency interval $\mathrm{d}f$ with respect to the average overall optical power of the laser. $\mathrm{RIN}(f)$ can hence be integrated over a specified measurement bandwidth to obtain a root-mean-squared (RMS) value of the dimensionless RIN, which may be specified in percent. The RIN of a laser source is usually quantified by specifying the RIN within a reference bandwidth of 1 Hz on a dB scale, indicated by the unit $\mathrm{dBHz}^{-1}$.

[17] In fact, frequency noise refers to the instantaneous frequency deviation of the laser tone under consideration from an ideal tone with constant frequency and corresponds to the time-derivative of the associated phase deviations. An ideally constant frequency corresponds to a linear increase of phase as a function of time — any random deviation of the time-dependent phase from this purely linear phase evolution can therefore be attributed to frequency noise.

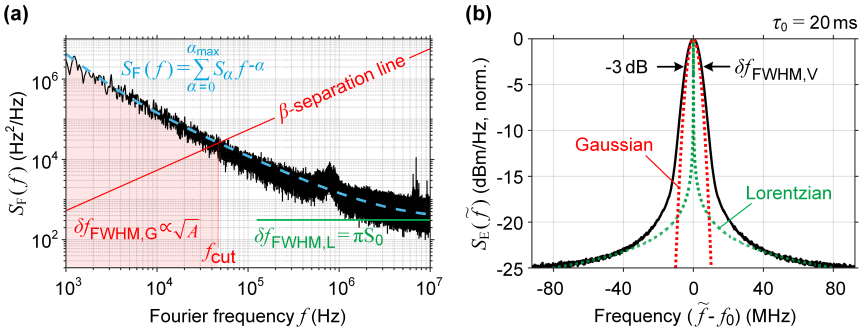


**Fig. 2.4:** Typical frequency-noise spectrum $S_\mathrm{F}(f)$ and associated line shape $S_\mathrm{E}(\tilde{f})$ of a single-frequency laser oscillating at $f_0 = 1.55\,\mu\mathrm{m}$. **(a)** The frequency-noise spectrum can be modeled as a sum of individual noise contributions $S_\alpha f^{-\alpha}$ of integer order $\alpha$, and the corresponding fit is given by the blue dashed line ($\alpha_\mathrm{max} = 3$). Depending on the observation time $\tau_0$, different parts of the frequency-noise spectrum influence the associated line shape in fundamentally different ways. The frequency-noise spectrum can therefore be divided in two distinct regions, defined by the so-called $\beta-$separation line $S_\beta(f) = (8\ln(2)\,f)/\pi^2$, for which $S_\mathrm{F}(f_\mathrm{cut}) = S_\beta(f_\mathrm{cut}) = (8\ln(2)\,f_\mathrm{cut})/\pi^2$ holds true. For long observation times $\tau_0$, higher-order noise contributions ($\alpha \geq 1$) at low Fourier frequencies dominate, and the linewidth $\delta f_\mathrm{FWHM,G}$ is proportional to the red-shaded area $\sqrt{A}$, which is defined by $f_\mathrm{cut}$ and by the minimum observable Fourier frequency $f_\mathrm{min} = 1/\tau_0$. For sufficiently short observation times $\tau_0$, the relevant part of the frequency-noise spectrum at Fourier frequencies $f > f_\mathrm{min}$ becomes purely white ($\alpha = 0$), and the associated linewidth is given by $\delta f_\mathrm{FWHM,L} = \pi S_0 \approx 1\,\mathrm{kHz}$ (green line). **(b)** The line shape $S_\mathrm{E}(\tilde{f})$ for an observation time of $\tau_0 = 20\,\mathrm{ms}$ can be well approximated in the central region by a Gaussian ($\delta f_\mathrm{FWHM,G}$, red dotted line), whereas the tails are best reproduced by a Lorentzian function ($\delta f_\mathrm{FWHM,L}$, green dotted line). The overall line shape can be modeled by a Voigt function, leading to the linewidth $\delta f_\mathrm{FWHM,V}$.

"line shape" $S_\mathrm{E}(\tilde{f})$, which is defined as the PSD of the optical field, Fig. 2.4(b). While both approaches complement each other, knowledge of the frequency-noise spectrum generally provides more comprehensive information about the origin of the laser frequency noise as will be motivated in the following [88, 89].

As a starting point, we consider an optical field with a constant amplitude[18] $E_0$ (in units of $\sqrt{W}$) oscillating at the frequency $f_0$ which is described by $\underline{E}(t) = E_0 \mathrm{e}^{\mathrm{j}[2\pi f_0 t + \varphi(t)]}$, where $\varphi(t)$ are random phase fluctuations. The instantaneous frequency $\tilde{f}(t)$ is then given by the temporal derivative of the overall phase,

[18] Note that $E_0$ can effectively be considered to be constant since amplitude fluctuations are strongly damped as a result of gain saturation in the laser resonator [90]. The influence of amplitude noise on the phase fluctuation $\varphi(t)$ is therefore neglected.

i.e., $\tilde{f}(t) = f_0 + \frac{\mathrm{d}\varphi}{\mathrm{d}t}/(2\pi) = f_0 + \delta\tilde{f}(t)$ with the term $\delta\tilde{f}(t)$ describing the fluctuations of the instantaneous frequency originating from the random phase $\varphi(t)$. We further assume that the phase change $\Delta\varphi(t_1, t_2) = \varphi(t_2) - \varphi(t_1)$ in-between times $t_1$ and $t_2$ can be described by a zero-mean stationary Gaussian random process, which means that its characteristics such as the variance do not depend on the choice of the origin of time, but rather on the time difference $\tau$ only, i.e., $\Delta\varphi(t, \tau) = \varphi(t+\tau) - \varphi(t)$. The coherence function (autocorrelation) associated with the fluctuations of the instantaneous frequency deviation $\delta\tilde{f}(t)$ is then given as $\Gamma_{\delta\tilde{f}}(\tau) = \overline{\delta\tilde{f}(t)\,\delta\tilde{f}(t+\tau)}$, and the frequency-noise spectrum $S_\mathrm{F}(f)$ can be calculated as the associated Fourier transform[19],

$$S_\mathrm{F}(f) = \mathcal{F}\Big\{\Gamma_{\delta\tilde{f}}(\tau)\Big\} = 2\,\Re\left\{\int_0^{+\infty} \Gamma_{\delta\tilde{f}}(\tau)\,\mathrm{e}^{-\mathrm{j}2\pi f\tau}\,\mathrm{d}\tau\right\}. \tag{2.4}$$

A typical frequency-noise spectrum of a single-frequency laser ($f_0 = 1.55\,\mu\mathrm{m}$) is shown in Fig. 2.4(a). It can be conveniently modeled as a sum of the individual noise contributions[20] of integer order $\alpha \geq 0$, as given by

$$S_\mathrm{F}(f) = \sum_{\alpha=0}^{\alpha_\mathrm{max}} S_\alpha f^{-\alpha}. \tag{2.5}$$

The frequency-noise spectrum can hence be considered as a superposition of a spectrally constant white frequency noise $S_0 f^0$ ($\alpha = 0$), flicker frequency noise $S_1 f^{-1}$ ($\alpha = 1$), random-walk frequency noise $S_2 f^{-2}$ ($\alpha = 2$) as well as higher-order frequency-noise contributions ($\alpha > 2$). A fit for $\alpha_\mathrm{max} = 3$ is

[19] This is known as the Wiener-Khinchin theorem [91, 92], which states that the spectral decomposition of the autocorrelation function of a stationary random process is defined by its power spectrum. Note that we consider single-sided spectral densities throughout this thesis. Since all phase and frequency signals are real signals, their PSD are even functions and the negative frequency half-plane is therefore redundant.

[20] The primary source of phase noise is rooted in quantum effects, specifically the spontaneous emission in the gain medium and quantum noise linked to optical losses. Additionally, technical and environmental factors such as vibrations and fluctuations of the pump current or temperature contribute to the overall noise.

illustrated in Fig. 2.4(a) by the blue dashed line. In close analogy, we can define the coherence function of the optical light field as $\Gamma_E(\tau) = \overline{\underline{E}^*(t)\,\underline{E}(t+\tau)}$, where $(.)^*$ denotes the complex conjugate. Inserting the ansatz for $\underline{E}(t)$ yields

$$\Gamma_E(\tau) = E_0^2\,\mathrm{e}^{\mathrm{j}2\pi f_0\tau}\,\overline{\mathrm{e}^{\mathrm{j}\,\Delta\varphi(t,\tau)}}. \tag{2.6}$$

We then use the definition of the so-called moment-generating function for a zero-mean random Gaussian process to find [93]

$$\overline{\mathrm{e}^{\mathrm{j}\,\Delta\varphi(t,\tau)}} = \mathrm{e}^{-\overline{\Delta\varphi(t,\tau)^2}/2} = \mathrm{e}^{-\sigma^2_{\Delta\varphi}/2}, \tag{2.7}$$

where $\sigma^2_{\Delta\varphi}$ denotes the variance of the phase difference. As shown in [88, 94], the variance $\sigma^2_{\Delta\varphi}$ may be written in terms of the frequency-noise spectrum as

$$\sigma^2_{\Delta\varphi} = 4\int_0^{+\infty} S_{\mathrm{F}}(f)\frac{\sin^2(\pi f\tau)}{f^2}\,\mathrm{d}f. \tag{2.8}$$

By inserting Eqs. 2.7 and 2.8 in Eq. 2.6, the coherence function is re-written as

$$\Gamma_E(\tau) = E_0^2\,\mathrm{e}^{\mathrm{j}2\pi f_0\tau}\,\mathrm{e}^{-2\int_0^{+\infty} S_{\mathrm{F}}(f)\frac{\sin^2(\pi f\tau)}{f^2}\,\mathrm{d}f}. \tag{2.9}$$

Using Eq. 2.9, the spectral line shape $S_{\mathrm{E}}(\tilde{f})$ is finally calculated as the Fourier transform of the coherence function $\Gamma_E(\tau)$, i.e.,

$$\begin{aligned} S_{\mathrm{E}}(\tilde{f}) &= 2\,\Re\left\{\int_0^{+\infty}\Gamma_E(\tau)\,\mathrm{e}^{-\mathrm{j}2\pi\tilde{f}\tau}\,\mathrm{d}\tau\right\}, \\ &= 2\,\Re\left\{\int_0^{+\infty} E_0^2\;\mathrm{e}^{-\mathrm{j}2\pi(\tilde{f}-f_0)\tau}\,\mathrm{e}^{-2\int_0^{+\infty} S_{\mathrm{F}}(f)\frac{\sin^2(\pi f\tau)}{f^2}\,\mathrm{d}f}\,\mathrm{d}\tau\right\}, \\ &= 2\,E_0^2\int_0^{+\infty}\cos[2\pi(\tilde{f}-f_0)\tau]\,\mathrm{e}^{-2\int_0^{+\infty} S_{\mathrm{F}}(f)\frac{\sin^2(\pi f\tau)}{f^2}\,\mathrm{d}f}\,\mathrm{d}\tau. \end{aligned} \tag{2.10}$$

In the general case of a frequency-noise spectrum according to Eq. 2.5, it is not possible to obtain an analytical expression for Eq. 2.10. The laser line shape in Fig. 2.4(b) was therefore numerically calculated[21] from the associated frequency-noise spectrum in Fig. 2.4(a). To calculate the line shape using the Fourier transform in Eq. 2.10, one has to integrate for an infinite time. In real measurements, however, this is of cause not possible and instead a finite observation time $\tau_0$ is chosen, which can then be considered as the upper limit of the outer integral in Eq. 2.10. The minimum Fourier frequency $f_{\mathrm{min}}$ that is considered in such a measurement is given by the inverse of the observation time, $f_{\mathrm{min}} = 1/\tau_0$. This value can then be considered as the lower limit of the integral over $S_{\mathrm{F}}(f)$ in Eq. 2.10. The result of Eq. 2.10 hence depends on the choice of this observation time $\tau_0$, whereby the exact shape of the frequency-noise spectrum $S_{\mathrm{F}}(f)$ plays a crucial role. However, it has been shown [95] that the frequency-noise spectrum $S_{\mathrm{F}}(f)$ can be divided in two distinct regions, which influence the resulting line shape $S_{\mathrm{E}}(\tilde{f})$ in fundamentally different ways depending on the observation time $\tau_0$. The line isolating these two areas is called $\beta-$ separation line, which is given by the relation [95]

$$S_\beta(f) = \frac{8\ln 2}{\pi^2} f. \tag{2.11}$$

The intersection point of the actual frequency-noise spectrum and the line according to Eq. 2.11 defines a "cutoff" frequency $f_{\mathrm{cut}}$, for which $S_{\mathrm{F}}(f_{\mathrm{cut}}) = S_\beta(f_{\mathrm{cut}}) = (8\ln(2)\, f_{\mathrm{cut}})/\pi^2$ holds true. In Fig. 2.4(a), the $\beta-$ separation line is drawn in red, and from the intersection point with $S_{\mathrm{F}}(f)$ we find $f_{\mathrm{cut}} \approx 47\,\mathrm{kHz}$. The range $f < f_{\mathrm{cut}}$ of the frequency-noise spectrum plays a role in particular for long observation times, whereas the range $f > f_{\mathrm{cut}}$ has an effect predominantly for short observation times. This is explained in more detail in the following.

[21] Importantly, knowledge of the frequency-noise PSD $S_{\mathrm{F}}(f)$ enables retrieval of the laser line shape $S_{\mathrm{E}}(\tilde{f})$, while the reverse process, i.e., finding the frequency-noise spectrum from the laser line shape is not generally possible as the origin of the noise sources and underlying statistics are not captured in the line shape. The relation between the frequency-noise spectrum and the line shape is hence not bijective [88, 95].

**Long observation times:** For long observation times $\tau_0 \gg 1/f_{\mathrm{cut}}$, the extracted line shape $S_{\mathrm{E}}(\tilde{f})$ will be predominantly determined by the frequency-noise contributions at low Fourier frequencies $f < f_{\mathrm{cut}}$. As can be inferred from Fig. 2.4(a), higher-order noise sources ($\alpha \geq 1$) are most pronounced in this regime. It has been shown [95], that such noise contributions with a spectral density $S_{\mathrm{F}}(f)$ larger than their respective Fourier frequency $f$ give rise to an autocorrelation function which is governed by a multiplication of various Gaussian functions [95], and the spectral line shape $S_{\mathrm{E}}(\tilde{f})$, which is given as the Fourier transform in Eq. 2.10, can consequently be approximated by a Gaussian function as well, i.e.,

$$S_{\mathrm{E}}(\tilde{f})\Big|_{f<f_{\mathrm{cut}}} \propto \mathrm{e}^{-\frac{(\tilde{f}-f_0)^2}{2\sigma_{\mathrm{G}}^2}}. \tag{2.12}$$

The associated FWHM linewidth $\delta f_{\mathrm{FWHM,G}} = 2\sqrt{2\ln 2}\,\sigma_{\mathrm{G}}$ is often referred to as the "effective" or "long-term" linewidth of the laser. The minimum Fourier frequency that is considered in a measurement is given by the inverse of the observation time, $f_{\mathrm{min}} = 1/\tau_0$, and for $f_{\mathrm{cut}} > 5f_{\mathrm{min}}$, a good approximation of the associated linewidth[22] is given by

$$\delta f_{\mathrm{FWHM,G}} \approx \sqrt{8\ln 2 \times A} \propto \sqrt{A}, \tag{2.13}$$

where $A = \int_{f_{\mathrm{min}}}^{f_{\mathrm{cut}}} S_{\mathrm{F}}(f)\,\mathrm{d}f$. In Fig. 2.4(a), $A$ can be interpreted as the red-shaded area under the frequency-noise spectrum in the region $S_{\mathrm{F}}(f_{\mathrm{min}} < f < f_{\mathrm{cut}})$. For our example, we find $\delta f_{\mathrm{FWHM,G}} \approx 6\,\mathrm{MHz}$ for an observation time of $\tau_0 = 20\,\mathrm{ms}$, and the associated Gaussian function (red dotted line) represents a good fit to the central line shape region, see Fig. 2.4(b).

[22] In the presence of noise contributions with $\alpha > 0$, the approximation obviously yields larger values for long-term linewidths $\delta f_{\mathrm{FWHM,G}}$ for measurements with smaller $f_{\mathrm{min}}$, i.e., the effective linewidth $\delta f_{\mathrm{FWHM,G}}$ increases with the observation time $\tau_0$. In fact, for infinitely long observation times, the area $A$ and consequently Eq. 2.13 diverge, which is consistent with the picture of a random-walk process for which the standard deviation tends to infinity with time.

**Short observation times:** The impact on the line shape $S_{\mathrm{E}}(\tilde{f})$ for short observation times $\tau_0 \ll 1/f_{\mathrm{cut}}$ is primarily determined by the high Fourier frequency contributions $f > f_{\mathrm{cut}}$. Notably, if the lower frequency limit $f_{\mathrm{min}} = 1/\tau_0$ can be assumed to be high enough, the impact of higher-order noise contributions is fully excluded. In this case, the relevant part of the frequency-noise spectrum can be considered purely white ($\alpha = 0$), and Eq. 2.9 can be analytically solved for a constant noise floor $S_{\mathrm{F}}(f) = S_0$. This results in

$$\Gamma_E(\tau) = E_0^2\, \mathrm{e}^{\mathrm{j}2\pi f_0 \tau}\, \mathrm{e}^{-\pi^2 S_0 |\tau|} = E_0^2\, \mathrm{e}^{\mathrm{j}2\pi f_0 \tau}\, \mathrm{e}^{-\pi \delta f_{\mathrm{FWHM,L}} |\tau|}, \tag{2.14}$$

and using Eq. 2.10 we find a Lorentzian line shape

$$S_{\mathrm{E}}(\tilde{f})\Big|_{f>f_{\mathrm{cut}}} \propto \frac{1}{\pi}\, \frac{(\delta f_{\mathrm{FWHM,L}}/2)}{(\tilde{f} - f_0)^2 + (\delta f_{\mathrm{FWHM,L}}/2)^2}. \tag{2.15}$$

The associated FWHM linewidth is given as

$$\delta f_{\mathrm{FWHM,L}} = \pi S_0, \tag{2.16}$$

and is often referred to as the "intrinsic", "instantaneous", "short-term" or "fundamental" linewidth of the laser. Importantly, the linewidth $\delta f_{\mathrm{FWHM,L}}$ may be easily extracted from the frequency-noise spectrum by fitting Eq. 2.5 to the measurement data and finding $S_0$ in the high-frequency limit, as indicated by the green line in Fig. 2.4(a). For our example, we find $\delta f_{\mathrm{FWHM,L}} \approx 1\,\mathrm{kHz}$ with the help of Eq. 2.16, and the tails of the line shape are well reproduced by the associated Lorentzian function (green dotted line), see Fig. 2.4(b).

For quantifying the degree of temporal coherence, we may equivalently define the so-called coherence time $\tau_{\mathrm{c}}$ as the time over which $\Gamma_E(\tau)$ has decayed to $1/\mathrm{e}$ of its maximum value at $\tau = 0$. Using Eq. 2.14, we find $\Gamma_E(\tau_{\mathrm{c}}) \stackrel{!}{=} \Gamma_E(0)/\mathrm{e} \leftrightarrow 1 - \pi \delta f_{\mathrm{FWHM,L}}\, \tau_{\mathrm{c}} \stackrel{!}{=} 0$, leading to a coherence time $\tau_{\mathrm{c}} = (\pi\, \delta f_{\mathrm{FWHM,L}})^{-1}$ which scales inversely with the laser linewidth. For our example we find $\tau_{\mathrm{c}} \approx 0.3\,\mathrm{ms}$, which corresponds to a coherence length of about $95\,\mathrm{km}$ in air.

Remarkably, the linewidth $\delta f_{\mathrm{FWHM,L}}$ as derived in the previous paragraph matches the fundamental (quantum-limited) linewidth as already predicted by Schawlow and Townes in 1958 before the first laser was even invented [96]. With the corrections introduced by Lax in 1967 [97], and the additions made by Henry in 1982 [98], the fundamental linewidth can be written as[23]

$$\delta f_{\mathrm{FWHM,L}} = \frac{\pi\, h f_0\, \Delta f_{\mathrm{cav}}^2}{P} = \frac{v_{\mathrm{g}}^2\, h f_0\, (\alpha_{\mathrm{i}} + \alpha_{\mathrm{m}})\, \alpha_{\mathrm{m}}\, n_{\mathrm{sp}}}{4\pi\, P}(1 + \alpha_{\mathrm{H}}^2). \qquad (2.17)$$

In this relation, $hf_0$ is the photon energy with Planck's constant $h$, $\Delta f_{\mathrm{cav}} = (2\pi\tau_{\mathrm{p}})^{-1} = v_g(\alpha_{\mathrm{i}} + \alpha_{\mathrm{m}})/(2\pi)$ is the FWHM bandwidth of the passive laser cavity given in terms of the photon lifetime $\tau_{\mathrm{p}}$, or, equivalently, in terms of the distributed modal power loss of the laser waveguide $\alpha_{\mathrm{i}}$ (not including contributions from band-to-band transitions), the distributed power loss of the two mirrors $\alpha_{\mathrm{m}}$ (both in units of 1/m), and the group velocity $v_{\mathrm{g}}$. $P$ relates to the laser output power, $n_{\mathrm{sp}}$ is the spontaneous emission factor [99], and $\alpha_{\mathrm{H}}$ is the so-called Henry or linewidth-enhancement factor [98, 100], which takes into account linewidth-broadening effects due to amplitude-phase coupling that result from a dependence of the refractive index on the carrier density. Typical values for semiconductor lasers are of the order of $\alpha_{\mathrm{H}} = 2 \ldots 5$ and can reach up to 9 [100], thus causing a significant increase of $\delta f_{\mathrm{FWHM,L}}$.

It should also be noted that the overall laser line shape $S_{\mathrm{E}}(\tilde{f})$ is sometimes represented as a Voigt function [93, 101], which is effectively the result of a convolution of a Gaussian and a Lorentzian profile. The resulting FWHM linewidth $\delta f_{\mathrm{FWHM,V}}$ is referred to as the "integrated" linewidth, and for the depicted example, we can simply extract $\delta f_{\mathrm{FWHM,V}} \approx 8\,\mathrm{MHz}$ from the $-3\,\mathrm{dB}$ points in Fig. 2.4(b). A single definition of the laser linewidth $\delta f$, which can fully describe the laser frequency noise, does hence not exist, and the full frequency-noise spectrum $S_{\mathrm{F}}(f)$ needs to be measured and analyzed instead. Although in many applications, such as in coherent optical communications, a measurement

[23] The first expression in Eq. 2.17 corresponds to the original formula as derived by Schawlow and Townes, which holds true only for a purely white noise limited four-level single-frequency laser without amplitude-phase coupling [96].

of the laser linewidth $\delta f_{\mathrm{FWHM,L}}$ often suffices[24], a more thorough understanding of the spectral distribution of the frequency fluctuations is required in, e.g., spectrometry, metrology, or sensing applications [104].

### 2.2.2 Linewidth reduction in external-cavity lasers

By taking a closer look at Eq. 2.17, first strategies for reducing the intrinsic laser linewidth can already be deduced: Considering that $\delta f_{\mathrm{FWHM,L}} \propto \Delta f_{\mathrm{cav}}^2$, lowering the bandwidth $\Delta f_{\mathrm{cav}}$ of the passive laser resonator is certainly a good starting point. For gaining a more detailed understanding of the underlying parameters, we first introduce the cavity round-trip length $2L$ and the associated round-trip time $\tau_{\mathrm{rt}} = 2L/v_{\mathrm{g}}$. In a second step, the cavity bandwidth is then simply rewritten in terms of the round-trip time and cavity length as $\Delta f_{\mathrm{cav}} = 2L(\alpha_{\mathrm{i}} + \alpha_{\mathrm{m}})/(2\pi\tau_{\mathrm{rt}})$ [105]. Two effective recipes for reducing the linewidth are hence to increase the round-trip time $\tau_{\mathrm{rt}} \propto L$, i.e., making the cavity longer, as well as to minimize the round-trip losses $2L(\alpha_{\mathrm{i}} + \alpha_{\mathrm{m}})$ [104].

In the case of integrated external-cavity lasers (ECL), one side of a Fabry-Pérot diode laser consisting of a gain section with length $L_{\mathrm{gain}}$ is connected to an external passive feedback circuit of length $L_{\mathrm{pass}}$, thereby extending the cavity to $L_{\mathrm{ECL}} = L_{\mathrm{gain}} + L_{\mathrm{pass}} \gg L_{\mathrm{gain}}$. At the same time, minimizing the distributed resonator losses $\alpha_{\mathrm{i}} + \alpha_{\mathrm{m}}$ as determined by the gain element, passive waveguide (WG) sections as well as the coupling interfaces in-between, is of great importance. This can for example be achieved by using low-loss silicon nitride ($Si_3N_4$) WG [11, 16, 17] for the passive sections and by maintaining low coupling losses within the cavity. Importantly, the external cavity needs to exhibit a strong dispersive behavior in order to provide frequency-selectivity and permit single-mode operation in spite of the long laser cavity. In practice, various types of integrated

[24] The impact of frequency noise in optical communication links depends, e.g., on the specific symbol duration and modulation format used. Shorter symbol durations are generally less prone to frequency noise, as the associated short observation times lead to the line shape being mainly determined by the frequency-noise contributions at high Fourier frequencies [102, 103].

extended cavities have been demonstrated [106], among which single-frequency Bragg gratings [107] and (frequency-tunable) ring resonators [20, 108] are most commonly used. Surprisingly, if the lasing mode of an ECL is appropriately detuned with respect to the resonant reflection of the external feedback, the influence of the amplitude-phase coupling related to the Henry factor $\alpha_{\mathrm{H}}$ in Eq. 2.17 can be counteracted [109–111]. The associated linewidth narrowing thereby enables the operation at fundamental linewidths even below the Schawlow-Townes limit.

In order to shed light on the origins of this effect, we first consider a simple Fabry-Pérot diode laser with cavity length $L_{\mathrm{gain}}$ and (amplitude) reflection coefficients $r_1$ and $r_2$ of the two mirrors. We can then start from two well-known conditions that must be fulfilled to achieve lasing operation: First, the distributed cavity power gain $g$ (in units of 1/m) must equal the distributed cavity losses $\alpha_{\mathrm{i}} + \alpha_{\mathrm{m}}$, i.e.,

$$g \stackrel{!}{=} \alpha_{\mathrm{i}} + \alpha_{\mathrm{m}} = \alpha_{\mathrm{i}} - \ln(r_1^2\, r_2^2)/2L_{\mathrm{gain}} = \alpha_{\mathrm{i}} - \ln(r_1 r_2)/L_{\mathrm{gain}}. \tag{2.18}$$

In this expression, the distributed mirror loss $\alpha_{\mathrm{m}} = -\ln(r_1 r_2)/L_{\mathrm{gain}}$ is expressed in terms of the two reflection coefficients $r_1$ and $r_2$ as well as the cavity round-trip length $2L_{\mathrm{gain}}$. Second, the accumulated phase during one round-trip through the resonator must be an integer multiple of $2\pi$, i.e., $2L_{\mathrm{gain}}\beta(\omega) \stackrel{!}{=} 2\pi\, m$ for $m \in \mathbb{N}$ with the intra-cavity propagation constant $\beta(\omega) = \omega n_{\mathrm{e}}(\omega)/c$. Hereby, $n_{\mathrm{e}}(\omega)$ is the so-called effective refractive index of the associated WG mode, which depends on the materials and the geometry of the underlying WG structure [112]. In this context, it is common practice to express $\beta(\omega)$ as a Taylor series around an angular carrier frequency $\omega_{\mathrm{c}} = 2\pi f_{\mathrm{c}}$ of an optical field of interest,

$$\beta(\omega) = \sum_{n=0}^{\infty} \frac{1}{n!}\, \beta_{\mathrm{c}}^{(n)} (\omega - \omega_{\mathrm{c}})^n, \qquad \beta_{\mathrm{c}}^{(n)} = \left.\frac{\partial^n \beta(\omega)}{\partial\, \omega^n}\right|_{\omega=\omega_{\mathrm{c}}}. \tag{2.19}$$

Is is usually sufficient to only consider the first three Taylor coefficients $\beta_\mathrm{c}^{(0)}$, $\beta_\mathrm{c}^{(1)}$ and $\beta_\mathrm{c}^{(2)}$, which are given as

$$\begin{aligned}
\beta_\mathrm{c}^{(0)} &= \frac{\omega_\mathrm{c} n_\mathrm{e,c}}{c}, \\
\beta_\mathrm{c}^{(1)} &= \frac{1}{c}\left[n_\mathrm{e}(\omega) + \omega\frac{\partial\, n_\mathrm{e}(\omega)}{\partial\,\omega}\right]\bigg|_{\omega=\omega_c} = \frac{n_\mathrm{eg,c}}{c} = \frac{1}{v_\mathrm{g,c}}, \\
\beta_\mathrm{c}^{(2)} &= \frac{\partial\beta^{(1)}(\omega)}{\partial\,\omega}\bigg|_{\omega=\omega_c} = \frac{1}{c}\,\frac{\partial\, n_\mathrm{eg}(\omega)}{\partial\,\omega}\bigg|_{\omega=\omega_c}.
\end{aligned} \tag{2.20}$$

In these relations, $n_\mathrm{eg}(\omega) = n_\mathrm{e}(\omega) + \omega\frac{\partial\, n_\mathrm{e}(\omega)}{\partial\,\omega} = c/v_\mathrm{g}(\omega)$ is the effective group refractive index and the subscript c is used to denote quantities at the carrier frequency $\omega = \omega_\mathrm{c}$. Using Eq. 2.19 and 2.20 to approximate $\beta(\omega)$ by the first two Taylor coefficients ($n_\mathrm{max} = 1$) yields the round-trip phase condition [111]

$$2L_\mathrm{gain}\beta(\omega) \approx 2L_\mathrm{gain}\left[\frac{\omega_\mathrm{c} n_\mathrm{e,c}}{c} + \frac{\omega-\omega_\mathrm{c}}{v_\mathrm{g,c}} - \alpha_\mathrm{H}\frac{g}{2}\right] \stackrel{!}{=} 2\pi\, m, \quad m \in \mathbb{N}, \tag{2.21}$$

where $n_\mathrm{e,c}$ refers to the effective refractive index at a gain of $g = 0$ and the term $\alpha_\mathrm{H} g/2$ is introduced due to amplitude-phase coupling[25].

In a next step, we analyze the influence of a frequency-dependent facet reflectivity as caused by an external-feedback circuit using the so-called effective mirror model [111]. One of the two mirror reflectivities is therefore replaced by a complex amplitude reflection coefficient, i.e., $r_2 \to \underline{r}_\mathrm{eff}(\omega) = |r_\mathrm{eff}(\omega)|\mathrm{e}^{\mathrm{j}\Phi(\omega)}$. To still fulfill the lasing conditions given by Eqs. 2.18 and 2.21, the new phase term $\Phi(\omega)$ must be added to the left-hand sides of Eq. 2.21, whereas the mirror reflectivity $r_2$ in Eq. 2.18 is exchanged by the effective reflectivity $|r_\mathrm{eff}(\omega)|$. We then find the change in gain $\delta g_\mathrm{ECL}$ associated with the fluctuations of the angular ECL emission frequency $\delta\tilde{\omega}_\mathrm{ECL}$ by linearizing the modified Eq. 2.18

[25] The factor of $1/2$ accounts for the conversion from power to amplitude gain.

with respect to an operating point $g_0 = g(\omega_0)$, which is located above threshold. To this end, we first derive Eq. 2.18 with $r_2 = |r_{\mathrm{eff}}(\omega)|$ with respect to $\omega$,

$$\frac{\mathrm{d}g}{\mathrm{d}\omega} = \frac{\mathrm{d}}{\mathrm{d}\omega}\alpha_{\mathrm{i}} - \frac{1}{L_{\mathrm{gain}}}\frac{\mathrm{d}\ln(\mathrm{r}_1|\mathrm{r}_{\mathrm{eff}}(\omega)|)}{\mathrm{d}\omega} = -\frac{1}{L_{\mathrm{gain}}}\frac{\mathrm{d}\ln(|\mathrm{r}_{\mathrm{eff}}(\omega)|)}{\mathrm{d}\omega}. \tag{2.22}$$

Eq. 2.22 can then be used to obtain the relation [111]

$$\delta g_{\,\mathrm{ECL}} = g_0 - \frac{1}{L_{\mathrm{gain}}}\frac{\mathrm{d}\ln(|\mathrm{r}_{\mathrm{eff}}(\omega)|)}{\mathrm{d}\omega}\,\delta\tilde{\omega}_{\mathrm{ECL}}. \tag{2.23}$$

Note that in the case of a facet reflectivity which does not depend on frequency, we would find $\mathrm{d}g/\mathrm{d}\omega = 0$ from Eq. 2.22. As a direct consequence, the gain of a Fabry-Pérot diode laser in the absence of external feedback is constant over frequency and given by $g_0$. Similarly, we can linearize the round-trip phase condition governed by Eq. 2.21 with the added term $\Phi(\omega)$ by first finding the derivative with respect to $\omega$,

$$\frac{\mathrm{d}}{\mathrm{d}\omega}\Big[2L_{\mathrm{gain}}\beta(\omega) + \Phi(\omega)\Big] \approx \frac{2L_{\mathrm{gain}}}{v_{\mathrm{g,c}}} - \alpha_{\mathrm{H}}L_{\mathrm{gain}}\frac{\mathrm{d}g}{\mathrm{d}\omega} + \frac{\mathrm{d}\Phi(\omega)}{\mathrm{d}\omega} \stackrel{!}{=} 0, \tag{2.24}$$

and thereby a second expression for $\delta g_{\,\mathrm{ECL}}$ related to $\delta\tilde{\omega}_{\mathrm{ECL}}$ [111],

$$\delta g_{\,\mathrm{ECL}} = \frac{2}{\alpha_{\mathrm{H}}v_{\mathrm{g,c}}}\Big(1 + \frac{v_{\mathrm{g,c}}}{2L_{\mathrm{gain}}}\frac{\mathrm{d}\Phi(\omega)}{\mathrm{d}\omega}\Big)\,\delta\tilde{\omega}_{\mathrm{ECL}}. \tag{2.25}$$

With Eqs. 2.23 and 2.25 the term $\delta g_{\,\mathrm{ECL}}$ can be eliminated, and solving for $\delta\tilde{\omega}_{\mathrm{ECL}}$ yields an expression for the instantaneous angular frequency fluctuations of a laser under frequency-dependent external feedback. This term can be conveniently written as [111]

$$\delta\tilde{\omega}_{\mathrm{ECL}} = \frac{\delta\tilde{\omega}_0}{F(\omega)}, \quad F(\omega) = 1 + \underbrace{\frac{1}{\tau_{\mathrm{rt,c}}}\frac{\mathrm{d}\Phi(\omega)}{\mathrm{d}\omega}}_{A(\omega)} + \underbrace{\frac{\alpha_{\mathrm{H}}}{\tau_{\mathrm{rt,c}}}\frac{\mathrm{d}\ln|r_{\mathrm{eff}}(\omega)|}{\mathrm{d}\omega}}_{B(\omega)}, \tag{2.26}$$

where $\delta\tilde{\omega}_0 = g_0 \alpha_\mathrm{H} v_\mathrm{g,c}/2$ are the instantaneous angular frequency fluctuations in the absence of external feedback and $\tau_\mathrm{rt,c} = 2L_\mathrm{gain}/v_\mathrm{g,c}$ is the round-trip time in the Fabry-Pérot cavity, both at $\omega = \omega_\mathrm{c}$. As becomes apparent from Eq. 2.26, $\delta\tilde{\omega}_0$ is reduced by a factor of $F(\omega)$ by virtue of the frequency-dependent feedback. It can furthermore be shown [98, 111], that the same factor $F(\omega)$ is responsible for reducing the phase fluctuations in an ECL, and the Lorentzian linewidth, which depends on the square of these fluctuations, reduces by a factor of $F^2(\omega)$ compared to the linewidth $\delta f_0$ of a Fabry-Pérot diode laser with facet reflectivities $r_1$ and $|r_\mathrm{eff}(\omega)|$, i.e., $\delta f_\mathrm{ECL} = \delta f_0 / F^2(\omega)$. By combining Eq. 2.17 with $F(\omega)$ as defined in Eq. 2.26, the fundamental linewidth of an ECL is thus given as

$$\delta f_\mathrm{ECL} = \frac{\delta f_0}{F^2(\omega)} = \frac{v_\mathrm{g,c}^2 \, h f_\mathrm{ECL} \, (\alpha_\mathrm{i} + \alpha_\mathrm{m}) \, \alpha_\mathrm{m} \, n_\mathrm{sp} \, (1 + \alpha_\mathrm{H}^2)}{4\pi \, P \left[1 + \frac{1}{\tau_\mathrm{rt,c}} \frac{\mathrm{d}\Phi(\omega)}{\mathrm{d}\omega} + \frac{\alpha_\mathrm{H}}{\tau_\mathrm{rt,c}} \frac{\mathrm{d} \ln |r_\mathrm{eff}(\omega)|}{\mathrm{d}\omega}\right]^2}. \tag{2.27}$$

From a physical point of view, the term $A(\omega)$ in Eq. 2.26 accounts for the increase in round-trip accumulated phase — it therefore corresponds to the factor by which the coherence time $\tau_\mathrm{c}$ is increased by the extended cavity compared to the solitary Fabry-Pérot diode laser. On the other hand, the term $B(\omega)$ in Eq. 2.26 is related to the slope of the loss curve associated with the frequency-dependent mirror reflectivity $|r_\mathrm{eff}(\omega)|$. If the lasing mode is detuned with respect to the resonant reflection of the external feedback, the linewidth broadening due to amplitude-phase coupling can be counteracted — an operating principle which is therefore also referred to as detuned loading [110]. Importantly, this effect can only be observed when operating the ECL on the low-frequency side with respect to the external mirror resonance (red-detuned), as can be understood from the following considerations [104, 110]: If the operating point of the laser is initially chosen on the low-frequency side, an increase in frequency, i.e., towards the mirror resonance, causes an increase in reflectivity, which in turn increases the photon density in the cavity and reduces the carrier density in the gain section. The refractive index is thus increased through the free-carrier plasma dispersion effect [113], and as a consequence the frequency of the laser is pulled down, thereby stabilizing the laser oscillation. On the contrary, operating the laser on the high-frequency side can lead to linewidth broadening. Since the laser must always satisfy the phase

condition in Eq. 2.21, such a detuned operation may be achieved by introducing an additional controllable phase shifter within the resonator which permits tuning the frequency of the laser mode independently of the mirror resonance.

In the following, we give a practical example of how Eq. 2.27 can be used to numerically estimate the linewidth of an integrated ECL based on the parameters and cavity layout presented in Chapter 3 and the associated Appendix A — an overview over the various parameters is given in Table 2.1 at the end of this section. We start our considerations by defining the terms $|r_{\mathrm{eff}}(\omega)|$ and $\mathrm{d}\Phi(\omega)/\mathrm{d}\omega$ associated with the schematic ECL arrangement shown in Fig. 2.5(a). The ECL is modeled as a three-section device consisting of a gain section, typically made up of a direct bandgap III-V material, a passive section comprising, e.g., on-chip WG of the external-feedback circuit or various coupling interfaces[26], and a resonant frequency-selective mirror. We model the gain element as well as the $K$ passive sub-sections by their respective length $L_i$ and effective group refractive index $n_{\mathrm{eg},i} = c/v_{\mathrm{g},i}$ at $\omega = \omega_{\mathrm{c}}$. The associated power transmission of the individual sections is $\eta_{\mathrm{pass},i}$, which leads to a single-pass amplitude transmission of $\sqrt{\eta_{\mathrm{pass}}}$ for the full passive section. The laser is then simplified to a single active section in-between two reflecting facets as shown in Fig. 2.5(b), where the back facet maintains it frequency-independent amplitude reflection coefficient $r_1$, while the front facet (red line) possesses a frequency-dependent complex amplitude reflection coefficient $\underline{r}_{\mathrm{eff}}(\omega) = |r_{\mathrm{eff}}(\omega)|\mathrm{e}^{\mathrm{j}\Phi(\omega)}$. Thus, the entire extended laser cavity is lumped into $\underline{r}_{\mathrm{eff}}(\omega)$, where the magnitude $|r_{\mathrm{eff}}(\omega)|$ accounts for the constant round-trip amplitude transmission $(\sqrt{\eta_{\mathrm{pass}}})^2$ of the passive section and the amplitude reflection of the mirror $|r_{\mathrm{m}}(\omega)|$. For a full round-trip, we thus find

$$|r_{\mathrm{eff}}(\omega)| = \sqrt{\eta_{\mathrm{pass}}}\ |r_{\mathrm{m}}(\omega)|\sqrt{\eta_{\mathrm{pass}}} = \Big[\prod_{i=1}^{K}(\sqrt{\eta_{\mathrm{pass},i}})^2\Big]\ |r_{\mathrm{m}}(\omega)|. \tag{2.28}$$

[26] Note that the effective mirror model does not take into account back-reflections at the various interfaces, e.g., in-between the gain element and the first passive section, which could be based on a completely different material platform. Therefore, anti-reflection coatings and tilted WG are commonly employed to avoid spurious back-reflections into the gain element.

On the other hand, the term $\mathrm{d}\Phi(\omega)/\mathrm{d}\omega$ accounts for the accumulated phase shifts due to the propagation through the passive section $\Phi_{\mathrm{pass}}(\omega)$ as well as the frequency-dependent phase shift $\Phi_{\mathrm{m}}(\omega)$ associated with the highly dispersive mirror. In the most general case, the phase contribution from the mirror is given by $\Phi_{\mathrm{m}}(\omega) = \arg\{\underline{r}_{\mathrm{m}}(\omega)\}$, and with a constant phase offset $\Phi_0$ we find

$$\begin{aligned} \Phi(\omega) &= \Phi_0 \; + \; 2\Phi_{\mathrm{pass}}(\omega) \; + \; \Phi_{\mathrm{m}}(\omega) \\ \rightarrow \frac{\mathrm{d}\Phi}{\mathrm{d}\omega} &= 2\Big[\sum_{i=1}^{K} \frac{L_i n_{\mathrm{eg},i}}{c}\Big] \; + \; \frac{\mathrm{d}}{\mathrm{d}\omega} \arg\Big\{\underline{r}_{\mathrm{m}}(\omega)\Big\}. \end{aligned} \tag{2.29}$$

The frequency-selective mirror is implemented as a Sagnac loop with a Vernier pair of tunable racetrack resonators R1 and R2, see Fig. 3.1(b) and associated explanations. In Eqs. 2.28 and 2.29, the magnitude $|r_{\mathrm{m}}(\omega)|$ and phase $\Phi_{\mathrm{m}}(\omega)$ of the mirror reflectivity are therefore given by the magnitude and phase of the complex reflection from the Sagnac loop mirror, which results from the multiplication of the individual drop-port transmissions of the two racetrack resonators R1 and R2 [J1]. The associated round-trip amplitude transmission factor $a$, amplitude transmission and coupling coefficients $\tau$ and $\kappa$ of the coupling zones, as well as the frequency-dependent round-trip phase $\theta(\omega)$ of R1 and R2 are derived in Appendix A.1 and summarized in Table 2.1. For simplicity, we assume that the resonance frequencies of both resonators perfectly coincide at or near the lasing frequency $f_{\mathrm{ECL}}$, leading to a reflection spectrum as shown in Fig. A.1. By introducing and controlling an additional phase shift within the cavity, the frequency $f_{\mathrm{ECL}}$ of the lasing resonator mode can be independently tuned with respect to the peak of the reflection spectrum of the external Sagnac loop mirror at $f_{\mathrm{res}}$, leading to a detuning $f_{\mathrm{ECL}} - f_{\mathrm{res}}$. The frequency-selective mirror is combined with passive $Si_3N_4$ WG on a common PIC, which is connected to the gain element by means of a 3D-printed PWB. We thus take into account $K = 2$ passive sub-sections to find $\sqrt{\eta_{\mathrm{pass}}}$ and $\mathrm{d}\Phi_{\mathrm{pass}}(\omega)/\mathrm{d}\omega$ from the lengths $L_{\mathrm{PWB}}$ and $L_{\mathrm{SiN}}$, effective group refractive indices $n_{\mathrm{eg,PWB}}$ and $n_{\mathrm{eg,SiN}}$, and associated power transmissions $\eta_{\mathrm{PWB}}$ and $\eta_{\mathrm{SiN}}$ of the PWB and $Si_3N_4$ external-feedback circuit, respectively.

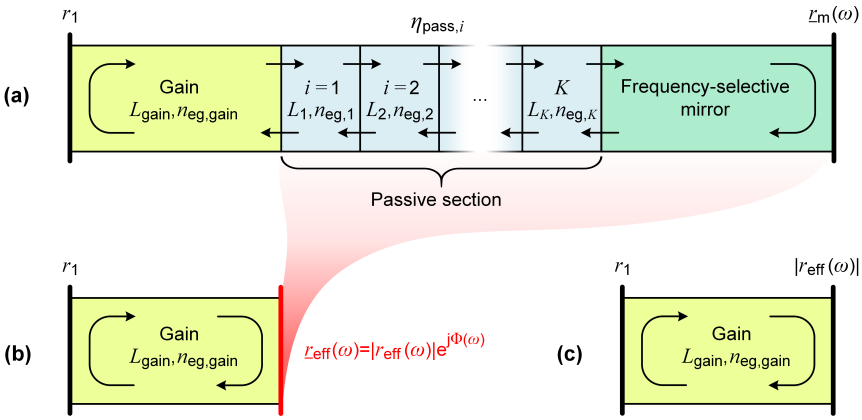


**Fig. 2.5:** Modeling of a laser with a resonant frequency-selective mirror as an extended cavity following the so-called effective mirror model [111]. **(a)** Block diagram representation of the three-section external-cavity laser (ECL): The ECL consists of a gain section with constant reflection coefficient $r_1$, $K$ passive sub-sections with associated power transmission $\eta_{\mathrm{pass},i}$, and a frequency-selective mirror with complex reflection $\underline{r}_{\mathrm{m}}(\omega)$. **(b)** The laser is simplified to a single active section, where the entire extended cavity is lumped into a frequency-dependent complex amplitude reflection $\underline{r}_{\mathrm{eff}}(\omega)$ of the front facet (red line). **(c)** For evaluating the linewidth reduction due to the extended cavity, a Fabry-Pérot diode laser with facet reflectivities $r_1$ and $|r_{\mathrm{eff}}(\omega)|$ is considered as a reference.

Figure 2.6 shows the calculated parameters $A(\omega)$, $B(\omega)$ and $F(\omega)$ according to Eq. 2.26 as well as the corresponding linewidths $\delta f_{\mathrm{ECL}}$ and $\delta f_0$ of the ECL and reference Fabry-Pérot diode laser (compare Fig. 2.5(c)) according to Eq. 2.27, all as a function of the detuning $f_{\mathrm{ECL}} - f_{\mathrm{res}}$. As expected, the term $A(\omega)$ (blue dashed line) reflects the increase in laser cavity length due to the accumulated phase, determined by a constant factor from the passive sections and a frequency-dependent portion from the two racetrack resonators with the maxima located at resonance, i.e., $f_{\mathrm{ECL}} = f_{\mathrm{res}}$. On the contrary, the term $B(\omega)$ (red dashed line) is related to the slope of the loss curve associated with the frequency-dependent mirror reflectivity. $B(\omega)$ is an odd function with respect to the laser detuning, and $F(\omega)$ (black line) thus has its maximum located towards the low-frequency side. In Fig. 2.6(b), the fundamental linewidth $\delta f_{\mathrm{ECL}}$ of the ECL (green line) is therefore significantly reduced compared to the linewidth $\delta f_0$ of the reference Fabry-Pérot diode laser (magenta line) at the coinciding low-frequency side (red-detuned,

$f_{\mathrm{ECL}} < f_{\mathrm{res}}$), while linewidth broadening can be observed for positive detuning (blue-detuned, $f_{\mathrm{ECL}} > f_{\mathrm{res}}$), where $|F| < 1$. For similar reasons, the operating points associated with maximum output power ($f_{\mathrm{ECL}} = f_{\mathrm{res}}$) and with minimal linewidth ($f_{\mathrm{ECL}} < f_{\mathrm{res}}$) can not be assumed to be identical. The zoom-in in Fig. 2.6(b) predicts a minimum achievable linewidth of $\delta f_{\mathrm{ECL}} \approx 1\,\mathrm{kHz}$ for a PWB loss of $a_{\mathrm{PWB}} = -10\log_{10}\eta_{\mathrm{PWB}} = 1.6\,\mathrm{dB}$ and a detuning of approximately $-1.4\,\mathrm{GHz}$, which is in excellent agreement to the linewidth $\delta f_{\mathrm{FWHM,L}} \approx 1\,\mathrm{kHz}$ extracted from the measurement shown in Section 2.2.1. The green dashed lines in the zoom-in of Fig. 2.6(b) further indicate the linewidth for varying loss $a_{\mathrm{PWB}}$ in steps of $3\,\mathrm{dB}$. For a given external-feedback circuit and gain element, the achievable linewidth of the ECL is generally limited by the contribution of the coupling loss between those two components to the overall passive resonator losses. Therefore, using low-loss 3D-printed coupling structures such as PWB can fundamentally improve the performance of ECL [J2].

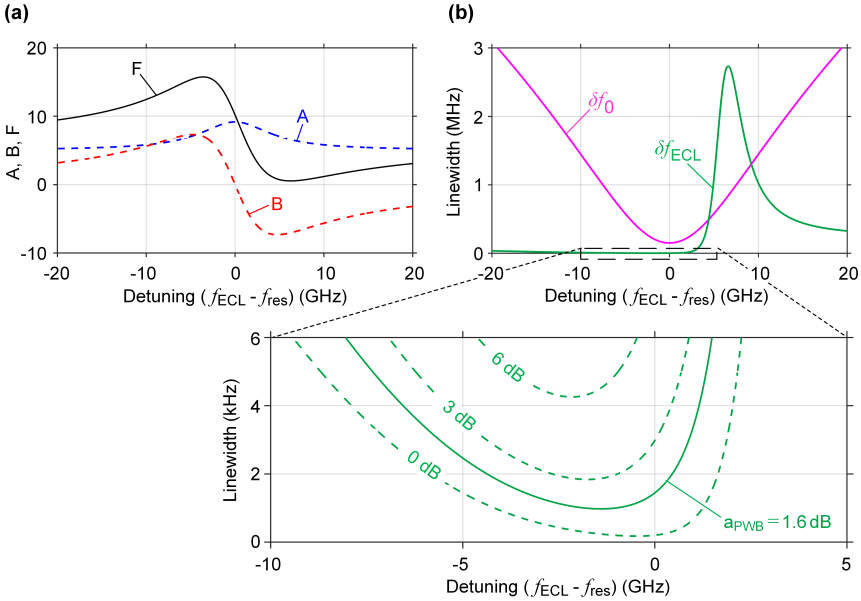


**Fig. 2.6:** Theoretically estimated linewidths of an ECL as a function of the detuning of the laser emission $f_{\mathrm{ECL}}$ with respect to the resonance frequency $f_{\mathrm{res}}$ of a frequency-selective Sagnac loop mirror. The frequency-dependence of the facet reflectivity allows to counteract amplitude-phase coupling related to the Henry factor $\alpha_{\mathrm{H}}$ if the laser is operated under appropriate feedback conditions, thereby leading to significant linewidth narrowing. **(a)** Calculated parameters $A(\omega)$, $B(\omega)$, and $F(\omega)$ according to Eq. 2.26. The term $A(\omega)$ (blue dashed line) reflects the increase in laser cavity length, determined by a constant factor from the passive sections and a frequency-dependent portion from the two racetrack resonators in the Sagnac loop mirror. The term $B(\omega)$ (red dashed line) is related to the slope of the loss curve associated with the frequency-dependent mirror reflectivity. $B(\omega)$ is an odd function with respect to the laser detuning, and $F(\omega)$ (black line) thus has its maximum located towards the low-frequency side. **(b)** Corresponding linewidth of the ECL (green line) and reference Fabry-Pérot diode laser (magenta line) according to Eq. 2.27. The fundamental linewidth $\delta f_{\mathrm{ECL}}$ is drastically reduced compared to the linewidth $\delta f_0$ at the coinciding low-frequency side (red-detuned, $f_{\mathrm{ECL}} < f_{\mathrm{res}}$), while linewidth broadening can be observed for positive detuning (blue-detuned, $f_{\mathrm{ECL}} > f_{\mathrm{res}}$), where $|F| < 1$. The green dashed lines in the zoom-in indicate the achievable linewidths for varying losses $a_{\mathrm{PWB}} = -10\log_{10}\eta_{\mathrm{PWB}}$ in steps of 3 dB. For a PWB loss of $a_{\mathrm{PWB}} = 1.6\,\mathrm{dB}$ and a detuning of approximately $-1.4\,\mathrm{GHz}$, the minimum achievable linewidth is $\delta f_{\mathrm{ECL}} \approx 1\,\mathrm{kHz}$.

**Table 2.1:** Summary of parameters and values used for the calculation of the theoretical laser linewidths.

| Symbol | Description | Value, extracted from / source |
|---|---|---|
| $hf_{\mathrm{ECL}}$ | Photon energy | $0.813\,\mathrm{eV}$ at a center frequency of $f_{\mathrm{c}} = 196.6\,\mathrm{THz}$ |
| $L_{\mathrm{SiN}}$ | Length of passive WG on $Si_3N_4$ chip | $6.7\,\mathrm{mm}$, compare also [114] |
| $L_{\mathrm{PWB}}$ | Length of full PWB trajectory | $317\,\mu\mathrm{m}$, from microscope measurements |
| $L_{\mathrm{gain}}$ | Length of gain section | $700\,\mu\mathrm{m}$, see Section 3.2.2 |
| $n_{\mathrm{eg,SiN}}$ | Effective group refractive index of on-chip $Si_3N_4$ WG | 1.73, see Appendix A.1 |
| $n_{\mathrm{eg,PWB}}$ | Effective group refractive index of intra-cavity PWB | 1.46, from simulation of PWB cross-section |
| $n_{\mathrm{eg,gain}}$ | Effective group refractive index of active gain section | 3.422, from gain ripple frequency spacing of RSOA [J1] |
| $\eta_{\mathrm{PWB}}$ | Power transmission of PWB | $69.2\,\%$ ($1.6\,\mathrm{dB}$), see Appendix A.2 |
| $\eta_{\mathrm{SiN}}$ | Power transmission of $Si_3N_4$ WG | $98.5\,\%$ ($6.7\,\mathrm{mm}$-long $Si_3N_4$ WG with propagation loss of $0.1\,\mathrm{dB/cm}$ [17, 115]) |
| $a$ | Round-trip amplitude transmission factor of racetrack resonator R1 & R2 | 0.999, see Appendix A.1 |
| $\tau$ | Amplitude transmission coefficient of the coupling zones of R1 & R2 | 0.928, see Appendix A.1 |
| $\kappa$ | Amplitude coupling coefficient of the coupling zones of R1 & R2 | 0.372, see Appendix A.1 |
| $n_{\mathrm{sp}}$ | Spontaneous emission factor | 1.5, average value from typical range of $1.25 \ldots 1.75$ [99] |
| $\alpha_{\mathrm{H}}$ | Henry factor of gain section | 3.5, average value from typical range of $2 \ldots 5$ [100] |
| $\alpha_{\mathrm{i}}$ | Distributed modal power loss of gain section | $17\,\mathrm{cm}^{-1}$, average of estimated range of $(14 \ldots 20)\,\mathrm{cm}^{-1}$ [J1] |
| $r_1$ | Back facet amplitude reflection factor | $\sqrt{90\,\%}$, see Section 3.2.2 |
| $P$ | Total output power | $15.85\,\mathrm{mW}$ ($12\,\mathrm{dBm}$), see Section 3.2.4 |

### 2.2.3 Generation of narrow-linewidth Kerr combs

An optical frequency comb features a characteristic optical spectrum comprising many phase-locked, evenly-spaced tones which would ideally have identical intensities. Kerr frequency combs are generated by coupling a high-power CW pump laser[27] with angular frequency $\omega_\mathrm{p}$ into a Kerr-nonlinear optical microresonator, see Fig. 2.7(a) [118]. The resonance frequencies of the microresonator are given by $\omega_{\mathrm{res},n}$ with the resonance index $n$. The microresonator further features anomalous group-velocity dispersion (GVD), i.e., $\beta_\mathrm{c}^{(2)} = \frac{\partial^2}{\partial\omega^2}\beta(\omega)|_{\omega=\omega_\mathrm{c}} = \frac{\partial}{\partial\omega}v_\mathrm{g}^{-1}(\omega)|_{\omega=\omega_c} < 0$ holds true, where $\beta(\omega)$ is the intra-cavity propagation constant, see Section 2.2.2 and the definitions in Eqs. 2.19 and 2.20. The resonance frequencies of the microresonator are separated by the free spectral range (FSR) $\Delta\omega_{\mathrm{res},n} = 2\pi v_{\mathrm{g},n}/L$, where $v_{\mathrm{g},n}$ represents the group velocity at the respective resonance $\omega_n$. Note that the presence of GVD implies that the microresonator FSR becomes frequency-dependent, i.e., for anomalous GVD $\frac{\partial}{\partial\omega}v_{\mathrm{g},n} > 0$ leads to $\frac{\partial}{\partial\omega}\Delta\omega_{\mathrm{res},n} > 0$ and thus to an increasing FSR with frequency and resonance index $n$. Given that the power build-up in the cavity reaches the threshold of modulation instability, a frequency comb forms, which is partially coupled out to the WG again. Hereby, four-wave mixing (FWM) leads to the formation of a large number of spectral lines as a result of pair-wise conversion of pump photons to photons which are up- and down-shifted in frequency [119]. Energy conversion ensures that all comb lines have an equidistant spacing $\Delta\omega_\mathrm{FSR}$ that is very similar to the microresonator FSR at the pumped resonance $\omega_{\mathrm{res},0}$, i.e., $\Delta\omega_\mathrm{FSR} \approx \Delta\omega_{\mathrm{res},0}$. Thus, the spectrum of the frequency comb can be written as $\omega_\mu = \omega_0 + \mu\,\Delta\omega_\mathrm{FSR}$ with the (finite) comb line index $\mu \in \mathbb{Z}$. As a consequence of the frequency-dependent microresonator FSR, a mismatch between the comb line spacing $\Delta\omega_\mathrm{FSR}$ and the resonance frequencies $\omega_n$ of the microresonator arises that increases for comb lines further away from $\omega_0$. This ultimately limits the bandwidth of the generated frequency comb.

[27] Other schemes without the requirement for an external laser source do exist [116, 117], but will not be further discussed in this work.

Importantly, the generation of Kerr combs requires a careful balancing of the pulse broadening associated with the cavity dispersion with the nonlinear phase delay introduced by self-phase modulation (SPM) as a result of the optical Kerr-effect at high intensities. Dispersion arises from the fundamental frequency-dependence of the refractive index associated with the resonator medium as well as the geometry of the underlying WG structure. In this context, the term $\beta_c^{(2)}$ is used to quantify the GVD and associated temporal pulse broadening. Remarkably, if a medium features anomalous GVD ( $\beta^{(2)} < 0$), e.g., by proper choice of materials and careful design of the WG cross-section, the spectral broadening caused by SPM may be fully compensated[28]. The shape and spectral composition of the propagating pulses are thus retained over time, leading to the formation of soliton pulses that circulate in the cavity. The relatively high losses in a microresonator associated with the WG losses and the coupling between the resonator and the bus WG necessitate a constant CW background in order to maintain a soliton state by providing sufficient parametric gain. Such soliton-based frequency combs are therefore commonly referred to as dissipative Kerr solitons (DKS). As illustrated in Fig. 2.7(a), the output spectrum of the microresonator is composed of a superposition of the DKS spectrum (equidistant blue lines) with the strong signal at $\omega_0$ (red line) originating from the pump laser. In the time domain, this corresponds to a series of pulses occurring at a fixed spacing $t_R = 2\pi/\Delta\omega_{FSR}$.

Microresonators can also support the co-existence of several soliton pulses circulating in the cavity at the same time, a state which is referred to as multi-soliton (MS) state. Hereby, the exact shape of the comb envelope depends on the specific number of circulating solitons and their spacing [119]. For many applications, the so-called single-soliton (SS) state featuring a single ultra-short pulse is of particular interest due to the associated spectrum featuring a smooth and broadband spectral envelope, as schematically illustrated in Fig. 2.7(a). It is therefore of great interest to find a deterministic route for reaching the SS state

[28] Note that it is theoretically possible to generate Kerr combs in resonators featuring normal GVD, but in practice this is hardly observed due to temperature effects [120]. In such a case, e.g., "dark" solitons can form, which correspond to very localized drops of intensity in the field circulating the Kerr-nonlinear resonator.

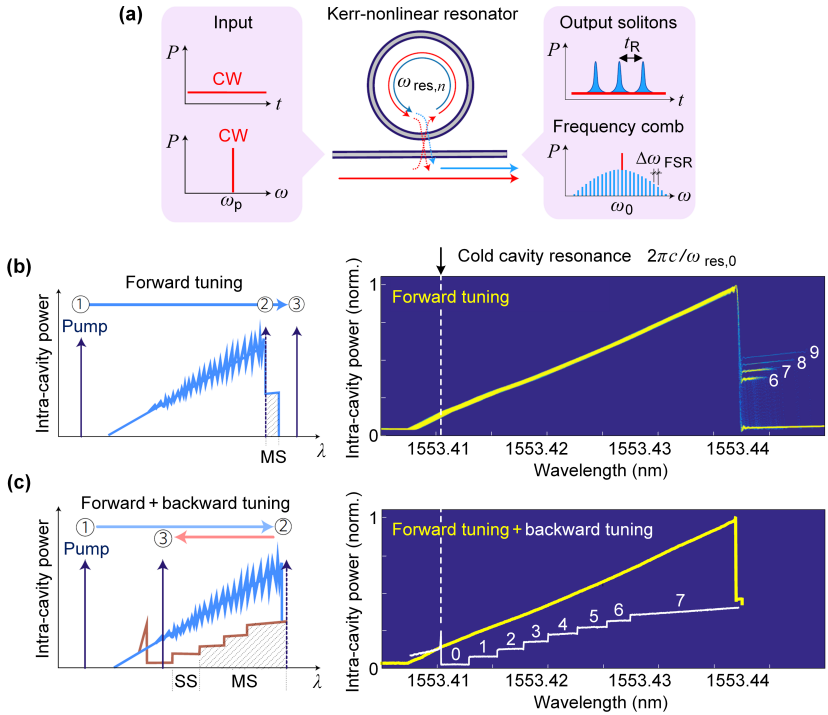


**Fig. 2.7:** Generation of frequency combs in Kerr-nonlinear microresonators. **(a)** A high-power continuous-wave (CW) laser emitting at angular frequency $\omega_\mathrm{p}$ is coupled into a high-$Q$ Kerr-nonlinear microresonator featuring anomalous group-velocity dispersion (GVD), and is precisely detuned with respect to a resonance $\omega_{\mathrm{res,n}}$ of the cold cavity. **(b)** Intra-cavity power vs. pump wavelength for the forward tuning scheme: The pump laser is tuned from the low-wavelength side (blue-detuned, $\omega_\mathrm{p} > \omega_{\mathrm{res},0}$, Position ①) of a cold cavity resonance $2\pi c/\omega_{\mathrm{res},0}$ to the high-wavelength side (red-detuned, $\omega_\mathrm{p} < \omega_{\mathrm{res},0}$, Position ②), giving rise to modulation instability. In addition to the Kerr-nonlinear resonance shift, the position of the "hot" resonance is subject to a thermally-induced resonance shift. The pump laser thus stays effectively blue-detuned with respect to the hot cavity (blue power trace). By further tuning of the pump laser (towards Position ③), the system enters a bistable regime, where multiple dissipative Kerr solitons circulate in the microresonator. The switching to this multi-soliton (MS) state is accompanied by a step-like decrease in the intra-cavity power. **(c)** Intra-cavity power vs. pump wavelength for the combined forward + backward tuning scheme: The forward tuning is stopped once a MS state and the associated drop in intra-cavity power are observed (Position ②). The pump laser is then tuned backwards to lower wavelengths (blue-detuning, towards Position ③), which allows the successive extinction of intra-cavity solitons down to the single-soliton (SS) state as apparent from the staircase-like power trace. This is enabled by the thermal nonlinearity of the microresonator which leads to a reduction of the thermally-induced resonance shift each time a soliton is lost. The scheme permits further backwards tuning of the pump while still maintaining an operation in the effectively red-detuned regime (red power trace) within the soliton existence range. *Adapted and reproduced with permission from Springer Nature [118].*

in a reliable way. Various techniques for the generation of DKS have been experimentally demonstrated, among which tuning the frequency of a CW pump-laser is the method of choice in most experiments[29] [118, 119, 125]. This technique requires carefully tuning the frequency $\omega_\mathrm{p}$ with respect to a pumped cavity resonance $\omega_{\mathrm{res},0}$ to control the detuing $\delta\omega = \omega_{\mathrm{res},0} - \omega_\mathrm{p}$. The two most commonly used principles, namely the forward and the combined forward + backward tuning approach [118], are illustrated in Fig. 2.7(b) and (c), respectively. Initially, the pump is operated in the blue-detuned regime, i.e., at a lower wavelength $\lambda$ compared to the cold cavity resonance $2\pi c/\omega_{\mathrm{res},0}$. When tuning the laser from the left side of the cold resonance (blue-detuned, $\delta\omega < 0$, Position ①) to the right-hand side (red-detuned, $\delta\omega > 0$, Position ②), the intra-cavity power gradually increases. This induces a shift of the hot cavity resonance towards higher wavelengths as a result of the Kerr-effect, whereby the refractive index increases with the intensity. An additional resonance shift results from the absorbed light leading to an increased temperature and thereby an expansion of the microresonator, as well as to an increased refractive index. This may be expressed in terms of an effective detuning $\delta\omega_\mathrm{eff} = \delta\omega - \Delta_\mathrm{T}$, where $\Delta_\mathrm{T}$ accounts for the thermally induced resonance shift. The pump laser thus stays effectively blue-detuned with respect to the hot cavity resonance during the tuning procedure ($\delta\omega_\mathrm{eff} < 0$, blue power trace in Fig. 2.7(b)). If the gain threshold of modulation instability is reached, initial comb formation can be observed. By further tuning the pump laser towards Position ③ in Fig. 2.7(b), the system enters a bistable regime where mode-locked operation becomes possible and multiple DKS can circulate in the microresonator. This switching to the MS state is accompanied by a step-like response in the power trace as shown in Fig. 2.7(b), whereby an effective zero detuning ($\delta\omega_\mathrm{eff} = 0$) of the hot resonance is reached at the associated wavelength. Reducing the number of solitons or even switching to a SS state may in principle occur by further tuning of the pump laser into the effectively red-detuned regime ($\delta\omega_\mathrm{eff} > 0$). In fact, it

[29] Other approaches include shifting the pumped resonance $\omega_{\mathrm{res},0}$ of the Kerr-nonlinear resonator while keeping the operating frequency constant, e.g., by using integrated micro-heaters [23, 121], temperature tuning through varying pump power [122], electro-optic tuning [123], or single-sideband modulation [124].

has been shown [119] that solitons are supported only for a certain range of the effective detuning $\delta\omega_{\mathrm{eff}}$ in the effectively red-detuned regime, also referred to as the soliton existence range. The main challenge therefore lies in the thermally-induced resonance shift $\Delta_{\mathrm{T}}$ that acts in addition to the Kerr-nonlinear resonance shift, but on a much slower timescale. Reaching the soliton state without the resonator being in thermal equilibrium implies further changes to the detuning $\delta\omega_{\mathrm{eff}}$, which will destabilize the system and commonly make the SS state inaccessible by the forward tuning technique [118]. This phenomenon is visualized in the right-hand side graph in Fig. 2.7(b), where a multitude of experimentally recorded power traces associated with the normalized intra-cavity power have been overlaid, revealing the predominant formation of MS states with six to nine solitons in the depicted example.

To overcome this problem, the combined forward + backward tuning scheme is usually employed, providing a reliable and robust way to access the SS state in a Kerr-nonlinear resonator. As outlined in Fig. 2.7(c), the initial forward tuning is stopped once a MS state and the associated drop in intra-cavity power are observed ($\delta\omega > 0$, Position ②). Then, the pump laser is tuned back to lower wavelengths (blue-detuning, towards Position ③), which allows the successive extinction of intra-cavity solitons down to the SS state. Importantly, this is enabled by the thermal nonlinearity of the microresonator which leads to a reduction of $\Delta_{\mathrm{T}}$ each time a soliton is lost. This in turn increases the effective detuning $\delta\omega_{\mathrm{eff}}$, which permits further backwards tuning of the pump laser to lower wavelengths (lowering $\delta\omega$) while still maintaining an operation in the effectively red-detuned regime of the hot cavity, i.e., $\delta\omega_{\mathrm{eff}} > 0$ all along the red trace in Fig. 2.7(c) within the soliton existence range[30]. As shown in Fig. 2.7(c), the backward tuning thus leads to a staircase-like decay of the intra-cavity power with equal step heights and widths until the SS state is reached. Neglecting the strong peak stemming from the CW pump laser, the spectral envelope of the various comb tones (index $\mu$) associated

[30] In practice, the backward tuning must be carried out in an adiabatic way with a speed much smaller than the thermal relaxation rate. This ensures that thermal equilibrium is reached in each MS state, before further backward tuning of the CW pump laser is pursued [118].

with this SS state can be described as [119, 126]

$$\Psi(\mu) \propto \mathrm{sech}^2\left(\frac{\pi}{2}\sqrt{\frac{\beta'}{\zeta}}\,\mu\right), \tag{2.30}$$

where $\beta' \propto -\beta_c^{(2)}$ and $\zeta \propto \delta\omega$ are normalized quantities (without any unit) describing the dispersion and detuning, respectively. As can be inferred from Eq. 2.30, $\beta' > 0$ and $\zeta > 0$ must hold true for $\Psi(\mu)$ to be real, thus implying anomalous GVD ($\beta_c^{(2)} < 0$). Note that broadband combs require the pre-factor $\sqrt{\beta'/\zeta}$ in the argument of the $\mathrm{sech}^2$ function to be as small as possible, which may be achieved by proper choice of detuning and cavity dispersion [25, 126].

While comb generation was successfully demonstrated over the previous years in a plethora of Kerr-nonlinear microresonators such as silica toroidal cavities [127] or crystalline whispering-gallery mode microresonators [128], Kerr comb generators based on integrated $Si_3N_4$-based devices hold particular promise since they can be efficiently fabricated on a wafer level, and since $Si_3N_4$ WG offer low propagation loss and do not suffer from two-photon-induced free-carrier absorption. This permits fabrication of high-$Q$ microresonators that significantly reduce the intensity levels required for reaching the threshold of modulation instability compared to earlier Kerr-comb concepts. To generate "high-performance" Kerr combs, one requires CW pump lasers that ideally fulfill three characteristics: First, the emission wavelength of the pump needs to be tunable. This is especially important in order to precisely control the detuning $\delta\omega$ as needed for Kerr-comb generation, see the discussion in the previous paragraphs. Comb generators that are based on self-injection locking (SIL) of the pump laser to the Kerr-nonlinear resonator [23–26, 129–131] do not fulfill this condition, as the pump tone cannot be independently detuned from the resonance of the cold ring. Therefore, SS states with a large detuning and broad bandwidth may be hard to obtain. Secondly, the pump laser must feature low frequency-noise performance, as the frequency noise of the individual comb lines is dictated by the frequency noise of the CW pump. Lastly, the assembly of such pump lasers should be similarly scalable as the fabrication of the underlying $Si_3N_4$ PIC themselves. Hybrid ECL

based on $Si_3N_4$ feedback circuits fulfill these requirements in an almost ideal way. In this context, ring resonators on the $Si_3N_4$ PIC can be used for tuning the frequency-selective feedback, thereby enabling the independent control of the ECL emission wavelength with respect to the pumped cavity resonance[31]. Furthermore, hybrid ECL using $Si_3N_4$-based feedback circuits can operate with ultra-low linewidths as a result of the low passive WG losses and large optical cavity length, see Section 2.2.2 for a more detailed discussion. Finally, 3D-printed coupling elements such as PWB and FaML permit scalable assembly of associated integrated systems. More details on the practical implementation of such pump lasers and Kerr-comb generators based on $Si_3N_4$ PIC can be found in Chapter 3.

### 2.2.4 Characterization techniques

The measurement of the laser frequency noise in the form of the line shape $S_{\mathrm{E}}(\tilde{f})$ or the frequency-noise spectrum $S_{\mathrm{F}}(f)$ is far from a trivial task, in particular because the evolution of the phase must be compared to a known reference. Traditional diffraction-grating based optical spectrum analyzers (OSA) offer a wide wavelength scanning range and large dynamic range, but the spectral resolution is typically limited to the gigahertz level[32]. The rapid evolution and widespread adoption of narrow-linewidth lasers and frequency combs has likewise increased the demand for suitable characterization techniques. Commonly utilized measurement methodologies are depicted in Fig. 2.8, among which the heterodyne beating with an ultra-stable reference laser and frequency discriminator method have been employed in the course of this thesis. These approaches are described in more detail in the following.

[31] Strictly speaking, the emission of the pump ECL at $f_{\mathrm{ECL}}$ and the resonance $f_{\mathrm{res}}$ of the frequency-selective Sagnac loop mirror need to be synchronously tuned [114] with respect to the resonance of the Kerr-nonlinear resonator $\omega_{\mathrm{res},0}$, such that $f_{\mathrm{ECL}} - f_{\mathrm{res}} = \mathrm{const.}$ in Fig. 2.6. In practice, however, tuning $f_{\mathrm{ECL}}$ by a dedicated phase shifter usually suffices, since the detuning $\delta\omega = \omega_{\mathrm{res},0} - 2\pi(f_{\mathrm{ECL}} - f_{\mathrm{res}})$ in the final SS state is comparatively small, thereby not imposing a dramatic change on the operating point of the ECL pump.

[32] See for example: `https://tmi.yokogawa.com/solutions/products/optical-measuring-instruments/optical-spectrum-analyzer/`.

**Heterodyne beating with a reference laser:** A conceptually simple measurement method is based on recording the beat note of a laser under test (LUT, $f_{\mathrm{LUT}}$) with a highly-stable reference laser ($f_{\mathrm{ref}}$) [132], see Fig. 2.8(a). The tones emitted by the LUT and reference laser each pass an isolator and a polarization controller (PC), before being superimposed on a photodetector (PD). The reference laser is tuned close[33] to the LUT such that the resulting beat note in the photocurrent centered about the difference frequency $|f_{\mathrm{ref}} - f_{\mathrm{LUT}}|$ can be measured using an electrical spectrum analyzer (ESA). The spectral line shape $S_{\mathrm{E}}(\tilde{f})$ of the beat note hereby represents the convolution of the LUT and the reference laser spectrum. In the case of a frequency comb, multiple beat notes with a separation of the FSR can be observed. If the frequency noise of the reference laser is negligible compared to the LUT ($\delta f_{\mathrm{ref}} \ll \delta f_{\mathrm{LUT}}$), the measured spectrum of the beat note directly represents the LUT line shape. Alternatively, a reference laser with similar noise performance can be chosen ($\delta f_{\mathrm{ref}} \approx \delta f_{\mathrm{LUT}}$), and the LUT linewidth is extracted by taking into account the spectral broadening due to the convolution of the two spectra[34]. In order to extract the full frequency-noise spectrum $S_{\mathrm{F}}(f)$, more sophisticated evaluation schemes based on the coherent detection of the phase differences need to be employed, e.g., using offline digital signal processing (DSP) based on a carrier phase recovery [133] or by replacing the combiner with a $90^\circ$ optical hybrid followed by a digital coherent receiver [88, 133].

**Delayed self-homodyne / self-heterodyne interferometric measurement:** An often more convenient method, which eliminates the need for a reference laser, is based on an interferometric measurement of the LUT using an imbalanced interferometer [134], see Fig. 2.8(b). The incident light is first split into the two arms of an imbalanced Mach-Zehnder interferometer (MZI), and a delay $\tau_{\mathrm{d}}$ much

[33] In practice, the difference frequency $|f_{\mathrm{ref}} - f_{\mathrm{LUT}}|$ is selected such that it largely exceeds the spectral half-width of the investigated laser line shape, thereby avoiding impairments due to spectral foldback of negative frequency components in the real-valued photocurrent.

[34] Note, however, that in such a scenario the factor by which the measured line shape of the electrical spectrum is broadened with respect to the actual line shape of the LUT depends on whether the underlying spectra of the LUT and reference laser are better resembled by a Gaussian or a Lorentzian function given the observation time $\tau_0$. In practice, the FWHM linewidth of the LUT is therefore smaller by a factor $\sqrt{2}$ (Gaussian) . . . 2 (Lorentzian).

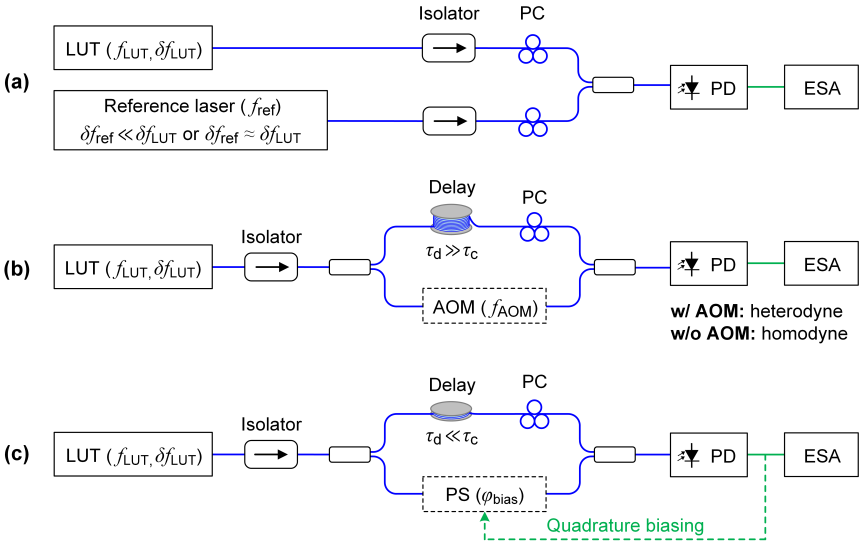


**Fig. 2.8:** Overview of measurement techniques for laser frequency noise and linewidth. Abbreviations: AOM – acousto-optic modulator; ESA – electrical spectrum analyzer; LUT – laser under test; PC – polarization controller; PD – photodetector; PS – phase shifter. **(a)** Heterodyne beating with a reference laser: The signals from a laser under test (LUT) and a reference laser are superimposed on a photodetector (PD), and the spectrum of the photocurrent is measured using an electrical spectrum analyzer (ESA). The retrieved line shape allows the extraction of the linewidth if the reference laser noise is either negligible or of similar performance as the LUT. **(b)** Delayed self-homodyne / self-heterodyne interferometric measurement: To remove the need for a reference laser, an interferometric measurement using an imbalanced Mach-Zehnder interferometer (MZI) can be performed. For delays $\tau_\mathrm{d}$ much larger than the coherence time $\tau_\mathrm{c} \propto (\delta f_\mathrm{LUT})^{-1}$, the noise of the delayed reference becomes uncorrelated to the LUT and the recorded line shape is a simple self-convolution. The lower arm of the MZI can either be left as is (delayed self-homodyne), or an acousto-optic modulator (AOM, $f_\mathrm{AOM}$) is inserted to slightly shift the beat note frequency (delayed self-heterodyne). **(c)** Frequency discriminator technique: A direct measurement of the frequency-noise spectrum is enabled by a frequency discriminator, based, e.g., on an imbalanced MZI with a delay $\tau_\mathrm{d}$ much smaller than the coherence time $\tau_\mathrm{c}$ leading to a beating at the PD. The resulting output intensity becomes linearly proportional to the phase difference $\Delta\varphi(t) = \varphi(t+\tau_\mathrm{d}) - \varphi(t)$ for small delay-time differences $\tau_\mathrm{d}$ if the interferometer is held in the quadrature-point. This condition is maintained by introducing a phase shift $\varphi_\mathrm{bias}$, which is controlled by means of a feedback loop or locking circuit.

larger than the coherence time $\tau_\mathrm{c} \propto (\delta f_\mathrm{LUT})^{-1}$ of the LUT is introduced in one of the paths, such that the noise of the delayed reference becomes uncorrelated to the noise of the LUT. Therefore, the line shape $S_\mathrm{E}(\tilde{f})$ — which is again found

from the spectrum of the photocurrent beat note recorded by the ESA — becomes a simple self-convolution of the LUT line shape, from which its linewidth can be retrieved. The lower arm of the MZI can either be left as is, leading to a beat signal centered around 0 Hz (delayed self-homodyne), or an AOM is inserted to shift the center frequency to $f_{\mathrm{AOM}}$ (delayed self-heterodyne), thus avoiding the noisy low-frequency range in the measurement of the photocurrent. However, when measuring an LUT with ultra-low linewidth (i.e. very long coherence time $\tau_c$), an excessively long delay length $\tau_{\mathrm{d}}$ is required for decorrelation of the two arms. Such a long fiber delay renders the delayed self-homodyne / self-heterodyne measurements highly susceptible to environmental influences such as acoustic noise, which appear at low offset frequencies, leading to spectral line broadening and limiting the measurement to a detection of the envelope of the frequency-drifting "perfect" Lorentzian source [94, 135, 136]. To partially circumvent these limitations, adapted concepts using recirculating fiber loops [137, 138], a combination of short and long fibers [139], or shorter delay lines in conjunction with more sophisticated mathematical analysis have been proposed [140–142].

**Frequency discriminator technique:** Another method for characterizing the frequency noise of a LUT is to convert the fluctuations of the instantaneous frequency $\delta\tilde{f}(t)$ to intensity fluctuations $I(t)$ using an optical frequency discriminator, based, e.g., on an imbalanced interferometer or a high-finesse reference cavity [143–145], see Fig. 2.8(c). In case of an imbalanced MZI, the incident light is again split into two arms, but this time a delay $\tau_{\mathrm{d}}$ much shorter than the coherence time $\tau_{\mathrm{c}}$ of the laser tone under test is introduced in one of the paths. This leads to a coherent beating at the PD, and the output intensity of the interferometer is proportional to the phase difference of the two arms, i.e., $I(t) \propto \frac{1}{2}[1+\cos(\Delta\varphi(t)+2\pi f_{\mathrm{LUT}}\tau_{\mathrm{d}})]$. In this relation $\Delta\varphi(t) = \varphi(t+\tau_{\mathrm{d}})-\varphi(t)$ is the phase difference introduced by the delay-time difference $\tau_{\mathrm{d}}$, and the term $2\pi f_{\mathrm{LUT}}\tau_{\mathrm{d}}$ is an additional phase shift between the combined optical fields [145]. If the interferometer is held in the quadrature-point such that $2\pi f_{\mathrm{LUT}}\tau_{\mathrm{d}} = \pi/2 \pm 2\pi N$ is fulfilled for $N = 0, 1, 2, \ldots$, the intensity fluctuations become directly proportional to the phase difference (if $\Delta\varphi(t)$ is kept

small[35]), i.e., $I(t) \propto \frac{1}{2}[1 \mp \sin(\Delta\varphi(t))] \propto \Delta\varphi(t)$. This condition is usually maintained by an additional phase shift $\varphi_{\mathrm{bias}}$ in the second arm, which is controlled by means of a feedback loop or locking circuit. The interferometer can therefore be considered as a black box which linearly transforms the frequency variations at the input into a photocurrent variation of the PD at the output. The frequency-noise spectrum $S_{\mathrm{F}}(f)$ can then be computed from the recorded PSD by taking into account the relation between the phase difference and instantaneous frequency, which can be estimated by $\delta\tilde{f}(t) \approx \Delta\varphi(t)/(2\pi\tau_{\mathrm{d}})$ for sufficiently small $\tau_{\mathrm{d}}$ [88]. Although the requirement for a continuous quadrature biasing makes this measurement scheme more complex at first sight, it comes with the added benefit of retrieving the full noise characteristics within much shorter measurement times and without the need for cumbersome data evaluation.

## 2.3 Space-division multiplexing in short-reach systems

The relentless proliferation of digital services has led to an unprecedented surge in data demand within optical communication networks. However, the inherent scaling disparities between CMOS-based computing and storage systems required for, e.g., the generation and processing of data on the one hand, and the communication network resources on the other hand are starting to manifest in a network "capacity-crunch" [146, 147], posing a challenge to existing data transmission paradigms. One approach to cope with the capacity requirements in modern communication networks is to utilize advanced multiplexing techniques, involving the simultaneous transmission of multiple signals over a shared medium. Hereby, the five physical dimensions time, frequency, quadrature, polarization, and space may be exploited as illustrated in Fig. 2.9 [148]:

[35] In fact, it must be assured that the photocurrent variations due to the discrimination of the frequency noise dominate when compared to the laser intensity noise. In practice, these effects can be separated by taking multiple measurements on opposite slopes of the biased discriminator [145].

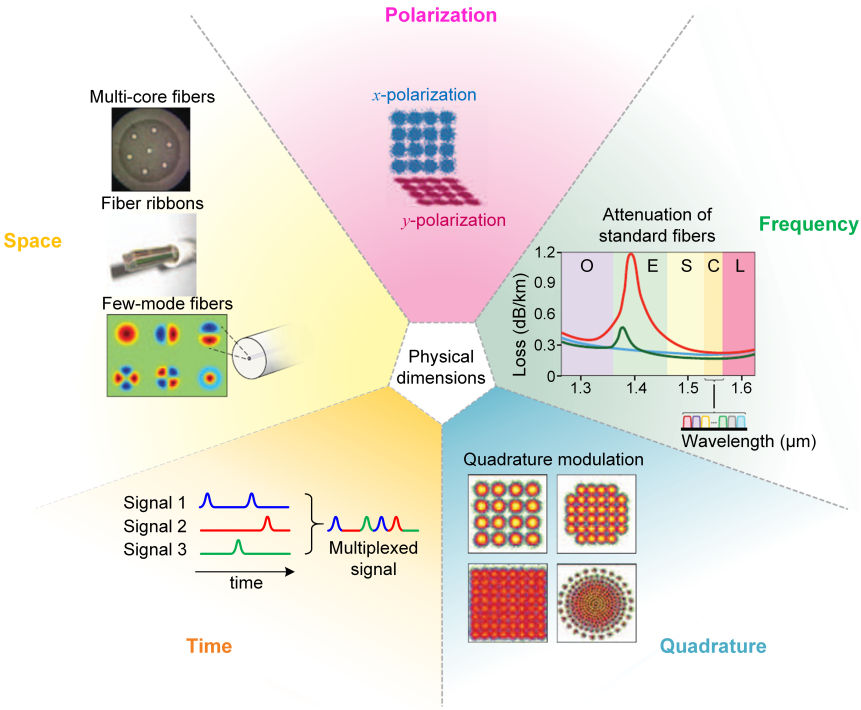


**Fig. 2.9:** Overview of multiplexing techniques in optical fiber communications. To cope with the ever-increasing capacity requirements, advanced multiplexing techniques for simultaneous transmission of multiple signals over a shared medium can be utilized, exploiting the five physical dimensions time, frequency, quadrature, polarization, and space. *Adapted and reproduced with permission from Springer Nature [148].*

- **Time:** In the temporal domain, data streams are traditionally segmented into distinct time slots which define the rate at which information can be carried over a communication link. Time-division multiplexing (TDM) may be employed to transmit multiple optical signals over a common medium by assigning individual transmission time slots to each data source. To this end, the associated temporal pulse-trains of the signals can be interleaved, and a multiplexed signal with an increased aggregate line rate is generated [149].

- **Quadrature:** Quadrature multiplexing methods exploit both the amplitude and phase of electromagnetic waves to encode data. Advancements in DSP have enabled coherent optical communications with higher-order modulation formats [150, 151] such as so-called quadrature amplitude modulation (QAM), which has become a mainstay of current long-reach optical communication systems [152]. However, owing to the logarithmic scaling of an information channel's capacity with the SNR[36], these higher-order modulation formats always come at the cost of more stringent optical SNR (OSNR) requirements [146, 154]. Recent advances in constellation shaping techniques already permit the operation close to the Shannon limit [155].

- **Polarization:** Polarization-division multiplexing (PDM) relies on the two orthogonal polarization states of light to transmit data. However, drifts in the polarization state can occur due to environmental effects acting on the fiber network, which eventually leads to rapid and erratic rotation of the polarized light's Jones vector over the entire Poincaré sphere. This needs to be coped with at the receiver side by advanced DSP techniques [156].

- **Frequency:** Multiple signals can also be transmitted by utilizing a multitude of distinct carrier frequencies. In optical communications, this principle is well-known as wavelength-division multiplexing (WDM) and widely adopted in long-haul communication systems since the 1980s. However, in some cases, further scalability of this approach is hampered by the limited spectral bandwidth of the communication channel, which is often dictated by the associated optical amplifiers and which sets an upper bound to the usable transmission capacity of a single optical fiber [146, 154]. More specifically, standard single-mode fibers (SMF) and equipment such as optical amplifiers and multiplexers are usually optimized for operation in the telecommunication C-band ($1530\,\mathrm{nm}\ldots1565\,\mathrm{nm}$). Using a

[36] This is well known as the Shannon-Hartley theorem [153], which defines the theoretical upper bound of the information rate that can be transmitted error-free for a certain $\mathrm{SNR} = S/N$ and bandwidth $B$ as $C = B\log_2(1+\mathrm{SNR})$. Herein, $S$ and $N$ are the average signal and noise power over the bandwidth $B$ of the associated Gaussian distributions, respectively, and it is assumed that the communication channel is linear and only subject to additive white Gaussian noise (AWGN).

larger number of WDM channels beyond this frequency range might necessitate impractical and costly system designs and implementations [146].

- **Space:** Space-division multiplexing (SDM) relies on parallel transmission through different spatial channels within optical fiber links. The spatially separated channels rely, e.g., on different spatial modes or physically separated fiber cores, provided by fiber bundles, fiber ribbons or multi-core fibers (MCF) in single- or multi-mode configurations [157]. While the concept of SDM is almost as old as optical communication through fibers itself, only recently serious attention has been given to network platforms exploiting MCF due to the need for extensive changes in the system architecture as well as associated challenges in maintaining compatibility with existing fiber networks [148]. Nevertheless, space is the only remaining dimension that promises a long-term linear scaling of system capacity by orders of magnitude [146]. As a result, SDM has become the new research frontier, with novel types of fibers building a base for the evolution of optical communication systems towards massive parallelism.

In the context of short-reach interconnects ($< 100\,\mathrm{m}$), scaling of the achievable data rates through, e.g., parallel transmission via spatially separated channels is seen as an especially attractive approach [146, 158]. This involves, for example, board-to-board or rack-to-rack communications in intra-datacenter links or high-performance computing systems, where hundreds of thousands of interconnects are required. Each of these interconnects requires transceivers at either end, which represent the major contribution to the overall cost. Such transceiver assemblies must hence be very cost-effective. This can be achieved by keeping the symbol rates of individual links comparatively low, thereby alleviating the cost of associated electronic circuitry such as, e.g., analog-to-digital and digital-to-analog converters (ADC / DAC). Instead, parallel transmission over many physically separated fiber cores, provided by fiber ribbons or MCF, is commonly employed for scaling of the aggregate data rates. Active optical cables (AOC) based on intensity-modulated (IM) vertical-cavity surface-emitting lasers (VCSEL) and direct-detection (DD) via photodiodes (PD) have been the main workhorse for optical interconnects in this field. VCSEL are semiconductor lasers which emit

light in a direction perpendicular to the chip surface. They feature an extremely short cavity (cavity length of the order of a few micrometers), comprising a quantum-well gain section, which is sandwiched in-between two distributed Bragg reflectors (DBR) as resonator mirrors. The associated fabrication processes allow for wafer-level production and testing of individual devices or two-dimensional device arrays, making them suitable for mass production at very low cost. The short optical cavity further permits lasing in a single longitudinal mode as well as modulation frequencies well in the gigahertz range due to the small associated cavity volume. The lateral size of the active region can be adjusted to optimize the VCSEL, e.g., for achieving low threshold currents by using small device diameters of the order of a few micrometers, or high output-power levels of tens of mW obtained for large device diameters of the order of tens of micrometers. However, since increasing the diameter of the active region will inevitably lead to the support of multiple transverse modes, VCSEL with high beam-quality[37] are usually limited to an output power of a few mW. Compared to edge-emitting devices, VCSEL furthermore feature a low beam divergence and symmetric beam profile, which, in combination with appropriate lenses, enable efficient coupling into commonly utilized multimode fibers (MMF) with core sizes of the order of $50\,\mu\text{m}$. Especially VCSEL emitting at a wavelength of $850$ nm in combination with graded-index MMF find broad commercial application [158].

Typical single channel line rates in AOC are of the order of $25$ Gbit/s for on-off-keying (OOK) or $50$ Gbit/s using four-level pulse-amplitude modulation (PAM4) [160]. For achieving higher aggregate data rates, AOC conventionally employ linear arrays of VCSEL and PD which are interconnected to the outside world via spatially separated fiber optic links. As an example of such an SDM-based transmission link, the IEEE 802.3 industry standard specifies the use of linear $4 \times 1$ arrays[38] of VCSEL and PD at line rates of $25$ Gbit/s (OOK) to reach

[37] As a general rule of thumb, VCSEL employing an oxide aperture for current confinement typically emit in a single transverse mode for diameters of the active region of up to $4\,\mu\text{m}$. For larger diameters, VCSEL become transverse multi-moded and tend to develop ring-shaped near- and far-field patterns [159].

[38] Owing to the four-fold increase in the line rate, the associated AOC are commonly referred to as quad small form-factor pluggable (QSFP) modules according to the IEEE 802.3 standard [161].

aggregate line rates of 100 Gbit/s [161]. For achieving higher data rates at similarly low cost, the channel count needs to be scaled up through the implementation of even larger device arrays [162], which will inevitably lead to a bottleneck in terms of the economical feasibility of currently implemented packaging concepts. Further scalability is thus hampered by the increasing cost as a result of the growing number of fibers as well as space constraints arising from the physical size of the associated plugs. Multimode MCF (MM-MCF) comprising many cores which are more densely spaced compared to conventional MMF arrays have therefore stepped into the forefront, promising a significant reduction of the associated fiber installations. However, AOC employing MCF suffer from challenges related to the optical assembly. Specifically, individual cores of MCF must be connected with linear arrays of VCSEL or PD having industry-standard pitches of, e.g., 250 µm. Commonly employed coupling schemes therefore rely on bulky fan-out structures, often in conjunction with custom connector and fiber arrangements. Such solutions are technically complex and challenging to scale, in particular when it comes to compact short-reach datacenter transceivers that are subject to stringent constraints in footprint and in assembly costs. In this context, 3D-printed optical coupling elements such as facet-attached microlenses (FaML) represent a promising avenue for interconnecting active components such as VCSEL and PD with MM-MCF without the need for extensive active alignment [J3]. More details on the practical implementation of such transceiver assemblies can be found in Chapter 4.

## 2.4 Fundamentals of millimeter-wave (mmW) and terahertz (THz) technology

Positioned between the microwave and IR regions, millimeter-waves (mmW) and terahertz (THz) signals hold immense promise for a wide variety of applications. This chapter summarizes the fundamentals that are required to understand the concepts developed and presented within this thesis. First, the guidance of electromagnetic waves via electric transmission lines, in particular coplanar waveguides (CPW), is addressed. In a next step, basic principles for the measurement of

two-port networks are introduced. Lastly, we cover basic performance parameters concerning the radiation of electromagnetic waves and associated antenna metrics, especially in the context of slot antennas which are fed via CPW.

### 2.4.1 Electrical transmission lines

If the physical size of an electrical circuit is significantly smaller than the wavelength of the electrical signal under consideration, the components within the network can be treated as lumped elements which are connected by ideal (lossless) wires. However, at high frequencies, the dimensions of the network become comparable to a significant fraction of the wavelength, and the assumption of lumped elements can no longer be used. This leads to variations in currents and voltages along the circuit, requiring rigorous application of Maxwell's equations for accurate representation of networks. For simplification, microwave theory has therefore devised models that make use of circuit theory for analyzing such networks also at higher frequencies. One example is the propagation of voltages and currents along a conductor of a transmission line, which can be represented by a concatenation of many infinitesimally short sections, each with a length denoted as $\Delta z$ and an equivalent circuit as depicted in Fig. 2.10. Hereby, $\Delta z$ is chosen small enough such that the assumption of lumped elements is justified within each section. Each of these sections is then modeled by a series resistance $R'\Delta z$, a series inductance $L'\Delta z$, a parallel conductance $G'\Delta z$, and a parallel capacitance $C'\Delta z$, where the values $R'$, $L'$, $G'$ and $C'$ represent differential quantities of the transmission line given per length with units $\Omega$/m, H/m, S/m, and F/m, respectively [163].

The time-dependent voltages and currents along the transmission line are governed by the so-called telegrapher equations [163], which may be directly derived from the equivalent circuit shown in Fig. 2.10:

$$\begin{aligned} \frac{\partial\, u(z,t)}{\partial\, z} &= -R'\, i(z,t) \;-\; L'\, \frac{\partial\, i(z,t)}{\partial\, t} \\ \frac{\partial\, i(z,t)}{\partial\, z} &= -G'\, u(z,t) \;-\; C'\, \frac{\partial\, u(z,t)}{\partial\, t}. \end{aligned} \tag{2.31}$$

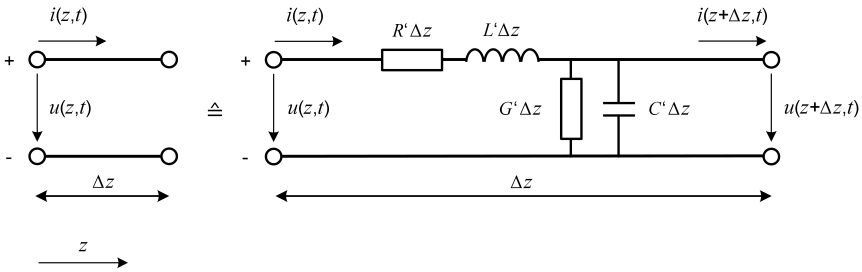


**Fig. 2.10:** Equivalent circuit of a short section of transmission line with length $\Delta z$, where $\Delta z$ is chosen small enough such that the assumption of lumped elements is justified. The transmission line is then given by a concatenation of many such unit elements, where each section is modeled by a series resistance $R'\Delta z$, a series inductance $L'\Delta z$, a parallel conductance $G'\Delta z$, and a parallel capacitance $C'\Delta z$. Hereby, the values $R'$, $L'$, $G'$ and $C'$ represent differential quantities which are given per length with units $\Omega$/m, H/m, S/m, and F/m, respectively.

The two relations given in Eq. 2.31 can be simplified for time-harmonic voltages $u(z,t) = \Re\{U(z)\mathrm{e}^{\mathrm{j}\omega t}\}$ and currents $i(z,t) = \Re\{I(z)\mathrm{e}^{\mathrm{j}\omega t}\}$, and by combining the two resulting expressions, we can derive wave equations for the voltage $U(z)$ and current $I(z)$, which are solved by a superposition of forward and backward traveling waves[39],

$$\begin{aligned} U(z) &= U_0^+ \mathrm{e}^{-\underline{\gamma} z} + U_0^- \mathrm{e}^{\underline{\gamma} z} \\ I(z) &= I_0^+ \mathrm{e}^{-\underline{\gamma} z} + I_0^- \mathrm{e}^{\underline{\gamma} z}. \end{aligned} \tag{2.32}$$

In these relations, $\underline{\gamma} = \sqrt{(R' + \mathrm{j}\omega L')(G' + \mathrm{j}\omega C')}$ is the complex-valued propagation constant[40], and the terms $U_0^+$, $I_0^+$ and $U_0^-$, $I_0^-$ are the amplitudes associated with the forward and backward traveling voltage and current waves at $z = 0$,

[39] Note that in the used convention the current is counted with a positive sign when flowing along the positive $z$-direction, irrespective of the propation direction of the underlying forward and backward traveling current waves. The amplitude $I_0^-$ of the backward propagating current wave is thus negative, leading to a positive line impedance $\underline{Z}_\mathrm{L}$ in Eq. 2.35.

[40] The propagation parameter $\underline{\gamma}$ can further be written as $\underline{\gamma} = \alpha + \mathrm{j}\beta$, where $\alpha$ represents an amplitude attenuation and $\beta$ is the effective propagation constant. Note, however, that in optics $\alpha$ commonly refers to the power attenuation (compare, e.g., the distributed power-loss parameters $\alpha_\mathrm{rt}$, $\alpha_\mathrm{m}$ and $\alpha_\mathrm{gain}$ in Section 2.2).

respectively. The solution for the voltage wave $U(z)$ in Eq. 2.32 can then be used in conjunction with the wave equation as derived from Eq. 2.31 for time-harmonic signals to determine the current $I(z)$ on the line,

$$I(z) = \frac{\underline{\gamma}}{R' + \mathrm{j}\omega L'} \left(U_0^+ \mathrm{e}^{-\underline{\gamma} z} - U_0^- \mathrm{e}^{\underline{\gamma}}\right). \tag{2.33}$$

Comparing Eq. 2.33 to the solution for the current wave $I(z)$ in Eq. 2.32 permits the definition of a so-called characteristic (line) impedance [163]

$$\underline{Z}_\mathrm{L} = \frac{R' + \mathrm{j}\omega L'}{\underline{\gamma}} = \sqrt{\frac{R' + \mathrm{j}\omega L'}{G' + \mathrm{j}\omega C'}}, \tag{2.34}$$

which relates the voltage and current of the waves on the line, i.e,

$$\underline{Z}_\mathrm{L} = \frac{U_0^+}{I_0^+} = -\frac{U_0^-}{I_0^-}. \tag{2.35}$$

In these relations, both $\underline{\gamma}$ and $\underline{Z}_\mathrm{L}$ are generally complex-valued quantities, which are fully determined by $R'$, $L'$, $G'$ and $C'$ and hence depend on the specific cross-section of the transmission line. Signal propagation is thus described by the characteristic line impedance $\underline{Z}_\mathrm{L}$ in combination with the length $z = L$ and propagation constant $\underline{\gamma}$ of the transmission line. Note that for low-loss transmission lines, the assumptions $\omega L' \gg R'$ and $\omega C' \gg G'$ are commonly made for high frequencies, i.e., large $\omega$. Equation 2.34 hence reduces to $Z_\mathrm{L} \approx \sqrt{L'/C'} \in \mathbb{R}$ [163].

A fundamental property of distributed systems are wave reflections, which may be observed at transitions between interconnected circuit elements. Figure 2.11 shows a schematic representation of a transmission line, which is connected to a lumped termination impedance $\underline{Z}_\mathrm{trm}$ at $z = 0$ and which is fed by an incident wave $U_0^+ \mathrm{e}^{-\underline{\gamma} z}$ from a source located at $z < 0$. We further assume that all backward propagating waves are absorbed at the left end of the transmission line such that no further back-reflection from the left has to be considered. As was shown in the previous paragraphs and Eq. 2.35, the ratio of voltage to current for such a

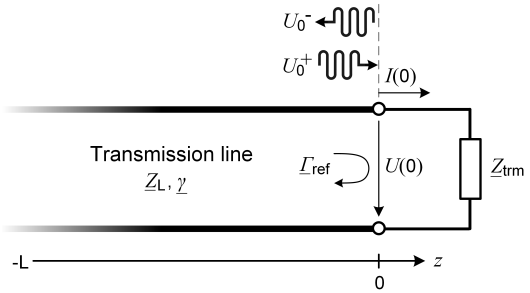


**Fig. 2.11:** Schematic representation of a transmission line with characteristic line impedance $\underline{Z}_\mathrm{L}$, length $L$ and propagation constant $\underline{\gamma}$, which is fed by an incident wave $U_0^+ \mathrm{e}^{-\underline{\gamma} z}$ from a source located at $z < 0$ and terminated with a load impedance $\underline{Z}_\mathrm{trm}$. The voltage $U(z)$ and current $I(z)$ must be related by $\underline{Z}_\mathrm{trm}$ at $z = 0$, thus giving rise to a reflected wave $U_0^- \mathrm{e}^{\underline{\gamma} z}$ in case $\underline{Z}_\mathrm{trm} \neq \underline{Z}_L$. Choosing $\underline{Z}_\mathrm{trm} = \underline{Z}_\mathrm{L}$ results in $\underline{\Gamma}_\mathrm{ref} = 0$. Such a load is thus said to be matched to the transmission line, since no reflection of the incident wave can be observed.

traveling wave is given by the characteristic line impedance $\underline{Z}_\mathrm{L}$. However, when the line is terminated with an arbitrary load $\underline{Z}_\mathrm{trm} \neq \underline{Z}_\mathrm{L}$, the voltage $U(z)$ and current $I(z)$ must be related by $\underline{Z}_\mathrm{trm}$ at $z = 0$. This gives rise to a reflected wave $U_0^- \mathrm{e}^{\underline{\gamma} z}$ to satisfy the boundary condition, which can be formulated with the help of Eqs. 2.32 – 2.35 as

$$\underline{Z}_\mathrm{trm} \stackrel{!}{=} \frac{U(z=0)}{I(z=0)} = \frac{U_0^+ + U_0^-}{U_0^+ - U_0^-} \underline{Z}_\mathrm{L}. \tag{2.36}$$

From Eq. 2.36, we find the complex amplitude reflection coefficient [163]

$$\underline{\Gamma}_\mathrm{ref} = \frac{U_0^-}{U_0^+} = \frac{\underline{Z}_\mathrm{trm} - \underline{Z}_\mathrm{L}}{\underline{Z}_\mathrm{trm} + \underline{Z}_\mathrm{L}}. \tag{2.37}$$

As becomes apparent from Eq. 2.37, choosing $\underline{Z}_\mathrm{trm} = \underline{Z}_\mathrm{L}$ results in $\underline{\Gamma}_\mathrm{ref} = 0$. Such a load is thus said to be matched to the transmission line, since no reflection of the incident wave can be observed. Matching the characteristic impedances within mmW and THz circuits, e.g., for feeding a device under test with a transmission line, is thus crucial to minimize signal reflection at the various interfaces.

### Coplanar waveguide (CPW) transmission lines

Coplanar waveguides (CPW) as originally proposed by Cheng P. Wen in 1969 [164], represent a special type of planar electrical transmission line which consists of three metallic conductors of thickness $h_{\mathrm{m}}$ positioned atop a dielectric substrate with a complex relative permittivity $\underline{\epsilon}_{\mathrm{r}} = \epsilon' - \mathrm{j}\epsilon''$, see Fig. 2.12. A central planar conductor (width $w_{\mathrm{S}}$) is flanked by two planar conductors situated at a distance $d_{\mathrm{SG}}$, where in the ideal case the outer conductors are semi-infinitely extended and the substrate is infinitely thick. In real-world implementations, see Fig. 2.12, both the outer conductor width $w_{\mathrm{G}}$ and substrate height $h$ are finite.

CPW support propagation of two fundamental modes with no lower cut-off frequency [164, 165], the electric and magnetic field distributions of which are depicted in Fig. 2.12(a) and (b). Figure 2.12(a) shows the so-called "even" or CPW mode, characterized by the two outer ground conductors (labeled "G") having the same potential, which is distinct from the potential of the central signal conductor (labeled "S"). The even mode is a quasi-transverse electromagnetic (TEM) mode without any longitudinal field component, where the electric field lines begin (or end) at the signal line and end (or begin) at the two surrounding ground planes. The magnetic field lines enclose the signal conductor. Figure 2.12(b) shows the so-called "odd" or slot-line mode, characterized by the two outer conductors with potentials of opposite sign. Some electric field lines directly traverse from one ground plane to the other without them touching the signal line at all. Typically, the "even" mode is desired for CPW signal propagation as no change of the associated transmission line parameters is ideally observed with frequency[41]. The even mode consequently features very low dispersion, thereby permitting broadband operation up to the mmW and THz frequency range [165]. For the following explanations, we therefore always refer to the "even" mode of the CPW.

[41] To prevent unintentional excitation of the parasitic "odd" mode, the two ground planes must be kept at the same potential. This is commonly achieved by means of air bridges [165] or the use of measurement probes in ground-signal-ground (GSG) configuration.

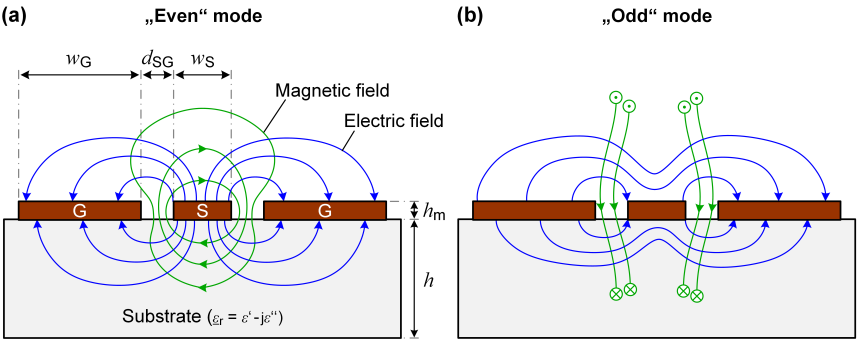


**Fig. 2.12:** Field distributions of the two fundamental modes of a coplanar waveguide (CPW) which consists of three metallic conductors positioned atop a dielectric substrate. **(a)** Field distributions of the so-called "even" or CPW mode, characterized by the two outer ground conductors (labeled "G") having the same potential, which is distinct from the potential of the central signal conductor (labeled "S"). The even mode is a quasi-transverse electromagnetic (TEM) mode without any longitudinal field component and is usually preferred due to favorable dispersion characteristics. **(b)** Field distributions of the so-called "odd" or slot-line mode, characterized by the two outer conductors with potentials of opposite sign. In this case, the magnetic field has longitudinal components.

In the realm of monolithic microwave integrated circuits (MMIC), CPW have proven to offer numerous advantages over, e.g., microstrip transmission lines [165]. Since all conductors are confined to a single plane, no via holes are required, enabling the straightforward series and parallel implementation of active and passive devices. Moreover, the presence of two ground planes minimizes cross-talk between neighboring lines and thereby permits more condensed circuit designs. Additionally, due to the fundamental CPW modes not requiring any backside-metallization for propagation, CPW can in principle work with arbitrarily thick substrates. This eliminates the need for technologically demanding and costly backside-preparation and substrate-thinning techniques. Within this thesis, the key advantages of CPW lie in their straightforward fabrication, in the flexibility in adjusting the characteristic line impedance $\underline{Z}_L$ over a wide range, see Appendix D.2, as well as in the availability of simple on-wafer measurement techniques for the characterization of associated mmW and THz devices.

One reason that kept CPW from extensive application in the past was the long lasting lack of an accurate and flexible design basis [165]. As an example, no closed form expressions exist for the exact description of the line impedance $Z_{\mathrm{L,CPW}}$ of a CPW. However, by applying quasi-static approximations[42], the characteristics of a CPW can be analytically evaluated, e.g., using the so-called conformal mapping technique. Hereby, the complex geometry of a CPW is mapped into an analytically more manageable structure, often a parallel-plate configuration. The associated capacitance can then be simply calculated and is a measure of the cross-sectional differential line capacitance $C'_{\mathrm{CPW}}$ of the CPW. The line impedance $Z_{\mathrm{L,CPW}}$ is then given by Eq. 2.34 for the case of low-losses and in the limit of high frequencies, whereby we assume that the differential inductance $L' = (C' v_{\mathrm{ph}}^2)^{-1}$ can be expressed in terms of the differential capacitance $C'_0$ of the same WG arrangement in vacuum, i.e., the phase velocity $v_{\mathrm{ph}}$ is given by the speed of light $c$ [164, 165],

$$Z_{\mathrm{L,CPW}} \approx \sqrt{\frac{L'_{\mathrm{CPW}}}{C'_{\mathrm{CPW}}}} = \sqrt{\frac{1}{C'_{\mathrm{CPW}}\, C'_0 c^2}} = \sqrt{\frac{\epsilon_0 \mu_0}{C'_{\mathrm{CPW}} C'_0}}. \tag{2.38}$$

In this relation, $\epsilon_0$ and $\mu_0$ are the vacuum permittivity and permeability, respectively, which are related to the speed of light by $c = 1/\sqrt{\epsilon_0 \mu_0}$. Under the same assumptions, we can also determine the propagation constant $\underline{\gamma}$, compare Eq. 2.34. All derivations of the transmission line parameters hence reduce to the calculation of a differential line capacitance $C'_0$ in absence of a dielectric, and the differential line capacitance $C'_{\mathrm{CPW}}$ of the CPW. Expressions for all these differential capacitances are readily available in the literature for various conductor arrangements [164, 165].

To give some practical examples, the various feed CPW utilized in Chapter 5 can be evaluated both via the approximate conformal mapping technique given by Eq. 2.38 as well as by a numerical time-domain solver (CST Microwave Studio,

[42] Note that these assumptions imply that only the fundamental quasi-TEM mode of the CPW is considered. In such a case, lumped element models similar to the ones in Section 2.4.1 can be employed [163].

see Section 5.5 for details). To check the consistency of both approaches, the line impedances $Z_{\mathrm{L,CPW}}$ are evaluated for an operating frequency of $f = 0.3\,\mathrm{THz}$ and for CPW dimensions as given in Table 5.1 in Section 5.5 along with a metallization thickness of $h_{\mathrm{m}} = 3\,\mu\mathrm{m}$. We further assume an alumina ($Al_2O_3$) substrate with relative permittivity $\epsilon' = 9.9$ and height $h = 635\,\mu\mathrm{m}$. For the feed lines used in the experiments with the THz probes, we find the differential capacitances $C'_0 \approx 26\,\mathrm{pF/m}$ and $C'_{\mathrm{CPW}} \approx 144\,\mathrm{pF/m}$ using the conformal mapping technique. This results in an approximate line impedance of $Z_{\mathrm{L,CPW}} \approx 54.5\,\Omega$, which is within $0.5\,\Omega$ of the result retrieved from numerical simulations. The relative error is hence below $1\,\%$, thereby proving the validity of the approach. With the conformal mapping technique it becomes not only possible to analyze the CPW line impedance from the cross-sectional geometry of the line [165], but also to find analytic expressions for estimating the losses in CPW [166–168].

Clearly, CPW structures are seldom as ideal as assumed in the previous paragraphs. For example, the dielectric material of the substrate may consist of multiple layers, or the medium above the conductors may be different from vacuum, e.g., in cased where a cladding is deposited on top of the CPW. The metal conductors are thus embedded within multiple dielectric slabs, each featuring a characteristic layer height and relative permittivity. It is therefore convenient to first split such multi-layer arrangements into multiple single-layer slabs with modified dielectric constants, such that the already mentioned conformal mapping techniques can be applied again [169, 170]. The differential capacitance $C'_{\mathrm{CPW}}$ of the CPW is then approximated by the sum of the partial capacitances associated with the individual single-layer arrangements (Veyers–Fouad Hanna approximation [171]). Importantly, this method requires extensive use of the magnetic-wall boundary condition[43] at the various dielectric/dielectric interfaces, which implies that the dielectric constants of the layers must decrease when going away from the metal strips of the CPW [170]. However, typical permittivities of 3D-printable photoresists commonly range from $\epsilon' = 2.5 \ldots 3.5$ in the mmW and THz frequency

[43] A magnetic wall acts like a perfect magnetic conductor, where the magnetic field becomes zero inside. As a consequence, tangential components of the magnetic field as well as normal components of the electric field are zero all over the surface [172].

range [173, 174] — significantly lower than the permittivities associated with the underlying substrate materials such as alumina ($\epsilon' = 9.9$). For arrangements where a CPW-like geometry is formed on top of a 3D-printed polymeric support, e.g., by directive metal coating, numerical simulations are thus required for accurate modeling of the line impedance $Z_{\mathrm{L,CPW}}$.

### 2.4.2 Characterization of two-port networks

When describing mmW and THz networks consisting of multiple circuit elements, one is usually only interested in a certain set of quantities such as the voltage, current, or power flow at a specific set of terminals, also referred to as ports[44], within the network — as opposed to a rigorous description of the fields at all points in space. Linear electrical networks are therefore commonly regarded as "black boxes", which can contain various interconnected circuit components or lumped elements and which are described using a square matrix of complex frequency-dependent functions, the so-called scattering parameters. For analyzing an entire system of components, the various "black boxes" can then simply be connected through the associated input and output ports to consider effects such as reflections or loss.

In the following, we restrict our explanations to linear two-port networks which can be described using complex-valued $(2 \times 2)$-matrices for relating the incident wave amplitude $a_1$ and the reflected wave amplitude $b_1$ at the input (Port 1) to the incident and reflected wave amplitudes $a_2$ and $b_2$ at the output (Port 2). Two-port representations used in this work include for example the scattering matrix $\underline{\mathbf{S}}$, which relates the incident and reflected wave amplitudes as [163, 175]

$$\begin{pmatrix} b_1 \\ b_2 \end{pmatrix} = \underbrace{\begin{pmatrix} \underline{S}_{11} & \underline{S}_{12} \\ \underline{S}_{21} & \underline{S}_{22} \end{pmatrix}}_{\underline{\mathbf{S}}} \begin{pmatrix} a_1 \\ a_2 \end{pmatrix}. \tag{2.39}$$

[44] At each port, the current flowing from outside the circuit into the terminal is equal to the current flowing out of the terminal [163].

A schematic representation of such a two-port network is shown in Fig. 2.13, where the voltage and current at the respective port $i$ with (generally complex) reference impedance $\underline{Z}_i$ are denoted as $U_i$ and $I_i$ for $i \in \{1, 2\}$, respectively. The incident and reflected wave amplitudes $a_i$ and $b_i$ (in units of $\sqrt{W}$) can then be defined by the overall voltage $U_i$ and current $I_i$, or equivalently by the respective incident and reflected voltage and current wave amplitudes through the relations $U_i = U_i^+ + U_i^-$ and $I_i = I_i^+ + I_i^- = (U_i^+ - U_i^-)/\underline{Z}_i$, compare Eqs. 2.32 and 2.33, [163, 175]

$$\begin{aligned} a_i &= \frac{1}{2}\frac{U_i + \underline{Z}_i I_i}{\sqrt{\Re\{\underline{Z}_i\}}} = \frac{U_i^+}{\sqrt{\Re\{\underline{Z}_i\}}}, \\ b_i &= \frac{1}{2}\frac{U_i - \underline{Z}_i^* I_i}{\sqrt{\Re\{\underline{Z}_i\}}} = \frac{U_i^-}{\sqrt{\Re\{\underline{Z}_i\}}}. \end{aligned} \tag{2.40}$$

The definition according to Eq. 2.40 is especially useful since the power transported by the associated incident and reflected waves is given by $|a_i|^2/2$ and $|b_i|^2/2$, respectively, with the net power flowing into the system at port $i$ being $(|a_i|^2 - |b_i|^2)/2$. This makes wave amplitudes particularly convenient for systems where voltages and currents cannot be straightforwardly defined, such as hollow WG [163]. From the definitions in Eq. 2.40, the generalized scattering parameters as introduced in Eq. 2.39 are given as

$$\underline{S}_{ij} = \frac{b_i}{a_j} = \frac{U_i^-}{U_j^+}\sqrt{\frac{\Re\{\underline{Z}_j\}}{\Re\{\underline{Z}_i\}}}\Bigg|_{a_k = 0 \text{ for } k \neq j}, \tag{2.41}$$

where the subscripts $i, j \in \{1, 2\}$ refer to the transmission between or the reflection at the respective ports. More specifically, $\underline{S}_{11} = b_1/a_1 = U_1^-/U_1^+$ can be imagined as a complex-valued voltage reflection coefficient, describing the ratio of the outgoing to the ingoing wave amplitude at Port 1 of the network for the case where Port 2 is terminated with a matched load impedance $\underline{Z}_2$, i.e., $a_2 = 0$. The magnitude of $\underline{S}_{11}$ is often referred to via the dB-value of the associated power reflection coefficient $|\underline{S}_{11}|^2$, i.e., $S_{11,\mathrm{dB}} = 10\log_{10}(|\underline{S}_{11}|^2)$.

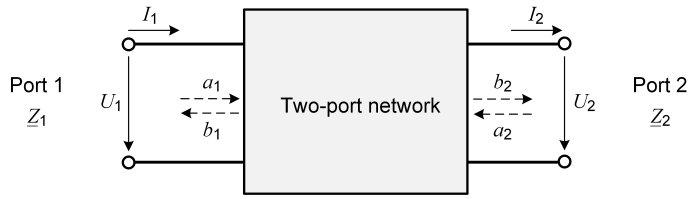


**Fig. 2.13:** Schematic representation of a two-port network, where the current and voltage at port $i$ with generally complex-valued reference impedance $\underline{Z}_i$ are denoted as $I_i$ and $U_i$ for $i \in \{1, 2\}$, respectively. The incident and reflected wave amplitudes are indicated by the respective arrows labeled $a_i$ and $b_i$.

Similarly, the term $\underline{S}_{21} = b_2/a_1 = (U_2^- \sqrt{\Re\{\underline{Z}_1\}})/(U_1^+ \sqrt{\Re\{\underline{Z}_2\}})$ defines the complex-valued transmission coefficient for a wave incident at Port 1 and measured at Port 2, again for the case where all other ports are terminated with a matched load impedance. The associated power transmission $|\underline{S}_{21}|^2$ is often referred to in decibels as $S_{21,\mathrm{dB}} = 10\log_{10}(|\underline{S}_{21}|^2)$. Note that in many textbooks identical reference impedances of the ports are tacitly assumed, thereby dropping the term $\sqrt{\Re\{\underline{Z}_j\}/\Re\{\underline{Z}_i\}}$ in Eq. 2.41. This is because $50\,\Omega$ cables and components are commonly utilized in measurement systems or in conjunction with vector network analyzers (VNA), and the obtained $S$-parameters are thus almost exclusively referred to $\underline{Z}_i = Z_0 = 50\,\Omega \in \mathbb{R}$. If a linear network contains only passive elements and reciprocal materials[45] as is the case within this thesis, $\underline{\mathbf{S}}$ additionally becomes reciprocal (meaning $\underline{S}_{ij} = \underline{S}_{ji}$ holds true).

Unfortunately, the $S$-parameter definition according to Eq. 2.39 does not allow to efficiently describe a simple concatenation of systems matrices, since knowledge of the wave amplitudes related to both ports is required for calculating the system response. An easier description of cascaded networks may be obtained through

[45] Non-reciprocal materials are, e.g., subject to the so-called magneto-optic effect which leads to an alternation of the electromagnetic wave propagating through the respective medium by the presence of a quasistatic magnetic field. Such materials can therefore be used for the fabrication of non-reciprocal passive devices such as isolators.

the use of so-called transfer matrices[46] $\underline{\mathbf{T}}$, where the input wave amplitudes $a_1$ and $b_1$ are represented in terms of the output wave amplitudes $a_2$ and $b_2$ [176],

$$\begin{pmatrix} a_1 \\ b_1 \end{pmatrix} = \underbrace{\begin{pmatrix} \underline{T}_{11} & \underline{T}_{12} \\ \underline{T}_{21} & \underline{T}_{22} \end{pmatrix}}_{\underline{\mathbf{T}}} \begin{pmatrix} b_2 \\ a_2 \end{pmatrix}. \tag{2.42}$$

A schematic representation of such a cascaded two-port network is shown in Fig. 2.14. Network A (Port 1, Port 2) and Network B (Port 2, Port 3) are connected through the common Port 2, and the various reference impedances are denoted as $\underline{Z}_i$ for $i \in \{1, 2, 3\}$. The superscripts (A) and (B) of the incident and reflected wave amplitudes $a_i$ and $b_i$ are chosen for an easier distinction between the two networks. To find a relationship for the cascaded network (Port 1, Port 3), we can start by using the definition in Eq. 2.42 to write down the $\underline{\mathbf{T}}$-matrices of the individual Networks A and B as

$$\begin{pmatrix} a_1^{(\mathrm{A})} \\ b_1^{(\mathrm{A})} \end{pmatrix} = \underline{\mathbf{T}}_{\mathrm{A}} \begin{pmatrix} b_2^{(\mathrm{A})} \\ a_2^{(\mathrm{A})} \end{pmatrix}, \qquad \begin{pmatrix} a_2^{(\mathrm{B})} \\ b_2^{(\mathrm{B})} \end{pmatrix} = \underline{\mathbf{T}}_{\mathrm{B}} \begin{pmatrix} b_3^{(\mathrm{B})} \\ a_3^{(\mathrm{B})} \end{pmatrix}. \tag{2.43}$$

The port conditions $b_2^{(\mathrm{A})} = a_2^{(\mathrm{B})}$ and $a_2^{(\mathrm{A})} = b_2^{(\mathrm{B})}$ relating the wave amplitudes at the output of Network A to the input of Network B can then be used to find

$$\begin{pmatrix} a_1^{(\mathrm{A})} \\ b_1^{(\mathrm{A})} \end{pmatrix} = \underline{\mathbf{T}}_{\mathrm{A}} \begin{pmatrix} a_2^{(\mathrm{B})} \\ b_2^{(\mathrm{B})} \end{pmatrix} = \underbrace{\underline{\mathbf{T}}_{\mathrm{A}} \underline{\mathbf{T}}_{\mathrm{B}}}_{\underline{\mathbf{T}}_{\mathrm{cascade}}} \begin{pmatrix} b_3^{(\mathrm{B})} \\ a_3^{(\mathrm{B})} \end{pmatrix}. \tag{2.44}$$

Equation 2.44 conveniently relates the input and output wave amplitudes of the cascaded network (Port 1, Port 3) through the $T$-parameter matrix $\underline{\mathbf{T}}_{\mathrm{cascade}}$ that is simply the multiplication of the $\underline{\mathbf{T}}$-matrices associated with the individual networks. Although there is no simple physical means to measure the $T$-parameters of a

[46] Note that the definition of the transfer matrix $\underline{\mathbf{T}}$ in Eq. 2.42 is not unique, as the order of the incident and reflected wave amplitudes at each port could be swapped. Therefore, special care must be taken when comparing such parameters among different sources [176].

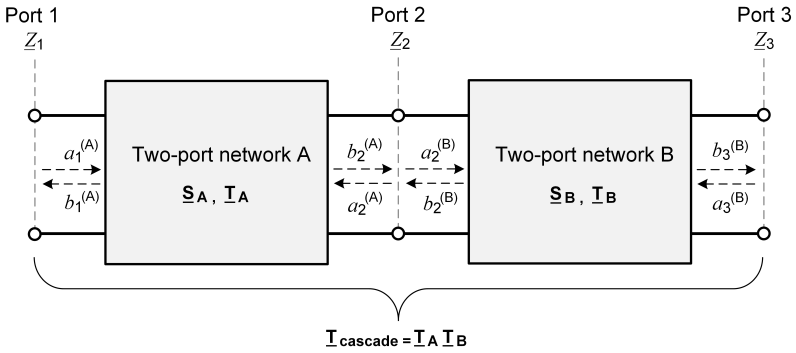


**Fig. 2.14:** Schematic representation of cascaded two-port networks. Network A (Port 1, Port 2) and Network B (Port 2, Port 3) are connected through the common Port 2, and the various reference impedance are denoted as $\underline{Z}_i$ for $i \in \{1, 2, 3\}$. The superscripts (A) and (B) of the incident and reflected wave amplitude $a_i$ and $b_i$ are chosen for an easier distinction between the two networks. If $N$ individual networks are cascaded and represented by their respective transfer matrices $\underline{\mathbf{T}}_\mathrm{A}, \underline{\mathbf{T}}_\mathrm{B}, \ldots \underline{\mathbf{T}}_\mathrm{N}$, the transfer matrix of the cascaded network can simply be calculated as $\underline{\mathbf{T}}_\mathrm{cascade} = \underline{\mathbf{T}}_\mathrm{A}\underline{\mathbf{T}}_\mathrm{B} \cdots \underline{\mathbf{T}}_\mathrm{N}$.

given system, formulas for converting between $\underline{\mathbf{S}}$ and $\underline{\mathbf{T}}$ matrices are readily available [176],

$$\underline{\mathbf{T}} = \begin{pmatrix} \underline{T}_{11} & \underline{T}_{12} \\ \underline{T}_{21} & \underline{T}_{22} \end{pmatrix} = \begin{pmatrix} 1/\underline{S}_{21} & -\underline{S}_{22}/\underline{S}_{21} \\ \underline{S}_{11}/\underline{S}_{21} & -\det(\underline{\mathbf{S}})/\underline{S}_{21} \end{pmatrix}, \tag{2.45}$$

$$\underline{\mathbf{S}} = \begin{pmatrix} \underline{S}_{11} & \underline{S}_{12} \\ \underline{S}_{21} & \underline{S}_{22} \end{pmatrix} = \begin{pmatrix} \underline{T}_{21}/\underline{T}_{11} & \det(\underline{\mathbf{T}})/\underline{T}_{11} \\ 1/\underline{T}_{11} & -\underline{T}_{12}/\underline{T}_{11} \end{pmatrix}. \tag{2.46}$$

Hereby, $\det(\underline{\mathbf{S}}) = \underline{S}_{11}\underline{S}_{22} - \underline{S}_{12}\underline{S}_{21}$ and $\det(\underline{\mathbf{T}}) = \underline{T}_{11}\underline{T}_{22} - \underline{T}_{12}\underline{T}_{21}$ are the determinant of the $S$-parameter matrix $\underline{\mathbf{S}}$ and $T$-parameter matrix $\underline{\mathbf{T}}$, respectively. Individually measured $S$-parameter matrices $\underline{\mathbf{S}}_\mathrm{A}, \underline{\mathbf{S}}_\mathrm{B}, \ldots \underline{\mathbf{S}}_\mathrm{N}$ may hence be converted to the equivalent $\underline{\mathbf{T}}$ matrices $\underline{\mathbf{T}}_\mathrm{A}, \underline{\mathbf{T}}_\mathrm{B}, \ldots \underline{\mathbf{T}}_\mathrm{N}$ using Eq. 2.45. Equation 2.44 may then be generalized to a cascade of $N$ systems, i.e., the transfer matrix of the cascaded network can simply be calculated as $\underline{\mathbf{T}}_\mathrm{cascade} = \underline{\mathbf{T}}_\mathrm{A}\underline{\mathbf{T}}_\mathrm{B} \cdots \underline{\mathbf{T}}_\mathrm{N}$. The $S$-parameters associated with the cascaded system are finally found by converting $\underline{\mathbf{T}}_\mathrm{cascade}$ to $\underline{\mathbf{S}}_\mathrm{cascade}$ using Eq. 2.46. Equivalently, any two-port network may be represented as a concatenation of individual two-ports, which permits

the successive mathematical removal of the outermost circuit elements by multiplication with the respective inverse matrices $\underline{\mathbf{T}}_{\mathrm{A}}^{-1}, \underline{\mathbf{T}}_{\mathrm{B}}^{-1} \ldots \underline{\mathbf{T}}_{\mathrm{N}}^{-1}$ — a process commonly referred to as de-embedding [177, 178]. Practical examples of this technique are given in Appendices D.4 and D.5.

### 2.4.3 Antennas

Antennas transform guided waves into free-space waves. The electric and magnetic fields radiated by an antenna are commonly categorized into the following three regions depending on the radial distance $r$ from the antenna center-point, whereby the boundaries can be defined in terms of the wavelength $\lambda = c/f$ of the radiated free-space wave and the biggest geometrical extension $L_{\max}$ of the antenna [179]:

- **Reactive near-field region:** $0 < r < 0.62\sqrt{L_{\max}^3/\lambda}$
  The reactive near-field is the region immediately surrounding the antenna, wherein the electromagnetic fields are changing very quickly due to evanescent waves created by surface currents. Electric and magnetic fields are $90^\circ$ out of phase, and the emitted fields are thus purely reactive (non-radiating), which leads to the power oscillating within this region.

- **Radiating near-field (Fresnel) region:** $0.62\sqrt{L_{\max}^3/\lambda} \leq r < 2\,(L_{\max}^2/\lambda)$
  In the radiating near-field region, radiation fields start to dominate, and the angular field distribution of the antenna begins to smoothen and form lobes depending on the distance $r$.

- **Far-field (Fraunhofer) region:** $2\,(L_{\max}^2/\lambda) \leq r < \infty$
  In the far-field region, the Poynting vector of the radiated wave is predominately real and power can thus be transmitted. The electric and magnetic components of the radiated wave are normal with respect to each other and to the Poynting vector, which is oriented along the radial propagation direction. Hence, a quasi-TEM wave is formed and the radiation pattern can be simply described in spherical coordinates using only the azimuthal angle $\varphi$ and the elevation angle $\theta$.

All antenna configurations considered within this thesis are observed in the far-field region, for which the various performance metrics are illustrated in Fig. 2.15. The radiation pattern of an antenna is described by the dependence of the emitted intensity on the direction, given by the azimuthal angle $\varphi$ and the elevation angle $\theta$. Quantitatively, the radiation pattern $\xi(\varphi, \theta)$ is defined as the radiated power per unit solid angle $\mathrm{d}\Omega = \sin\theta \, \mathrm{d}\theta \, \mathrm{d}\varphi$. We can hence find the total radiated power $P_{\mathrm{rad}}$ of an antenna by integrating the radiation pattern $\xi(\varphi, \theta)$ over all solid angles $\mathrm{d}\Omega$ [179],

$$P_{\mathrm{rad}} = \oiint_{\Omega} \xi(\varphi, \theta) \, \mathrm{d}\Omega = \int_0^{2\pi} \int_0^{\pi} \xi(\varphi, \theta) \sin\theta \, \mathrm{d}\theta \, \mathrm{d}\varphi. \tag{2.47}$$

For an isotropic radiator, $\xi(\varphi, \theta) = \xi_{\mathrm{iso}}$ becomes independent of the direction, and with Eq. 2.47 we can find the equivalent total radiated power $P_{\mathrm{rad}} = 4\pi\xi_{\mathrm{iso}}$. We can then define the directivity $D(\varphi, \theta)$ of any antenna by relating the radiated power per solid angle $\xi(\varphi, \theta)$ to the radiated power per solid angle $\xi_{\mathrm{iso}}$ of a fictitious isotropic source with an equivalent radiated power $P_{\mathrm{rad}}$,

$$D(\varphi, \theta) = \frac{\xi(\varphi, \theta)}{\xi_{\mathrm{iso}}} = 4\pi \frac{\xi(\varphi, \theta)}{P_{\mathrm{rad}}}. \tag{2.48}$$

Obviously, the directivity $D(\varphi, \theta)$ is a measure describing purely the directional properties of an antenna but does not relate to the efficiency with which power is transformed from the ongoing guide wave to the outgoing free-space wave or vice versa. This aspect is covered by several efficiency metrics, which take into account losses at the input port due to reflections stemming from impedance mismatch or losses within the antenna itself, e.g., as a result of dielectric and conductor losses [179, 180], see the illustrations in Fig. 2.15. Therefore, another useful metric describing the performance of an antenna is the direction-dependent gain, which is defined as

$$G(\varphi, \theta) = \eta_{\mathrm{rad}} D(\varphi, \theta), \tag{2.49}$$

where $\eta_{\mathrm{rad}} \leq 1$ is the radiation efficiency taking into account losses within the antenna structure. Finally, Eq. 2.49 can be adapted to take into account losses when the antenna element is connected to a feed transmission line with characteristic

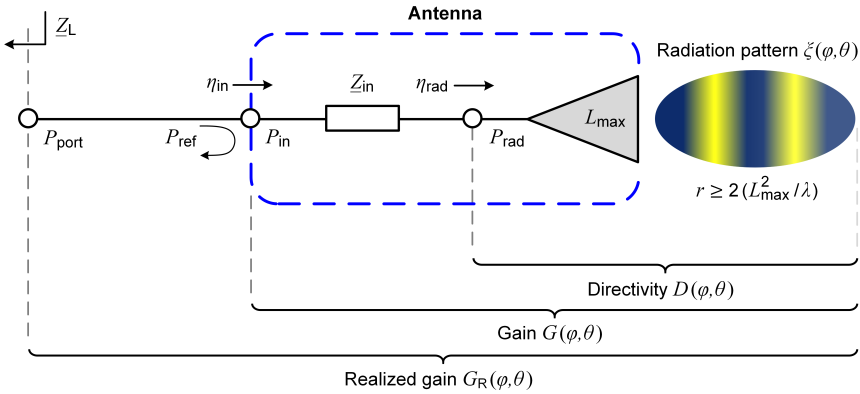


**Fig. 2.15:** Illustration of the performance metrics related to the far-field ($r \geq 2\,[L_{max}^2/\lambda]$) power-transfer characteristics of an antenna. The total radiated power $P_{rad}$ is given by integrating the radiation pattern $\xi(\varphi,\theta)$ (in units of power per solid angle) over all spherical directions. The directivity $D(\varphi,\theta)$ is a measure describing the directional properties of the antenna by relating the radiated power per solid angle $\xi(\varphi,\theta)$ to the radiated power per solid angle of a fictitious isotropic source. In addition, a series of efficiencies are used to take into account losses at the input port due to reflections stemming from impedance mismatch ($\eta_{in}$) or losses within the antenna itself ($\eta_{rad}$). Another useful performance measure is hence the realized gain $G_R(\varphi,\theta)$, which is related to the gain $G(\varphi,\theta)$ and directivity $D(\varphi,\theta)$ by the two efficiencies as $G_R(\varphi,\theta) = \eta_{in} G(\varphi,\theta) = \eta_{in}\eta_{rad} D(\varphi,\theta)$.

impedance $\underline{Z}_L$, see Fig. 2.15. If the input impedance of the antenna is given as $\underline{Z}_{in}$, any impedance mismatch leads to the partial reflection $P_{ref}$ of the feed port power $P_{port}$ at the antenna input, i.e., $P_{ref} = |\underline{\Gamma}_{ref}|^2 P_{port}$ according to Eq. 2.37. Therefore, the power $P_{in}$ fed to the actual antenna input is reduced accordingly,

$$P_{in} = (1 - |\underline{\Gamma}_{ref}|^2) P_{port} = \left(1 - \left|\frac{\underline{Z}_{in} - \underline{Z}_L}{\underline{Z}_{in} + \underline{Z}_L}\right|^2\right) P_{port}. \tag{2.50}$$

Equation 2.50 may be equivalently represented by an input-matching efficiency $\eta_{in} = (1 - |\underline{\Gamma}_{ref}|^2) \leq 1$, which allows to define the so-called realized gain as

$$G_R(\varphi,\theta) = \eta_{in} G(\varphi,\theta) = \eta_{in}\eta_{rad} D(\varphi,\theta). \tag{2.51}$$

Equation 2.51 thus describes the direction-dependent ratio of the radiated power per solid angle with respect to the radiated power per solid angle that would

be obtained if the accepted power by an antenna was radiated isotropically[47]. The measured gain patterns are usually given in decibels and visualized in polar plots for certain cross-sectional planes that are associated with, e.g., the azimuthal or elevation angle.

### CPW-fed slot antennas

The antenna structures considered within this thesis are CPW-fed slot antennas, see Fig. 2.17(b), which are elevated from the underlying high-index substrate for increased radiation efficiency in the surface-normal direction. In planar mmW circuits, this type of antenna has gained increasing attention due the ease of fabrication and the increased bandwidths compared to microstrip-based patch antennas. The symmetric conductor arrangement of CPW furthermore promotes the propagation of balanced signals, where the electrical fields associated with the two CPW slots are equal but point in opposing directions, see Fig. 2.12(a). This greatly simplifies the connection to center-fed slot antennas, where the terminals require voltages which are equal but opposite in sign due to the inherent symmetry of the arrangement. Therefore, no dedicated circuits for the transformation between balanced and unbalanced transmission lines are required[48] [181].

Figure 2.16(a) shows a schematic slot antenna with a slot width $w \ll \lambda$ and slot length $L$ in a metallic sheet that is excited by a voltage from a feed line across the transverse direction at its center[49]. If the metal sheet surrounding the slot is perfectly conducting, infinitely extended and very thin, the slot antenna is complementary to a planar dipole as shown in Fig. 2.16(b). According to

[47] For perfectly matched ($\underline{Z}_{\mathrm{L}} = \underline{Z}_{\mathrm{in}} \rightarrow \eta_{\mathrm{in}} = 1$) and lossless ($\eta_{\mathrm{rad}} = 1$) antennas, Eq. 2.51 hence simplifies to $G_{\mathrm{R}}(\varphi, \theta) = G(\varphi, \theta) = D(\varphi, \theta) \propto \xi(\varphi, \theta)$.

[48] A device or circuit performing this transformation is commonly referred to as balun (short form for "balanced-unbalanced").

[49] When the center of the slot is excited by a voltage, current can flow along the perimeter of the slot. This results in an electric field distribution along the extension of the slot in the $x$-direction in Fig. 2.16(a) which is considered to follow a sinusoidal, where the electrical field becomes zero at the two outermost points of the slot.

Babinet's principle[50], the electric and magnetic field distributions of complementary structures are simply interchanged, and the sign of the electric and magnetic fields must change from one side of a metal sheet to the other [183]. We may hence write down[51] the components of the fields associated with the slot antenna by considering the respective terms of a very thin ($w \ll L$) dipole of finite length $L$ [179, 180], and by introducing the $\varphi$-dependent proportionality factor $\Lambda(\varphi)$ for taking into account the change in field direction, i.e.,

$$\begin{aligned} H_{\theta,\mathrm{slot}}(\varphi,\theta) &\mathrel{\widehat{=}} E_{\theta,\mathrm{dipole}}(\varphi,\theta) \propto \Lambda(\varphi)\,\frac{\cos(\pi\frac{L}{\lambda}\sin\theta)-\cos(\pi\frac{L}{\lambda})}{\cos\theta}\times\frac{1}{r}, \\ E_{\varphi,\mathrm{slot}}(\varphi,\theta) &\mathrel{\widehat{=}} H_{\varphi,\mathrm{dipole}}(\varphi,\theta) \propto \frac{H_{\theta,\mathrm{slot}}(\varphi,\theta)}{Z_\mathrm{W}}, \end{aligned} \tag{2.52}$$

with

$$\Lambda(\varphi) = \begin{cases} 1 & \text{if} \quad \varphi = -\frac{\pi}{2}\ldots\frac{\pi}{2} \\ -1 & \text{if} \quad \varphi = \ \ \frac{\pi}{2}\ldots\frac{3\pi}{2} \end{cases}. \tag{2.53}$$

In these relations, the subscripts $\varphi$ and $\theta$ refer to the respective field component and $Z_\mathrm{W} = \sqrt{\mu_0/\epsilon_0} \approx 120\pi\,\Omega \approx 377\,\Omega$ denotes the intrinsic wave impedance of free-space. We can then find the far-field radiation pattern $\xi(\varphi,\theta)$ of the slot antenna depicting its directional properties,

$$\xi(\varphi,\theta) \propto \frac{r^2}{Z_\mathrm{W}}\,|H_{\theta,\mathrm{slot}}(\varphi,\theta)|^2 = \left|\Lambda(\varphi)\,\frac{\cos(\pi\frac{L}{\lambda}\sin\theta)-\cos(\pi\frac{L}{\lambda})}{\cos\theta}\right|^2. \tag{2.54}$$

Note that the sign change described by $\Lambda(\varphi)$ does not effect Eq. 2.54 as long as Eq. 2.53 holds true, and the resulting radiation pattern would hence be constant

[50] Babinet's principle was originally introduced in optics [182], stating that the diffraction patterns of two mutually complementary apertures (e.g. a slit and a wire of the same thickness) are the same outside the region in which the geometrical-optical image falls. However, it does not consider the phase nor polarization which are vital parts of antenna theory. Extensions to Babinet's principle for putting it in the context of antennas have therefore been introduced by Booker [183].

[51] The coordinate axis have been chosen for consistency with the plots in Chapter 5 and Appendix D.

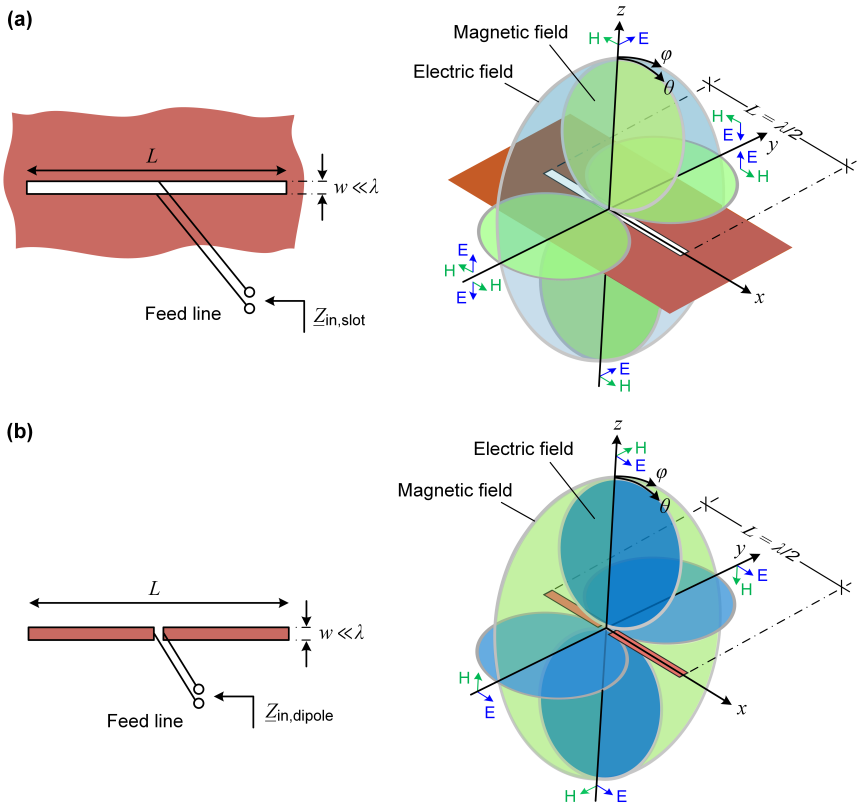


**Fig. 2.16:** Schematic configuration and far-field distributions of a slot antenna and a complementary dipole antenna with a slot width $w \ll \lambda$ and slot length $L$. Electric and magnetic field distributions are conceptually drawn for $L = \lambda/2$. The solid blue and green arrows indicate the direction of the electric ($E$) and magnetic ($H$) field, respectively. By virtue of Babinet's principle, the electric and magnetic field distributions are simply interchanged, with the exception of the electric field of the slot antenna normal to the sheet, which reverses its direction from one side of the sheet to the other. Similarly, the direction of the tangential component of the magnetic field is flipped. The line impedances $\underline{Z}_{\mathrm{in,slot}}$ and $\underline{Z}_{\mathrm{in,dipole}}$ are related through the intrinsic wave impedance of free-space $Z_{\mathrm{W}}$ by Eq. 2.55. **(a)** Slot antenna in an infinitely extended metal sheet and associated electric and magnetic field distributions. The field components are given by $H_{\theta,\mathrm{slot}}(\varphi,\theta)$ and $E_{\varphi,\mathrm{slot}}(\varphi,\theta)$, which are constant with respect to $\varphi$ but change sign depending on the side of the metal sheet. If the metallic sheet is finite, diffraction of the electromagnetic wave occurs. **(b)** Complementary dipole antenna and associated electric and magnetic field distributions. The field components are given by $E_{\theta,\mathrm{dipole}}(\varphi,\theta) \mathrel{\widehat{=}} H_{\theta,\mathrm{slot}}(\varphi,\theta)$ and $H_{\varphi,\mathrm{dipole}}(\varphi,\theta) \mathrel{\widehat{=}} E_{\varphi,\mathrm{slot}}(\varphi,\theta)$, which are constant with respect to $\varphi$.

with respect to $\varphi$. However, if the metallic sheet is finite, diffraction of the electromagnetic wave occurs. Although it has been shown [180] that the influence of a limited sheet extension on the antenna impedance and the $\theta$-dependency of the radiation pattern in Eq. 2.54 is negligible, the $\varphi$-dependency of the field components as governed by $\Lambda(\varphi)$ starts to deviate significantly[52] from Eq. 2.53.

The various electric and magnetic field distributions for both the dipole as well as the complementary slot antenna with infinitely extended metal sheet are conceptually drawn in Fig. 2.16(a) and (b) for $L = \lambda/2$. The solid blue and green arrows indicate the direction of the electric ($E$) and magnetic ($H$) field, respectively. Note that the directions of $E$ and $H$ are simply interchanged, with the exception of the electric field of the slot antenna normal to the sheet, which reverses its direction from one side of the sheet to the other as indicated by the arrows and described by the factor $\Lambda(\varphi)$ in Eq. 2.52. Similarly, the direction of the tangential component of the magnetic field is flipped. For a measured radiation pattern, one often refers to so-called $E$- or $H$-planes. Hereby, $E$-planes describe the plane containing the electric field vector and the direction of maximum radiation. Similarly, $H$-planes describe the plane containing the magnetic field vector and the direction of maximum radiation [179]. In Fig. 2.16, the planes of the illustrated electric and magnetic field distributions coincide with the $E$- and $H$-planes of the depicted antennas, respectively.

One of the main problems with CPW-fed slot antennas is the matching of the input impedance $\underline{Z}_{\mathrm{in,slot}}$ to a feed transmission line with reference impedance $\underline{Z}_{\mathrm{L}}$ [184]. Multiple approaches have been demonstrated, including impedance tuning based on on-center [185] or off-center [186] feeding of the slot as well as inductive [181, 184] or capacitive [187] coupling techniques. As a direct result of Babinet's

[52] In fact, no power can be radiated in the direction of the sheet, i.e., in the directions associated with $\varphi = \pm\pi/2$ in Eq. 2.53, as the electric fields on both sides of the metal sheet have the same magnitude but opposite signs, see Fig. 2.16(a). The associated electrical fields thus cancel, leading to a null in all directions in the plane of the sheet. In addition, diffraction at the sheet edges causes an alternation of $E_{\varphi,\mathrm{slot}}(\varphi,\theta)$ along the $\varphi$-direction, whereby the number of such undulations in the pattern increases while the magnitude decreases for increasing sheet extension [180].

principle, we can estimate the input impedance $\underline{Z}_{\mathrm{in,slot}}$ of a slot antenna using the input impedance $\underline{Z}_{\mathrm{in,dipole}}$ of the complementary dipole antenna as [183]

$$\underline{Z}_{\mathrm{in,slot}} = \frac{Z_{\mathrm{W}}^2}{4\,\underline{Z}_{\mathrm{in,dipole}}}. \tag{2.55}$$

Although extensive closed-form expressions for the input impedance of finite dipoles with length $L$ and diameter $D$ have been derived, these formulas are still only valid for very thin ($D \ll L$) configurations[53]. For thicker antennas, however, the current distribution deviates significantly from a sinusoidal, and numerical methods are required to approximate the input impedance using, e.g., Pocklington's integro-differential equation or the Hallén integral equation [179, 180]. While a detailed discussion of these methods is outside the scope of this thesis, the input impedances $\underline{Z}_{\mathrm{in,dipole}}$ obtained for dipoles with thicker diameters can be readily used in combination with Eq. 2.55 for the design of slot antennas [180].

Figure 2.17(a) details a specific design of a cylindrical dipole antenna, for which a length of $L = 0.925\lambda$ and a diameter of $D = 0.033\lambda$ are chosen. Interestingly, approximations using the Hallén-integral method [189] indicate that the input impedance of such a conductor configuration becomes purely resistive with a value $\underline{Z}_{\mathrm{in,dipole}} \approx 710\,\Omega$. From Eq. 2.55 we find that the input impedance of the complementary slot antenna becomes $\underline{Z}_{\mathrm{in,slot}} \approx 50\,\Omega$ [180], thereby allowing for a simplified matching to the usual $50\,\Omega$ reference impedance. The associated complementary slot antenna is illustrated in Fig. 2.17(b), where the length $L = 0.925\lambda$ is identical and the equivalent width is given by $w = 2D = 0.066\lambda$, i.e., the length to width ratio amounts to $L/w \approx 14$. The antennas designed within this thesis are therefore fixed to this length to width ratio. When using high-index substrates such as alumina ($\epsilon' = 9.9$) for implementing antenna structures, it is crucial to mitigate losses that stem from the coupling to surface waves and resonant substrate modes as well as dielectric losses associated with the substrate material. One commonly followed approach is to raise the antenna above the high-index substrate, thereby reducing the influence of the substrate dielectric on the radiated

[53] It has been shown [188], that the accuracy is typically within 10 % for ratios of $L/D > 60$.

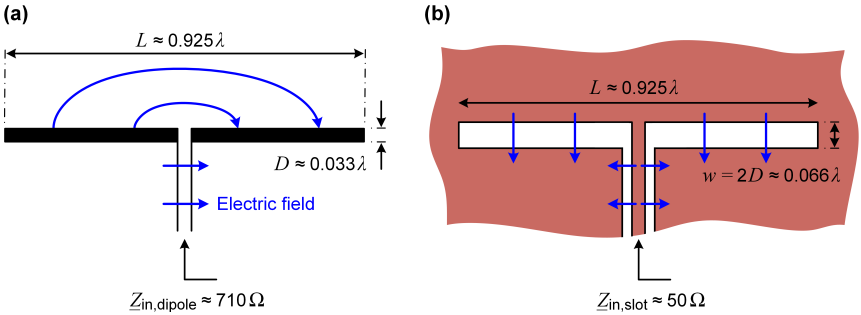


**Fig. 2.17:** Design of a cylindrical dipole antenna resulting in a complementary CPW-fed slot antenna with a purely resistive input impedance close to $50\,\Omega$ according to Babinet's principle. **(a)** The cylindrical dipole antenna features a length of $L = 0.925\lambda$ and a diameter of $D = 0.033\lambda$. The input impedance of such a conductor configuration is approximately purely resistive with a value $\underline{Z}_{\mathrm{in,dipole}} \approx 710\,\Omega$. **(b)** Complementary slot antenna having the same length $L = 0.925\lambda$ as the cylindrical dipole antenna and an equivalent width of $w = 2D = 0.066\lambda$. An input impedance of $\underline{Z}_{\mathrm{in,slot}} \approx 50\,\Omega$ is found using Eq. 2.55.

free-space wave and increasing the radiation efficiency. To this end, 3D-printing of support structures which are selectively metal coated for forming the associated electrical transmission lines atop (see Section 5.2 for details on the concept and fabrication) offers a particularly attractive approach for fabricating freeform mmW and THz antennas which are suspended form the underlying substrate. This technique offers unprecedented geometrical design freedom in combination with the possibility for precise alignment of the resulting mmW and THz structures with respect to, e.g., feed CPW on the underlying planar substrate. For the specific implementations in Chapter 5, an overall slot length of $L = 822\,\mu\mathrm{m}$ is chosen in combination with a slot width of $w = 60\,\mu\mathrm{m} \approx L/14$ for achieving an input impedance $\underline{Z}_{\mathrm{in,slot}} \approx 50\,\Omega$ close to the CPW feed line.

# 3 3D-printed coupling elements for external-cavity lasers with $Si_3N_4$ resonator offering sub-kHz linewidth

This chapter reports on 3D-printed optical coupling elements such as intra-cavity photonic wire bonds (PWB) and facet-attached microlenses (FaML) for silicon nitride ($Si_3N_4$)-based hybrid integrated external-cavity lasers (ECL) that are used as a tunable pump laser to generate a Kerr frequency comb. It has been published in the *Journal of Lightwave Technology* [J2]. The material from the publication has been adapted to comply with the layout and the structure of this thesis.

The experiments were conceived jointly by Yung Chen, Yilin Xu, Yiyang Bao, Matthias Blaicher, Philipp-Immanuel Dietrich, Huanfa Peng, Christian Koos, and the author. Matthias Blaicher, Yilin Xu, and the author developed the advanced lithography tools required for precise fabrication of the PWB and FaML at device facets. The ECL assemblies were fabricated by the author, supported by discussions with Yilin Xu. Philipp-Immanuel Dietrich provided the photoresist used in the experiments. Dimitri Geskus and Ronald Dekker provided the $Si_3N_4$ (TriPleX®) filter chips for the ECL. The author performed the experimental characterization of the various ECL assemblies and analyzed the measurement data. Yung Chen fabricated the assemblies used for the Kerr comb generation, and the associated experiments were executed and evaluated by Yung Chen, Huanfa Peng, and the author. Yiyang Bao helped with the automation of the ECL tuning. Junqiu Liu provided the $Si_3N_4$ chips with the high-$Q$ microresonators used in the Kerr comb modules. All authors discussed the data. The project was

supervised by Sebastian Randel, Wolfgang Freude, Tobias J. Kippenberg, and Christian Koos. The author wrote the manuscript with support by Wolfgang Freude and Christian Koos. The manuscript is partially based on the prior conference contribution [C1] to ECOC 2022.

*[Beginning of paper [J2]. This article is reprinted under the terms of a Creative Commons Attribution 4.0 License.]*

**Sub-kHz-linewidth external-cavity laser (ECL) with $Si_3N_4$ resonator as a tunable pump for a Kerr frequency comb**

*Journal of Lightwave Technology, Volume 41, Issue 11, pp. 3479–3490 (2023)*

https://doi.org/10.1109/JLT.2023.3243471

Pascal Maier[1,2], Yung Chen[1], Yilin Xu[1,2], Yiyang Bao[1,2], Matthias Blaicher[1,2], Dimitri Geskus[3], Ronald Dekker[3], Junqiu Liu[4], Philipp-Immanuel Dietrich[1,2,5], Huanfa Peng[1], Sebastian Randel[1], Wolfgang Freude[1], Tobias J. Kippenberg[4,6] & Christian Koos[1,2,5,6]

[1] Institute of Photonics and Quantum Electronics (IPQ), Karlsruhe Institute of Technology (KIT), Engesserstr. 5, 76131 Karlsruhe, Germany.

[2] Institute of Microstructure Technology (IMT), Karlsruhe Institute of Technology (KIT), Hermann-von-Helmholtz Platz 1, 76344 Eggenstein-Leopoldshafen, Germany.

[3] LioniX International B.V., P.O. Box 456, 7500 AL Enschede, The Netherlands.

[4] École Polytechnique Fédérale de Lausanne (EPFL), Rte Cantonale, 1015 Lausanne, Switzerland.

[5] Vanguard Automation GmbH, Gablonzer Str. 10, 76185 Karlsruhe, Germany.

[6] Deeplight S.A., Fondation EPFL Innovation Park – Bâtiment C, 1015 Lausanne, Switzerland.

Combining optical gain in direct-bandgap III-V materials with tunable optical feedback offered by advanced photonic integrated circuits is key to chip-scale external-cavity lasers (ECL), offering wideband tunability along with low optical linewidths. External feedback circuits can be efficiently implemented using low-loss silicon nitride ($Si_3N_4$) waveguides, which do not suffer from two-photon

absorption and can thus handle much higher power levels than conventional silicon photonics. However, co-integrating III-V-based gain elements with tunable external feedback circuits in chip-scale modules still represents a challenge, requiring either technologically demanding heterogeneous integration techniques or costly high-precision multi-chip assembly, often based on active alignment. In this work, we demonstrate $Si_3N_4$-based hybrid integrated ECL that exploit 3D-printed structures such as intra-cavity photonic wire bonds and facet-attached microlenses for low-loss optical coupling with relaxed alignment tolerances, thereby overcoming the need for active alignment while maintaining the full flexibility of multi-chip integration techniques. In a proof-of-concept experiment, we demonstrate an ECL offering a 90 nm tuning range (1480 nm – 1570 nm) with on-chip output powers above 12 dBm and side-mode suppression ratios of up to 59 dB in the center of the tuning range. We achieve an intrinsic linewidth of 979 Hz, which is among the lowest values reported for comparable feedback architectures. The optical loss of the intra-cavity photonic wire bond between the III-V gain element and the $Si_3N_4$-based tunable feedback circuit amounts to approximately $(1.6 \pm 0.2)$ dB. We use the ECL as a tunable pump laser to generate a dissipative Kerr soliton frequency comb. To the best of our knowledge, our experiments represent the first demonstration of a single-soliton Kerr comb generated with a pump that is derived from a hybrid ECL.

## 3.1 Introduction

Tunable lasers are key building blocks of integrated optics. In this context, hybrid external-cavity lasers (ECL) are particularly interesting, opening the possibility to combine optical amplification in direct-bandgap III-V-based gain elements with tunable optical feedback offered by advanced passive photonic integrated circuits (PIC). Such feedback circuits can be efficiently implemented on the silicon photonic (SiP) platform [J1, 31–33, 108, 190–192]. Alternatively, silicon nitride ($Si_3N_4$) waveguides can be used for the feedback circuits [20, 23, 114, 193–197], offering much lower linear and nonlinear losses than their SiP counterparts.

This increases the intrinsic $Q$-factors of resonator-based feedback circuits and eliminates two-photon absorption (TPA) as a critical impairment at high power levels, thereby permitting greatly reduced phase noise and small linewidths [18, 20, 21]. However, the co-integration of III-V-based gain elements and tunable external-cavity circuits in chip-scale packages still represents a challenge. Specifically, heterogeneous integration based on transfer of InGaAsP epitaxial layers to pre-processed passive silicon or silicon nitride PIC paves a path towards high-density monolithic integration, but the underlying processes are still complex [30] and mostly limited to the SiP platform. This approach is hence mainly suited for high-volume applications that justify the associated technological overhead. Alternatively, III-V-dies and passive feedback circuits can first be processed on separate substrates and then be combined in a compact multi-chip module using a hybrid approach. This concept allows the components to be optimized and tested individually and facilitates thermal decoupling of the gain element from temperature-sensitive feedback circuits. However, assembly of hybrid photonic multi-chip modules crucially relies on high-precision alignment of the underlying optical dies, often requiring active alignment techniques, where the coupling efficiency is continuously measured and optimized during the assembly process [20, 23, 31, 114, 192–194, 196, 197]. This leads to limited fabrication throughput and often hinders cost-efficient scalability to high volumes.

In this paper, we demonstrate $Si_3N_4$-based hybrid integrated ECL that exploit photonic wire bonds (PWB) as intra-cavity coupling elements between reflective semiconductor optical amplifiers (RSOA) and the associated external-cavity circuits [C1]. PWB are structured *in-situ* in a fully automated process with shapes adapted to the mode-field sizes and the positions of the chips at both ends, thus offering low coupling loss even for vastly dissimilar waveguide cross sections and limited placement accuracy of the underlying dies [40]. In a proof-of-concept experiment, we demonstrate an ECL offering a 90 nm tuning range (1480 nm – 1570 nm) with on-chip output powers above 12 dBm and side-mode suppression ratios (SMSR) of up to 59 dB in the center of the tuning range. We measure an intrinsic linewidth of 979 Hz, which is among the lowest values reported for comparable feedback architectures. The optical loss of the intra-cavity PWB between

the III-V gain element and the $Si_3N_4$-based tunable feedback circuit amounts to approximately $(1.6 \pm 0.2)$ dB. At the output, the $Si_3N_4$-based tunable feedback circuit is coupled to an array of single-mode fibers using 3D-printed facet-attached microlenses (FaML) [3, J3, J5, C2]. To demonstrate the performance and the versatility of the device, we use the ECL as narrow-linewidth tunable pump laser for generation of dissipative Kerr soliton (DKS) frequency combs in high-$Q$ $Si_3N_4$ microresonators. To the best of our knowledge, our experiments represent the first demonstration of a single-soliton Kerr comb generated with a pump that is derived from a hybrid integrated ECL.

## 3.2 Integrated hybrid ECL

### 3.2.1 Device concept

The concept of a hybrid integrated ECL with 3D-printed intra-cavity photonic wire bond (PWB) and facet-attached microlenses (FaML) is shown in Fig. 3.1(a). The assembly consists of two dies on a common aluminum (Al) submount — an InP reflective semiconductor optical amplifier (RSOA) attached to a copper (Cu) heatsink and a $Si_3N_4$-based external-cavity circuit with a fiber array at the output. The device is controlled via an electronic circuit on a printed circuit board (PCB), which is attached to an Al base plate together with the submount. Figure 3.1(b) provides a top-view schematic of the InP RSOA and the $Si_3N_4$ chip, the latter comprising a Sagnac loop mirror with a Vernier pair of tunable racetrack resonators R1 and R2, a cavity phase tuner (CPT), and a tunable output coupler implemented as a Mach-Zehnder interferometer (MZI). The RSOA has a back facet with a high-reflectivity (HR) coating, while the front facet is angled at $9.0^\circ$ and has an anti-reflection (AR) coating with respect to polymer. A PWB bridges the gap between the RSOA front facet and the edge coupler (EC) on the $Si_3N_4$ chip. This EC consists of a tapered waveguide (WG) which is oriented at an angle of $19.9^\circ$ with respect to the facet normal. A side-view schematic of the

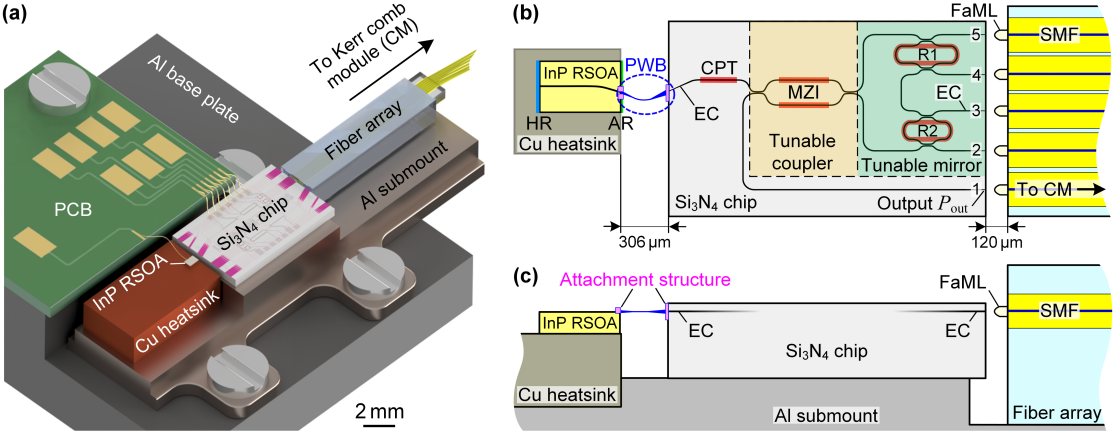


**Fig. 3.1:** Concept of a hybrid integrated ECL module with a 3D-printed intra-cavity photonic wire bond (PWB) and facet-attached microlenses (FaML). **(a)** The ECL assembly consists of two dies on a common aluminum (Al) submount – an InP reflective semiconductor optical amplifier (RSOA) attached to a copper (Cu) heatsink and a $Si_3N_4$-based external-cavity circuit with a fiber array at the output. The device is controlled via an electronic circuit on a printed circuit board (PCB), which is attached to an Al base plate together with the submount. The fiber-coupled ECL output can be connected to the Kerr comb module (CM), see Fig. 3.3(a). **(b)** Top-view schematic of the InP RSOA and the $Si_3N_4$ chip, the latter comprising a Sagnac loop mirror with a Vernier pair of tunable racetrack resonators R1 and R2, a cavity phase tuner (CPT), and a tunable output coupler implemented as a Mach-Zehnder interferometer (MZI). The RSOA has a back facet with a high-reflectivity (HR) coating, while the front facet is angled at $9.0°$ and has an anti-reflection (AR) coating with respect to polymer. The intra-cavity PWB bridges the gap of 306 µm between the RSOA front facet and the edge coupler (EC) on the $Si_3N_4$ chip. This EC consists of a tapered waveguide (WG), which is oriented at an angle of $19.9°$ with respect to the facet normal. Note that the PWB approach allows for connecting the two dies even though the emission direction of the on-chip waveguides at its ends are not matched, emphasizing the flexibility of the concept. In our device implementation, the CPT is 1 mm long and the Vernier pair of racetrack resonators have perimeters of 885.1 µm (R1) and 857.4 µm (R2). Four auxiliary waveguides WG 2…5 and the output WG 1 are routed to the $Si_3N_4$ chip edge and connected to associated tapered EC having a pitch of 127 µm. All five waveguide Ports 1…5 are coupled to a single-mode fiber (SMF) array via 3D-printed FaML. **(c)** Side-view schematic of the module. Each end of the PWB is equipped with additional attachment structures that improve mechanical stability. A step on the Al submount is used to align the height of the RSOA chip surface to that of the WG layer containing the EC on the $Si_3N_4$ side.

module is provided in Fig. 3.1(c). Each end of the PWB is equipped with additional attachment structures that improve mechanical stability. Note that the PWB approach allows for connecting the two dies even though the emission angle of the RSOA output and the direction of the input EC of the $Si_3N_4$ chip are not matched, emphasizing the flexibility of the concept. The $Si_3N_4$ racetrack resonators, MZI, and CPT are tuned by thermal phase shifters. The CPT is used to adjust the cavity round-trip phase to an integer multiple of $2\pi$ at the wavelength corresponding to the maximum mirror reflectivity. The tunable MZI-based output coupler is used to set the ratio between the light extracted from the laser cavity and the feedback to the RSOA.

In the device implementation discussed in the following, the CPT is $1$ mm long, and the Vernier pair of racetrack resonators have perimeters of $885.1$ µm (R1) and $857.4$ µm (R2). Four auxiliary waveguides WG $2 \ldots 5$ and the output WG $1$ are routed to the $Si_3N_4$ chip edge and connected to tapered EC having a pitch of $127$ µm. All five waveguide Ports $1 \ldots 5$ are coupled to a single-mode fiber (SMF) array (FA) via 3D-printed FaML.

### 3.2.2 Component characterization

To fully evaluate our integration concept, all components of the ECL are individually characterized prior to assembly. The assembly of fully characterized known-good components highlights one of the key advantages of our hybrid approach compared to other integration concepts. The following sections describe the measured performance of the RSOA and of the $Si_3N_4$ feedback circuit.

The C-band RSOA (Fraunhofer Heinrich-Hertz-Institut, Germany) is $700$ µm long, has a back facet with a HR coating ($90$ % reflectivity with respect to air) and an angled front facet ($9.0°$) with AR coating designed for emission into polymer ($n = 1.56$). The intensity distribution has an approximately circular shape with a $1/e^2$-diameter of $3.6$ µm. The device is similar to the RSOA used in [J1], and further details relating to the measurement techniques are described in the associated Supplementary Information. At a pump current of $100$ mA, the

measured maximum small-signal gain is 22 dB, and the saturated output power is $P_{\mathrm{sat}} = 11.4$ dBm, both obtained at a wavelength of $\lambda = 1550$ nm. The RSOA characterization results are given in more detail in Appendix A.2, see Fig. A.2(a) and the associated description.

Frequency-selective optical feedback is provided by an ECL filter chip comprising a Vernier pair of racetrack resonators on the $Si_3N_4$ chip (TriPleX®, LioniX International B.V., The Netherlands), Fig. 3.1(b). The underlying waveguides are based on a symmetric double-stripe geometry consisting of a pair of stacked $Si_3N_4$ layers buried in a $SiO_2$ cladding - a standard structural element of the TriPleX® platform [17, 115]. The low propagation loss of less than 0.1 dB/cm is achieved with a width of the two $Si_3N_4$ stripes of 1.1 µm and a height of only 175 nm for the top and 75 nm for the bottom $Si_3N_4$ stripe, respectively. Both racetrack resonators have equal WG cross sections, leading to identical propagation constants and slightly different free spectral ranges (FSR) achieved by slight differences of the perimeters. The individual racetrack resonators are characterized by power transmission measurements in a loop-back configuration through the two auxiliary waveguide Ports 3 and 4, see Fig. 3.1(b). The measured transmission can be fit to a model to estimate the resonator parameters such as the loaded $Q$-factors and the FSR, see Appendix A.1 and [J1] for more details. At a wavelength of 1525 nm, corresponding to the center of our tuning range, we extract FSR of 195.7 GHz and 202.0 GHz for R1 and R2, respectively, along with approximately equal loaded $Q$-factors of 20 000. With the parameters obtained from the fit, we can calculate a 0.1 dB on-chip reflection loss of the tunable mirror, measured at the top of the reflection peak in case a resonance of R1 is perfectly aligned with a corresponding resonance of R2.

### 3.2.3 Module assembly

In a first step of module assembly, the RSOA is glued to a copper (Cu) heatsink with an electrically conductive adhesive (EPO-TEK® H20E, Epoxy Technology Inc., USA). The Cu heatsink with the RSOA and the $Si_3N_4$ chip are then coarsely

aligned to each other and glued to an Al submount, see Fig. 3.1(a). A step on the Al submount is used to adjust the height of the RSOA chip surface to that of the WG layer containing the EC on the $Si_3N_4$ external-cavity chip. The PWB trajectory depends on the exact positions and emission directions of the RSOA and $Si_3N_4$ EC facets, see Fig. 3.1(b). The EC on the external-cavity chip rely on spot-size converters (SSC) that are implemented by simultaneously tapering the thickness of the top $Si_3N_4$ layer as well as the width of the two stacked $Si_3N_4$ stripes, while maintaining a constant thickness of the intermediate $SiO_2$ layer. In the EC used for our devices, the thickness of the top $Si_3N_4$ layer is tapered down from the usual $175$ nm to zero close to the end-facets, effectively only leaving the bottom $Si_3N_4$ stripe with $75$ nm thickness. At the input of the chip, the $Si_3N_4$ stripes start with an initial width of $2$ µm at the facet, which is reduced to the standard width of $1.1$ µm at the end of the taper section. This leads to a measured elliptical mode-field with $1/e^2$-width of $7.2$ µm in the horizontal and $4.6$ µm in the vertical direction, and the rectangular cross-section of the PWB is chosen to have a width of $8.0$ µm and a height of $5.0$ µm for best coupling to the mode-field size at the chip facet. In our implementation, the PWB bridges a gap of $306$ µm between the two dies. The PWB on the RSOA side comprises a taper with an initial cross-section of $4.0$ µm $\times$ $4.0$ µm, matched to the mode-field size at the RSOA facet. The PWB cross-section is then reduced to the usual $2.4$ µm $\times$ $2.0$ µm. At the facet of the $Si_3N_4$ chip, the PWB is up-tapered to the above-mentioned final cross-section of $8.0$ µm $\times$ $5.0$ µm connecting to the on-chip $Si_3N_4$ EC. Between the tapers, the PWB maintains the constant cross-section of $2.4$ µm $\times$ $2.0$ µm, while the trajectory describes an arc to smoothly connect to the edge-coupled on-chip WG at either end, which feature notably different directions. Printed attachment structures on both the RSOA and the $Si_3N_4$ chip facets improve the mechanical stability of the PWB, see Fig. 3.1(c).

Fiber-chip coupling at the output of the $Si_3N_4$ chip relies on five identical FaML, printed to the facets of the FA. These FaML have been designed for the specific EC used at the output facets of the external-cavity chip towards the fiber array (waveguide Ports $1\ldots5$). The EC again rely on a pair of $Si_3N_4$ stripes, which are now down-tapered from the standard width of $1.1$ µm to a final width of $0.8$ µm

at the facet, with the bottom $Si_3N_4$ layer keeping its constant thickness of $75\,\mathrm{nm}$ while the thickness of the upper layer is reduced from the initial value of $175\,\mathrm{nm}$ to zero at the facet. The resulting mode-field diameter was measured to be $7.5\,\mu\mathrm{m}$ in both directions. The FaML are $70\,\mu\mathrm{m}$ long and offer a working distance of $50\,\mu\mathrm{m}$ between the apices of the lenses and the $Si_3N_4$ WG facets. The distance between the FA and the $Si_3N_4$ chip facet hence amounts to $120\,\mu\mathrm{m}$, see Fig. 3.1(b). Both the PWB and the FaML are made from a negative-tone photoresist (VanCore A, Vanguard Automation GmbH, Germany; refractive index $n = 1.53$) by *in-situ* multi-photon lithography. The fabricated PWB and FaML are developed in propylene-glycol-methyl-etheracetate (PGMEA), flushed with isopropanol, and finally blow-dried. The FaML on the FA are 3D-printed in a separate step for subsequent assembly with a custom pick-and-place machine [J3]. Figure 3.2(a) shows a microscope image of the fully assembled ECL module. Inset (i) displays a scanning-electron microscope (SEM) image of the false-colored PWB along with the dimensions of the various PWB cross-sections. Inset (ii) shows a microscope image of the five FaML on the FA facing the corresponding edge-coupled waveguide Ports $1 \ldots 5$ on the $Si_3N_4$ chip.

### 3.2.4 Module characterization

The ECL wavelength is selected by aligning the two racetrack resonators to a common resonance, which may be detected through the two auxiliary waveguide Ports $3$ and $4$ in a loop-back configuration. After the alignment of the resonances, the cavity phase and the tunable coupler are adjusted for maximum on-chip output power $P_{\mathrm{out}}$, see Fig. 3.1(b). From the power-current characteristics ($P$–$I$-curve) in Fig. 3.2(b) measured at a wavelength $\lambda = 1550\,\mathrm{nm}$, we extract a threshold current of $19\,\mathrm{mA}$ and an average slope efficiency of $132\,\mathrm{mW/A}$. We further estimate a PWB loss of $(1.6 \pm 0.2)\,\mathrm{dB}$ by measuring the ECL emission power $P_{\mathrm{out}}$ and by comparing it to the measured saturated output power $P_{\mathrm{sat}}$ of the RSOA at the same wavelength $\lambda$ and at the same injection current $I$. Details relating to the estimation of the PWB losses can be found in Appendix A.2. The measured PWB loss is on par with previously reported coupling losses of $(1.6 \pm 1.0)\,\mathrm{dB}$ between RSOA and

$Si_3N_4$-based PIC using passive alignment [198], outperforming many previous demonstrations featuring typical RSOA-to-chip insertion losses of $(2 \ldots 3)$ dB [23, 107, 193, 195, 197]. Butt-coupling losses below 1 dB are also feasible, but the associated devices require carefully laid-out SSC on the passive chips [31, 32] or inverse tapers on both the active and passive chips [33, 34], usually in conjunction with active alignment techniques for precise positioning.

Figure 3.2(c) depicts superimposed ECL lasing spectra with tuning steps of 5 nm within the tuning range $(1480 \ldots 1570)$ nm for a fixed injection current of $I = 100$ mA. A maximum on-chip output power $P_{\mathrm{out}}$ of 12 dBm is measured at wavelengths near the center of the tuning range ($\lambda_{\mathrm{c}} = 1525$ nm), close to the center wavelength of the RSOA gain spectrum. The SMSR is at least 45 dB over the whole tuning range and reaches 59 dB in the center of the tuning range, see Fig. A.2(b) below.

We further measure the phase noise of the emitted laser line using a frequency discriminator (LWA-1k 1550, HighFinesse GmbH, Germany). The measurements are carried out for an emission wavelength close to 1550 nm, where we re-adjust the tunable output coupler for minimum intrinsic linewidth. The associated FM noise spectrum is shown in Fig. 3.2(d). The intrinsic (Lorentzian) linewidth is obtained by first fitting a model function of the form $S_{\mathrm{F}}(f) = S_0 + S_1 f^{-1} + S_2 f^{-2} + S_3 f^{-3}$ to the measured FM noise spectrum (blue dashed line). This leads to $S_0 = 311\,\mathrm{Hz^2/Hz}$, corresponding to an intrinsic linewidth of $\delta f = \pi S_0 = 979$ Hz (solid blue line), which is among the lowest values reported for similar feedback architectures [20, 31, 32, 114, 190, 191, 193, 194]. The low phase noise results from the large effective optical cavity length of $L_{\mathrm{eff}} = 48.7$ mm) at the center of the emission range ($\lambda_{\mathrm{c}} = 1525$ nm), the low passive WG losses (0.1 dB/cm), and the small RSOA-to-chip coupling loss (1.6 dB). The effective optical cavity length $L_{\mathrm{eff}}$ accounts for the group delay of all cavity elements including the RSOA waveguide, the PWB, the on-chip $Si_3N_4$ waveguides as well as the highly dispersive racetrack resonators R1 and R2 and is hence much larger than the geometrical cavity length. Minimizing losses in the extended laser cavity, which are dictated mainly by the RSOA-to-chip coupling loss, is essential to obtain low laser linewidths [107]. Our results are on par with lately demonstrated linewidths of 895 Hz [194],

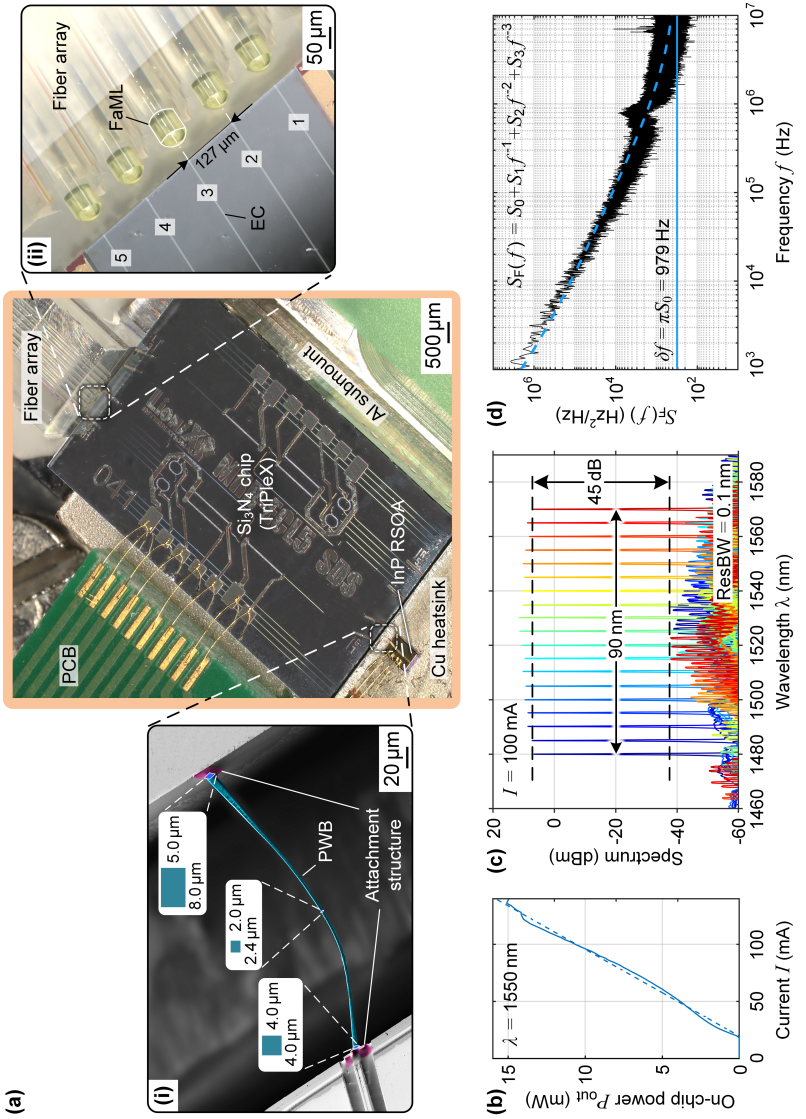


**Fig. 3.2:** (Caption next page.)

**Fig. 3.2:** Implementation of ECL module and performance characterization. **(a)** Microscope image of the assembled ECL module according to Fig. 3.1(a). Inset (i) shows a scanning-electron microscope (SEM) image of the false-colored PWB between the RSOA and $Si_3N_4$ (TriPleX®) chip. The various cross-sections at different positions along the PWB are marked. Inset (ii) displays a microscope image of the five FaML on the FA having a pitch of $127\,\mu m$ and facing the corresponding EC of the waveguide Ports $1 \ldots 5$ on the $Si_3N_4$ chip. **(b)** On-chip output power $P_{\mathrm{out}}$ vs. injection current $I$ for lasing at $1550\,nm$, leading to a threshold current of $19\,mA$ and an average slope efficiency of $132\,mW/A$ (fit by dashed straight line). **(c)** Superimposed ECL lasing spectra with tuning steps of $5\,nm$ within the tuning range $(1480 \ldots 1570)\,nm$ for $I = 100\,mA$. The maximum on-chip output power is $12\,dBm$ near a wavelength of $1525\,nm$. The side-mode suppression ratio (SMSR) is at least $45\,dB$ and can reach $59\,dB$ in the center of the tuning range, see Fig. A.2(b) below. **(d)** FM noise spectrum with fit (blue dashed line). The intrinsic (Lorentzian) linewidth is $\delta f = \pi S_0 = 979\,Hz$ (fit by solid blue line).

achieved with actively aligned $Si_3N_4$-based external-cavity circuits featuring only a pair of Vernier-type ring resonators. Note that previously reported demonstrations of such devices usually reached values of the order of 2 kHz [20, 114]. Lower intrinsic linewidths may be achieved by using external-cavity circuits with three or more ring resonators: Using shallow-etched low-loss SiP rib WG in combination with three-ring external-cavity circuits, heterogeneously integrated ECL with linewidths down to 95 Hz have been demonstrated [108]. The linewidths of three-ring ECL can be further reduced down to 40 Hz by using $Si_3N_4$-based external-cavity circuits with large optical cavity lengths of the order of 0.5 m [196]. Note that feedback circuits based on standard SiP strip WG generally lead to larger intrinsic linewidths of, e.g., 12 kHz, demonstrated with a hybrid integrated ECL based on a pair of Vernier-type SiP ring resonators in combination with a Mach-Zehnder-type delay interferometer that additionally suppresses Vernier side-lobes in the filter transfer function [192].

## 3.3 Kerr comb generation

To demonstrate the versatility of our hybrid ECL, we use the device as a precisely tunable pump laser to generate dissipative Kerr soliton (DKS) frequency combs in $Si_3N_4$ microresonators. Figure 3.3(a) shows a schematic of the associated experimental setup: The ECL fiber output is connected to an optical isolator, followed by an erbium-doped fiber amplifier (EDFA) and a polarization controller (PC). The light is then fed via a PWB to a separately packaged comb module (CM), consisting of a ring resonator (R3, diameter 1286 µm, free spectral range 35.4 GHz, $Q \approx 15 \times 10^6$), which was fabricated using the photonic Damascene reflow process [16, 22]. More details on the characterization procedures and results for the $Si_3N_4$-based chip used for the CM are given in Appendix A.3. A microscope image of the CM is shown at the bottom of Fig. 3.3(a) along with a top-view schematic of the $Si_3N_4$ chip. Besides the ring resonator R3 of interest, the chip contains two additional rings that were not used in our experiments. The output of the ring resonator R3 is connected to a subsequent FA by a PWB. The input and output FA as well as the $Si_3N_4$ chip are fixed to a common Al submount.

The start-up process for the comb source is illustrated in Fig. 3.3(b) [86, 118]. The left axis indicates the absolute wavelength of the ECL, whereas the axis on the right shows the associated detuning $f_{\mathrm{ECL}} - f_{\mathrm{R3,cold}}$ of the ECL frequency $f_{\mathrm{ECL}}$ with respect to the cold resonance of R3 $f_{\mathrm{R3,cold}} = 193.5348\,\mathrm{THz}$ (horizontal green line). Initially, the ECL wavelength (♦, I) is blue-detuned with respect to the cold resonance of R3. Then the ECL emission wavelength is increased by ramping up the CPT heater power, see black dots in Fig. 3.3(b) and Arrow ①. Upon reaching the red-detuned regime, $f_{\mathrm{ECL}} < f_{\mathrm{R3,cold}}$, a multi-soliton state can be observed (♦, II). Subsequently, the ECL pump is tuned backwards [86, 118] (Arrow ②), thereby reducing the number of solitons circulating in the cavity (♦, III), until finally, a single-soliton state is reached at an ECL wavelength slightly above the cold resonance of R3 (♦, IV). For the states (♦, III) and (♦, IV), we record the spectrum using an optical spectrum analyzer (OSA), Fig. 3.3(c) and Fig. 3.3(d). The spectral envelope of the single-soliton state (♦, IV) is smooth and can be well approximated by the typical $\mathrm{sech}^2$-characteristic, Fig. 3.3(d), whereas the multi-soliton state (♦, III) is characterized by spectral fringes, Fig. 3.3(c). To the best of our knowledge, our experiments represent the first demonstration of a single-soliton Kerr comb generated with a pump that is derived from a hybrid integrated ECL.

We also measure the FM noise spectrum of a typical single-soliton comb line, Fig. 3.3(e), by beating it with a highly stable reference laser tone (Koheras X15, NKT Photonics A/S, Denmark; intrinsic linewidth $\delta f < 100\,\mathrm{Hz}$) on a photodetector (PD). The photocurrent at the intermediate frequency is sent to a phase-noise analyzer (PNA; FSWP50, Rohde & Schwarz GmbH & Co. KG, Germany). From the recorded FM noise spectrum, an intrinsic linewidth of $\delta f = 3\,\mathrm{kHz}$ is estimated, dictated by the phase noise of the ECL. Note that the operating point of the ECL was not optimized for minimum phase noise and that the linewidth was therefore slightly higher than the one shown in Fig. 3.2(d). Note also that the Kerr comb generator used here features a threshold pump power of the order of $(10...15)\,\mathrm{mW}$ [16, 199, 200], which may be reduced further to below $5\,\mathrm{mW}$ [23], e.g., by increasing the quality factor of the ring resonator [16, 23, 129]. Leveraging the full $15\,\mathrm{mW}$ of on-chip ECL power by co-integrating the $Si_3N_4$ microresonators with the external

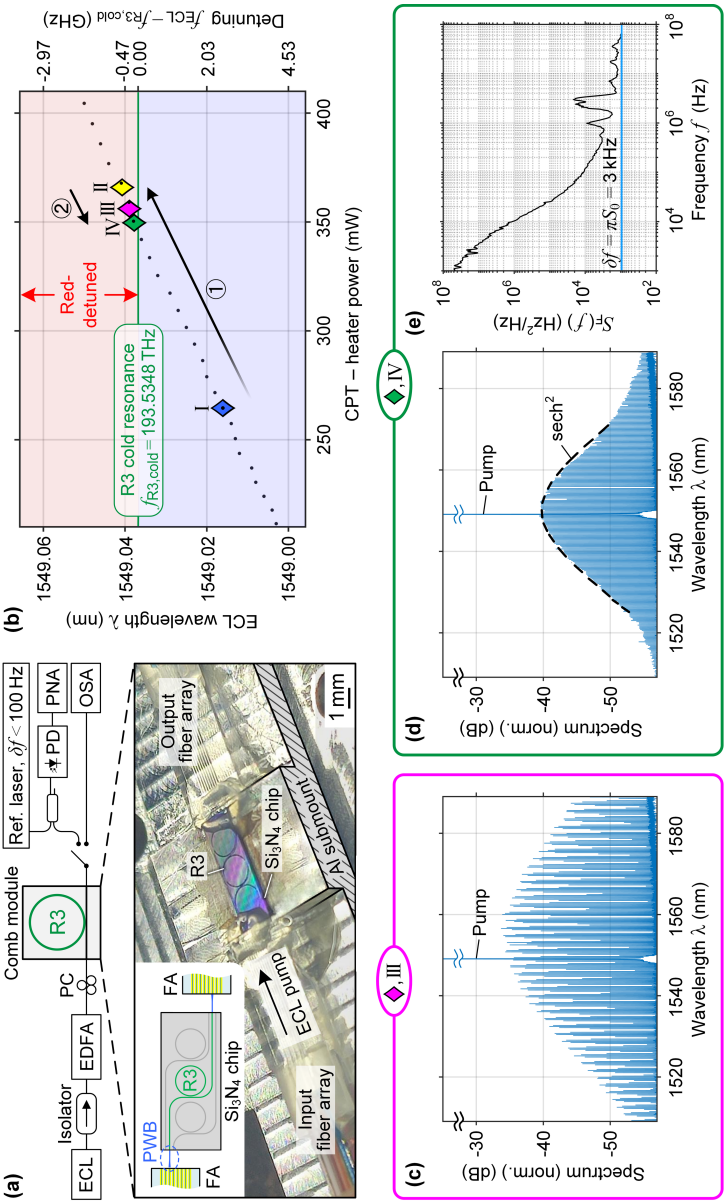


**Fig. 3.3:** (Caption next page.)

**Fig. 3.3:** Dissipative Kerr soliton (DKS) frequency comb generation in a high-$Q$ $Si_3N_4$ microresonator (R3) using the ECL module as a precisely tunable pump laser. **(a)** Schematic of the associated experimental setup: The ECL fiber output is connected to an optical isolator followed by an erbium-doped fiber amplifier (EDFA) and a polarization controller (PC). The light is then fed via a PWB to a separately packaged comb module (CM), consisting of a ring resonator (R3, diameter 1286 µm, free spectral range 35.4 GHz, $Q \approx 15 \times 10^6$), which was fabricated using the photonic Damascene process. A microscope image of the CM is shown in the bottom part of the figure along with a top-view schematic of the $Si_3N_4$ chip. Besides the ring resonator R3 of interest, the chip contains two additional rings that were not used in our experiments. The output of the ring resonator R3 is connected to a subsequent FA by a second PWB. The input and output FA as well as the $Si_3N_4$ chip are fixed to a common Al submount. The output of the CM is either monitored on an optical spectrum analyzer (OSA) or beat with a highly stable reference laser tone. The photocurrent at the intermediate frequency is sent to a phase-noise analyzer (PNA). **(b)** Start-up process for the comb source, relying on precise tuning of the ECL emission wavelength. The left axis indicates the absolute wavelength of the ECL, whereas the axis on the right shows the associated detuning $f_{\mathrm{ECL}} - f_{\mathrm{R3,\,cold}}$ of the ECL frequency $f_{\mathrm{ECL}}$ with respect to the cold resonance of R3 $f_{\mathrm{R3,\,cold}} = 193.5348\,\mathrm{THz}$ (horizontal green line). Initially, the ECL wavelength (♦, I) is blue-detuned with respect to the cold resonance of R3. Then the ECL emission wavelength is increased by ramping up the CPT heater power, see black dots and Arrow ① in Subfigure (b). Upon reaching the red-detuned regime, $f_{\mathrm{ECL}} < f_{\mathrm{R3,cold}}$, a multi-soliton state can be observed (♦, II). Subsequently, the ECL pump is tuned backwards (Arrow ②), thereby reducing the number of solitons circulating in the cavity (♦, III), until finally, a single-soliton state is reached at an ECL wavelength slightly above the cold resonance of R3 (♦, IV). **(c)** Spectrum of an exemplary multi-soliton comb, characterized by spectral fringes. The multi-soliton state is indicated by a pink diamond (♦, III) in (b). **(d)** Spectrum of single-soliton comb, characterized by a smooth spectral envelope, which can be well approximated by the typical $\mathrm{sech}^2$-characteristic. The single-soliton state is indicated by a green diamond (♦, IV) in (b). **(e)** FM noise spectrum of a typical single-soliton comb line. We estimate an intrinsic linewidth of $\delta f = 3\,\mathrm{kHz}$.

feedback circuit of the ECL would allow to omit the EDFA and to build a fully integrated Kerr comb module similar to the one demonstrated in [23].

Our experiments show that the frequency agility of a thermally tunable ECL is already sufficient to generate a Kerr soliton frequency comb, which requires a precise control of the emission frequency to follow a tuning profile with respect to a resonance of the high-$Q$ microresonator. Note also that using independently tunable ECL as a pump offers distinct advantages over integrated Kerr comb generators that are based on self-injection locking (SIL) of the pump laser to the Kerr-nonlinear resonator [23–26, 129–131]. Specifically, pumping a Kerr comb generator by a freely tunable continuous-wave (CW) laser allows to independently control the detuning of the pump tone from the resonance of the cold ring, which is impossible for SIL. This additional degree of freedom allows to optimize the generated frequency comb, e.g., with respect to bandwidth or achievable comb-line power [25]. Specifically, single-soliton states with a large detuning and broad bandwidth may be hard to obtain in the SIL regime [131]. Note that when using a separate CW laser as a pump for Kerr-comb generation, the frequency noise of the comb lines is mainly dictated by the pump laser. A narrow-linewidth pump laser is hence crucial to achieve low-noise frequency combs.

Our demonstration further shows the importance of hybrid integration concepts, that can efficiently combine different PIC technologies in a chip-scale package. Specifically, the two $Si_3N_4$ chips used for our assemblies are based on different material platforms, namely the TriPleX® platform for the ECL filter circuit and the photonic Damascene process for the high-$Q$ microresonator. Both platforms have their own highly specific fabrication workflows that have been individually optimized and that cannot be straightforwardly combined in monolithically integrated devices on a single substrate. Using PWB or FaML for assembly of such hybrid multi-chip systems can overcome such limitations and pave the path towards efficient co-integration of TriPleX®-based ECL filter circuits with dedicated $Si_3N_4$ chips for Kerr-comb generation in a compact module, potentially using additional booster semiconductor optical amplifiers (BSOA) between the chips.

## 3.4 Summary

We demonstrate a hybrid integrated ECL that exploits an intra-cavity photonic wire bond (PWB) for connecting an InP reflective semiconductor optical amplifier (RSOA) to a $Si_3N_4$-based tunable external-cavity circuit. Photonic wire bonding overcomes the need for high-precision alignment during assembly, thereby permitting fully automated mass production of hybrid photonic multi-chip assemblies. The ECL offers a $90\,\text{nm}$ tuning range ($1480\,\text{nm}$–$1570\,\text{nm}$) with on-chip output powers above $12\,\text{dBm}$ and side-mode suppression ratios of up to $59\,\text{dB}$ in the center of the tuning range. Upon optimization of the operating point, we measure an intrinsic linewidth of $979\,\text{Hz}$, which is among the lowest values reported for two-ring feedback architectures. The versatility of the ECL is demonstrated by using the device as narrow-linewidth tunable pump laser for Kerr frequency comb generation in a high-$Q$ $Si_3N_4$ microresonator. To the best of our knowledge, our experiments represent the first demonstration of a single-soliton Kerr comb generated with a pump that is derived from a hybrid integrated ECL. Frequency-tunable hybrid ECL can generally serve a wide range of applications from coherent communications [31] to frequency-modulated continuous-wave (FMCW) light detection and ranging (LIDAR) [194] and to optical coherence tomography (OCT) [C3], but the success of such concepts will finally rely on the scalability of the underlying fabrication techniques. Our experiments address this challenge and pave a path towards highly versatile hybrid light sources that combine the scalability advantages of monolithic integration with the performance and flexibility of hybrid multi-chip assemblies.

*[End of paper [J2]]*

# 4 3D-printed facet-attached optical elements for connecting VCSEL and photodiodes to fiber arrays and multi-core fibers

This chapter reports on 3D-printed optical elements for low-loss and alignment-tolerant coupling of multimode fiber arrays as well as individual cores of multimode multicore fibers to standard arrays of vertical-cavity surface-emitting lasers (VCSEL) or photodiodes (PD) in datacenter transceiver assemblies. It has been published in *Optics Express* [J3]. The material from the publication has been adapted to comply with the layout and the structure of this thesis.

Note that Yilin Xu and the author of this dissertation contributed equally to this publication. The experiments were conceived by Yilin Xu, Mareike Trappen, Philipp-Immanuel Dietrich, Matthias Blaicher, Christian Koos, and the author. Matthias Blaicher, Yilin Xu, and the author developed advanced lithography tools and processes required for precise fabrication of the facet-attached microlenses (FaML). The FaML were designed by Yilin Xu and the author. The FaML on the fiber facets in the MT ferrules were fabricated by the author, and the FaML on the VCSEL / PD chips were fabricated by Matthias Lauermann, with a photoresist provided by Philipp-Immanuel Dietrich. Philipp-Immanuel Dietrich contributed the data related to long-term stability tests. Achim Weber designed and implemented the assembly machine. Preliminary assembly experiments were conducted by Yilin Xu, Mareike Trappen, Torben Kind, and the author. The final transceiver assemblies were jointly fabricated by Yilin Xu and the author. The author performed the experimental characterization of the various

assemblies with the support of Yilin Xu and Mareike Trappen and analyzed the measurement data. The associated data-transmission experiments were executed and evaluated by Alexandra Henniger-Ludwig, Hermann Kapim and the author. All authors discussed the data. The project was supervised by Achim Weber, Clemens Wurster, Sebastian Randel, Wolfgang Freude, and Christian Koos. The author wrote the manuscript with support by Yilin Xu, Wolfgang Freude, and Christian Koos. The manuscript is partially based on the prior conference contribution [C2] to OFC 2022.

*[Beginning of paper [J3]. This article is reprinted under the terms of Optica Publishing Group's "Copyright Transfer and Open Access Publishing Agreement".]*

**3D-printed facet-attached optical elements for connecting VCSEL and photodiodes to fiber arrays and multi-core fibers**

*Optics Express, Volume 30, Issue 26, pp. 46602–46625 (2022)*

https://doi.org/10.1364/OE.470676

Pascal Maier[1,2,†], Yilin Xu[1,2,†], Mareike Trappen[1,2], Matthias Lauermann[3], Alexandra Henniger-Ludwig[4], Hermann Kapim[4], Torben Kind[5], Philipp-Immanuel Dietrich[1,2,3], Achim Weber[3,5], Matthias Blaicher[1,2], Clemens Wurster[6], Sebastian Randel[1], Wolfgang Freude[1] & Christian Koos[1,2,3]

[1] Institute of Photonics and Quantum Electronics (IPQ), Karlsruhe Institute of Technology (KIT), Engesserstr. 5, 76131 Karlsruhe, Germany.

[2] Institute of Microstructure Technology (IMT), Karlsruhe Institute of Technology (KIT), Hermann-von-Helmholtz Platz 1, 76344 Eggenstein-Leopoldshafen, Germany.

[3] Vanguard Automation GmbH, Gablonzer Str. 10, 76185 Karlsruhe, Germany.

[4] Rosenberger Hochfrequenztechnik GmbH & Co. KG, Hauptstr. 1, 83413 Fridolfing, Germany.

[5] ficonTEC Service GmbH, Im Finigen 3, 28832 Achim, Germany.

[6] Rosenberger OSI GmbH & Co. OHG, Endorferstr. 6, 86167 Augsburg, Germany.

† authors contributed equally to the work.

Multicore optical fibers and ribbons based on fiber arrays allow for massively parallel transmission of signals via spatially separated channels, thereby offering attractive bandwidth scaling with linearly increasing technical effort. However, low-loss coupling of light between fiber arrays or multicore fibers and standard linear arrays of vertical-cavity surface-emitting lasers (VCSEL) or photodiodes (PD) still represents a challenge. In this paper, we demonstrate that 3D-printed facet-attached microlenses (FaML) offer an attractive path for connecting multimode fiber arrays as well as individual cores of multimode multicore fibers to standard arrays of VCSEL or PD. The freeform coupling elements are printed *in-situ* with high precision on the device and fiber facets by high-resolution multi-photon lithography. We demonstrate coupling losses down to $0.35$ dB along with lateral 1 dB alignment tolerances in excess of $10$ µm, allowing to leverage fast passive assembly techniques that rely on industry-standard machine vision. To the best of our knowledge, our experiments represent the first demonstration of a coupling interface that connects individual cores of a multicore fiber to VCSEL or PD arranged in a standard linear array without the need for additional fiber-based or waveguide-based fan-out structures. Using this approach, we build a $3 \times 25$ Gbit/s transceiver assembly which fits into a small form-factor pluggable module and which fulfills many performance metrics specified in the IEEE 802.3 standard.

## 4.1 Introduction

In recent years, increasing throughput of optical communication systems has primarily relied on higher symbol rates and advanced modulation formats [201]. Giving the steadily rising demand for communication bandwidth, however, the limits of these approaches are becoming increasingly obvious [146, 157], especially for short-reach intra-datacenter links, where cost- and energy-efficient implementation is key. Parallel transmission via spatially separated channels is seen as an attractive alternative for bandwidth scaling with linearly increasing technical effort [146, 158]. To maintain the associated fiber installations manageable, significant effort has been spent to replace single fibers by more compact fiber ribbons [202–210],

comprising fiber arrays (FA), or by multicore fibers (MCF) [211–220]. However, low-loss coupling of light between FA or MCF and standard linear arrays of vertical-cavity surface-emitting lasers (VCSEL) or photodiodes (PD) still remains challenging. Current solutions for coupling of VCSEL or PD to FA rely on, e.g., high-precision injection-molded plastic parts that contain refractive and reflective optical elements to adapt the spot size of the emitted light for efficient coupling to the corresponding fiber [202–204, 207, 209, 221]. However, these schemes often require multi-step assembly processes, starting with a precise mechanical socket that needs to be carefully aligned and fixed to the on-board VCSEL / PD array. This socket is equipped with a pluggable interface to a detachable mechanical connector that has to be glued to a FA in a separate step and that can then be connected to the on-board socket. These schemes require high-precision visual alignment of the socket with respect to the VCSEL / PD array as well as precise mounting of the connector to the FA, while typical losses range between 1 dB and 2 dB [207, 222]. Moreover, these schemes are not applicable to MCF, which either have to rely on fan-out structures to address individual fiber cores [211, 223, 224], often in conjunction with custom connector and fiber arrangements [211–213, 225], or which require device [214–218, 220] or grating coupler (GC) [219] arrays in non-standard 2D arrangements that are precisely matched to the cross-section of the respective MCF. Such solutions are technically complex and challenging to scale, in particular when it comes to compact short-reach datacenter transceivers that are subject to stringent constraints in footprint and in assembly costs.

In this paper, we show that 3D-printed facet-attached microlenses (FaML) [3] may offer an attractive alternative for efficiently connecting multimode fiber arrays (MM-FA) as well as individual cores of multimode multicore fibers (MM-MCF) to standard arrays of VCSEL or PD having industry-standard pitches of, e.g., 250 µm. The FaML are printed directly on the device and fiber facets by multi-photon lithography [68], thereby ensuring sub-100 nm precision in a fully automated fabrication step. The freeform coupling elements are designed to collimate the associated beams to large diameters of tens of micrometers, which greatly relaxes alignment tolerances such that subsequent assembly steps can entirely rely on passive positioning using industry-standard machine vision. We demonstrate

the viability of the proposed concepts in a series of proof-of-concept experiments. In a first set of experiments, we show connections between VCSEL / PD arrays and MM-FA, achieving average coupling losses as low as $0.35\,\mathrm{dB}$ for the transmitter (Tx) and $0.70\,\mathrm{dB}$ for the receiver (Rx) along with lateral $1\,\mathrm{dB}$ alignment tolerances of $\pm 17\,\mu\mathrm{m}$ (Tx) and $\pm 62\,\mu\mathrm{m}$ (Rx), respectively. To the best of our knowledge, these results are among the lowest losses and the highest alignment tolerances so far demonstrated for coupling between VCSEL / PD arrays and MM-FA. In a second set of experiments, we extend this concept to MM-MCF containing densely spaced cores with a separation of $39\,\mu\mathrm{m}$. Using appropriately designed FaML, these cores can be connected to VCSEL and PD that are arranged in linear arrays with a standard pitch of $250\,\mu\mathrm{m}$, reaching average coupling losses of $0.67\,\mathrm{dB}$ (Tx) and $0.63\,\mathrm{dB}$ (Rx) along with lateral $1\,\mathrm{dB}$ alignment tolerances of $\pm 18\,\mu\mathrm{m}$ (Tx) and $\pm 25\,\mu\mathrm{m}$ (Rx), respectively. To the best of our knowledge, these experiments represent the first demonstration of a coupling interface that connects individual cores of an MCF to VCSEL / PD arranged in a standard linear array without the need for additional fiber-based or waveguide-based fan-out structures. Using this approach, we finally build a $3 \times 25\,\mathrm{Gbit/s}$ transceiver assembly which fits into a small form-factor pluggable (SFP) module and which fulfills many performance metrics specified in the IEEE 802.3 standard.

## 4.2 Coupling concept

Figure 4.1 illustrates the concept of using 3D-printed facet-attached microlenses (FaML) for connecting linear arrays of vertical-cavity surface-emitting lasers (VCSEL) and photodiodes (PD) to fiber arrays (FA) and multicore fibers (MCF). The VCSEL and PD arrays transmit light to or receive light from the associated FA or MCF, which are glued into an industry-standard mechanical transfer (MT) ferrule. MT ferrules are commercially available at high quality and low cost and can be handled with standard gripper tools. Moreover, in future implementations, MT ferrules could allow to arrange fibers in two-dimensional arrays, Fig. 4.1(a), thereby increasing the number of parallel fiber channels.

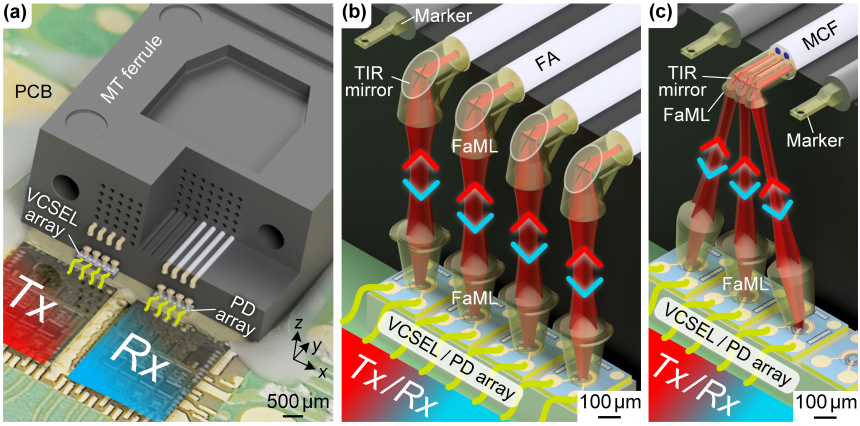


**Fig. 4.1:** Concept of a multi-lane transceiver assembly using 3D-printed facet-attached microlenses (FaML) for connecting linear arrays of vertical-cavity surface-emitting lasers (VCSEL) and photodiodes (PD) to fiber arrays (FA) or multicore fibers (MCF). The VCSEL and PD arrays transmit light to or receive light from the associated FA or MCF, which are glued into an industry-standard mechanical transfer (MT) ferrule. The FaML are designed to redirect, expand, and collimate the beams emitted or accepted by the VCSEL, the PD, the FA or the MCF such that the alignment tolerances increase both in axial and transverse direction with respect to the beam. **(a)** Overview of a transceiver assembly. Transmitter (Tx), receiver (Rx), and MT ferrule are mounted to a printed circuit board (PCB) in a small form-factor pluggable (SFP) layout. **(b)** Four linearly arranged VCSEL or PD of a Tx or Rx array, respectively, coupled to four fibers of a FA. The device and fiber facets are equipped with 3D-printed FaML, which contain curved refractive surfaces as well as total-internal-reflection (TIR) mirrors to shape and redirect the beams. 3D-printed markers facilitate passive alignment during the assembly process. **(c)** A linear array of three VCSEL or PD is used to couple to three cores of a single MCF. The receiving (emitting) MCF are glued to the MT ferrule such that the axes of three fiber cores lie in a common $z$-normal plane. To compensate for the pitch mismatch between the MCF cores and the VCSEL / PD, the outer FaML are designed to produce beams that are slightly inclined with respect to the $z$-direction. Note that this concept could in principle be extended further to also utilize the remaining cores of the depicted seven-core MCF. This could open a path to using two-dimensional device arrays in combination with one-dimensional MCF arrays and more complicated FaML arrangements on the fiber facets.

The assemblies illustrated in Fig. 4.1 can be build up in two steps: In a first step, FaML are printed to the VCSEL / PD chips and to the fiber facets using multi-photon lithography [68]. This approach allows to use the full design freedom of 3D-printed freeform structures and ensures highly precise alignment with deviations well below 100 nm in a fully automated fabrication step. The FaML-equipped devices can then be combined in a separate assembly step

using passive alignment techniques based on industry-standard camera-based machine vision and height measurements. To this end, the FaML illustrated in Fig. 4.1 are designed to redirect, expand, and collimate the beams emitted or accepted by the VCSEL, the PD, the FA or the MCF such that the alignment tolerances increase both in axial and in transverse direction of the beam. The simultaneously decreased angular tolerance can be usually accepted when using industry-standard assembly machinery. Note that the FaML approach can also be used for increasing the alignment tolerances of single-mode coupling interfaces [3]. Note also that, for assemblies like those shown in Fig. 4.1, coupling through FaML may have distinct advantages over the photonic wire bonding schemes used for fiber-chip interfaces in previous demonstrations [40, 42, 226]. Specifically, FaML-based coupling schemes allow to bridge comparatively large distances in the millimeter range, possibly with intermediate free-space micro-optical elements. This is impossible with photonic wire bonds (PWB), for which both facets have to be accessible within a single write field (typical size $300\,\mu\text{m} \times 300\,\mu\text{m}$) and within the limitations of a rather small working distance of the high-NA lithography objective (typically $250\,\mu\text{m}$). Moreover, FaML can be printed to device and fiber facets prior to module assembly. It is thus not necessary to expose the full assembly to the solvents used in the development process, which is unavoidable for PWB-based assembly workflows.

Figure 4.1(b) illustrates the concept for connecting individual VCSEL or PD of a linear Tx or Rx array, respectively, to a MM-FA having the same pitch. On the VCSEL (PD) side, a single FaML is used to emit (receive) a collimated beam. Within the FaML on the fiber facet, the beam is redirected by a total-internal-reflection (TIR) mirror. We further demonstrate that VCSEL and PD in a linearly arranged array can be connected to individual cores of a single MM-MCF using appropriately designed FaML, see Fig. 4.1(c). In the example shown in Fig. 4.1(c), the MCF are glued to the MT ferrule in a well-defined orientation such that the axes of three fiber cores lie in a common $z$-normal plane. To compensate for the pitch mismatch between the MCF cores and the VCSEL / PD, the outer FaML are tilted such that the emitted or received beams are slightly inclined with respect to the $z$-direction. We have performed proof-of-concept experiments of both the

arrangements shown in Fig. 4.1(b) and (c), which we describe in more detail in the following sections. Note that the concept shown in Fig. 4.1(c) could in principle be extended further to also utilize the remaining cores of the depicted seven-core MCF. This could open a path to using two-dimensional device arrays in combination with one-dimensional MCF arrays and more complicated FaML arrangements on the fiber facets.

## 4.3 Connecting VCSEL / PD to multimode fiber arrays (MM-FA)

We demonstrate the viability of the coupling concept shown in Fig. 4.1(b) by connecting four linearly arranged VCSEL (Broadcom AFCD-V64JZ, $\lambda = 850$ nm [227]) and PD (Broadcom SPD2025-4X, responsivity $S = 0.5$ A/W [228]) of a pair of Tx / Rx modules to a MM-FA, see Fig. 4.2(a). The MM-FA feature a pitch of $250\,\mu$m, matched to the pitch of the VCSEL / PD array, and are equipped with MM fibers having a core diameter of $2a = 26\,\mu$m. Figure 4.2(b) provides a more detailed view of the Tx VCSEL array connected to four MM fibers of the MT ferrule. The Rx PD array is connected via an identical arrangement but differently designed FaML. Inset (i) of Fig. 4.2(b) shows the FaML on the fiber side, each comprising a TIR mirror and a beam-expander lens, while Inset (ii) depicts the expander FaML at the VCSEL. Technical drawings with further details are given in Fig. 4.2(c), where the left-hand side shows a projection of a FaML pair along the $y$-direction ("front view"). For better visibility, the distance between the two FaML has been reduced in the drawing. Note that the MT ferrule used in our experiment was equipped with MM fibers (OFS MCF-MM-7-39) containing seven cores each, out of which only the central one was used, see cross section at the upper left in Fig. 4.2(c). The right-hand side of Fig. 4.2(c) shows a cut through the FaML arrangement along the $x$-normal plane through the line A–A' as indicated on the left.

To achieve high coupling efficiency, the shapes of the refractive surfaces are optimized using a home-made wave-propagation algorithm, which is based on

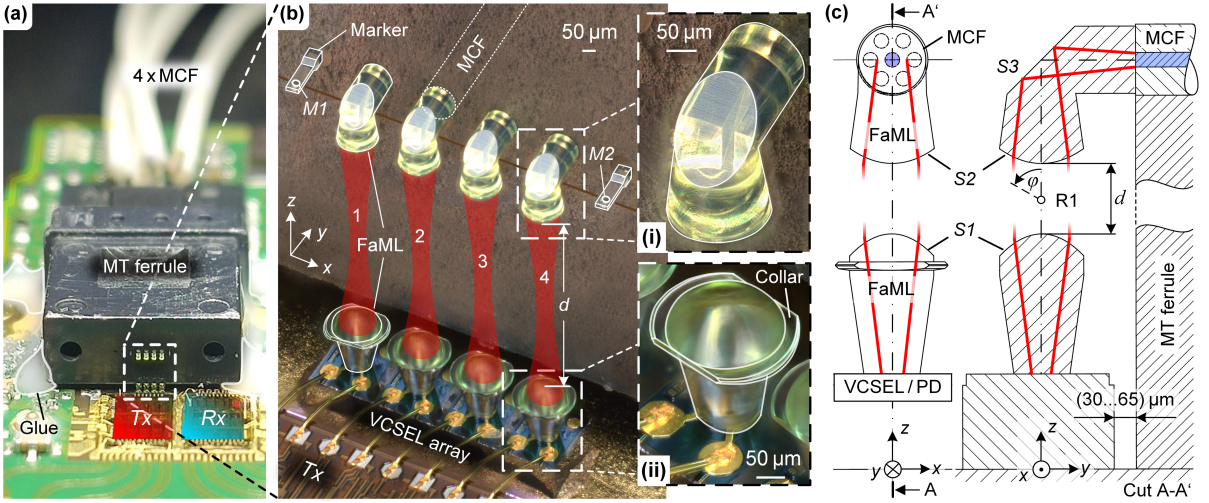


**Fig. 4.2:** Photograph and technical drawings of a four-lane transceiver (Channels 1, 2, 3, and 4), implemented according to the concept in Fig. 4.1(b). Four VCSEL are connected to the cores of four MM fibers, arranged in an array with a standard 250 µm pitch. **(a)** Overview photograph of the Tx side. **(b)** Microscope image showing the Tx VCSEL array and the associated FaML. The PD array is connected with a similar arrangement. Inset (i) shows the FaML on the fiber side, containing TIR mirrors and beam-expander lenses. Inset (ii) depicts the FaML on the VCSEL facet. A collar surrounds the VCSEL FaML for facilitating image recognition during passive assembly. Two markers are 3D-printed to the facet of the MT ferrule for reliable detection of the $z$-position and tilt correction. **(c)** Technical drawings of coupling structures. Left: Projection of a FaML pair along the $y$-direction ("front view"). Right: Cross-sectional view along the $x$-normal plane through the line A–A' shown on the left. The beam is shaped and redirected by the refractive Surfaces S1 and S2 as well as by the TIR mirror S3. The distance between the apices of Surfaces S1 and S2 amounts to $d = 1150$ µm. For measuring the angular misalignment loss, the MT ferrule is rotated in $\varphi$-direction about the rotation axis R1, that is parallel to the $x$-axis and that passes through the mid-points between the corresponding FaML apices.

the theory described in [229] and which has been successfully used for similar tasks [J6, 43]. Multimode light propagation through the FaML assembly is emulated by using Gaussian beams with an effective wavelength $\lambda_{\text{eff}} = M^2\lambda$, where $M^2 = 4.2 \ldots 5.4$ is the measured beam quality factor, see Appendix B.1 and B.2 for a more detailed explanation. At the Tx, the refractive Surface S1 on the laser side is designed to produce a mode-field diameter (MFD) of $49\,\mu\text{m}$ half-way between the two FaML. The beam then enters the FaML on the Tx fiber facet through refractive Surface S2, which is designed to illuminate the central core of the MM-MCF up to 70 % of the core radius $a = 13\,\mu\text{m}$ upon redirection by a flat TIR mirror with Surface S3, see Section 4.3.2 for a more detailed discussion of the launch conditions [230]. The distance between the apices of Surfaces S1 and S2 amounts to $d = 1150\,\mu\text{m}$, Fig. 4.2(c). We also connected a PD array to a MM-FA. At the Rx side, the refractive Surface S2 is designed to produce a MFD of $61\,\mu\text{m}$ half-way between the two FaML. The refractive Surface S1 on the PD is designed to focus the incoming beam to a spot with a MFD of $12\,\mu\text{m}$, well within the light-sensitive PD area, which has a diameter of $32\,\mu\text{m}$. As before, the distance between the apices of Surfaces S1 and S2 amounts to $d = 1150\,\mu\text{m}$.

### 4.3.1 Module assembly

As a first step of the assembly process, the VCSEL array and the PD array are mounted to the PCB next to the Tx and Rx driver IC. The FaML are then printed separately to the VCSEL / PD chips and to the facet of the MT ferrule using high-resolution multi-photon lithography [68]. Note that this sequence is not mandatory – the FaML can also be printed to the device facets on a wafer level, before mounting the devices to the PCB. The two printing steps are carried out using negative-tone photoresists with a refractive index $n = 1.54$ at $850\,\text{nm}$. Precise alignment of the FaML relative to the respective facet is ensured by machine vision. After exposure, the fabricated structures are developed in propylene-glycol-methyl-etheracetate (PGMEA) for $15$ minutes, flushed with isopropanol, and subsequently blow-dried. For more details on the fabrication technique, see Appendix B.3. Note that the FaML on the VCSEL / PD are fabricated from a photoresist (VanCore B,

Vanguard Automation GmbH), which is compatible with industry-standard reflow soldering processes and for which long-term stability has been experimentally confirmed in damp-heat tests at a temperature of $85\,°\text{C}$ and at a relative humidity of $85\,\%$, see Appendix B.4.

A custom pick-and-place machine is then used to mount the MT ferrule to the PCB in a fully automated process, relying solely on industry-standard camera-based machine vision and height measurements with a confocal chromatic imaging sensor (Precitec CHRocodile S [231]). During the assembly procedure and the associated measurements, the MT ferrule is gripped by an air-pressure activated tool (gripper), which features mechanical stops that keep the outer edges of the MT ferrule aligned. In addition, a cable management system included in our pick-and-place machine ensures that the fiber strands attached to the MT ferrule do not experience any strain. During the assembly process, the PCB is fixed to the assembly zone of the pick-and-place machine using a holder placed on a vacuum chuck. For alignment, we first detect the centers of the FaML belonging to the outermost VCSEL / PD channels and extract the connecting line. For improving the accuracy of the image recognition, the FaML on the VCSEL / PD are surrounded by a collar, see Fig. 4.2(b) and lower inset. The MT ferrule is then gripped by the air-pressure activated tool, and the line between the two 3D-printed marker holes, denoted M1 and M2 in Fig. 4.2(b), is extracted. In a next step, the MT ferrule is moved in $x$- and $y$-direction to align the connection M1–M2 to the formerly found connecting line defined by the VCSEL / PD FaML. The ferrule is then laterally shifted along the M1–M2 connection for positioning the upper FaML exactly vertically above the corresponding lower FaML. In doing so, we iteratively correct for any tilt of the fiber plane in relation to the plane on which the VCSEL / PD chips are mounted, until an angular tilt of the two planes by less than $0.1\,°$ is reached. Finally, the $z$-position of the MT ferrule is adjusted to the designed distance of $d = 1150\,\mu\text{m}$ between the FaML apices using the chromatic confocal imaging sensor. This final position is fixed by applying a low-shrinkage UV-curable epoxy glue to the four corners of the MT ferrule (EMI Optocast 3410 Gen2), Fig. 4.2(a). Until the glue is cured, we maintain the position of the MT ferrule by electronically stabilizing the height of the stage.

### 4.3.2 Alignment tolerance and coupling loss

Prior to applying the glue, we quantify the alignment tolerances by moving the MT ferrule in $x$- and $y$-direction or by introducing a known tilt angle $\varphi$. The tilt is defined with respect to a rotation axis R1 that is parallel to the $x$-axis and that passes through the mid-points between the corresponding FaML apices, see Fig. 4.2(c). Note that due to the strongly expanded spot size of the beams, the Rayleigh length is rather large (approx. 2 mm), such that misalignment along the beam direction ($z$-direction) does not impair the coupling efficiency to a significant degree. We confirmed this notion by repeating the alignment process 100 times and by comparing the positions from the passive and active alignment procedures [232]. We found that the $z$-position can be reproduced with a standard deviation of only 1.5 µm and a maximum error of 7 µm. The corresponding excess coupling loss amounts to less than 0.1 dB and can be safely neglected.

For measuring the coupling losses, we either let the VCSEL emit light into the central core of one of the four Tx MM-MCF, or we receive light from one of the MM-MCF cores by the associated PD. In the experiment, we measure the misalignment excess loss by comparison to loss measured in the optimum position. Note that the various modes of an MM fiber may experience vastly different propagation losses and that a reliable quantification of coupling losses should hence refer to a "steady-state" modal distribution that is reached in the limit of long propagation distances [230, 233]. Such a steady-state distribution of modal power can approximately be achieved by a so-called limited phase-space (LPS) launch [230]. In this approach, the fiber is fed by a multimode excitation field, having a Gaussian power distribution for which the $1/e^2$ diameter of the intensity profile corresponds to 70 % of the fiber-core diameter while the $1/e^2$ divergence angle is adjusted to 70 % of the maximum acceptance angle, which is found in the center of the core in case of graded-index MM fibers. In our experiment, it was not possible to simultaneously fulfill both requirements. In our lens design, we therefore adjusted the beam diameter to 70 % of the core diameter, while the acceptance cone was filled by more than 70 %. To arrive at a realistic estimate

of the coupling losses, we used a cladding-mode stripper consisting of a piece of fiber that was coiled around an approximately 20 mm-thick metal rod [234]. The power of the resulting steady-state modal power distribution was finally measured by an integrating sphere.

For active alignment of the MM-FA to the Tx VCSEL array, we estimate absolute coupling losses of $0.05$ dB, $0.25$ dB, $0.62$ dB, and $0.46$ dB for Channels 1, 2, 3, and 4 as defined in Fig. 4.2(b), respectively. This leads to an average coupling loss of $0.35$ dB with a standard deviation of $0.25$ dB. Note that this standard deviation is very likely overestimated: For quantifying the losses at the Tx side, we first measured the output power of the VCSEL array to obtain a baseline to which we can refer the fiber-coupled power levels. During these pre-characterization experiments, it was unfortunately not possible to individually measure the output power of each VCSEL in the Tx array. This problem was caused by an electronics-related issue that prevented us from individually switching the four VCSEL in the Tx array on and off. Since the VCSEL are closely spaced, we could hence only capture the overall power emitted by all four VCSEL, from which we calculate the average emission power per device. The reported loss variations hence contain the variations of the VCSEL output powers within the array, which are specified as $\pm 7.5$ % ($\pm 0.3$ dB) in the associated data-sheet [227]. The true variation of the FaML coupling efficiency is hence presumably below the measured $0.25$ dB.

In a next step, we measure the lateral misalignment excess loss related to the optimum position ($x = 0\,\mu$m, $y = 0\,\mu$m) for one of the four nominally identical FaML-based VCSEL-fiber connections of the Tx module, see Fig. 4.3(a). The absolute coupling loss of the displayed VCSEL-fiber connection, which corresponds to Channel 1 in Fig. 4.2(b), amounts to the above-mentioned $0.05$ dB, measured in the $0$ dB point of Fig. 4.3(a). White curves indicate the contour lines of constant loss. For a $1$ dB loss, a deviation of $\Delta x = \pm 17\,\mu$m in $x$-direction and of $\Delta y = \pm 13\,\mu$m in $y$-direction can be tolerated. The position obtained by the machine-vision-based automated passive assembly procedure is also indicated by a white cross in the first quadrant of Fig. 4.3(a) at ($x = 1\,\mu$m, $y = 5\,\mu$m), see white lettering "$\times$ passive". We attribute the larger positioning uncertainty along the $y$-direction to errors in measuring the tilt of the VCSEL bar about the $x$-axis.

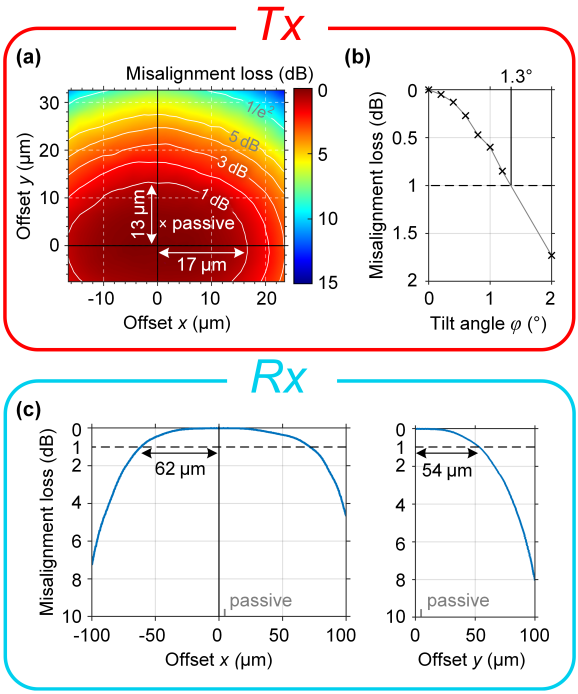


**Fig. 4.3:** Measured misalignment excess loss of a four-lane transmitter (Tx, VCSEL) and receiver (Rx, PD), where each device is coupled to a corresponding core of a MM-FA. We move the MT ferrule along the $x$- and $y$-direction, and we rotate it in $\varphi$-direction about the rotation axis R1, see Fig. 4.2(c). The excess loss is zero at the optimum position. Cladding-mode strippers are used to approximate a steady-state distribution of modal power within the MM fiber. **(a)** Excess loss for lateral misalignment measured for one of the four nominally identical FaML-based VCSEL-fiber connections at the Tx. White curves indicate the contour lines of constant loss. For a 1 dB loss, a deviation of $\Delta x = \pm 17\,\mu\text{m}$ in $x$-direction and of $\Delta y = \pm 13\,\mu\text{m}$ in $y$-direction can be tolerated. Using active alignment, the absolute coupling loss of the displayed VCSEL-fiber connection (Channel 1 in Fig. 4.2(b)) amounts to 0.05 dB, measured in the 0 dB point. The position obtained from automated passive assembly at ($x = 1\,\mu\text{m}$, $y = 5\,\mu\text{m}$) is indicated by a white cross ("passive"), leading to an excess loss of 0.15 dB. **(b)** Angular misalignment excess loss measured at the Tx by rotating the MT ferrule in $\varphi$-direction about axis R1 in Fig. 4.2(c). The angular 1 dB tolerance is 1.3°. **(c)** Lateral misalignment excess loss measured at the Rx for one of the four nominally identical FaML-based fiber-PD connections. For simplicity, we restrict our experiment to linear movements along the $x$-direction (left panel) and along the $+y$-direction (right panel). Note that the movement in $-y$-direction is restricted to avoid collision of the MT ferrule and the PD chip, see Fig. 4.2(c). For a 1 dB loss, a deviation of $\Delta x = \pm 62\,\mu\text{m}$ in $x$-direction and of $\Delta y = {}^{\pm}_{[}54\,\mu\text{m}$ in $y$-direction can be tolerated. The position obtained from automated passive assembly at ($x = 4\,\mu\text{m}$, $y = 4\,\mu\text{m}$) is indicated by grey tick labels ("passive"). The associated excess loss can be neglected. The absolute average coupling loss in the optimum position ($x = 0\,\mu\text{m}$, $y = 0\,\mu\text{m}$) amounts to 0.70 dB.

Note that the long side of the VCSEL bar is aligned along the $x$-direction, while the short axis is parallel to the $y$-direction, see Fig. 4.2(b). Since our tilt measurements rely on sampling the $z$-position of the chip surface with the confocal chromatic imaging sensor, we thus expect larger uncertainties for tilts about the long axis ($x$) as compared to tilts about the short axis ($y$). For an incorrectly compensated tilt about the $x$-axis, the emitted beam will hit the corresponding FaML on the fiber facet with a small offset in the $y$-direction, which is observed in our measurements shown in Fig. 4.3(a). Still, the automated passive alignment loss is well inside the 1 dB tolerance. To evaluate the angular alignment tolerance, we rotate the MT ferrule by the tilt angle $\varphi$ about the rotation axis R1, see Fig. 4.2(c). Note that the movement in $-\varphi$-direction was restricted to avoid collision of the MT ferrule and the VCSEL chip, see Fig. 4.2(c). The results are plotted in Fig. 4.3(b). The angular 1 dB tolerance is $1.3\,^{\circ}$.

In a next step of the experiment, we use passive alignment techniques, relying on the top- and bottom-view cameras of our assembly system and on the confocal chromatic imaging sensor (Precitec CHRocodile S [231]). We obtain a $0.15$ dB penalty for Channel 1 with respect to the actively aligned MM-FA, see Fig. 4.3(a), and we expect similar penalties for the other channels. This would lead to an average coupling loss of $0.50$ dB for all four channels.

These measured coupling losses and alignment tolerances can well compete with those obtained for more complex multi-step assembly techniques relying on precision molded plastic parts which were actively aligned to the underlying VCSEL array [202–204, 207, 209]. For active alignment, lateral 1 dB alignment tolerances of $\pm 17$ µm in combination with minimum coupling losses of $0.5$ dB have been demonstrated in [204]. In a similar experiment [209], the lateral 1 dB alignment tolerances were increased to $\pm 35$ µm at the expense of a slightly higher coupling loss of 1 dB. Note that the MM fibers used in our experiment have core diameters of only 26 µm – significantly smaller than the more standard core diameters of 50 µm, that have, e.g., been used in [209]. Using larger core diameters would further increase the alignment tolerances in our experiment. For passive alignment, our estimated average losses of $0.5$ dB can well compete with those obtained in previous demonstrations of coupling interfaces between VCSEL and

MM-FA [205], where losses down to $0.7\,\mathrm{dB}$ along with alignment tolerances of $\pm 18\,\mu\mathrm{m}$ have been reached for comparatively large core diameters of $62.5\,\mu\mathrm{m}$.

For measuring the coupling losses to the PD at the Rx side, we inject light into each of the central cores of the four Rx fibers and measure the power of the associated steady-state distribution after the mode stripper using an integrating sphere. The power incident on the PD is obtained from the respective photocurrents and the data-sheet specification of the responsivity $S$. For active alignment of the MM-FA to the Rx PD array, we measure absolute coupling losses of $0.63\,\mathrm{dB}$, $0.66\,\mathrm{dB}$, $0.77\,\mathrm{dB}$, and $0.72\,\mathrm{dB}$, leading to an average coupling loss of $0.70\,\mathrm{dB}$ with a relatively small standard deviation of only $0.06\,\mathrm{dB}$. The small variation of the losses is due to the fact that the active area of the Rx PD ($32\,\mu\mathrm{m}$ diameter) is much larger than the spot of the received beam, which is focused down to a diameter of $12\,\mu\mathrm{m}$ on the PD facet by the associated FaML.

We also measure the lateral misalignment excess loss for one of the four nominally identical FaML-based fiber-PD connections of the Rx module, see Fig. 4.3(c). For simplicity, we only perform one-dimensional movements of the MT ferrule along the $x$-direction (left panel) and along the $+y$-direction (right panel). Note that the movement in $-y$-direction was restricted to avoid collision of the MT ferrule and the PD chip, see Fig. 4.2(c). For a $1\,\mathrm{dB}$ loss, a deviation of $\Delta x = \pm 62\,\mu\mathrm{m}$ in $x$-direction and of $\Delta y = {}^{+}_{[-]}54\,\mu\mathrm{m}$ in $y$-direction can be tolerated, where the boundary for a movement to the $-y$-direction was estimated from its counterpart in $+y$-direction. The position obtained by the machine-vision-based passive assembly procedure is indicated at ($x = 4\,\mu\mathrm{m}$, $y = 4\,\mu\mathrm{m}$), see grey tick label "passive". Again, the automated passive alignment loss is well inside the $1\,\mathrm{dB}$ tolerance, and no penalty could be quantified within the measurement accuracy. These measured coupling losses and alignment tolerances are slightly worse than the $0.5\,\mathrm{dB}$ that have previously been demonstrated both for actively and for passively aligned interfaces between PD and MM-FA [205, 209], while the alignment tolerances are comparable.

We finally compare the performance of our approach to commercially available coupling schemes based on high-precision injection-molded plastic parts [207, 222]. The most prominent example is the PRIZM® LightTurn® [207, 221], which has become a widely used solution for coupling between fiber and device arrays with standard pitches of $250\,\mu m$. In terms of coupling losses, the $0.5\,dB$ (Tx) and the $0.7\,dB$ (Rx) demonstrated for our FaML-based passive assembly approach can well compete with the specified sub-$2\,dB$ losses of the PRIZM® LightTurn® [222]. The presumably overestimated standard deviations of $0.25\,dB$ (Tx) and $0.06\,dB$ (Rx) for the FaML-based approach also compares favorably with the standard deviation of $0.22\,dB$ (Tx) and $0.34\,dB$ (Rx) achieved with the PRIZM® LightTurn® [207]. In this context, it should be noted that the PRIZM® LightTurn® also requires precise alignment to ensure that the underlying socket is mounted to the PCB in the correct position with respect to the VCSEL / PD arrays. The alignment precision required in this step is related to the diameter of the beam at the corresponding VCSEL / PD facet, which is smaller than the beam diameter in the collimated free-space beam section between the FaML, dictating the alignment accuracy in the FaML approach. We hence believe that our approach can offer higher alignment tolerances along with comparable or lower losses, while offering a path towards parallel coupling to the individual cores of MCF, see next section.

Based on our experiments, indicating comparatively large alignment tolerances, we believe that coupling of larger fiber arrays to corresponding VCSEL or PD arrays should not represent a problem. These expectations are also supported by similar experiments that were performed with arrays of single-mode fiber (SMF) and single-mode waveguides [3, 235], which are much more sensitive to alignment errors. In these experiments [235], arrays of silicon photonic (SiP) waveguides with rather small mode-field diameters of the order of $2.5\,\mu m$ were coupled to arrays of SMF, equipped with FaML consisting of TIR mirrors and focusing lens surfaces. It was found that the resulting position variations of the generated beam foci were dominated by the position variations of the SMF cores within the underlying fiber array. Variations of the 3D-printed FaML did not play a significant role, indicating the precise alignment of the FaML to the respective fiber cores during the fabrication process.

## 4.4 Coupling of VCSEL / PD to multiple cores of an MCF

In a second set of experiments, we demonstrate the viability of our concept by connecting linear VCSEL and PD arrays to MM-MCF. The associated coupling scheme of Fig. 4.1(c) is displayed in more detail for the Tx in Fig. 4.4(a) and for the Rx in Fig. 4.4(b). In Figure 4.4(a), three Tx VCSEL are coupled to three MM-MCF cores of the Tx fiber labeled ❶, ❷, and ❸ that lie in a common $z$-normal plane. Figure 4.4(b) shows the corresponding coupling of three Rx PD to three cores of the Rx fiber, labelled ❹, ❺, and ❻. The outer FaML ❶ and ❸ on the VCSEL as well as the outer FaML ❹ and ❻ on the PD are tilted. Figure 4.4(c) and (d) display technical drawings of the Tx coupling scheme ❷ and of the Rx coupling arrangement ❺, respectively, in an $x$-normal plane. For the Tx, Fig. 4.4(c), the refracting Surface S1 collimates the VCSEL beam to a MFD of 28 µm, measured half-way between the two FaML. The entrance Surface S2 of the center FaML on the Tx MM-MCF is located at a distance $d = 525$ µm from the apex of the corresponding FaML on the VCSEL. Surface S2 is designed to reduce the MFD at the position of the TIR mirror S3 to 22 µm to avoid clipping due to the limited lateral size of the TIR mirror as dictated by the 39 µm pitch of the fiber cores. Refracting Surface S4 forms the beam such that the MM-MCF core is illuminated up to 70 % of the core radius $a = 13$ µm and up to 70 % of the numerical aperture of 0.21. This excitation approximates an LPS launch [230] such that, in combination with a cladding-mode stripper, an under-estimation of the coupling loss is avoided. For the Rx, Fig. 4.4(d), a TIR mirror S5 redirects the beam towards the PD. The exit Surface S6 of the FaML at the MCF collimates the beam to a MFD of 28 µm, measured again half-way between the two FaML, while the input Surface S7 of the FaML at the PD focuses the expanded beam to a spot with a MFD of 15 µm, significantly smaller than the diameter of 32 µm of the light-sensitive PD area. The apices of Surfaces S6 and S7 are again separated by $d = 525$ µm. Figure 4.4(e) shows a technical drawing of the FaML ❸ and ❻ in a $y$-normal plane. The VCSEL / PD beam is redirected by an angled Surface S0, designed for a beam tilt angle $\alpha = 14.6°$ with respect to the $z$-axis.

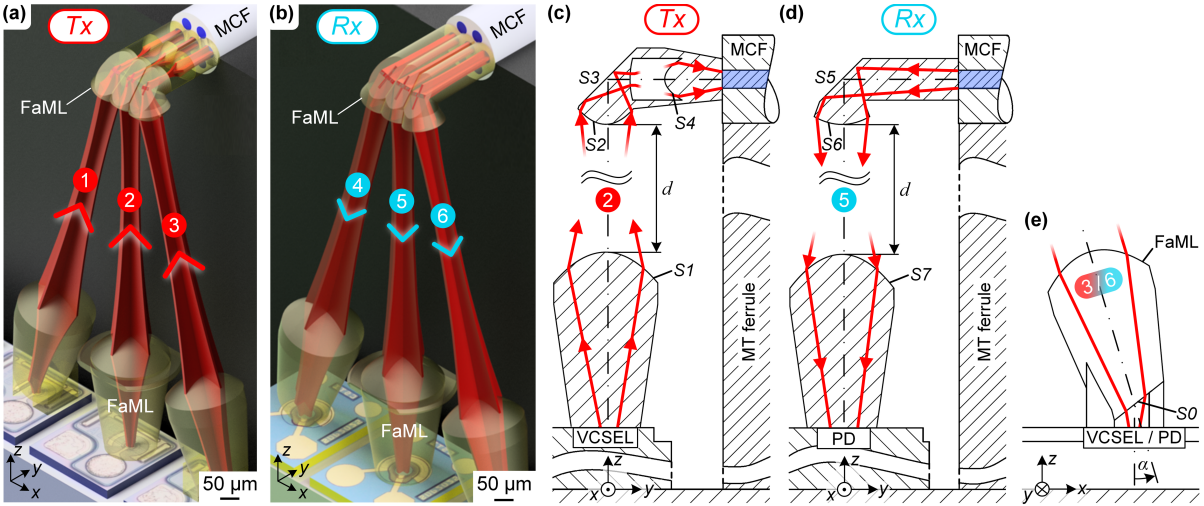


**Fig. 4.4:** Concept for coupling of VCSEL and PD arrays to MM-MCF as shown in Fig. 4.1(c) along with corresponding technical drawings. **(a)** Three VCSEL coupled to three MCF cores, labeled 1, 2, and 3, that lie in a common $z$-normal plane. **(b)** Three PD coupled to three cores of the Rx fiber, labelled 4, 5, and 6. **(c)** Technical drawing of the Tx coupling scheme 2. The refracting Surface S1 collimates the VCSEL beam. The entrance refracting Surface S2 of the FaML on the MCF is located at a distance $d = 525\,\mu\text{m}$. It reduces the MFD at the position of the TIR mirror S3 to avoid clipping that would occur due to the limited lateral size of the TIR mirror as dictated by the 39 µm pitch of the fiber cores. Refracting Surface S4 forms the beam for illuminating the MM-MCF core up to 70 % of the core radius, and up to 70 % of the numerical aperture for approximating an LPS launch [230]. **(d)** Technical drawing of the Rx coupling scheme 5. A TIR mirror S5 redirects the beam towards the PD. The exit Surface S6 of the FaML at the MCF collimates the beam, and Surface S7 at the entrance face of the FaML at the PD focuses the beam to a spot, significantly smaller than the diameter of the light-sensitive PD area. The apices of Surfaces S6 and S7 are again separated by $d = 525\,\mu\text{m}$. **(e)** Technical drawing of FaML 3 and 6 viewed in $y$-direction. The outer Tx FaML 1, 3 and the Rx FaML 4, 6 are tilted. The VCSEL / PD beam is directed by an angled Surface S0, designed for a beam tilt angle $\alpha = 14.6\,^\circ$ with respect to the $z$-axis.

A photograph of the transceiver module following the concept in Fig. 4.1(c) is depicted in Fig. 4.5(a). Figure 4.5(b) shows a close-up of three VCSEL / PD, each connected to three cores of a Tx / Rx MM-MCF, respectively. Inset (i) of Fig. 4.5(b) gives a magnified view of the FaML on the fiber facet containing TIR mirrors and beam-expander lenses. Inset (ii) of Fig. 4.5(b) depicts the FaML attached to the VCSEL array.

### 4.4.1 Module assembly

In contrast to the assemblies discussed in Section 4.3, where Tx and Rx fibers were mounted into separate MT ferrules, the MM-MCF scheme relies on a single MT ferrule that contains both the Tx and the Rx MCF, see Fig. 4.5(a). As a consequence, the VCSEL / PD arrays need to be mounted to the PCB collinearly with the correct pitch. Specifically, the distance between the center VCSEL and PD elements 2 and 5 needs to match the distance of 1750 µm between the central cores of the Tx and the Rx MM-MCF, see Fig. 4.5(b). Given the rather high positioning tolerances of the MM coupling interfaces, this step is well manageable using state-of-the-art pick-and-place equipment. Apart from this, the assembly process for the MM-MCF scheme relies on the same machine and is largely similar to the procedure used for the Tx and the Rx modules presented in Section 4.3.1. In a first step, we grip the MT ferrule and perform a tilt correction to align the plane defined by the fiber axes exactly parallel to the plane in which the PD and VCSEL arrays are mounted. We then use camera-based machine vision to detect the positions of the FaML at the Tx VCSEL 2 and Rx PD 5, exploiting a collar that surrounds the FaML to improve the accuracy of the image recognition, see Fig. 4.5(b). We then extract the connecting line between VCSEL 2 and PD 5 as a reference for aligning the MT ferrule. The MT ferrule is then moved in $x$- and $y$-direction for adjusting the line M1–M2 between the 3D-printed marker holes M1, M2 vertically above the connecting line between VCSEL 2 and PD 5, Fig. 4.5(b). For lateral alignment, we extract the mid-point of the connecting line between markers M1 and M3 to locate the position of the apex belonging to FaML 2 on the fiber side. This apex point is then laterally shifted along

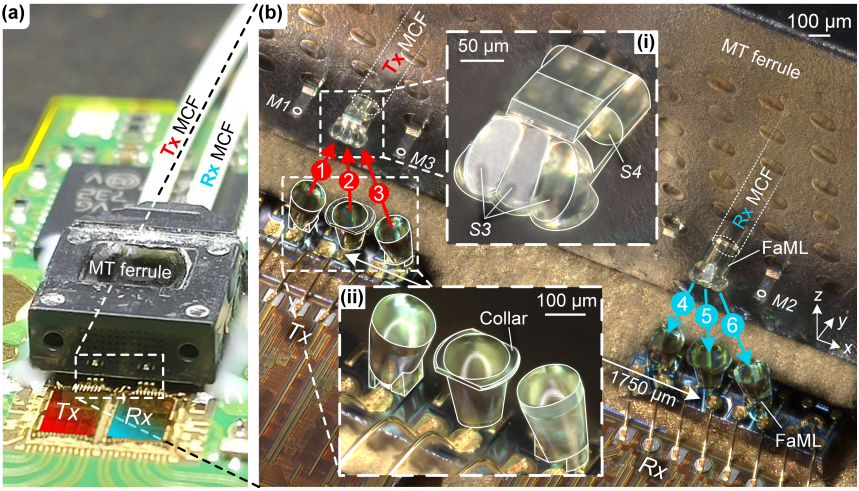


**Fig. 4.5:** Three-channel transceiver module implemented on a small form-factor pluggable PCB. Three Tx VCSEL 1, 2, and 3 and three Rx PD 4, 5, and 6 are connected to three cores of the associated MM-MCF. **(a)** Overview photograph corresponding to schemes illustrated in Fig. 4.4(a) and (b). **(b)** Micrograph of the optical couplers. Inset (i) gives a magnified view of the fiber-attached optical elements, see technical drawing in Fig. 4.4(c) for details. Inset (ii) depicts the expander lenses attached to the three VCSEL, and the "collar" supporting machine vision.

the M1–M3 connection to position it exactly vertically above the FaML on top of VCSEL 2. The $z$-position of the MT ferrule is then adjusted to provide the designed distance of $d = 525\,\mu\text{m}$ between the apices of the center FaML on VCSEL 2 and PD 5 and the corresponding apex on the MCF FaML, see Fig. 4.4(c) and (d). A low-shrinkage UV-curable epoxy glue (EMI Optocast 3410 Gen2) is used at the four corners of the MT ferrule to fix its final position.

### 4.4.2 Alignment tolerance and coupling loss

For quantifying the alignment tolerances, we repeat the experiments described in Section 4.3.2, where we move the MT ferrule in $x$- and $y$-direction prior to applying the glue. Note that due to the expanded spot size of the beams a precise alignment along the beam direction ($z$-direction) is again not required. By recording the

power in the three cores 1, 2, and 3 of the Tx MCF and by measuring the photocurrents of the three Rx PD 4, 5, and 6, we extract the respective excess loss at the Tx and Rx coupling interfaces for lateral displacements along the $x$- and $+y$-direction, see Fig. 4.6(a) and (c). The average optimum position maximizing the sum of the powers in all three Tx channels is at ($x = 0\,\mu\text{m}$, $y = 0\,\mu\text{m}$), and the excess losses of the individual Tx and Rx channels are indicated in relation to the loss of the respective channel found at this position. For a 1 dB excess loss for the Tx coupling, a deviation of $\Delta x = \pm 18\,\mu\text{m}$ in $x$-direction and of $\Delta y = {}^{+}_{[-]}13\,\mu\text{m}$ in $y$-direction can be tolerated, where the movement to negative $y$-coordinates was again restricted to avoid collision of the MT ferrule and the VCSEL chip, see Fig. 4.4(a), and where the boundary for a movement to the $-y$-direction was estimated from its counterpart in $+y$-direction. For passive alignment of the MT ferrule, we find offsets of $x = 1\,\mu\text{m}$ measured along the longer side of the VCSEL chip base and of $y = 4\,\mu\text{m}$ measured along the shorter side – these positions are again marked by the tick labels "passive" in Fig. 4.6(a) and (c). The offset along the $y$-direction is again larger than the offset along the $x$-direction, which we attribute to the fact that the tilt measurement of the VCSEL chip about its long axis is subject to higher uncertainties, see Section 4.3.2 for a more detailed discussion.

Using active alignment, the average power in the Tx MCF cores 1, 2, and 3 reaches $1.93\,\text{dBm}$ for a bias current of $3.3\,\text{mA}$ applied to the VCSEL. This corresponds to an absolute average coupling loss of $0.67\,\text{dB}$. We estimate absolute coupling losses of $1.38\,\text{dB}$, $-0.16\,\text{dB}$, and $0.93\,\text{dB}$ for VCSEL 1, 2, and 3 as defined in Fig. 4.5(b), using again the average VCSEL emission power as a reference. This leads to the reported average coupling loss of $0.67\,\text{dB}$ with a standard deviation of $0.79\,\text{dB}$. We attribute the again rather high standard deviation as well as the unphysical negative dB-value of the coupling efficiency for VCSEL 2 to the fact that the reported coupling efficiencies are subject to the unknown variations of the underlying VCSEL emission powers, which could not be measured individually, see Section 4.3.2 for a more detailed explanation. Note also that the outer connections 1 and 3 require one additional lens Surface S0 for redirection of the beams, see Fig. 4.4(e), which is a possible reason for the increased loss compared to the central connection 2.

For the automated passive alignment of our assembly, we measure an average power of $1.59\,\mathrm{dBm}$, which corresponds to an average coupling loss of $1.0\,\mathrm{dB}$. The absolute coupling losses for the individual VCSEL-MCF connections amount to $1.55\,\mathrm{dB}$, $0.16\,\mathrm{dB}$, and $1.46\,\mathrm{dB}$ for VCSEL ❶, ❷, and ❸, respectively, taking again the average VCSEL emission power as a reference. The passive alignment penalties for the individual channels hence amount to $0.17\,\mathrm{dB}$ for VCSEL ❶, to $0.32\,\mathrm{dB}$ for VCSEL ❷, and to $0.53\,\mathrm{dB}$ for VCSEL ❸, leading to an average penalty of $0.33\,\mathrm{dB}$.

For measuring the absolute losses of the Rx PD, we use an MCF connector to inject a known power into the three relevant cores of the Rx MCF and measure the photocurrents of the respective Rx PD. The photocurrents are translated into optical power levels using the data-sheet specification of the responsivity $S$. For a $1\,\mathrm{dB}$ excess loss, a deviation of $\Delta x = \pm 23\,\mu\mathrm{m}$ in $x$-direction and of $\Delta y = {}^{+}_{[-]}25\,\mu\mathrm{m}$ in $y$-direction can be tolerated, where the movement to negative $y$-coordinates was again restricted to avoid collision of the MT ferrule and the PD chip, see Fig. 4.4(b), and where the boundary for a movement to the $-y$-direction was estimated from its counterpart in $+y$-direction. The position-dependent excess losses for the three channels ❹, ❺, and ❻ exhibit plateaus due to the fact that the $15\,\mu\mathrm{m}$ spot size generated by the FaML on the PD surface is smaller than the $32\,\mu\mathrm{m}$ diameter of the active PD area. The excess losses of the three Rx channels shown in Fig. 4.6(c) are again measured with respect to the absolute loss of the respective channel found at the optimum coupling position ($x = 0\,\mu\mathrm{m}$, $y = 0\,\mu\mathrm{m}$). The coupling losses of the individual MCF-PD connections at this position amount to $1.32\,\mathrm{dB}$ for PD ❹, to $0.40\,\mathrm{dB}$ for PD ❺, and to $0.30\,\mathrm{dB}$ for PD ❻, leading to an average coupling loss of $0.63\,\mathrm{dB}$ with a standard deviation of $0.56\,\mathrm{dB}$. For the automated passive alignment of our assembly, no penalty could be quantified within the measurement accuracy. This leads to equal coupling losses for the optimum Tx position ($x = 0\,\mu\mathrm{m}$, $y = 0\,\mu\mathrm{m}$) and for the passively aligned position, indicated again by tick marks "passive", see Fig. 4.6(c).

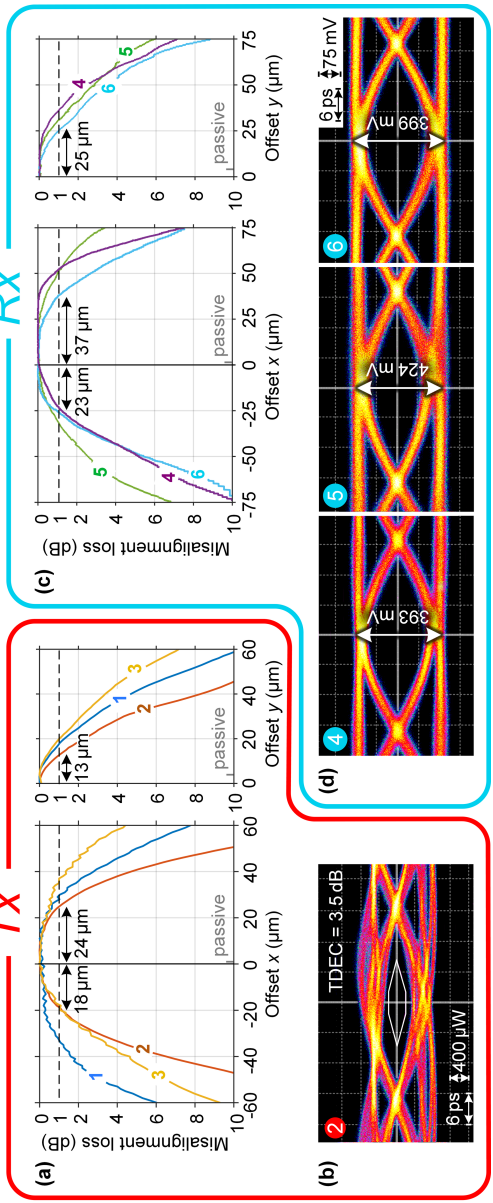


**Fig. 4.6:** (Caption next page.)

**Fig. 4.6:** Alignment tolerances and eye diagrams of a three-lane transmitter (Tx, VCSEL) ❶, ❷, and ❸, and a three-lane receiver (Rx, PD) ❹, ❺, and ❻, each lane coupled to one of three cores of a MCF, Fig. 4.4. We extract the respective excess loss at the Tx and Rx coupling interfaces for lateral displacements along the $x$- and $+y$-direction. The average optimum position maximizing the sum of the powers in all three Tx channels is at ($x = 0\,\mu\text{m}$, $y = 0\,\mu\text{m}$), and the excess losses of the individual Tx and Rx channels are indicated in relation to the loss of the respective channel found at this position. The excess loss for an automated passive assembly is indicated by the tick labels "passive". **(a)** Lateral misalignment excess loss measured at the Tx for the three FaML-based VCSEL-MCF connections. For simplicity, we restrict our experiment to linear movements along the $x$-direction (left panel) and along the $+y$-direction (right panel). For a 1 dB excess loss, a deviation of $\Delta x = \pm 18\,\mu\text{m}$ in $x$-direction and of $\Delta y = {}^{+}_{[-]}13\,\mu\text{m}$ in $y$-direction can be tolerated. Note that the movement to negative $y$-coordinates was restricted to avoid collision of the MT ferrule and the VCSEL / PD chip, Fig. 4.4(c) and (d), and that the boundary for a movement to the $-y$-direction was therefore estimated from its counterpart in $+y$-direction. The average excess loss for passive automated assembly at ($x = 1\,\mu\text{m}$, $y = 4\,\mu\text{m}$) is 0.33 dB. At the optimum position, we measure an absolute average coupling loss of 0.67 dB for the three Tx MCF cores ❶, ❷, and ❸. For the automated passive alignment, the absolute average coupling loss amounts to 1.0 dB. **(b)** Characterization of the Tx with on-off-keying (OOK) signals (PRBS31) at line rates of 25.78125 Gbit/s, which are coupled to the Tx driver IC, see Fig. 4.5. Each VCSEL is operated at a bias current of 3.3 mA and a peak-to-peak modulation current of 4 mA. The optical output from cores ❶, ❷, and ❸ of the Tx fiber is sent to a sampling oscilloscope. As an example, we show the eye diagram measured from Tx core ❷ while the two other Tx VCSEL ❶ and ❸ are in operation. The transmitter-and-dispersion eye-closure (TDEC) penalty is 3.5 dB, and an extinction ratio of 3.7 dB is measured. **(c)** Lateral misalignment excess loss measured at the Rx for the three FaML-based MCF-PD connections. For simplicity, we restrict our experiment to linear movements along the $x$-direction (left panel) and along the $+y$-direction (right panel). For a 1 dB excess loss, a deviation of $\Delta x = \pm 23\,\mu\text{m}$ in $x$-direction and of $\Delta y = {}^{+}_{[-]}25\,\mu\text{m}$ in $y$-direction can be tolerated, where the boundary for a movement to the $-y$-direction was again estimated from its counterpart in $+y$-direction. The position-dependent excess losses for the three channels ❹, ❺, and ❻ exhibit plateaus due to the fact that the 15 µm spot size generated by the FaML on the PD surface is smaller than the 32 µm diameter of the active PD area. As a consequence, the measured absolute average loss of the three Rx channels amounts to 0.63 dB both for the optimum Tx position at ($x = 0\,\mu\text{m}$, $y = 0\,\mu\text{m}$) and for the passively aligned position, indicated again by tick marks "passive". **(d)** Characterization of the Rx with OOK signals at a line rate of 25.78125 Gbit/s. The signal from an optical transmitter with known specifications is fed to the three cores ❹, ❺, and ❻ of the Rx MCF, detected by the Rx PD, and the output signals of the Rx driver IC are recorded by a sampling oscilloscope. The eye diagrams for Rx ❹, ❺, and ❻ are shown, indicating the peak-to-peak voltage of the corresponding receiver.

To the best of our knowledge, these experiments represent the first demonstration of a coupling interface that connects individual cores of an MCF to VCSEL / PD arranged in a standard linear array without the need for additional fiber-based or waveguide-based fan-out structures. Other approaches relying on custom device arrays in 2D arrangements matched to the cross-section of the respective MCF have been pursued [214–218]. Such demonstrations, however, still rely on active alignment, leading, e.g., to minimum coupling losses of $0.98$ dB between VCSEL and a seven-core MM-MCF [217]. These losses are slightly higher than the $0.67$ dB and the $0.63$ dB achieved by active alignment in our experiments for the Tx and Rx, respectively, and our passively assembled module can still well compare to these losses – besides avoiding non-standard device arrangements that are adapted to the cross section of the respective MCF. It should be noted that coupling schemes based on custom device arrays require a generally denser spacing of the VCSEL / PD compared to the traditional $250$ µm pitch, which may limit the high-speed performance of the devices due to higher temperatures [215].

Using FaML-based free-space fan-out schemes to address the individual cores of an MCF can also open a path towards connecting two-dimensional VCSEL or PD arrays to one-dimensional arrays of MCF. We believe that this approach has the potential to greatly increase the number of parallel channels per transceiver, while maintaining the fiber installations manageable. For the present work, such a demonstration was not possible due to the lack of 2D arrays of VCSEL and PD and of associated read-out electronics that can individually address the various devices in such a matrix.

### 4.4.3 Data-transmission experiments

To demonstrate the viability of the presented concept, the assembled $3 \times 25$ Gbit/s transceiver module was characterized by measuring the transmitter-and-dispersion eye-closure (TDEC) penalty, the Tx power per lane, the optical modulation amplitude (OMA), the extinction ratio, and the Rx power per lane – similar to the

procedures described in the IEEE 802.3 industry standard [161]. In-detail explanations of these metrics can be found in Appendix C. To this end, we use the SFP interfaces on the PCB to feed the Tx driver IC with three on-off-keying (OOK) signals at a line rate of 25.78125 Gbit/s. The drive signals were derived from a pseudorandom binary sequence of length $2^{31}-1$ (PRBS31). We set the bias current of the VCSEL to 3.3 mA and use a current modulation of $\pm 2$ mA, i.e., a peak-to-peak swing of 4 mA, for the OOK signals. The optical output from cores ❶, ❷, and ❸ of the Tx fiber, see Fig. 4.5, is sent to a sampling oscilloscope. Figure 4.6(b) shows an exemplary eye diagram measured from Tx core ❷ with the two other Tx VCSEL ❶ and ❷ in operation. We also evaluated the optical crosstalk by measuring the power coupled from Tx VCSEL ❶ to, e.g., Tx core ❷. All such experiments lead to negligible power readings in the "unwanted" Tx cores, indicating that the optical crosstalk was below our measurement sensitivity. From the recorded eye diagram, a TDEC of 3.5 dB is found, which is clearly below the maximum value of 4.3 dB specified for 100GBASE-SR4 transceivers in the IEEE 802.3 standard [161]. The average Tx power amounts to 1.56 mW (1.9 dBm) while an OMA of 1.35 mW (1.1 dBm) is measured – both of these values are well within the respective range specified in the IEEE 802.3 standard [161]. From these numbers, we extract a ratio of the OMA to the TDEC of 0.58 mW or $-2.4$ dBm, which is well above the minimum value of –7.3 dBm specified for the "launch power in OMA minus TDEC"-parameter in the IEEE 802.3 standard [161]. Finally, an extinction ratio of 3.7 dB and an average off-state transmitter power of –36 dBm are measured, which also fulfill the requirements imposed by the IEEE 802.3 standard [161].

For the receiver characterization, the signal from an optical transmitter with known specifications is fed to the three cores ❹, ❺, and ❻ of the Rx MCF. The signal is then detected by the PD, and the output signals of the Rx driver IC are recorded by a sampling oscilloscope. Figure 4.6(d) shows the eye diagrams for Rx ❹, ❺, and ❻, indicating the peak-to-peak voltage of the corresponding receiver. The average received power per lane amounts to 1.07 mW, 1.39 mW, and 1.18 mW, again fulfilling the respective specification of the IEEE 802.3 standard [161].

## 4.5 Summary

We demonstrate that 3D-printed facet-attached microlenses (FaML) open an attractive path for connecting multimode fiber arrays (MM-FA) as well as individual cores of multimode multicore fibers (MM-MCF) to standard arrays of vertical-cavity surface-emitting lasers (VCSEL) or photodiodes (PD) with pitches of $250\,\mu m$. The FaML, which can be printed by high-precision multi-photon lithography directly on the device and fiber facets, are designed to collimate the associated beams to large diameters of tens of micrometers, thereby greatly relaxing alignment tolerances in both the transverse and axial direction. To demonstrate the viability of the proposed concepts, we further perform a series of proof-of-concept experiments using a custom pick-and-place machine to mount the FaML-equipped fiber arrays to the PCB in a fully automated process, controlled by machine vision and height measurements. Using active alignment, we show connections between VCSEL / PD arrays and MM-FA, achieving average coupling losses as low as $0.35\,dB$ for the Tx and $0.70\,dB$ for the Rx along with lateral $1\,dB$ alignment tolerances of $\pm 17\,\mu m$ (Tx) and $\pm 62\,\mu m$ (Rx), respectively. When using the machine-vision based passive alignment process, we demonstrate average coupling losses of $0.50\,dB$ (Tx) and $0.70\,dB$ (Rx). To the best of our knowledge, these results are among the lowest losses and the highest alignment tolerances so far demonstrated for coupling between VCSEL / PD arrays and MM-FA. We further connect a linear VCSEL / PD array to distinct cores of a single MCF. When using active alignment, we achieve average coupling losses of $0.67\,dB$ (Tx) and $0.63\,dB$ (Rx) along with lateral $1\,dB$ alignment tolerances of $\pm 18\,\mu m$ (Tx) and $\pm 25\,\mu m$ (Rx), respectively. Using the machine-vision based passive alignment process, we achieve average coupling losses of $1.0\,dB$ (Tx) and $0.63\,dB$ (Rx). To the best of our knowledge, these experiments represent the first demonstration of a coupling interface that connects individual cores of an MCF to VCSEL / PD arranged in a standard linear array without the need for additional fiber-based or waveguide-based fan-out structures. Using this approach, we finally built a $3 \times 25\,Gbit/s$ transceiver assembly which fits into a small form-factor pluggable module and which fulfills many performance metrics specified in the IEEE 802.3

standard. We believe that 3D-printed FaML could pave a path towards highly scalable transceiver assemblies that exploit readily available VCSEL and PD arrays in combination with parallel transmission through multimode multicore fibers without the need for expensive multi-step assembly procedures or technically complex fan-out structures.

*[End of paper [J3]]*

# 5 Freeform terahertz structures fabricated by multi-photon lithography and metal coating

This chapter introduces and experimentally demonstrates a novel approach that allows to leverage multi-photon lithography for fabricating high-performance millimeter-wave (mmW) and terahertz (THz) structures that offer hitherto unachieved functionalities. This includes ultra-broadband chip-chip interconnects bridging the gap between electrical transmission lines on different planar substrates, cost-effective probe tips of unprecedented shape fidelity that lend themselves to testing of mmW and THz integrated circuits, and antennas that are raised above the underlying high-index substrate for increased radiation efficiency.

The approaches and experiments were conceived by Alexander Kotz, Joachim Hebeler, Tobias Harter, Christian Koos, and the author. The author developed the lithography techniques and processes required for fabrication of the 3D-printed metal-coated freeform structures. The THz devices were designed by the author with the support of Alexander Kotz, Christian Benz, and Tobias Harter. Alexander Quint supported the manufacturing of the transmission lines using the laser ablation system. Alexander Quint and Marius Kretschmann supported the measurement of the dielectric response of the photoresist. The THz assemblies were fabricated by the author, with support of Qiaoshuang Zhang for the inkjet-printing of the PMMA layers. The author performed the experimental characterization of the THz assemblies and analyzed the data, with support of Alexander Kotz, Joachim Hebeler, Thomas Zwick, and Christian Koos. All authors analyzed the results and discussed the data. The project was supervised by Sebastian Randel, Uli Lemmer,

Wolfgang Freude, Thomas Zwick, and Christian Koos. The author wrote the manuscript with support by Wolfgang Freude and Christian Koos.

The chapter is taken from a preprint [J4], that has been submitted for publication in a scientific journal. The manuscript is partially based on a conference contribution [C4] to OFC 2024. The material from the manuscript has been adapted to comply with the layout and the structure of this thesis. Further supplementary information can be found in Appendix D.

*[Beginning of paper [J4].]*

**Freeform terahertz structures fabricated by multi-photon lithography and metal coating**

Pascal Maier[1,2], Alexander Kotz[1,2], Joachim Hebeler[3], Qiaoshuang Zhang[4], Christian Benz[1,2], Alexander Quint[3], Marius Kretschmann[3], Tobias Harter[1], Sebastian Randel[1], Uli Lemmer[4], Wolfgang Freude[1], Thomas Zwick[3] & Christian Koos[1,2,5]

[1] Institute of Photonics and Quantum Electronics (IPQ), Karlsruhe Institute of Technology (KIT), Engesserstr. 5, 76131 Karlsruhe, Germany.

[2] Institute of Microstructure Technology (IMT), Karlsruhe Institute of Technology (KIT), Hermann-von-Helmholtz Platz 1, 76344 Eggenstein-Leopoldshafen, Germany.

[3] Institute of Radio Frequency Engineering and Electronics (IHE), Karlsruhe Institute of Technology (KIT), Engesserstr. 5, 76131 Karlsruhe, Germany.

[4] Light Technology Institute (LTI), Karlsruhe Institute of Technology (KIT), Engesserstr. 13, 76131 Karlsruhe, Germany.

[5] Vanguard Automation GmbH, Gablonzer Str. 10, 76185 Karlsruhe, Germany.

Direct-write multi-photon laser lithography (MPL) combines highest resolution on the nanoscale with essentially unlimited 3D design freedom. Over the previous years, the groundbreaking potential of this technique has been demonstrated in various application fields, including micromechanics, material sciences, microfluidics, life sciences as well as photonics, where *in-situ* printed optical coupling

elements offer new perspectives for package-level system integration. However, millimeter-wave (mmW) and terahertz (THz) devices could not yet leverage the unique strengths of MPL, even though the underlying devices and structures could also greatly benefit from 3D freeform microfabrication. One of the key challenges in this context is the fact that functional mmW and THz structures require materials with high electrical conductivity and low dielectric losses, which are not amenable to structuring by multi-photon polymerization. In this work, we introduce and experimentally demonstrate a novel approach that allows to leverage MPL for fabricating high-performance mmW and THz structures that offer hitherto unachieved functionalities. Our concept exploits *in-situ* printed polymer templates that are selectively coated through highly directive metal deposition techniques in combination with precisely aligned 3D-printed shadowing structures. The resulting metal-coated freeform structures (MCFS) offer high surface quality in combination with low dielectric losses and conductivities comparable to bulk material values while lending themselves to *in-situ* fabrication on planar mmW and THz circuits. We experimentally show the viability of our concept by demonstrating a series of functional THz structures such as ultra-broadband chip-chip interconnects, THz probe tips, and suspended THz antennas. We believe that our approach offers disruptive potential in the field of mmW and THz technology and may unlock an entirely new realm of laser-based 3D manufacturing.

## 5.1 Introduction

Functional terahertz (THz) structures crucially rely on precisely defined three-dimensional (3D) freeform geometries that combine highly conducting metal elements with low-loss dielectrics. Geometrical precision can be achieved by direct-write multi-photon laser lithography (MPL) [57, 68], offering highest resolution on the sub-micrometer scale along with precise alignment of the fabricated structures with respect to existing circuitry on the underlying substrate. These advantages have been extensively exploited in the realm of photonic integration [39], where 3D-printed waveguides, so-called photonic wire bonds (PWB) [J1, 40, 41, 236],

or facet-attached microlenses (FaML) [3, J5] offer interesting perspectives for scalable fully automated assembly of hybrid multi-chip systems. Transferring these concepts to THz assemblies, however, has so far been hindered by the lack of microfabrication techniques that can complement 3D-printed polymeric base structures by precisely defined highly conductive metal elements [39, 237–239]. Specifically, while two-photon-induced reduction of metal salts has been exploited to generate free-standing 3D metal structures [240, 241] or to decorate the surfaces of 3D-printed polymer structures with local silver [242–244] or platinum [239] lines, the resulting surface quality and the conductivity of the metal parts are still insufficient for low-loss millimeter-wave (mmW) or THz devices. Similar chemical reaction mechanisms can be used for fabricating gold-containing nanocomposite structures with 3D freeform shapes [245]. However, the achievable electrical conductivity is limited by the metal loading, which is generally dictated by the solubility of the metal ions [238] in the respective photoresist. Moreover, when the incident laser beam irradiates already fabricated metal structures during printing, thermal effects and localized surface plasmon resonances can lead to aggregation and crystallization of metal nanoparticles, rendering these processes hard to control. It should also be noted that all the aforementioned techniques have so far been limited to a rather small selection of metals such as silver [62, 240, 242–244, 246–249], gold [241, 245, 250–253], palladium [249, 254, 255], and platinum [62, 239, 254]. On the other hand, a combination of physical vapor deposition (PVD) techniques and subsequent electroplating of the PVD seed layer has been used for globally covering 3D-printed polymer templates with highly conductive metal coatings [256–258]. However, this concept has mainly been limited to bulky stand-alone hollow-core waveguides [256] or horn antennas [257, 258] and often requires additional mechanical assembly steps [257] to produce functional mmW or THz elements. Localized metal coatings can be fabricated on 3D-printed polymer templates by means of chemical surface functionalization followed by electro-less plating [242, 259, 260], but this approach often suffers from poor coating homogeneity and rather low conductivity of the fabricated metal structures [237] and is hence not well suited for high-performance mmW or THz elements.

In this paper, we introduce and experimentally demonstrate a novel concept for fabricating precisely defined mmW and THz structures that combine low-loss dielectrics and highly conductive metal elements in a well-defined 3D freeform geometry. Our concept exploits in-situ printed polymer support structures that are selectively coated through highly directive metal deposition techniques in combination with precisely aligned 3D-printed shadowing structures. The resulting metal-coated freeform structures (MCFS) offer high surface quality in combination with conductivities comparable to bulk material values and do not require any manual assembly steps. We demonstrate the viability of the concept in a series of experiments. In the first set of experiments, we use our approach to demonstrate THz interconnects that bridge the gap between transmission lines located on different substrates and that offer 3 dB-bandwidths exceeding $0.33$ THz. In a second set of experiments, we show that the vast design freedom offered by our fabrication technique can be leveraged for cost-effective THz probe tips that allow highly repeatable contacting over many probing cycles with 3 dB-bandwidths exceeding $0.19$ THz and with $6$ dB-bandwidths far beyond the $0.33$ THz range of our measurement system. A third set of experiments is finally dedicated to THz antennas, which are suspended from the underlying high-index substrate for better radiation efficiency. At a frequency of $0.27$ THz, a maximum realized gain of $5.5$ dBi in the direction perpendicular to the substrate is measured. The presented proof-of-principle experiments demonstrate the vast potential offered by the proposed fabrication technique. Our concept offers unprecedented design freedom and is widely applicable to a rich variety of use cases, thereby paving a path towards advanced mmW and THz systems in communications [261], sensing [262], or ultra-broadband signal processing [52].

## 5.2 Concept

An example of a THz system that exploits 3D-printed functional elements is illustrated in Fig. 5.1. The example depicted in Fig. 5.1(a) combines an optoelectronic signal source, relying on a photonic integrated circuit (PIC) with a balanced pair of high-speed photodetectors, with a subsequent amplifier, based

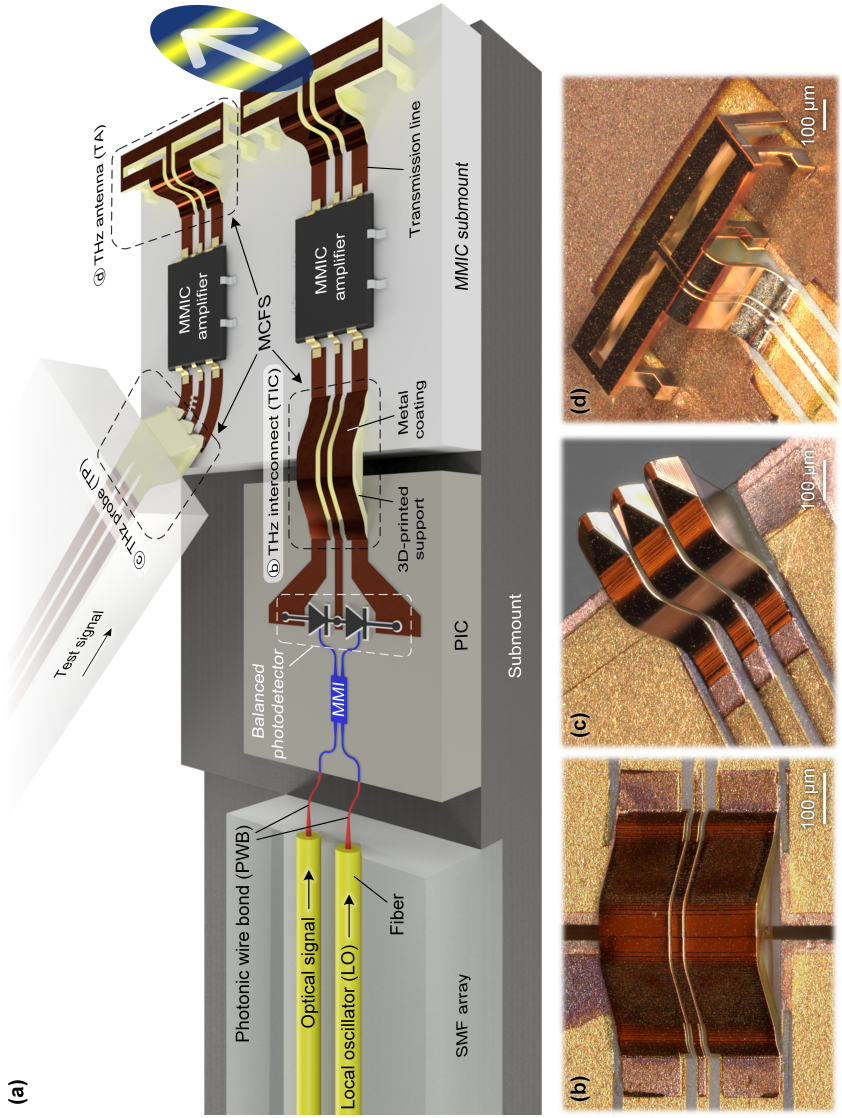


**Fig. 5.1:** (Caption next page.)

**Fig. 5.1:** Concept of a THz system exploiting 3D-printed functional elements based on metal-coated freeform structures (MCFS). **(a)** The system combines an optoelectronic signal source, relying on a balanced pair of high-speed photodetectors that are part of a photonic integrated circuit (PIC), with a subsequent THz amplifier, which is based on a monolithic microwave integrated circuit (MMIC), and a THz antenna, which is suspended from the surface of the underlying substrate for efficient emission to the surface-normal direction. The THz chip-chip interconnect between the PIC and MMIC as well as the suspended THz antenna are implemented as metal-coated freeform structures (MCFS). Each MCFS consists of a 3D-printed polymeric support that is locally coated with metal layers offering high bulk conductivity along with good surface quality. The same concept can be used to implement THz probes with unprecedented shape fidelity that lend themselves to testing of mmW and THz integrated circuits, see upper part of the figure. The polymeric support structures of the various MCFS are fabricated using high-resolution multi-photon lithography and can thus be efficiently combined with 3D-printed optical connections such as photonic wire bonds (PWB). **(b)** Micrograph of a THz interconnect (TIC) bridging the gap between coplanar waveguide transmission lines on different THz substrates. **(c)** Micrograph of a THz probe (TP) that is turned upside down for better visibility. **(d)** Micrograph of a THz antenna (TA) that is suspended from the underlying high-index substrate for increased radiation efficiency.

on a monolithic microwave integrated circuit (MMIC), and a THz antenna, which is suspended from the surface of the underlying substrate for efficient emission to the surface-normal direction. The balanced photodetectors are co-integrated with other functional photonic structures such as multi-mode-interference (MMI) couplers that are fed with an optical signal and an optical local-oscillator (LO) tone supplied by an array of single-mode fibers (SMF). The THz chip-chip interconnect between the PIC and MMIC as well as the suspended THz antenna are implemented as metal-coated freeform structures (MCFS). Each MCFS consists of a 3D-printed polymeric support that is locally coated with metal layers offering high bulk conductivity along with mmW-grade surface quality. The same concept can be used to implement THz probes with unprecedented shape fidelity that lend themselves to testing of mmW and THz integrated circuits, see upper part of Fig. 5.1(a). The polymeric support structures of the various MCFS are fabricated using high-resolution multi-photon lithography (MPL) and can thus be efficiently combined with 3D-printed optical connections such as photonic wire bonds (PWB). The viability of the concept shown in Fig. 5.1(a) is demonstrated in a series of proof-of-concept experiments — a selection of fabricated MCFS-based functional THz structures is shown in Fig. 5.1(b), (c), and (d). More specifically, Fig. 5.1(b) shows a THz interconnect (TIC) bridging the gap between coplanar waveguide (CPW) transmission lines on different THz substrates, Fig. 5.1(c) shows a THz probe (TP) that is turned upside down for better visibility, and Fig. 5.1(d) shows a THz antenna (TA) that is suspended from the underlying high-index substrate for increased radiation efficiency.

The fabrication of the MCFS relies on a dedicated multi-step process that is illustrated in Fig. 5.2. The process steps are shown exemplarily for the fabrication of a TIC, see Fig. 5.1(b). In a first step, two substrates with prefabricated planar THz structures such as CPW are coarsely placed to face each other with a gap in-between, see Fig. 5.2(a). As a basis for later directive metal coating, illustrated in Fig. 5.2(d), support and shadowing structures are 3D-printed using *in-situ* direct-write MPL, see Fig. 5.2(b). The structures are designed to support a metal layer which connects smoothly to the CPW on each substrate and comprise isolation trenches with undercut sidewalls to separate the deposited ground-signal-

ground (GSG) metal strips, see Insets in Fig. 5.2(b) and (d). For protecting the planar THz structures during the global metal deposition, the associated areas of the substrates are temporarily covered by a poly(methyl methacrylate) (PMMA) film using inkjet printing [263], Fig. 5.2(c). At the transitions between the PMMA-covered planar substrates and the 3D freeform polymeric support, additional 3D-printed shadowing structures are used to prevent short circuits. These shadowing structures, which are shaded in blue in Fig. 5.2(b)-(e), take the form of multiple arm-like roofs which locally prevent metal deposition, thereby defining isolating regions that separate the metal strips of the GSG transmission line and that seamlessly transition to the isolation trenches of the adjacent 3D support structure. Inset Ⓣ in Fig. 5.2(c) provides a top-view on one side of the support structure with the corresponding shadowing structures above — the isolation regions protected from metal deposition are shaded in blue. The shadowing structures are built upon a box-like hollow base, which acts as a flow-stop preventing inkjet-printed PMMA from wetting the entire support structure. In a next step, a highly directed physical vapor deposition (PVD) process is used to deposit metal along a surface-normal direction, see Fig. 5.2(d), thereby forming highly conductive layers on all surfaces with direct line of sight to the evaporation source. After metal deposition, the sacrificial PMMA layer is dissolved, thereby lifting off the unwanted metal areas, see Fig. 5.2(e). As a last step, the 3D-printed shadowing structures can be removed mechanically, leaving the final MCFS as shown in Fig. 5.2(f).

More details on the processes and the design considerations of the structures can be found in the Methods Section 5.5 and in Appendix D.2. Specifically, the width of the signal and ground conductors $w_{\mathrm{S}}$ and $w_{\mathrm{G}}$, as well as the associated distance $d_{\mathrm{SG}}$ of the TIC-based CPW were chosen to provide a desired line impedance of, e.g., $50\,\Omega$ along the entire TIC structure. To this end, the dimensions of the 3D-printed freeform support structure and the associated isolation trenches can be continuously varied along the propagation path of the signal, e.g., by continuously adapting the width of the gaps $w_{\mathrm{gap}}$, which defines the distance $\approx d_{\mathrm{SG}}$ between the signal and ground conductors at the respective height $h$, see Inset in Fig. 5.2(b) and (d). The metal residues which are deposited at the ground of the isolation trenches, see Inset in Fig. 5.2(d), do not influence the characteristics of the MCFS-based TIC if the undercuts are designed to offer sufficient depth $d_{\mathrm{it}}$.

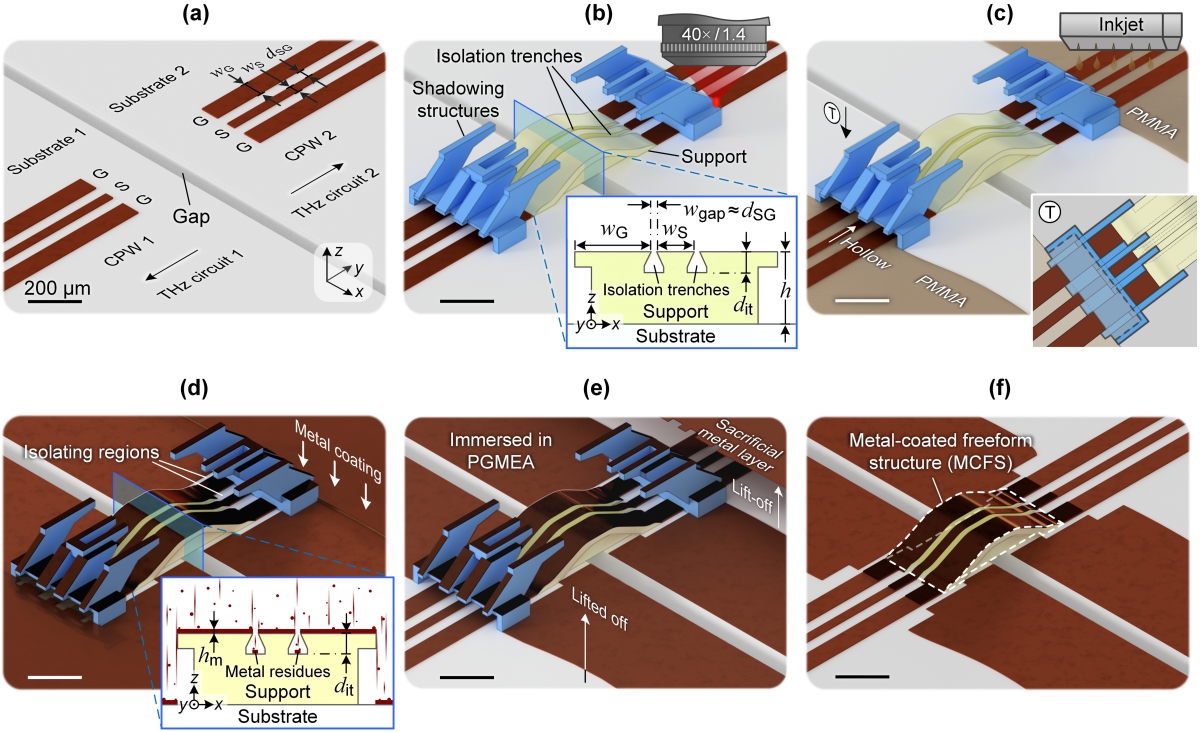


**Fig. 5.2:** (Caption next page.)

**Fig. 5.2:** Fabrication of metal-coated freeform structures (MCFS). The process steps are shown exemplarily for the fabrication of a THz interconnect (TIC) as depicted in Fig. 5.1(b). All scale bars correspond to 200 µm. **(a)** Two substrates with prefabricated planar THz structures such as coplanar waveguides (CPW) in ground-signal-ground (GSG) configuration are coarsely placed to face each other with a gap in-between. **(b)** Freeform support and shadowing structures are 3D-printed using *in-situ* multi-photon laser lithography. The structures are designed to support a metal layer which connects smoothly to the planar CPW on each substrate and comprise isolation trenches with undercut sidewalls, see Inset. These trenches are designed to separate the deposited GSG metal strips, see Subfigure (d). At the transitions between the planar substrates and the freeform polymeric support, additional 3D-printed shadowing structures are used to prevent short circuits. These shadowing structures take the form of multiple arm-like roofs, which locally prevent metal deposition, thereby defining isolating regions that separate the metal strips of the GSG transmission line and that partially overlap with the isolation trenches of the adjacent 3D support structure, see Subfigures (c) and (d). The shadowing structures are shaded in blue. **(c)** For protecting the planar THz structures during global metal deposition, the associated areas of the substrates are temporarily covered by a PMMA film using inkjet printing. Inset Ⓣ provides a top-view on one side of the support structure with the corresponding shadowing structure mentioned above. The shadowing structure is built upon a box-like hollow base, which acts as a flow-stop preventing inkjet-printed PMMA from wetting the entire support structure. **(d)** A highly directed physical vapor deposition (PVD) process is used to deposit metal along a surface-normal direction, forming highly conductive layers on all surfaces with direct line of sight to the evaporation source. **(e)** After metal deposition, the sacrificial PMMA layer is dissolved, thereby lifting off the unwanted metal areas. **(f)** As a last step, the 3D-printed shadowing structures can be removed mechanically, leaving the final MCFS.

To verify the high conductivity and surface quality of the deposited metal layers, we analyzed various fabricated MCFS. The surface roughness was measured using a white-light interferometer, revealing a root-mean-square (RMS) surface roughness of $R_{\mathrm{q,MCFS}} = (13 \ldots 14)$ nm, slightly larger than the roughness of the underlying 3D-printed support of $R_{\mathrm{q,support}} = (9 \ldots 10)$ nm, see Appendix D.3 for further information. The conductivity of the metal films was extracted from four-wire measurements [264] of metal strips which were separately fabricated on an oxidized silicon wafer using identical evaporation processes and metal layer stacks, see Methods Section 5.5 below. Assuming a homogeneous metal layer, we extract an effective conductivity of $\sigma_{\mathrm{MCFS}} = (3.29 \pm 0.12) \times 10^7$ S/m. This corresponds to $(57 \pm 2)$ % of the bulk material value of copper and is consistent with previously reported values using similar deposition techniques [265]. The slight conductivity reduction compared to bulk material is a known effect related to the grain boundaries of the deposited metal layers [265], which might be mitigated by further process optimization.

## 5.3 Experimental verification and discussion

To verify the viability of our concept and to quantify the associated performance parameters, we performed a series of experiments which were geared towards demonstration of the building blocks shown in Fig. 5.1(b), (c) and (d): THz interconnects (TIC) bridging the gap between transmission lines on different substrates, THz probes (TP) that allow repeatable contacting of THz circuits, and THz antennas (TA) that are suspended from the underlying high-index substrate for increased radiation efficiency. These experiments are discussed in the following.

### 5.3.1 THz interconnects (TIC)

A micrograph of three manufactured TIC connecting three pairs of CPW on two separate alumina substrates is shown in Fig. 5.3. For all structures, the CPW endings are separated by $L_{\mathrm{TIC}} \approx 0.5$ mm and seamlessly connect to the respective

TIC, labeled I, II, and III in Fig. 5.3(b). For characterization of the TIC, we first measure the compound $S$-parameters of the TIC and the associated feed lines, which are contacted using dedicated probes in Plane $1'$ and Plane $2'$, indicated as blue lines in Fig. 5.3(a). The length of the feed lines between the probes and the TIC amounts to $L_{\mathrm{feed}} = 4\,\mathrm{mm}$. The measured compound $S$-parameters are exemplarily depicted for TIC II in Fig. 5.3(c), where the blue curve refers to the transmission $S_{2'1',\mathrm{dB}} = 10\log_{10}(|\underline{S}_{2'1'}|^2)$ and the green curve to the reflection $S_{1'1',\mathrm{dB}} = 10\log_{10}(|\underline{S}_{1'1'}|^2)$. The measurements show excellent agreement with simulations (dashed black lines), see Methods Section 5.5 for details. To remove the influence of the feed lines, the reference planes need to be moved to Plane 1 and Plane 2, indicated as red lines in Fig. 5.3(a) and (b). To this end, we separately measure the $S$-parameters of a reference CPW with identical cross section and a length of $L_{\mathrm{feed}}$, which was fabricated on the same substrate. The $S$-parameters of the reference CPW are then used to de-embed the scattering parameters of the TIC, see Appendix D.4. Figure 5.3(d) shows the associated transmission characteristics $S_{21,\mathrm{dB}} = 10\log_{10}(|\underline{S}_{21}|^2)$ (red lines) for TIC I (upper), TIC II (center) and TIC III (lower), revealing 3 dB-bandwidths of $0.307\,\mathrm{THz}$, $> 0.330\,\mathrm{THz}$ and $0.290\,\mathrm{THz}$, respectively. We again performed simulations (dashed black lines), which agree very well with the measurements. Note that the measured $S$-parameters had to be acquired separately in different frequency ranges using dedicated signal sources, waveguides, and probes, thereby leaving a gap between $0.170\,\mathrm{THz}$ and $0.200\,\mathrm{THz}$, where no adequate signal sources were available. Note further that the depicted results rely on a de-embedding procedure using the transfer-matrix ($T$-matrix) approach [178] for frequencies up to $0.170\,\mathrm{THz}$, while, for frequencies beyond $0.200\,\mathrm{THz}$, the de-embedded $S$-parameters were estimated using a more robust scalar correction that is less prone to error multiplication. More details on the measurement setup and the de-embedding procedures are given in Appendix D.4. To the best of our knowledge, the demonstrated 3 dB-bandwidths in excess of $0.33\,\mathrm{THz}$ represent a record for in-plane mmW chip-chip connections and can already well compete with advanced CPW-based flip-chip interfaces [266, 267]. Competing approaches comprise aerosol-jet-printed conductive lines, deposited on dielectric ramps [268–271] or epoxy underfills [268, 272], as well as lithographically defined self-aligning metal nodules, that protrude

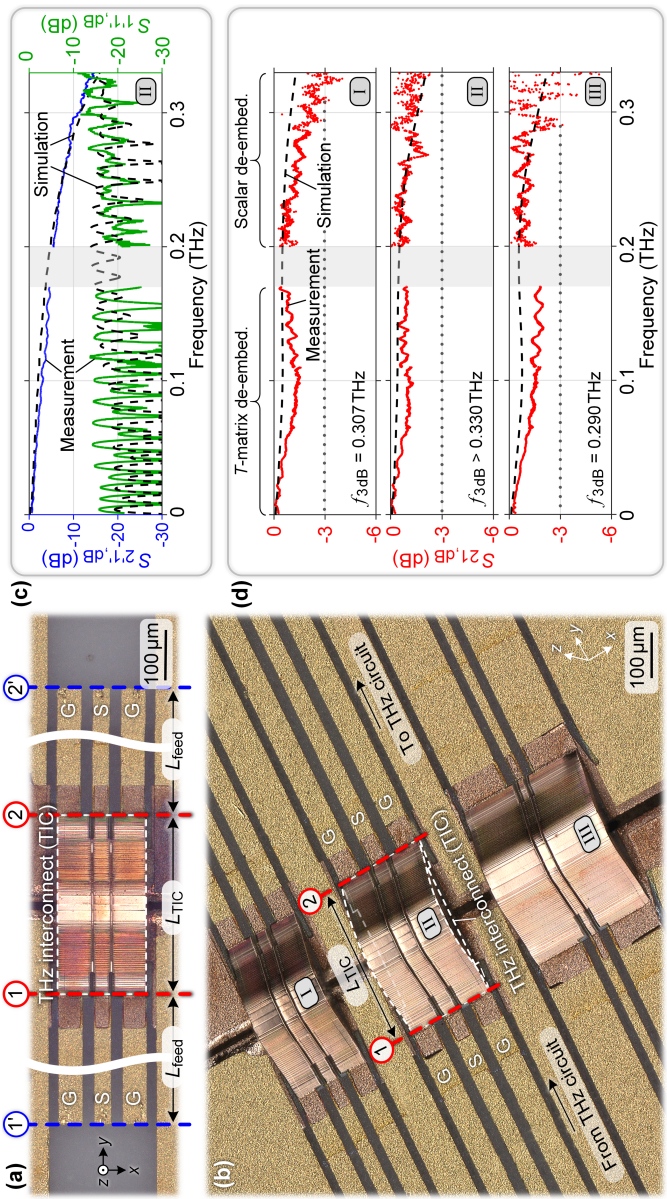


**Fig. 5.3:** (Caption next page.)

**Fig. 5.3:** Characterization of the THz interconnects (TIC). **(a)** Top view of a manufactured TIC, seamlessly connecting the GSG strips of two CPW on two alumina substrates. The CPW endings are separated by $L_{\mathrm{TIC}} \approx 0.5\,\mathrm{mm}$, and the length of the feed lines amounts to $L_{\mathrm{feed}} = 4\,\mathrm{mm}$. For characterization of the TIC, we first measure the compound $S$-parameters of the TIC and the associated feed lines, which are contacted using dedicated probes in Plane $1'$ and Plane $2'$ (blue lines), see Subfigure (c). We then apply a de-embedding procedure to obtain the $S$-parameters of the TIC only, associated with Plane 1 and Plane 2 (red lines), see Subfigure (d). **(b)** Micrograph of three manufactured TIC, labeled I, II and III. **(c)** Compound $S$-parameters of TIC II including the associated feed lines. The blue solid curve refers to the measured transmission $S_{2'1',\mathrm{dB}} = 10\log_{10}(|\underline{S}_{2'1'}|^2)$ and the green solid curve to the measured reflection $S_{1'1',\mathrm{dB}} = 10\log_{10}(|\underline{S}_{1'1'}|^2)$. The measurements show excellent agreement with a simulation of the associated structure (dashed black lines). **(d)** To remove the influence of the feed lines, we measure the $S$-parameters of a reference CPW on the same substrate and apply de-embedding procedures. The associated transmission characteristics $S_{21,\mathrm{dB}} = 10\log_{10}(|\underline{S}_{21}|^2)$ (red curves) are shown for TIC I (upper), II (center) and III (lower), revealing 3 dB-bandwidths of $0.307\,\mathrm{THz}$, $> 0.330\,\mathrm{THz}$ and $0.290\,\mathrm{THz}$, respectively. Measurements and simulations (dashed black lines) agree again well. The measured $S$-parameters are subject to a gap between $0.170\,\mathrm{THz}$ and $0.200\,\mathrm{THz}$ due to lack of adequate signal sources. For frequencies up to $0.170\,\mathrm{THz}$, a transfer-matrix ($T$-matrix) approach was used for de-embedding, whereas for frequencies beyond $0.200\,\mathrm{THz}$, the de-embedded $S$-parameters were estimated using a more robust scalar correction that is less prone to error multiplication, see Appendix D.4 for details.

from the facets of the chips and that require subsequent reflow fusing or electroless plating processes [273]. However, these approaches have only been demonstrated to work up to $0.22\,\mathrm{THz}$ in few cases [271, 273] and generally lack the precision and design flexibility offered by the presented MCFS concept.

### 5.3.2 THz probes (TP)

We further used the MCFS concept to fabricate broadband TP. The measurement setup for characterization of the TP is shown in Fig. 5.4(a). For the experiment, identical twins of TP ($L_{\mathrm{TP}} = 415\,\mu\mathrm{m}$, $h = 180\,\mu\mathrm{m}$) are fabricated on a sample chip at opposite sides of a CPW ($L_{\mathrm{conn}} = 3.8\,\mathrm{mm}$). The three tips (pitch $100\,\mu\mathrm{m}$, contact pad size $20 \times 40\,\mu\mathrm{m}^2$) protrude beyond the edges of the sample chip by a distance $d_{\mathrm{edge}}$. A second chip with two short CPW feeds ($L_{\mathrm{feed}} = 1.5\,\mathrm{mm}$) was used for contacting, where the distance between the endings of the CPW are slightly smaller than $L_{\mathrm{TP}} + L_{\mathrm{conn}} + L_{\mathrm{TP}}$. A vacuum chuck attached to a manual actuator moves the sample chip in the desired position above the contacting chip. With the sample chip in contact, $S$-parameters between Plane $1''$ and Plane $2''$ (brown lines in Fig. 5.4(a)) are measured. Using again dedicated de-embedding procedures, the reference planes are first moved to Plane $1'$ and Plane $2'$, corresponding to the blue lines in Fig. 5.4(a), see Appendix D.5 and associated Fig. D.6 for details. In a second step, we move the reference planes to Plane 1 and Plane 2 (red lines in Fig. 5.4(a)), thereby estimating the characteristics of a single TP — the associated transmission factor $S_{21,\mathrm{dB}} = 10\log_{10}(|\underline{S}_{21}|^2)$ is shown in Fig. 5.4(b). The $3\,\mathrm{dB}$-bandwidth amounts to $0.192\,\mathrm{THz}$, and the $6\,\mathrm{dB}$-bandwidth is far beyond the $0.330\,\mathrm{THz}$ range of our measurement system. Measurement and simulation (dashed black line) are again in reasonable agreement. We attribute the slight deviations above $0.1\,\mathrm{THz}$ to the probes used to connect the contacting chip to our measurement equipment. Specifically, these probes are intended for wafer-level measurements with surface qualities superior to the comparatively rough gold strips of the CPW feeds on our test substrates. More details on the measurement setup and the de-embedding procedures are

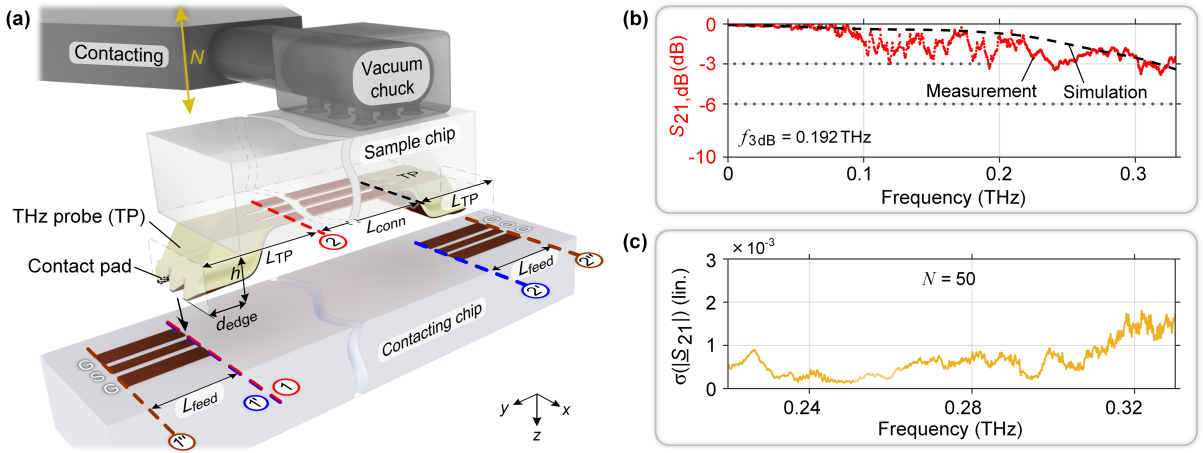


**Fig. 5.4:** Characterization of the THz probes (TP). **(a)** Identical twins of TP ($L_{\mathrm{TP}} = 415\,\mu\mathrm{m}$, $h = 180\,\mu\mathrm{m}$) are fabricated on a sample chip at opposite ends of a CPW ($L_{\mathrm{conn}} = 3.8\,\mathrm{mm}$). The three tips (pitch 100 µm) are designed for a contact pad size of $20 \times 40\,\mu\mathrm{m}^2$ or more and protrude beyond the edges of the sample chip by a distance $d_{\mathrm{edge}}$. A second chip with two short CPW feeds ($L_{\mathrm{feed}} = 1.5\,\mathrm{mm}$) was used for contacting (contacting chip), where the distance between the endings of the CPW are slightly smaller than $L_{\mathrm{TP}} + L_{\mathrm{conn}} + L_{\mathrm{TP}}$. A vacuum chuck attached to a manual actuator is used to move the sample chip in the desired position above the contacting chip. With the sample chip in contact, $S$-parameters between Plane $1''$ and Plane $2''$ (brown lines) are measured. Using dedicated de-embedding procedures, the reference planes are first moved to Plane $1'$ and Plane $2'$ (blue lines) and then to Plane 1 and Plane 2 (red lines), thereby extracting the characteristics of a single TP. **(b)** Estimated transmission characteristics $S_{21,\mathrm{dB}} = 10\log_{10}(|\underline{S}_{21}|^2)$ of a single TP. The 3 dB-bandwidth amounts to 0.192 THz, and the 6 dB-bandwidth is far beyond the 0.330 THz range of our measurement system. Measurement and simulation (dashed black line) are again in reasonable agreement. **(c)** To further demonstrate the robustness of our probes and to verify the repeatability of the connections, we repeat our measurement $N = 50$ times, detaching and re-establishing the contact between the sample and the contacting chip after each repetition. From the resulting data, we extract the standard deviation of the magnitude of the complex-valued amplitude transmission factor $\underline{S}_{21}$ as a function of frequency. We find a remarkably low maximum standard deviation of $\sigma(|\underline{S}_{21}|)_{\max} \approx 2 \times 10^{-3}$ near 0.32 THz, corresponding to $-55\,\mathrm{dB}$.

given in Appendix D.5. To the best of our knowledge, the demonstrated 3 dB-bandwidths in excess of $0.19\,\mathrm{THz}$ represent a record for additively manufactured electrical probes. Previous demonstrations were limited to the $(75-110)\,\mathrm{GHz}$ frequency band, with insertion losses of the order of $1\,\mathrm{dB}$ per probe [274]. To further demonstrate the robustness of our probes and to verify the repeatability of the connection, we repeat our measurement $N = 50$ times, detaching and re-establishing the contact between the sample and the contacting chip after each repetition. From the resulting data, we extract the standard deviation of the magnitude of the complex-valued amplitude transmission factor $\underline{S}_{21}$ as a function of frequency, see Fig. 5.4(c). We find a remarkably low maximum standard deviation of $\sigma(|\underline{S}_{21}|)_{\max} \approx 2 \times 10^{-3}$ near $0.32\,\mathrm{THz}$, corresponding to $-55\,\mathrm{dB}$. These results are already on-par with conventional commercially available probes fabricated via conventional micromachining techniques, where, e.g., standard deviations $\sigma(|\underline{S}_{21}|)$ in the range $(-60\ldots-43)\,\mathrm{dB}$ have been demonstrated for 2 mm-long CPW in the $0.3\,\mathrm{THz}$ band [275].

### 5.3.3 THz antennas (TA)

As a last implementation example, we explore TA. A schematic of a manufactured TA operating at a frequency centered around $0.28\,\mathrm{THz}$ is shown in Fig. 5.5(a). Connecting to the CPW feed ($L_{\mathrm{feed}} = 1.1\,\mathrm{mm}$), the 3D-printed support structure provides a mechanical base for guiding the signal and ground conductors of the CPW away from the substrate to form an elevated slot antenna for improved radiation into the upper half-space. The antenna comprises two slots, each having a width of $w_{\mathrm{slot}} = 60\,\mu\mathrm{m}$ and a length of $L_{\mathrm{slot}} = 400\,\mu\mathrm{m}$, equivalent to approximately half the guided wavelength at the targeted radiation frequency of $0.28\,\mathrm{THz}$. The height of the structure ($h = 250\,\mu\mathrm{m}$) was adapted such that the evaporated metal on the substrate simultaneously acts as a reflector. The measured radiation pattern for different elevation angles $\theta$ is shown in Fig. 5.5(b), where the blue area represents the realized gain $G_{\mathrm{R,TA,dBi}}(\theta) = 10\log_{10} G_{\mathrm{R,TA}}(\theta)$ in the upper half-space region ($H$-plane). A maximum realized gain of $5.5\,\mathrm{dBi}$ was measured perpendicular to the substrate near $0.274\,\mathrm{THz}$, in good agreement with

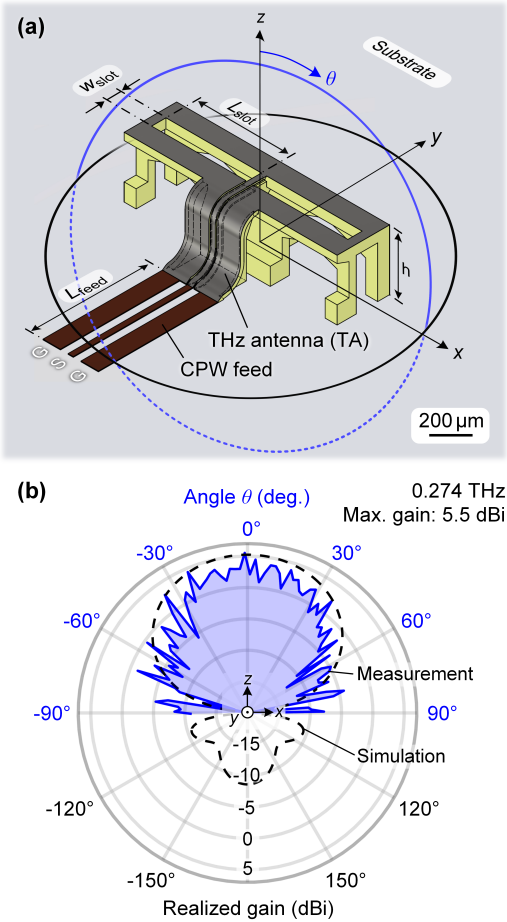


**Fig. 5.5:** Characterization of the THz antennas (TA). **(a)** Schematic of the manufactured TA operating at a frequency centered around 0.28 THz. Connecting to the CPW feed ($L_{\mathrm{feed}} = 1.1$ mm), the 3D-printed support structure provides a mechanical base for guiding the signal and ground conductors of the CPW away from the substrate to form an elevated slot antenna for improved radiation to the top. The antenna comprises two slots, each having a width of $w_{\mathrm{slot}} = 60\,\mu$m and a length of $L_{\mathrm{slot}} = 400\,\mu$m, equivalent to approximately half the guided wavelength at the targeted radiation frequency of 0.28 THz. The height of the support structure ($h = 250\,\mu$m) was adapted such that the evaporated metal on the substrate simultaneously acts as a reflector. **(b)** Measured radiation pattern for different elevation angles $\theta$ where the blue area represents the realized gain $G_{\mathrm{R,TA,dBi}}(\theta) = 10\log_{10} G_{\mathrm{R,TA}}(\theta)$ in the upper half-space region ($H$-plane). A maximum realized gain of 5.5 dBi was measured perpendicular to the substrate near 0.274 THz, in good agreement with the simulation (black dashed line).

the simulation (black dashed line). More details on the measurement setup and the characterization are given in Appendix D.6. To the best of our knowledge, our experiments represent the first demonstration of an additively manufactured 3D freeform mmW / THz antenna which does not require any manual assembly steps. Previous approaches have either been limited to the fabrication of bulky stand-alone horn antennas [257, 258] or are based on aerosol-jet-printed conductive structures on the surface of non-planar dielectric substrates [276], often requiring additional mechanical assembly steps to yield a functional device [257, 276].

## 5.4 Summary and outlook

We have introduced a novel concept for fabricating precisely defined mmW and THz structures, relying on *in-situ* printing of freeform polymer support structures that are selectively coated through highly directive metal deposition techniques. The resulting metal-coated freeform structures (MCFS) offer high surface quality in combination with conductivities comparable to bulk material values and do not require any manual assembly steps. The viability of the approach is shown in a series of proof-of-concept experiments. In a first set of experiments, we show THz interconnects (TIC) that bridge the gap between transmission lines located on different substrates and that offer 3 dB-bandwidths exceeding $0.33$ THz. In a second set of experiments, we demonstrate that the vast design freedom offered by our fabrication technique can be leveraged for cost-effective THz probes (TP) that allow highly repeatable contacting over many probing cycles. Our TP offer 3 dB-bandwidths exceeding $0.19$ THz and 6 dB-bandwidths far beyond the $0.33$ THz range of our measurement system. A third set of experiments is finally dedicated to THz antennas (TA), which are suspended from the underlying high-index substrate for better radiation efficiency. At a frequency of $0.27$ THz, a maximum realized gain of $5.5$ dBi in the direction perpendicular to the substrate is measured. Our proof-of-principle experiments show the vast potential offered by the proposed fabrication technique, and the demonstrated structures already offer unique performance parameters such as record-high bandwidths for in-plane mmW chip-chip connections and additively manufactured probes. Our concept

offers unprecedented design freedom, does not rely on expensive high-precision assembly steps, and is widely applicable to a rich variety of use cases, thereby paving a path towards advanced mmW and THz systems in communications [261], sensing [262], or ultra-broadband signal processing [52].

## 5.5 Materials and methods

**CPW design and fabrication:** The substrates that are used as the base for the subsequent fabrication steps have a total size of $100\,\mathrm{mm} \times 100\,\mathrm{mm}$ each and consist of a $635\,\mu\mathrm{m}$-thick alumina ($Al_2O_3$) layer with a single-sided gold coating (Reinhardt Microtech GmbH, Ulm, Germany) and a thin titanium adhesion layer in between. The $Al_2O_3$ layer exhibits a relative permittivity of $\epsilon' = 9.9$ and a loss tangent of $\tan(\delta) = 1 \times 10^{-4}$, both specified at a frequency of 1 MHz. The gold metallization has a thickness of $3\,\mu\mathrm{m}$ with a specified variance of $\pm 30\,\%$, and a root-mean-square (RMS) surface roughness of $R_{\mathrm{q,gold}} = (121 \ldots 129)\,\mathrm{nm}$ was measured using a white-light interferometer, see Appendix D.3 for further information. For achieving a characteristic CPW impedance of $50\,\Omega$, different combinations of the signal conductor width $w_{\mathrm{S}}$, ground conductor width $w_{\mathrm{G}}$, and signal-to-ground conductor distance $d_{\mathrm{SG}}$ were chosen. All CPW designs facilitate contacting with GSG probes with pitches of $100\,\mu\mathrm{m}$ for compatibility with existing measurement equipment.

The transmission lines used in the experiments for the TIC and TA were structured into the gold layer using a wet etching process. To this end, a $1.5\,\mu\mathrm{m}$-thick layer of positive-tone photoresist (AZ 1505, Microchemicals GmbH, Ulm, Germany) was first spin coated on the substrates and subsequently baked at a temperature of $95\,^{\circ}\mathrm{C}$ for five minutes. The resist was then structured using a direct-write laser lithography tool (DWL 66fs, Heidelberg Instruments Mikrotechnik GmbH, Heidelberg, Germany) and developed (AZ 400K 1:4, Microchemicals GmbH). To strip the metal in the uncoated regions, wet etching is performed with potassium iodide and titanium-tungsten etchants. Due to the significant variation of the metallization thickness across the substrate, over- and underetching of the

metal structures was hardly avoidable. As a result, $w_S$ and $w_G$ were generally found to be decreased, while $d_{SG}$ was increased compared to the original design. The dimensions of the fabricated CPW are indicated in Table 5.1 and show fair agreement with the design values. From simulations, the characteristic impedance is expected to be in the range $58\,\Omega \ldots 60\,\Omega$. These limitations can be overcome by an optimized fabrication process, relying on gold layers with better thickness uniformity, which would further improve the impedance matching and hence the performance of our MCFS-based THz structures.

In contrast to this, the transmission lines used in the experiments for the TP were structured into the gold layer using a commercially available laser ablation system (ProtoLaser R4, LPKF Laser & Electronics SE, Garbsen, Germany), equipped with a 515 nm picosecond laser with a typical beam diameter of 15 µm. We used 1.5 ps-wide pulses with 24 µJ pulse energy at repetition rates between 150 kHz and 300 kHz for structuring the substrates. The dimensions of the fabricated CPW are again listed in Table 5.1 and show good agreement with the design values. The characteristic impedance is expected to be approximately $55\,\Omega$.

**Table 5.1:** Overview of dimensions of manufactured CPW.

| Experiment | $L$ (mm) | $w_S$ (µm) | $w_G$ (µm) | $d_{SG}$ (µm) |
|---|---|---|---|---|
| TIC I | 4.0 | 45 | 65 | 30 |
| TIC II | 4.0 | 56 | 72 | 35 |
| TIC III | 4.0 | 30 | 150 | 30 |
| TP | 1.5 / 3.8 / 6.8 | 61 | 79 | 29 |
| TA | 1.1 | 22 | 89 | 16 |

**Sample preparation:** After structuring the CPW, a wafer saw was used for separation of the alumina substrates into individual chips. For easier handling, the individual chips were temporarily fixed to glass cover slides using UV glue (NOA 61, Norland Optical Adhesive Inc., Jamesburg, USA). For the experiments

with the TIC, see Fig. 5.3, the ends of the $4$ mm-long CPW feeds are approximately $230$ µm away from the diced chip edges, keeping the length of the bridging TIC ($L_{\mathrm{TIC}} \approx 0.5$ mm) manageable when the CPW are placed facing each other. The gap between the two substrates was roughly $40$ µm wide. The sample chip used in the TP experiments, see zoom-in in Appendix Fig. D.5, is roughly $4.4$ mm wide and $8.8$ mm long to provide sufficient area for pick-up with a custom vacuum tool ($3.5$ mm $\times$ $8$ mm). The connecting CPW ($L_{\mathrm{conn}} = 3.8$ mm) between the two TP ends approximately $320$ µm away from the diced chip edge on each side. This leaves enough room for a smooth routing of the signal and ground conductors, while ensuring that the tips of the TP protrude beyond the edges of the chip by a sufficient distance $d_{\mathrm{edge}}$ for better visibility via the top-view camera used in the experimental setup illustrated in Fig. D.5. In the areas between the ends of the transmission lines and the chip edge, the gold was removed from the alumina substrates for a more reliable height detection and better adhesion of the 3D-printed support structures, see next paragraph. Similarly, for the TA as shown in Fig. 5.5, the metal layer is removed from the surface of the substrate in a $250$ µm-long region following each end of the transmission line. The remainder of the gold layer was maintained to act as a reflector for the suspended TA.

**Multi-photon lithography:** The 3D-printed support and shadowing structures, see Fig. 5.1(b)-(d), were fabricated using an in-house-built lithography system with a $40\times$ / $1.4$ objective (PlanApochromat Oil DIC M27, Carl Zeiss Microscopy GmbH, Oberkochen, Germany), galvanometer-actuated mirrors, and a $780$ nm femtosecond laser with a pulse width of $58$ fs (C-Fiber 780 HP, Menlo Systems GmbH, Planegg, Germany). The samples were mounted in the lithography machine along with the associated glass cover slides, and the objective approaches the samples along the negative $z$-direction, see Figs. 5.3-5.5. For lithographic structuring, we use a liquid photoresist (VanCore B, Vanguard Automation GmbH, Karlsruhe, Germany), for which the dielectric response was independently measured, see Appendix D.1. All structures are printed to the substrates with the axis of the lithography beam perpendicular to the surface of the chips, i.e., along the $z$-direction, see Figs. 5.3-5.5. We use automated procedures for detecting the substrate surface with sub-$100$ nm precision. Where possible, the underlying

metal layer was removed to avoid scattering of the laser beam due to the roughness of the gold layer. For lateral alignment, we relied on the camera-based vision system of our lithography setup, which leads to a lateral alignment precision that is also of the order of 100 nm. Due to the limited write field, corresponding approximately to a circle with a diameter of 400 µm, the support and shadowing structures have to be printed in separate steps. The support structures of the TIC and TA are further split into two and three parts, respectively, which are printed one after another. Proper alignment of the separately printed models is ensured by a defined translation of the underlying chip using a precision stage in the lithography system. To reduce the required fabrication time, all structures are printed with a standard layer-to-layer distance (slicing distance) of 100 nm only for the outermost shell, whereas the inside of the structures is filled with a coarser spacing of 600 nm. After printing, unexposed photoresist is removed in a two-step development process using propylene-glycol-methyl-ether-acetate (PGMEA) as a developer for 15 minutes, followed by rinsing in isopropyl alcohol (2-propanol).

**PMMA ink preparation and inkjet printing:** For protecting the planar THz structures during the global metal deposition, see Fig. 5.2(c) and (e), we used an inkjet-printed poly(methyl methacrylate) (PMMA) layer, which was later removed by propylene-glycol-methyl-ether-acetate (PGMEA). Since PGMEA is also used in the development process of the 3D-printed structures, see Methods above, deterioration of the 3D-printed support structures during the PMMA lift-off is not to be expected. For the ink preparation, PMMA with an average molecular mass of $1.5 \times 10^4$ daltons (Sigma-Aldrich Inc., Saint Louis, USA) was dissolved in 1,3-dimethoxybenzene ($\geq$ 98 %, Sigma-Aldrich Inc.) to achieve a concentration of 80 g/L. We further added 5 % hexylbenzene (97 %, Sigma-Aldrich Inc.) to mitigate the coffee-ring effect [277]. Finally, the ink was filtered using polytetrafluoroethylene (PTFE) filters (pore size 200 nm) before being filled in the cartridges (FUJIFILM Dimatix Inc., Santa Clara, USA) of the inkjet printer (PiXDRO LP50, SÜSS MicroTec SE, Garching, Germany). The substrate and printhead temperatures were set to 50 °C and 27 °C, respectively. The build-in camera system of the printer was used to align the printing region with respect to the CPW and the shadowing structures on the chips. For all samples, the transmission lines are

covered over their full length up to the flow-stop that is part of the 3D-printed shadowing structure, see Fig. 5.2(c). To achieve sufficient coverage, a minimum of five layers were printed using a resolution of $550$ dpi.

**Shadowing and metal deposition:** For applying the highly-directive metal coating, see Fig. 5.2(d), an electron-beam physical vapor deposition (PVD) process is used (Univex 400, Leybold GmbH, Cologne, Germany) at a pressure of $8 \times 10^{-4}$ Pa. The sample chips are mounted with a large distance ($> 60$ cm) above the evaporation source, thereby achieving a small divergence of the vapor flow. The mounting plate carrying the samples can further be tilted in one direction and rotated around an axis that is normal to the mounting surface to improve the uniformity of the deposited layers. For the coating of the TIC and TP, the direction of evaporation is perpendicular to the substrates, i.e., along the negative $z$-direction in Figs. 5.2-5.4. For the TA in Fig. 5.5, the direction of deposition is set to an angle of $45^\circ$ with respect to the negative $z$-direction in the $(y, z)$-plane, i.e., the deposition is done along the $(0, 1, -1)$-direction of the coordinate system shown in Fig. 5.5(a), which permits coating of the support structure also in the ramp-like sections which are partially perpendicular to the substrate. The deposited layer stack comprises a sequence of different metals: First, a $5$ nm-thick adhesion film of titanium is applied, followed by the main layer consisting of $300$ nm copper. Afterwards, a $5$ nm titanium layer is deposited to act as a diffusion barrier between the copper and the final $10$ nm-thick gold passivation layer. For the TIC and TA, the process is repeated twice for a total thickness of the metal coating of $h_\mathrm{m} = 0.64\,\mu$m. For the TP, the initial titanium adhesion layer was replaced by a $30$ nm aluminum coating, leading to a layer stack with a thickness of $345$ nm. The process is repeated four times for a total metal thickness of $h_\mathrm{m} = 1.38\,\mu$m for the TP. This ensures that the thickness of the metal coating is always a multiple of the skin depth at the targeted operation frequency. For estimating the conductivity of our metal films, multiple metal strips with a length of $2$ mm and width of $10\,\mu$m and $15\,\mu$m were fabricated on a silicon wafer with a $1\,\mu$m-thick silicon dioxide isolating layer on top (Microchemicals GmbH). We use identical evaporation parameters and repeat the process

two times for achieving a metal layer stack with a thickness which was measured to be $h_\mathrm{m} \approx 590\,\mathrm{nm}$ using a profilometer (Tencor P-7, KLA Inc., Milpitas, USA). From four-wire measurements [264] using a precision source / measurement unit (B2902A, Keysight Technologies Inc., Santa Rosa, USA), we extract an effective sheet resistance of $R_\mathrm{S,MCFS} = (51.6 \pm 1.9)\,\mathrm{m\Omega/\square}$, corresponding to an effective conductivity of $\sigma_\mathrm{MCFS} = 1/(h_\mathrm{m} R_\mathrm{S,MCFS}) = (3.29 \pm 0.12) \times 10^7\,\mathrm{S/m}$. To mitigate offset errors as a result of the thermal electromotive force, measurements were carried out for both polarities of the driving current and by considering the average of the two associated voltage readings (reverse current method [264]).

**3D EM simulations:** The transmission and reflection characteristics of the TIC, see Fig. 5.3(c) and (d), the TP, see Fig. 5.4(b), as well as the far-field characteristics of the TA, see Fig. 5.5(b), are simulated using a commercially available numerical time-domain solver (CST Microwave Studio, Dassault Systèmes SE, Vélizy-Villacoublay, France). The alumina substrate is modeled using the manufacturer specifications of the relative permittivity and loss tangent, see paragraph on "CPW design and fabrication" above. The CPW are simulated using the "lossy metal" option of CST Microwave Studio, which models the penetration of electromagnetic fields inside a very good but still imperfect conductor by means of an internal one-dimensional surface impedance model [172]. This allows to take into account the skin effect without further mesh refinement. We also include the measured RMS surface roughness $R_\mathrm{q,gold}$ of the gold layer of the respective assembly, see above. This value is used as an input for the so-called gradient model provided within CST Microwave Studio, which accounts for the increased total loss and inner inductance effects that occur as a consequence of the rough surface [172]. The material characteristics of the 3D-printed support structures are modeled using the results of the dielectric response measurement of the underlying photoresist, see Appendix D.1. To this end, the measured values for the permittivity $\epsilon'$ and loss tangent $\tan(\delta)$ in the frequency range from $0.220\,\mathrm{THz}$ to $0.325\,\mathrm{THz}$ were imported into CST Microwave Studio and fitted using a dispersion model of first order. Another crucial aspect is the correct representation of the comparatively small isolation trenches inside the 3D-printed support structures, separating the deposited metal layers by a gap of the order of a view micrometers.

In the simulation of transmission lines and THz devices with dimensions up to the mm-range, a detailed representation of the field within these gaps and metal layers would lead to an unrealistic number of mesh cells that cannot be handled with the available computing resources. We therefore use a locally refined mesh inside the gaps in combination with the "thin panel" option of CST Microwave Studio, which relates the tangential electric and magnetic fields on the surface of the extended metal strips with the help of surface impedances [172]. Furthermore, the TA is simulated with open boundaries in combination with a so-called multilayer background to emulate an infinitely extended substrate. Using this approach, any reflections at the lateral edges of the substrate can be avoided, albeit the restricted simulation volume.

**Micrograph image acquisition:** The micrographs in Fig. 5.1(b)-(d) and in Fig. 5.3(b) are created using a digital microscope (VHX-7000, Keyence Ltd., Osaka, Japan) with a tiltable and motorized imaging head comprising a CMOS camera (VHX-7100, Keyence Ltd.). A magnification of $300\times$ and $150\times$ was used for the micrographs in Fig. 5.1(b), (c) and Fig. 5.1(d), respectively, and the micrograph in Fig. 5.3(b) was taken at a magnification of $80\times$. In all cases, the microscope was set to acquire large image stacks ($\sim 50 - 100$ images) with different focus distances, which were then combined into focus-stacked images using a commercially available software (Helicon Focus, Helicon Soft Ltd., Kharkiv, Ukraine).

*[End of paper [J4]]*

# 6 Summary and Outlook

Packaging and assembly of photonic and terahertz (THz) systems still represents a significant barrier for widespread adaption of photonic integrated circuits (PIC) and monolithic microwave integrated circuits (MMIC). Within this thesis, this technology gap is addressed by demonstrating photonic and THz assemblies that exploit 3D-printed coupling elements such as photonic wire bonds (PWB), facet-attached microlenses (FaML) and metal-coated freeform structures (MCFS). A detailed summary and outlook is given for each individual topic and application that is addressed within this thesis.

### 3D-printed coupling elements for highly versatile light sources

The concept of hybrid external-cavity lasers (ECL) based on 3D-printed intra-cavity coupling elements is expanded by replacing previously used silicon photonic (SiP) feedback circuits [J1] with their silicon-nitride-($Si_3N_4$)-based counterparts [J2]. As a result of the lower linear and nonlinear losses, intrinsic $Q$-factors of the underlying resonators are greatly increased and two-photon absorption is eliminated as a critical impairment at high power levels, thereby facilitating greatly reduced phase noise and small linewidth. A proof-of-concept device offers a $90\,\mathrm{nm}$ tuning range ($1480\,\mathrm{nm} - 1570\,\mathrm{nm}$) with on-chip output powers above $12\,\mathrm{dBm}$ and side-mode suppression ratios of up to $59\,\mathrm{dB}$ in the center of the tuning range. An intrinsic linewidth of $979\,\mathrm{Hz}$ is measured, which is one of the lowest values reported for comparable feedback architectures. Using 3D-printed coupling elements such as PWB for the assembly of hybrid ECL alleviates the need for costly high-precision alignment of the underlying dies and paves the path towards efficient

integration of associated systems. The versatility of the $Si_3N_4$-based hybrid ECL is demonstrated by using the device as a precisely tunable pump laser to generate dissipative Kerr soliton frequency combs in high-$Q$ $Si_3N_4$ microresonators.

This simple yet flexible integration approach may be leveraged in the future for implementing highly versatile light sources that can address vastly different frequency bands and hence a diverse set of applications. This was already shown in initial experiments, where the tunability of a hybrid SiP ECL was leveraged for swept-source optical coherence tomography (SS-OCT) demonstrations [C3]. By co-integrating other functional photonic structures such as delay lines or photodiodes (PD) on the same feedback circuit, the present demonstrations could be significantly advanced towards a fully integrated chip-scale OCT system. In this context, controlling the various phase shifters on the external-feedback circuit as required for precise control of the ECL emission wavelength represents a laborious task, necessitating the creation of look-up tables which might change over time. These calibration schemes are thus limited with respect to the stability of the pre-recorded operating points. Feedback-based active stabilization techniques would permit greatly improved long-term stability and resilience of the associated devices with respect to, e.g., environmental influences. Monitoring of the ECL emission can be realized by dedicated read-out electronics in conjunction with PD which are co-integrated on the same feedback circuit. Advancements with regards to the tuning speed of the light sources are further enabled by piezoelectric phase shifters based on, e.g., lead zirconium titanate (PZT) or aluminium nitride (AlN) [199]. At the time of writing, highly linear frequency sweeping over a bandwidth of more than 1 GHz has already been demonstrated by using the self-injection locking (SIL) phenomenon in combination with piezo-tunable $Si_3N_4$ microresonators [C5, C6]. In the future, advanced tuning schemes could enable ECL offering wideband tunability alongside unprecedented frequency-agility that can serve a wide range of applications from coherent communications to frequency-modulated continuous-wave (FMCW) light detection and ranging (LIDAR) and to OCT.

### 3D-printed optical elements for alignment-tolerant coupling in datacenter transceiver assemblies

Using FaML, low-loss and alignment-tolerant connections between individual cores of multi-core fibers and standard linear arrays of vertical-cavity surface-emitting lasers (VCSEL) / PD are demonstrated in transceiver assemblies that use space-division multiplexing (SDM) for parallel transmission of large data streams. The presented scheme does not require any additional fiber-based or waveguide-based fan-out structures. Average coupling losses of $0.67$ dB (Tx) and $0.63$ dB (Rx) are achieved, along with lateral $1$ dB alignment tolerances of $\pm 18$ µm (Tx) and $\pm 25$ µm (Rx), respectively. Using a machine-vision based passive alignment process, average coupling losses of $1.0$ dB (Tx) and $0.63$ dB (Rx) are shown. Using this approach, a $3 \times 25$ Gbit/s datacenter transceiver assembly which fits into a small form-factor pluggable module is built, fulfilling many of the performance metrics specified in the IEEE 802.3 standard. We further demonstrate low-loss and alignment-tolerant connections between multimode fiber arrays and standard linear arrays of VCSEL / PD. Average optical coupling losses as low as $0.35$ dB for the transmitter (Tx) and $0.70$ dB for the receiver (Rx) are achieved, along with lateral $1$ dB alignment tolerances of $\pm 17$ µm (Tx) and $\pm 62$ µm (Rx), respectively. Using a machine-vision based passive alignment process on a custom pick-and-place machine, average coupling losses of $0.50$ dB (Tx) and $0.70$ dB (Rx) are shown.

In future implementations, the underlying mechanical transfer (MT) ferrules in the presented transceiver assemblies could allow to arrange fibers in two-dimensional arrays, thereby increasing the number of parallel fiber channels significantly. Furthermore, the demonstrated concepts could in principle be extended to also utilize the remaining cores of the MCF. This would open a path to using two-dimensional device arrays in combination with one-dimensional MCF arrays and more complicated FaML arrangements on the fiber facets. The greatly increased number of parallel channels per transceiver would hence permit to scale the aggregate line rates tremendously. Alternatively, mode multiplexers are commonly utilized in SDM-based links for increasing the channel count through parallel data

transmission over multiple propagating modes. At the time of writing, ultra-compact 3D-printed mode multiplexers connecting the single core of a view-mode fiber to the cores of a single-mode MCF are already being investigated.

### Freeform terahertz structures fabricated by multi-photon lithography and metal coating

A novel concept for fabricating precisely defined millimeter-wave (mmW) and THz structures is introduced and experimentally verified, combining low-loss dielectrics and highly conductive metal elements in a well-defined 3D freeform geometry. The concept exploits *in-situ* printed polymer support structures that are selectively coated through highly directional metal deposition techniques in combination with precisely aligned 3D-printed shadowing structures. The resulting MCFS offer high surface quality in combination with conductivities comparable to bulk material values and do not require any manual assembly steps. In a first set of experiments, the fabrication approach is utilized for demonstrating THz interconnects that bridge the gap between transmission lines located on different substrates and that offer 3 dB-bandwidths exceeding $0.33$ THz. In a second set of experiments, we demonstrate THz probes offering unprecedented shape fidelity that lend themselves to testing of mmW and THz integrated circuits. Highly repeatable contacting over many probing cycles with 3 dB-bandwidths exceeding $0.19$ THz and with 6 dB-bandwidths far beyond the $0.33$ THz range of our measurement system are demonstrated. In a third set of experiments, THz antennas which are suspended from the underlying high-index substrate for better radiation efficiency are shown. At a frequency of $0.27$ THz, a maximum gain of $5.5$ dBi is measured in the surface-normal direction. Our proof-of-principle experiments show the vast potential offered by the proposed fabrication technique, and the demonstrated structures already offer unique performance parameters such as record-high bandwidths for in-plane mmW chip-chip connections and additively manufactured probes.

As a next step, the demonstrated proof-of-concept devices can be readily applied and adapted for the integration of more complex mmW and THz assemblies, comprising PIC and MMIC based on vastly different material platforms. Specifically, high-speed uni-traveling-carrier photodiodes (UTC-PD) co-integrated with other functional photonic building blocks on the $Si_3N_4$-platform could be combined with InP-based amplifiers and THz antennas for ultra-broadband signal generation and processing in chip-scale photonic-electronic packages. Furthermore, THz probes could be directly fabricated onto PD chips, thereby enabling flexible and broadband read-out of mmW and THz integrated circuits. In this context, incorporating 3D-printed optical coupling elements such as FaML or PWB in the already developed fabrication workflow may open attractive prospects for fully integrated hybrid electro-optic assemblies of unprecedented flexibility, which are applicable to applications in communications, sensing, and ultra-broadband signal processing. Additionally, various steps of the manufacturing process can be refined for a simplified fabrication of MCFS. At the time of writing, new photoresist materials comprising, e.g., copper nanoparticles are investigated for fabricating metal layers in the same multi-photon printer as the polymer support structures of the MCFS. For achieving sufficiently thick conductive layers, the deposited metal could potentially act as a seed layer for a subsequent electroplating step. This would allow to fully replace the directive metal evaporation under high-vacuum conditions and hence alleviates the need for a dedicated lift-off process for protecting the various PIC and MMIC from sacrificially deposited metal residues. Furthermore, new developments with respect to extending the write field of multi-photon printers or related to emerging printing technologies based on projection stereo-lithography might soon be able to offer much increased fabrication volumes while still providing sufficiently high resolution for mmW and THz structures. With respect to MCFS, this would permit significantly shorter writing times for the 3D-printing of associated support and shadowing structures.

# Appendices

# A 3D-printed coupling elements for external-cavity lasers with $Si_3N_4$ resonator offering sub-kHz linewidth

This chapter has been published as Appendix of [J2]. The material from the publication has been adapted to comply with the layout and the structure of this thesis.

*[Beginning of Appendix of paper [J2]]*

## A.1 Characterization of ECL filter circuit

For characterization of the ECL filter circuit (TriPleX® chip), the individual racetrack resonators are first characterized by power transmission measurements in a loop-back configuration through the two auxiliary waveguide Ports 3 and 4, see Fig. 3.11(b). Since the measured transmission spectrum contains resonances of both racetrack resonators, we first cut out relevant data segments around each resonance and assign them to the corresponding resonator. We then analyze the dispersion relations of both racetrack resonators by extracting the frequency-dependent round-trip phase delay $\theta(\omega) = -\beta(\omega)L$ of each device, where $\beta(\omega)$ represents the frequency-dependent propagation constant of the underlying waveguides and where $L$ is the perimeter of the respective resonator, which amounts

to $885.1\,\mu m$ for R1 and to $857.4\,\mu m$ for R2. The frequency-dependent round-trip phases of both racetrack resonators are fit by a second-order polynomial about the center frequency of our tuning range, $\omega_c = 2\pi f_c = 2\pi \cdot 196.6\,\mathrm{THz}$ ($\lambda_c = 1525\,\mathrm{nm}$)

$$\theta(\omega) = \theta_c^{(0)} + \theta_c^{(1)}(\omega - \omega_c) + \frac{1}{2}\theta_c^{(2)}(\omega - \omega_c)^2 \tag{A.1}$$

where $\theta_c^{(0)}$ corresponds to the round-trip phase delay at the center frequency $\omega_c$ whereas $\theta_c^{(1)}$ and $\theta_c^{(2)}$ give the corresponding first- and second-order derivatives. Note that $\theta_c^{(0)} = -\beta_c^{(0)} L$ is usually only know up to an integer multiple of $2\pi$ since the absolute value of the round-trip phase at the various resonances is hard to extract from the measured data. $\theta_c^{(1)} = -\beta_c^{(1)} L$ corresponds to the round-trip group delay at the center frequency $\omega_c$ and hence allows to directly extract the free spectral range (FSR) at the center frequency of the tuning range, $\Delta f_{\mathrm{FSR}} = \Delta\omega_{\mathrm{FSR}}/(2\pi) = 1/(2\pi\theta_c^{(1)})$, which is found to be $\Delta f_{\mathrm{FSR,R1}} = 195.7\,\mathrm{GHz}$ for R1 and $\Delta f_{\mathrm{FSR,R2}} = 202.0\,\mathrm{GHz}$ for R2. Using the relation $n_{\mathrm{eg}} = \beta_c^{(1)} c = -\theta_c^{(1)} c/L$, we find identical refractive indices of $n_{\mathrm{eg}} = 1.73$ for both resonators at a wavelength of $\lambda_c = 1525\,\mathrm{nm}$ which is in good agreement with the value of $n_{\mathrm{eg,TriPleX}} \approx 1.72$ specified for the TriPleX® platform at a wavelength of $1550\,\mathrm{nm}$ [17, 115]. $\theta_c^{(2)} = -\beta_c^{(2)} L$ is related to the group-delay dispersion (GDD) of the resonators and amounts to $824\,\mathrm{fs}^2$ for R1 and to $806\,\mathrm{fs}^2$ for R2. This can finally be related to the group-velocity dispersion (GVD) $\beta_c^{(2)}$ of the resonators, leading to $931\,\mathrm{fs}^2/\mathrm{mm}$ for R1 and to $940\,\mathrm{fs}^2/\mathrm{mm}$ for R2.

In a next step, we use the fitted dispersion relation $\theta(\omega)$ according to Eq. (A.1) in the through-port model of a single ring resonator with a pair of identical lossless coupling sections [112],

$$T_{\mathrm{thrgh}}(\omega) = \left| \frac{\tau - a\tau \mathrm{e}^{\mathrm{j}\theta(\omega)}}{1 - a\tau^2 \mathrm{e}^{\mathrm{j}\theta(\omega)}} \right|^2, \tag{A.2}$$

and fit it to the frequency-dependent power transmission through R1 and R2 measured in the vicinity of each resonance. In Eq. (A.2), $\tau$ is the real-valued

amplitude transmission coefficient describing the transmission through each of the two coupling sections of the racetrack resonator, and $a$ is the real-valued amplitude transmission factor representing the round-trip loss, see [J1] for a more detailed explanation. From fitting the model of Eq. (A.2) to our measurement data, we obtain parameters of $a \approx 0.999$ and $\tau \approx 0.928$, leading to an amplitude coupling coefficient of $\kappa = \sqrt{1-\tau^2} \approx 0.372$. The associated measurement data and fit curve are shown for one exemplary resonance dip of R1 in Fig. A.1(a). Using the extracted values for the parameters $n_{\mathrm{eg}}$, $\tau$ and $a$, we can estimate loaded $Q$-factors of approximately $20\,000$ at a wavelength of $1550\,\mathrm{nm}$ for each of the racetrack resonators R1 and R2 using the relation [278]

$$Q \approx \frac{n_{\mathrm{eg}}\,\omega L}{2c}\,\frac{\sqrt{a}\,\tau}{1-a\,\tau^2}. \tag{A.3}$$

With the extracted parameters of both resonators at hand, we can now simulate the response of the filter circuit, which comprises the Sagnac loop mirror with the Vernier pair of tunable racetrack resonators. To this end, we first calculate the frequency-dependent drop-port power transmission $T_{\mathrm{drp}}(\omega)$ of each individual resonator, which is given by

$$T_{\mathrm{drp}}(\omega) = \left| \frac{-\sqrt{a}\,\kappa^2 \mathrm{e}^{\mathrm{j}\theta(\omega)/2}}{1-a\,\tau^2 \mathrm{e}^{\mathrm{j}\theta(\omega)}} \right|^2 . \tag{A.4}$$

The overall frequency-dependent reflection of the Sagnac loop mirror finally results from the multiplication of the individual drop-port power transmissions [J1] and is shown in Fig. A.1(b). For the plot, we assume that the racetrack resonators R1 and R2 are tuned to maximum transmission at the center frequency of our tuning range, $f_{\mathrm{c}} = \omega_{\mathrm{c}}/(2\pi) = 196.6\,\mathrm{THz}$ corresponding to $\lambda_{\mathrm{c}} = 1525\,\mathrm{nm}$, such that the calculated resonances coincide at this wavelength. The peak at the common resonance indicates the on-chip reflection loss of the tunable mirror, which amounts to $0.1\,\mathrm{dB}$, see zoom-in in Fig. A.1(b), and is assumed to be essentially constant over the entire tuning range. From the depicted reflection

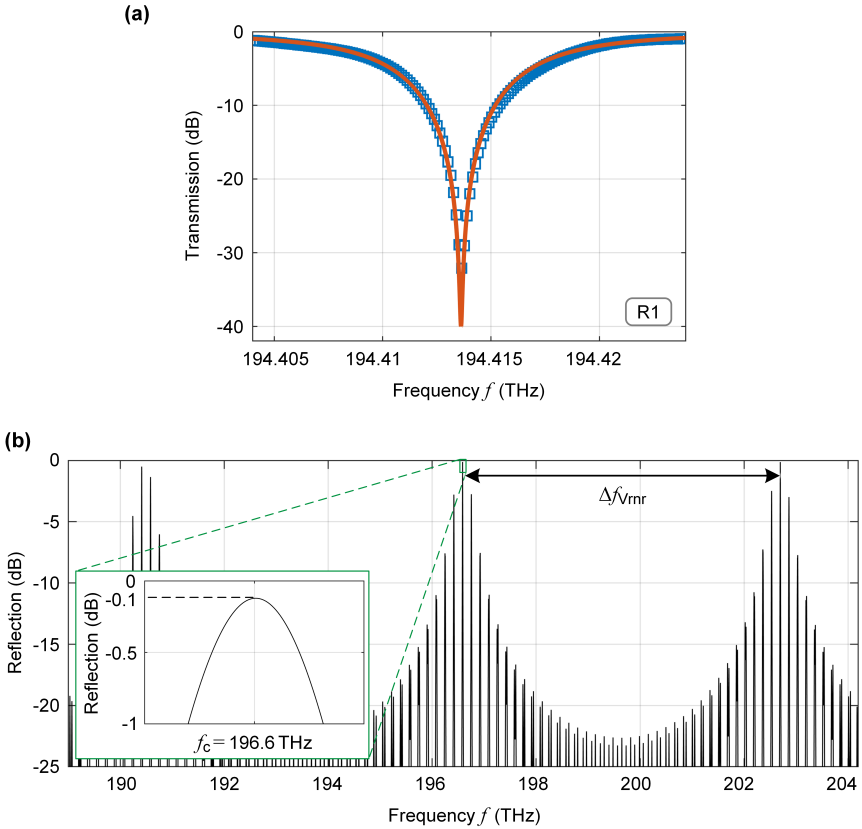


**Fig. A.1:** Characterization results of the ECL filter chip containing a Sagnac loop mirror with a Vernier pair of tunable racetrack resonators R1 and R2, see Fig. 3.1(b). **(a)** Measured through-port power transmission $T_{\mathrm{thrgh}}(\omega)$ (blue squares) and fit according to Eq. (A.2) (orange line), shown for one exemplary resonance dip of R1. **(b)** Overall frequency-dependent reflection of the Sagnac loop mirror resulting from the multiplication of the individual drop-port power transmissions of R1 and R2. The peak at the common resonance $f_{\mathrm{c}} = 196.6\,\mathrm{THz}$ indicates the on-chip reflection loss of the tunable mirror and amounts to $0.1\,\mathrm{dB}$, see zoom-in.

spectrum, we can further estimate the spectral spacing $\Delta f_{\mathrm{Vrnr}}$ between the strong main reflection peak and the two most prominent side peaks that are most prone to generate unwanted lasing modes, see Fig. A.1(b). For our device we find

$\Delta f_{\mathrm{Vrnr}} \approx 6.2\,\mathrm{THz}$, corresponding to $\Delta\lambda_{\mathrm{Vrnr}} \approx 48\,\mathrm{nm}$ when tuning the main peak to the center wavelength of $\lambda_{\mathrm{c}} = 1525\,\mathrm{nm}$, in accordance with the relation $\Delta f_{\mathrm{Vrnr}} = (\Delta f_{\mathrm{FSR,R1}} \Delta f_{\mathrm{FSR,R2}})/(\Delta f_{\mathrm{FSR,R2}} - \Delta f_{\mathrm{FSR,R1}}) \approx 6.3\,\mathrm{THz}$ [J1]. Note that, in contrast to earlier models of Vernier feedback structures [J1, 108, 190, 192, 193, 196], the consideration of GVD in Eq. (A.4) leads to an asymmetric reflection spectrum. When tuned to the center wavelength of the emission range, $\lambda_{\mathrm{c}} = 1525\,\mathrm{nm}$, we find the low-frequency side peak of the reflection spectrum around $f_{\mathrm{c}} - \Delta f_{\mathrm{Vrnr}}$ to be $0.4\,\mathrm{dB}$ lower than the main peak, whereas the high-frequency side peak around $f_{\mathrm{c}} + \Delta f_{\mathrm{Vrnr}}$ is only $0.01\,\mathrm{dB}$ lower than the main peak. Notably, while the spectral spacing $\Delta f_{\mathrm{Vrnr}}$ of the Vernier peaks is generally expected to limit the tuning range of the ECL, we find that our device features a tuning range for single-mode lasing of $11.6\,\mathrm{THz}$ ($90\,\mathrm{nm}$), which significantly exceeds the measured spacing of the Vernier peaks, $\Delta f_{\mathrm{Vrnr}} \approx 6.2\,\mathrm{THz}$ ($\Delta\lambda_{\mathrm{Vrnr}} \approx 48\,\mathrm{nm}$). This is consistent with previous demonstrations using the same TriPleX® filter chips [20, 114]. We attribute this effect to the fact that the cavity phase tuner (CPT) gives an additional degree of freedom to favor a certain desired longitudinal lasing mode of the overall cavity, while suppressing lasing at unwanted modes in the Vernier side peaks.

## A.2 Photonic wire bond loss estimation

For estimating the PWB loss, we compare the on-chip output power $P_{\mathrm{out}}$ of the ECL to the saturated output power $P_{\mathrm{sat}}$ of the RSOA at the same wavelength $\lambda$ and at the same injection currents $I$. As a first step, we use the data obtained from the RSOA characterization prior to assembly of the ECL module and extract the current-dependent saturated RSOA output power $P_{\mathrm{sat}}(I)$. To this end, we launch light at a wavelength $\lambda \approx 1550\,\mathrm{nm}$ into the RSOA through a circulator using an AR-coated lensed single-mode fiber (SMF) and measure the amplified signal after the circulator. The RSOA is similar to the one used in [J1], where the details of the measurement technique are described in the Supplementary Information. In our measurements, we vary the RSOA pump current between $20\,\mathrm{mA}$ and $100\,\mathrm{mA}$

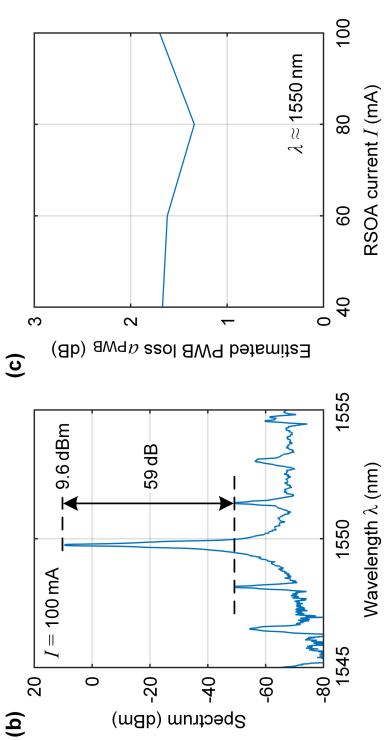


**Fig. A.2:** Procedure for PWB loss estimation. We compare the on-chip output power $P_{\mathrm{out}}$ of the ECL to the saturated output power $P_{\mathrm{sat}}$ of the RSOA at the same wavelength $\lambda \approx 1550\,\mathrm{nm}$ and the same injection currents $I$. **(a)** RSOA characterization results describing the current-dependent saturated output power $P_{\mathrm{sat}}(I)$ of the RSOA. The data was obtained by launching light at a wavelength $\lambda \approx 1550\,\mathrm{nm}$ into the RSOA through a circulator using an AR-coated lensed single-mode fiber (SMF) and by measuring the amplified signal after the circulator. We vary the RSOA pump current between 20 mA and 100 mA in steps of 20 mA and derive the associated relationships between the RSOA input and output power, both measured at the RSOA chip facet. The device was tested with 12 discrete input power levels – for better visibility, we indicated the full set of measurement points as individual dots only at a pump current of $I = 20\,\mathrm{mA}$. The saturated output power for each pump current is found at an on-chip input power of 2.2 dBm, indicated by the respective measurement points. The horizontal dashed line indicates the saturation power $P_{\mathrm{sat}}(100\,\mathrm{mA}) = 11.4\,\mathrm{dBm}$ at the RSOA facet. **(b)** Spectrum of the ECL emission when tuning the device to a wavelength of approximately $\lambda = 1550\,\mathrm{nm}$, indicating an SMSR of 59 dB. The injection current of $I = 100\,\mathrm{mA}$ leads to an on-chip output power of $P_{\mathrm{out}}(100\,\mathrm{mA}) = 9.6\,\mathrm{dBm}$. We again vary the pump current between 20 mA and 100 mA in steps of 20 mA and extract the peak powers $P_{\mathrm{out}}(I)$ from the spectra measured by an OSA. **(c)** Result of PWB loss estimation for different RSOA injection currents. Taking into account the attenuation of 0.1 dB of the resonance-aligned racetrack resonators and neglecting further on-chip losses, we find the output power $P_{\mathrm{out,PWB}}(I)$ of the PWB. The PWB coupling efficiency is then estimated by taking the previously measured saturation RSOA output power $P_{\mathrm{sat}}(I)$ as an input from the RSOA into the PWB in Fig. 3.1(b), $\eta_{\mathrm{PWB}} = P_{\mathrm{out,PWB}}(I)/P_{\mathrm{sat}}(I)$. This leads to an estimated insertion loss of the PWB of $\alpha_{\mathrm{PWB}} = -10\log_{10}(\eta_{\mathrm{PWB}}) = (1.6 \pm 0.2)\,\mathrm{dB}$.

in steps of 20 mA and derive the associated relationships between the RSOA input and output power, both measured at the RSOA chip facet, see Fig. A.2(a). The device was tested with 12 discrete input power levels – for better visibility, we indicated the full set of measurement points as individual dots only at a pump current of $I = 20$ mA. The saturated output power for each pump current is found at an on-chip input power of 2.2 dBm, indicated by the respective measurement points. The horizontal dashed line indicates the saturation power $P_{\mathrm{sat}}(100\,\mathrm{mA}) = 11.4\,\mathrm{dBm}$ at the RSOA facet.

To find the on-chip output power $P_{\mathrm{out}}$ of the ECL, we couple the light emitted from the $Si_3N_4$ output WG into an SMF. We then use the fiber-chip coupling loss, obtained from a straight reference WG on the same $Si_3N_4$ chip, to estimate the on-chip power levels $P_{\mathrm{out}}$. In this experiment, we again tune the emission wavelength to approximately $\lambda = 1550$ nm and again vary the pump current between 20 mA and 100 mA in steps of 20 mA. For each current, we record the output spectrum using an OSA, and extract the peak powers $P_{\mathrm{out}}(I)$. For an injection current of $I = 100$ mA an on-chip output power $P_{\mathrm{out}}(100\,\mathrm{mA}) = 9.6$ dBm is measured, see Fig. A.2(b) for an exemplary ECL spectrum. Taking into account the attenuation of 0.1 dB of the resonance-aligned racetrack resonators and neglecting further on-chip losses, we find the output power $P_{\mathrm{out,PWB}}(I)$ of the PWB. The PWB coupling efficiency is then estimated by taking the previously measured saturation RSOA output power $P_{\mathrm{sat}}(I)$ as an input from the RSOA into the PWB in Fig. 3.1(b), $\eta_{\mathrm{PWB}} = P_{\mathrm{out,PWB}}(I)/P_{\mathrm{sat}}(I)$. This leads to an estimated insertion loss of the PWB of $a_{\mathrm{PWB}} = -10\log_{10}(\eta_{\mathrm{PWB}}) = (1.6 \pm 0.2)$ dB, see Fig. A.2(c).

## A.3 Characterization of the $Si_3N_4$ chip in the Kerr comb module (CM)

The $Si_3N_4$ chip with the high-$Q$ ring resonator used for Kerr comb generation in the second part of the experiment was fabricated using the photonic Damascene reflow process [16, 22]. The waveguide cross section has a width of 2.2 µm and a height of 900 nm to ensure anomalous group-velocity dispersion (GVD)

as needed for generation of soliton Kerr combs. The EC located at the input and output facets rely on waveguide structures in a second $Si_3N_4$ layer, which is only 200 nm thick, and which is spaced from the 900 nm-thick layer by a 100 nm-thick $SiO_2$ layer — similar structures were also used in [279]. The waveguides in the 900 nm-thick layer are down-tapered over a length of 300 µm from the usual width of 2.2 µm to a final width of 200 nm at a distance of 300 µm from the chip edge. Over the length of this tapered section, the waveguides in the 200 nm-thick upper $Si_3N_4$ layer are simultaneously up-tapered from an initial width of 200 nm to 2.1 µm and are then down-tapered again to a final width of 300 nm at the chip facet. This leads to a slightly elliptical mode field with a measured $1/e^2$-width of 3.8 µm in the horizontal and of 3.5 µm in the vertical direction, which is coupled to a tapered PWB with initial cross-section of $4.6\,\mu\text{m} \times 4.0\,\mu\text{m}$.

For characterization of the $Si_3N_4$ chip, we employ frequency comb-calibrated laser spectroscopy [280, 281] for an exact measurement of the dispersion characteristics and the quality factor of R3. All characterization measurements and all comb-generation experiments are performed using the fundamental TE mode of the on-chip waveguides. The dispersion can again be extracted from the transmission spectrum. In contrast to the model of Eq. (A.1), the dispersion of the ring resonators for Kerr-comb generation is usually represented in terms of the deviation $D_{\text{int}}$ of the resonance frequencies from an equidistant grid, where the various resonant frequencies of R3 are given by $\omega_{\text{res},n}$, and where the index $n = 0$ corresponds to a central resonance frequency $\omega_{\text{res},0} = 2\pi \cdot 192.3\,\text{THz}$

$$D_{\text{int}} = \omega_{\text{res},n} - \big(\omega_{\text{res},0} + nD_1\big) = \sum_{m\,\geq 2} \frac{n^m D_m}{m!}. \tag{A.5}$$

In this representation, the spacing of the resonance frequencies $\omega_{\text{res},n}$ is given by $D_1$, corresponding to the reciprocal of $\theta_{\text{c}}^{(1)}$, i.e., $D_1 = \Delta\omega_{\text{FSR}} = 1/\theta_{\text{c}}^{(1)}$, whereas $D_2$ represents the GVD. A measured dispersion landscape for ring resonator R3 is given in Fig. A.3(a). Fitting Eq. (A.5) to the measured data, we can find an FSR of $D_1/(2\pi) = 35.4\,\text{GHz}$ as well as a positive second-order dispersion element $D_2/(2\pi) = 139.6\,\text{kHz} > 0$, indicating anomalous GVD as needed for Kerr-comb generation. To estimate the quality factor of the ring resonator R3,

each resonance of the measured transmission spectrum is fitted using a model based on coupled-mode theory [282, 283]. The results of a statistical analysis of the resonator transmission spectra is shown in Fig. A.3(b), revealing an average quality factor of $Q \approx 15 \times 10^6$.

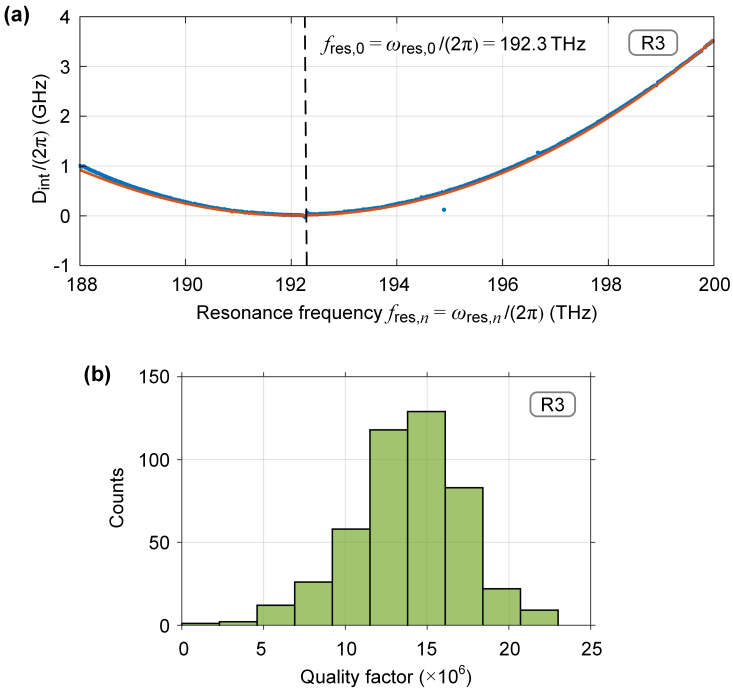


**Fig. A.3:** Characterization results of the high-$Q$ $Si_3N_4$ ring resonator R3 used for Kerr-comb generation. **(a)** Measured dispersion landscape [280] $D_{\mathrm{int}}/(2\pi)$ (blue dots) and fit according to Eq. (A.5) (orange line), revealing an FSR of $D_1/(2\pi) = 35.4$ GHz and a second-order dispersion element $D_2/(2\pi) = 139.6\,\mathrm{kHz} > 0$, corresponding to anomalous group velocity dispersion as needed for Kerr-comb generation. **(b)** Results of a statistical analysis of the various resonances of R3, revealing an average quality factor of $Q \approx 15 \times 10^6$.

*[End of Appendix of paper [J2]]*

# B 3D-printed facet-attached optical elements for connecting VCSEL and photodiodes to fiber arrays and multi-core fibers

This chapter has been published as Appendix of [J3]. The material from the publication has been adapted to comply with the layout and the structure of this thesis.

*[Beginning of Appendix of paper [J3]]*

## B.1 Beam quality measurements

For designing the facet-attached microlenses (FaML), multimode light propagation is emulated by using Gaussian beams with an effective wavelength $\lambda_{\text{eff}} = M^2\lambda$ that is increased with respect to the true vacuum wavelength $\lambda$ of the underlying device by the measured beam quality factor $M^2$. In the following, we shortly sketch the mathematical background of this approach, the foundations of which are explained in more detail in [284–293].

One of the most general mathematical descriptions valid for all types of coherent and non-coherent optical beams relies on the so-called Wigner distribution function (WDF), first introduced by Wigner in 1932 in the context of quantum states represented as a distribution in terms of both position and momentum [291]. In the following, we assume Cartesian coordinates $(x, y, z)$, where the beam axis

corresponds to the $z$-axis without loss of generality, and where the transverse position vector is given by $\vec{r}_\mathrm{t} = (x, y)^\mathrm{T}$. For the most general case, the complex-valued components $\underline{\vec{E}}(x, y, z)$ of the electric field are non-stationary stochastic processes in $x$ and $y$, and the associated coherence function (autocorrelation) $\Gamma(\vec{r}_{\mathrm{t},1}, \vec{r}_{\mathrm{t},2}; z)$ depends individually on both transverse positions $\vec{r}_{\mathrm{t},1}$ and $\vec{r}_{\mathrm{t},2}$ rather than on the difference $\vec{r}_{\mathrm{t},1} - \vec{r}_{\mathrm{t},2}$ only. The WDF is obtained by re-writing the coherence function as $\Gamma\big(\vec{r}_\mathrm{t} + \vec{r}\,'_\mathrm{t}/2, \vec{r}_\mathrm{t} - \vec{r}\,'_\mathrm{t}/2; z\big)$ with position vector $\vec{r}_\mathrm{t} = (x, y)^\mathrm{T}$ and offset vector $\vec{r}\,'_\mathrm{t} = (x', y')^\mathrm{T}$ and by computing the two-dimensional Fourier transform with respect to $\vec{r}\,'_\mathrm{t}$,

$$\tilde{W}(\vec{r}_\mathrm{t}, \vec{k}_\mathrm{t}; z) = \iint \Gamma\left(\vec{r}_\mathrm{t} + \frac{\vec{r}\,'_\mathrm{t}}{2}, \vec{r}_\mathrm{t} - \frac{\vec{r}\,'_\mathrm{t}}{2}; z\right) \mathrm{e}^{-\mathrm{j}\vec{k}_\mathrm{t}^\mathrm{T} \cdot \vec{r}\,'_\mathrm{t}} \,\mathrm{d}x'\mathrm{d}y'. \tag{B.1}$$

The corresponding components $k_{\mathrm{t},x}$ and $k_{\mathrm{t},y}$ of the transverse spatial-frequency vector $\vec{k}_\mathrm{t}$ can be interpreted as transversal projection $\vec{k}_\mathrm{t} = (k_{\mathrm{t},x}, k_{\mathrm{t},y})^\mathrm{T} = k\vec{\Theta}_\mathrm{t}$ of a paraxial wave-propagation vector $\vec{k}$, where $k = \omega n/c = 2\pi n/\lambda$ denotes the wavenumber in the respective medium with refractive index $n$ and where $\vec{\Theta}_\mathrm{t} = (\theta_x, \theta_y)^\mathrm{T}$ indicates the direction of the transverse wave-vector components. One can then rewrite Eq. (B.1) as

$$\begin{aligned} W\left(\begin{pmatrix} x \\ y \end{pmatrix}, \begin{pmatrix} \theta_x \\ \theta_y \end{pmatrix}; z\right) = \iint \Gamma\left(\begin{pmatrix} x \\ y \end{pmatrix} + \frac{1}{2}\begin{pmatrix} x' \\ y' \end{pmatrix}, \begin{pmatrix} x \\ y \end{pmatrix} - \frac{1}{2}\begin{pmatrix} x' \\ y' \end{pmatrix}; z\right) \\ \times\ \mathrm{e}^{-\mathrm{j}k(x'\theta_x + y'\theta_y)} \,\mathrm{d}x'\,\mathrm{d}y', \end{aligned} \tag{B.2}$$

where we use the notation $W$ without the tilde to denote the WDF in terms of the arguments $\theta_x$ and $\theta_y$. While it is difficult to assign a physical meaning to the WDF itself, the corresponding marginal distribution obtained by integration over $\theta_x$ and $\theta_y$ can be interpreted as the spatial intensity distribution $I(x, y; z)$,

$$I(x, y; z) = \left(\frac{k}{2\pi}\right)^2 \iint W\left(\begin{pmatrix} x \\ y \end{pmatrix}, \begin{pmatrix} \theta_x \\ \theta_y \end{pmatrix}; z\right) \mathrm{d}\theta_x \,\mathrm{d}\theta_y. \tag{B.3}$$

The total power $P$ of the beam is obtained by integrating the spatial intensity distribution over the two transverse coordinates $x$ and $y$,

$$\begin{aligned} P(z) &= \iint I(x, y; z)\,\mathrm{d}x\,\mathrm{d}y \\ &= \left(\frac{k}{2\pi}\right)^2 \iiiint W\left(\begin{pmatrix} x \\ y \end{pmatrix}, \begin{pmatrix} \theta_x \\ \theta_y \end{pmatrix}; z\right) \mathrm{d}\theta_x\,\mathrm{d}\theta_y\,\mathrm{d}x\,\mathrm{d}y. \end{aligned} \tag{B.4}$$

In analogy to Eqs. (B.3) and (B.4), the marginal distribution obtained by integration over $x$ and $y$ corresponds to the $z$-dependent spatial power spectrum, and the total power of the beam is again obtained by additionally integrating over $\theta_x$ and $\theta_y$. With the previous definitions in Eqs. (B.2)–(B.4), one can then define a normalized average value $\bar{f}(z)$ of any function $f(x, y, \theta_x, \theta_y)$ weighted by the WDF,

$$\bar{f}(z) = \frac{1}{P}\left(\frac{k}{2\pi}\right)^2 \iiiint f(x, y, \theta_x, \theta_y)\, W\left(\begin{pmatrix} x \\ y \end{pmatrix}, \begin{pmatrix} \theta_x \\ \theta_y \end{pmatrix}; z\right) \mathrm{d}\theta_x\,\mathrm{d}\theta_y\,\mathrm{d}x\,\mathrm{d}y. \tag{B.5}$$

In the following, we assume that the propagation of light in our assemblies can be described by so-called aligned simple astigmatic (ASA) beams, which is a common assumption for laser beams [292]. For ASA beams, the $x$- and the $y$-axis of the coordinate system can be chosen such that the WDF $W((x, y)^{\mathrm{T}}, (\theta_x, \theta_y)^{\mathrm{T}}; z)$ can be separated and expressed by a product of two functions $f_1(x, \theta_x; z)$ and $f_2(y, \theta_y; z)$, each of which depends only on one of the transverse directions $x$ or $y$ and on the corresponding transverse components $\theta_x$ or $\theta_y$ of the direction vector $\vec{\Theta}_{\mathrm{t}}$. In the case of light emitted by a laser, an ASA beam can be thought of as a beam with elliptical intensity distributions in the transverse plane, where the major and minor axis of the ellipses are aligned along the $x$- and the $y$-direction. The second

central moments $\sigma_x^2(z)$ and $\sigma_y^2(z)$ of the intensity distribution $I(x, y; z)$ can then be found by adopting Eq. (B.5) accordingly,

$$\begin{aligned}\sigma_x^2(z) &= \frac{\iint (x - \bar{x})^2 I(x, y; z)\,\mathrm{d}x\,\mathrm{d}y}{\iint I(x, y; z)\,\mathrm{d}x\,\mathrm{d}y},\\ \sigma_y^2(z) &= \frac{\iint (y - \bar{y})^2 I(x, y; z)\,\mathrm{d}x\,\mathrm{d}y}{\iint I(x, y; z)\,\mathrm{d}x\,\mathrm{d}y},\end{aligned} \tag{B.6}$$

where

$$\bar{x} = \frac{\iint x\, I(x, y; z)\,\mathrm{d}x\,\mathrm{d}y}{\iint I(x, y; z)\,\mathrm{d}x\,\mathrm{d}y}, \quad \bar{y} = \frac{\iint y\, I(x, y; z)\,\mathrm{d}x\,\mathrm{d}y}{\iint I(x, y; z)\,\mathrm{d}x\,\mathrm{d}y}, \tag{B.7}$$

denote the first moments of the intensity distribution $I(x, y; z)$. Assuming beams that propagate along the $z$-direction within the limitations of the paraxial approximation, it can be shown [290] that the second central moments $\sigma_x^2(z)$ and $\sigma_y^2(z)$ of the intensity distributions as given by Eq. (B.6) evolve according to a simple quadratic relationship,

$$\sigma_x^2(z) = \sigma_{0,x}^2 + \sigma_{\theta_x}^2 (z - z_{0,x})^2, \quad \sigma_y^2(z) = \sigma_{0,y}^2 + \sigma_{\theta_y}^2 (z - z_{0,y})^2. \tag{B.8}$$

The two expressions in Eq. (B.8) are governed by an overall six parameters: The waist positions $z_{0,x}$ and $z_{0,y}$, the associated variances $\sigma_{0,x}^2$ and $\sigma_{0,y}^2$ of the WDF or, equivalently, of the intensity distribution along the $x$- and the $y$-direction, and two additional parameters $\sigma_{\theta_x}^2$ and $\sigma_{\theta_y}^2$ that describe the divergence of the beam in $x$- and $y$-direction, respectively.

The previous relations can also be applied to a fundamental Gaussian $\mathrm{TEM}_{00}$ beam, i.e., a monochromatic Gaussian beam containing only the fundamental Hermite–Gaussian mode, propagating under the restrictions of paraxial optics. In this case, the divergences in the $x$- and $y$-direction are directly linked to the corresponding variances $\sigma_{\mathrm{G}0,x}^2$ and $\sigma_{\mathrm{G}0,y}^2$ of the intensity distributions in the respective waist at $z = z_{0,x}$ and $z = z_{0,y}$,

$$\sigma_{\mathrm{G},x}^2(z) = \sigma_{\mathrm{G0},x}^2 + \left(\frac{\lambda}{4\pi n\, \sigma_{\mathrm{G0},x}}\right)^2 (z - z_{0,x})^2,$$
$$\sigma_{\mathrm{G},y}^2(z) = \sigma_{\mathrm{G0},y}^2 + \left(\frac{\lambda}{4\pi n\, \sigma_{\mathrm{G0},y}}\right)^2 (z - z_{0,y})^2. \tag{B.9}$$

This leads to a constant product of the standard deviations $\sigma_{\mathrm{G0},x},\ \sigma_{\mathrm{G0},y}$ and of corresponding divergence parameters $\tan\psi_{\mathrm{G},x},\ \tan\psi_{\mathrm{G},y}$,

$$\sigma_{\mathrm{G0},x} \tan\psi_{\mathrm{G},x} = \sigma_{\mathrm{G0},y} \tan\psi_{\mathrm{G},y} = \frac{\lambda}{4\pi n}, \tag{B.10}$$

where

$$\tan\psi_{\mathrm{G},x} = \lim_{z\to\infty} \frac{\sigma_{\mathrm{G},x}(z)}{z} = \frac{\lambda}{4\pi n\, \sigma_{\mathrm{G0},x}},$$
$$\tan\psi_{\mathrm{G},y} = \lim_{z\to\infty} \frac{\sigma_{\mathrm{G},y}(z)}{z} = \frac{\lambda}{4\pi n\, \sigma_{\mathrm{G0},y}}. \tag{B.11}$$

Note that the variances $\sigma_{\mathrm{G},x}^2$ and $\sigma_{\mathrm{G},y}^2$ specified in Eq. (B.9) relate to the radius over which the Gaussian intensity profile has dropped by a factor of 1/e compared to the on-axis maximum of the intensity. These variances can be translated into more widely used definitions of beam radii $w_{\mathrm{G},x} = 2\sigma_{\mathrm{G},x}$ and $w_{\mathrm{G},y} = 2\sigma_{\mathrm{G},y}$, which refer to the $1/e^2$ intensity points. Similarly, the beam divergence parameters $\tan\psi_{\mathrm{G},x}$ and $\tan\psi_{\mathrm{G},y}$ refer to the half-angle of an elliptical cone defined by the 1/e intensity contour lines, whereas it is more common to specify beam divergences $\tan\theta_{\mathrm{G},x} = 2\tan\psi_{\mathrm{G},x}$ and $\tan\theta_{\mathrm{G},y} = 2\tan\psi_{\mathrm{G},y}$ that relate to the $1/e^2$ contours.

For multimode beams, the direct connection between the standard deviations and divergence parameters according to Eq. (B.10) does not apply anymore. Still, it can be shown that the product of the divergence parameters $\tan\psi_x,\ \tan\psi_y$ and the standard deviations $\sigma_{0,x},\ \sigma_{0,y}$ of the intensity distribution in the respective beam waist is an invariant property of the beam which is conserved by any lossless transformation of the beam, e.g., through lenses or mirrors [293]. The behavior of the multimode beam can thus be approximated by using a virtual fundamental

Gaussian $\mathrm{TEM}_{00}$ beam with an effectively increased wavelength $\lambda_{\mathrm{eff}} = M^2\lambda$ that leads to the same product of divergence parameter and corresponding variance of the intensity distribution. The beam-quality factor $M^2 = \lambda_{\mathrm{eff}}/\lambda \geq 1$ is then a measure of the multimodedness of the beam. This consideration can be done separately for the $x$- and the $y$-direction, which may result in separate beam quality factors $M_x^2$ and $M_y^2$,

$$\sigma_{0,x} \tan\psi_x = M_x^2 \frac{\lambda}{4\pi n}, \quad \sigma_{0,y} \tan\psi_y = M_y^2 \frac{\lambda}{4\pi n}. \tag{B.12}$$

The only remaining task is now to extract the quality factors $M_x^2$ and $M_y^2$ of the beams emitted by our devices. To this end, we measure the intensity profiles $I(x, y; z)$ in a series of positions along the propagation direction $z$ using a microscope objective and a camera. We drive the VCSEL and move it with respect to the fixed objective using a motorized stage. All measurements are performed at a bias current of 3.3 mA, which was also used for the coupling-loss and data-transmission experiments, see, e.g., Section 4.4.2. From the recorded beam intensity profiles $I(x, y; z)$, we extract the second central moments $\sigma_x^2$ and $\sigma_y^2$ in $x$- and $y$-direction according to Eq. (B.6). In the measurement, sensor saturation must be avoided, and any background illumination needs to be subtracted. The waist positions $z_{0,x}$ and $z_{0,y}$, the associated variances $\sigma_{0,x}^2$ and $\sigma_{0,y}^2$ of the intensity distribution, and the beam-divergence parameters $\sigma_{\theta_x}^2$ and $\sigma_{\theta_y}^2$ are then extracted via a parameter fit using Eq. (B.8). The beam quality factors $M_x^2$ and $M_y^2$ are then given by $M_x^2 = (4\pi n/\lambda)\,\sigma_{0,x} \tan\psi_x$ and $M_y^2 = (4\pi n/\lambda)\,\sigma_{0,y} \tan\psi_y$, where the vacuum wavelength amounts to $\lambda = 850\,\mathrm{nm}$.

The result of the VCSEL beam characterization is shown in Fig. B.1, where we plot the beam radii $w_x = 2\sigma_x$ (round markers) and $w_y = 2\sigma_y$ (square markers) as a function of the axial position $(z - z_{\mathrm{s}})$, where $z_{\mathrm{s}}$ corresponds to the surface of the VCSEL. Fitting the data to Eq. (B.8) yields the plots shown in blue and red, characterized by $M_x^2 = 5.4$ and $M_y^2 = 4.2$ for beam-waist radii of $w_{0,x} = w_{0,y} = 7\,\mu\mathrm{m}$ at $z_{0,x} = z_{0,y} = 0\,\mu\mathrm{m}$. The average Rayleigh length for the profiles in $x$- and in $y$-direction amounts to $z_{\mathrm{R}} = 38\,\mu\mathrm{m}$ as indicated by the vertical line.

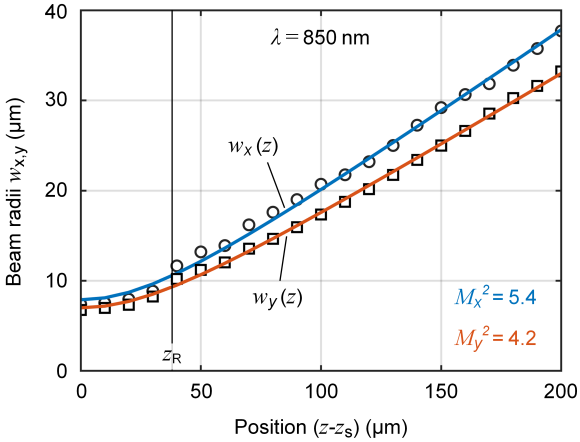


**Fig. B.1:** Result of the VCSEL beam characterization. The measurements were taken using a $100\times$ / 0.8 microscope objective. The round and the square markers depict the beam radii $w_x = 2\sigma_x$ and $w_y = 2\sigma_y$ as a function of the axial position $(z - z_s)$ where $z_s$ corresponds to the surface of the VCSEL. Solid lines indicate a data fit to Eq. (B.8), resulting in beam quality factors $M_x^2 = 5.4$ and $M_y^2 = 4.2$ for beam waist radii $w_{0,x} = w_{0,y} = 7\,\mu\text{m}$ at $z_{0,x} = z_{0,y} = 0\,\mu\text{m}$. The average Rayleigh length amounts to $z_R = 38\,\mu\text{m}$ as indicated by the vertical line.

## B.2 Microlens simulations

For simulation of the FaML, we use an in-house developed simulation software based on the scalar wide-angle unidirectional wave-propagation method for step-index structures [229]. For all lens surfaces in our experiments, we use a rotational symmetric even-order polynomial with three free parameters $c_0, c_2$ and $c_4$ to represent the lens surface height above the $(x, y)$-plane,

$$h(r) = c_0 + c_2 r^2 + c_4 r^4 + ..., \qquad r = \sqrt{x^2 + y^2}. \tag{B.13}$$

Simulations are carried out by using the effective beam quality factor $M_{\text{eff}}^2 = \sqrt{M_x^2 \times M_y^2} = 4.8$, which is obtained as the geometrical mean [292] of

the measured beam quality factors $M_x^2 = 5.4$ and $M_y^2 = 4.2$ along the respective principle axis of the beam, see Appendix B.1. Note that this simplified description by a single effective beam quality factor $M_{\text{eff}}^2$ in fact implies treating the beam as a stigmatic beam which is rotationally symmetric with respect to the $z$-axis [288]. This assumption is backed by the fact that the average ellipticity parameter $\bar{\varepsilon} = \big(1/N\big) \sum_{i=1}^{N} w_y(z_i)/w_x(z_i)$ over the $N = 21$ measured $z$-positions is larger than $0.87$ and the beam profiles may therefore be considered to be of circular symmetry according to the ISO/IEC 11146-1 standard [292]. The multimode beam at vacuum wavelength $\lambda = 850\,\text{nm}$ is consequently emulated by a single effective wavelength $\lambda_{\text{eff}} = \lambda M_{\text{eff}}^2 = 4.08\,\mu\text{m}$ [287, 289].

## B.3 Fabrication

The FaML in our assemblies discussed in Section 4.3 and 4.4 are printed separately to the VCSEL / PD chips and the facet of the MT ferrule using high-resolution multi-photon lithography [68]. For convenience, the two printing steps have been carried out simultaneously on separate machines with a known-good set of parameters for the respective photoresist used.

The FaML on the MT ferrule were fabricated using an in-house-built lithography system with a Zeiss Plan-Apochromat objective ($40\times$ / $1.4$ Oil DIC M27), galvanometer-actuated mirrors, and a $780\,\text{nm}$ femtosecond laser (Menlo C-Fiber 780 HP). To this end, the MT ferrule is mounted into a dedicated holder. The objective approaches the facets of the fibers in the MT ferrule along the $+y$-direction, see Fig. 4.1. After immersion in the liquid negative-tone photoresist (IP-Dip, Nanoscribe GmbH), the exact printing positions are found using machine vision. The lithography beam is oriented in parallel to the fiber axes, and the fiber cores are back-illuminated for easier detection.

The FaML on the VCSEL / PD chip are fabricated using a commercially available printing system (Sonata1000, Vanguard Automation GmbH). For simplicity, we print the FaML after mounting the VCSEL / PD arrays to the underlying PCB. In this step, the PCB is fixed by a dedicated holder, and liquid negative-tone photoresist (VanCore B, Vanguard Automation GmbH) is dispensed on the VCSEL / PD arrays. The lithography objective approaches the PCB along the $-z$-direction, see Fig. 4.1. Again, we use machine-vision to find the printing positions. The axis of the lithography beam is perpendicular to the facets of the VCSEL / PD arrays, and the photoresist serves as an immersion liquid.

Independently of the photoresist and lithography machine used, the exposed structures undergo the same post-processing. After development in propylene-glycol-methyl-etheracetate (PGMEA) for 15 minutes, the samples are flushed with isopropanol, and subsequently blow-dried.

## B.4 Long-term stability

Long-term stability of 3D-printed FaML is a key aspect with respect to practical application of the concept. To investigate this aspect, we monitor the evolution of the coupling loss under pertinent damp-heat test conditions. We use a simplified test structure, see Fig. B.2, store it in a climate chamber at $85\,°\mathrm{C}$ and $85\,\%$ relative humidity, and repeatedly measure the optical transmission at a wavelength of $\lambda = 1550\,\mathrm{nm}$ over the course of nearly $4000$ hours. The assembly consists of a pair of single mode fibers (SMF) glued into V-grooves. Each of the SMF facets carries a 3D-printed FaML, designed as a loopback: Light coupled into the left SMF enters the first FaML, is redirected by total-internal-reflection (TIR) at the mirror with Surface S0, collimated by the lens Surface S1, and collected by a symmetrically arranged counterpiece, see red beam path in Fig. B.2. The FaML consisted of the same photoresist (VanCore B, Vanguard Automation GmbH) used for fabrication of the FaML on the VCSEL / PD chips, see Sections 4.3 and 4.4.

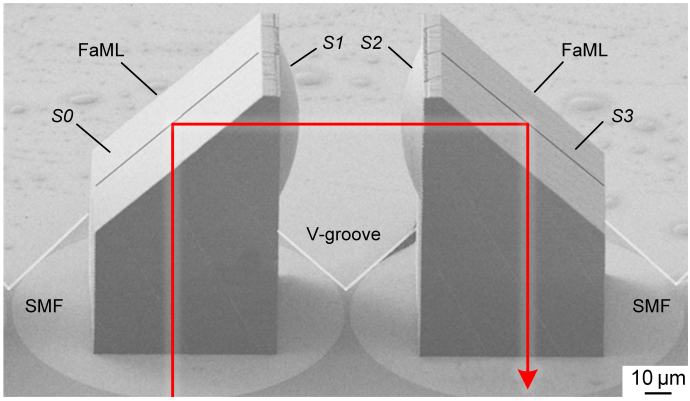


**Fig. B.2:** Scanning electron microscopy (SEM) image of a simplified test structure for evaluating the long-term stability of our 3D-printed facet-attached microlenses (FaML). The assembly consists of a pair of single mode fibers (SMF) glued into V-grooves. Each of the SMF facets carries a 3D-printed FaML, designed as a loopback: Light coupled into the left SMF enters the first FaML, is redirected by total-internal-reflection (TIR) at the mirror with Surface S0, and collimated by the lens Surface S1. The beam is then entering the second FaML through the lens Surface S2, is redirected by a second TIR mirror with Surface S3 and finally coupled into the core of the right SMF. The path of the signal is indicated by the red path and arrow. The line in the center of the TIR mirrors has been added for a better orientation.

We measured the transmission through five identical arrangements as in Fig. B.2. The results of these long-term stability tests are shown in Table B.1. Within our measurement accuracy, we did not find any sign of degradation for any of the five measured assemblies. The test had to be stopped after 3960 hours, because the single-mode connectors and the coating of the fibers had deteriorated to a degree that would not permit further reliable measurements. The FaML themselves did not show any visible degradation, see Fig. B.2.

In a further set of experiments, we investigated the stability of FaML similar to the ones shown in Fig. B.2 at standard reflow-soldering temperatures of up to 260 °C for several minutes. We did not observe any degradation of the measured transmission performance in these experiments.

**Table B.1:** Long-term stability tests of FaML at a temperature of 85 °C and at a rel. humidity of 85 %.

| Connection | Coupling loss [dB] | | | |
|---|---|---|---|---|
| | Initial | 400 h @ 80 °C/85 % | 1840 h @ 80 °C/85 % | 3960 h @ 80 °C/85 % |
| #1 | 1.4 | 1.4 | 1.5 | 1.3 |
| #2 | 1.2 | 1.2 | 1.3 | 1.4 |
| #3 | 1.5 | 1.6 | 1.9 | 1.5 |
| #4 | 1.4 | 1.6 | 1.8 | 1.5 |
| #5 | 1.5 | 1.6 | 1.5 | 1.5 |

# C Signal quality metrics for on-off-keying

In the following, we will give a brief description of a simplified IM-DD transceiver link and the associated signal quality metrics for non-return-to-zero on-off keying (NRZ-OOK), see Fig. C.1(a). The signal path consists of a laser driver, laser diode (LD), multimode fiber (MMF), photodetector (PD) and transimpedance amplifier (TIA). At the transmitter (Tx), a digital data stream consisting of logical "ones" and "zeroes" is fed to a laser driver at a rate $R$, corresponding to a time slot of width $T = 1/R$ per bit. The information is subsequently encoded onto an optical carrier emitted from the LD by direct modulation of the laser output power. This is, e.g., achieved by modulation of the LD injection current[1] with a peak-to-peak swing of $\Delta I_{\mathrm{mod}}$ about a bias current $I_{\mathrm{bias}}$. The output power of the LD is thus switched between the associated off- and on-state power levels $P_{\mathrm{Tx},0}$ and $P_{\mathrm{Tx},1}$, which correspond to a logical "0" and "1", respectively. The difference between the two Tx power levels $P_{\mathrm{Tx},1} - P_{\mathrm{Tx},0}$, i.e., the peak-to-peak swing of the transmit power around the average $\overline{P}_{\mathrm{Tx}}$, is denoted as the optical modulation amplitude (OMA). Another key parameter is the extinction ratio (ER), which is defined as the ratio of the Tx power levels $\mathrm{ER} = P_{\mathrm{Tx},1}/P_{\mathrm{Tx},0}$. After transmission of the signal over a MMF, direct detection is employed at the receiver (Rx). To this end, the received signal with the average Rx power $\overline{P}_{\mathrm{Rx}}$ is detected by a PD (responsivity $S$), which converts the input optical power variations into corresponding variations of the output electrical current about the average $\overline{I}_{\mathrm{Rx}}$.

[1] Other techniques for encoding NRZ-OOK data onto optical carries involve externally modulating a CW LD with, e.g., electro-absorption or Mach-Zehnder modulators. However, both schemes come at a higher cost, and are therefore not economically feasible for AOC.

A TIA converts the current into amplified voltage variations about the average value $\overline{U}_{\mathrm{Rx}}$, and a clock-and-data-recovery (CDR) circuit finally digitizes the received signal by sampling of the electrical signal, performing electrical-domain equalization and comparing the retrieved signal level to a threshold value at sampling times within the symbol time slot $T$. In the context of transceiver assemblies based on MCF as discussed in Chapter 4, each core effectively represents an independent transceiver link operating at a line rate of $R$. The aggregate line rate is consequently given by the multiplication of $R$ with the number of active cores in the MCF[2].

For the initial performance assessment, one often resorts to the so-called eye diagram and associated metrics. The eye diagram represents an oscilloscope display which is constructed by folding the parts of the waveform corresponding to each symbol interval into a single graph with signal amplitude on the vertical axis and time on the horizontal axis. It hence is a visualization of the probability of the signal being at each possible signal level within the duration of a unit time interval ($1\,\mathrm{UI} \equiv T = 1/R$). A typical eye diagram for NRZ-OOK at a line rate of $R = 25.78125\,\mathrm{Gbit/s}$ ($T \approx 39\,\mathrm{ps}$) and for a carrier wavelength of $850\,\mathrm{nm}$ is shown in Fig. C.1(c). Note that the vertical axis is given in units of optical power. Generally speaking, an open eye pattern corresponds to minimal signal waveform distortion, whereas intersymbol interference (ISI), system nonlinearities and noise tend to close the opening of the eye.

As elaborated in Section 2.3, cost-effectiveness is a key factor when it comes to AOC. Characterizing transceiver performance through extensive evaluation of the bit-error ratio (BER), e.g., via a dedicated BER tester (BERT) or reference Tx and Rx with known performance metrics, is therefore usually not economically

[2] While, strictly speaking, the IEEE 802.3 industry standards [161, 162] do not include data transmission over multiple cores of a multimode MCF (MM-MCF), the specifications still provide a good point of reference for comparing the performance to conventional transceiver assemblies. Specifically, the IEEE 802.3 provides validity ranges for parameters such as the average Tx and Rx power, ER, OMA and TDEC under specific signaling conditions and simultaneous transmission over all spatial channels [161]. For the purpose of this work, we thus simply adopted these specifications for the MCF link.

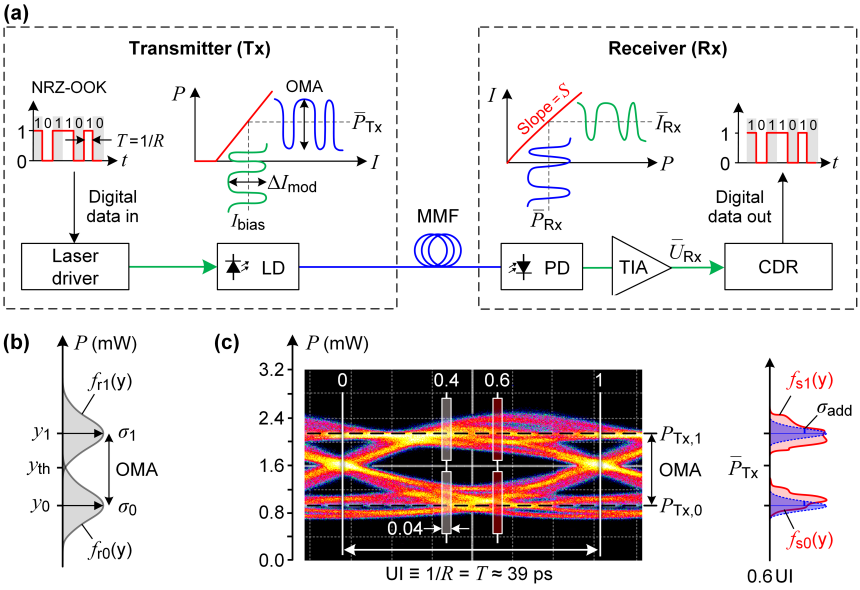


**Fig. C.1:** Schematic of a simplified intensity modulation and direct detection (IM-DD) transceiver link utilizing non-return-to-zero on-off-keying (NRZ-OOK) and exemplary eye diagram (line rate $R = 25.78125$ Gbit/s, carrier wavelength 850 nm). Abbreviations: CDR – clock-and-data-recovery; LD – laser diode; MMF — multimode fiber; OMA – optical modulation amplitude; PD – photodetector; TIA – transimpedance amplifier; UI – unit time interval. **(a)** At the transmitter (Tx), a digital data stream is fed into a laser driver and encoded onto an optical carrier by modulating the laser-diode (LD) injection current, thereby switching the output power of the LD between the associated off- and on-state power levels which correspond to a logical "0" and "1", respectively. After transmission over a fiber, direct detection is employed at the receiver (Rx). The received signal is detected by a PD (responsivity $S$), which converts the input optical power variations into corresponding variations of the output electrical current. A transimpedance amplifier (TIA) converts the current into amplified voltage variations, and a clock-and-data-recovery (CDR) circuit digitizes the received signal for retrieving the digital data stream. **(b)** If electronic additive white Gaussian noise (AWGN) dominates, the statistics of the received "ones" and "zeroes" can be well approximated by two Gaussian probability density functions (PDF) $f_{r1}(y)$ and $f_{r0}(y)$, respectively. For a given target bit-error ratio (BER) and Tx $\mathrm{OMA} = y_1 - y_0$, the $Q$-factor can be used to find a standard deviation $\sigma_1 = \sigma_0$ which represents a measure of the noise power that could be added at the Rx for the reception of an ideal Tx waveform, see Eq. C.2. **(c)** Exemplary Tx eye diagram at $R = 25.78125$ Gbit/s (1 UI $\equiv T = 1/R \approx 39$ ps) indicating the four histogram acquisition windows associated with the calculation of the transmitter-and-dispersion eye-closure (TDEC). The two PDF $f_{s1}(y)$ and $f_{s0}(y)$ captured at the right side with respect to the eye's center position (0.6 UI, red-shaded acquisition windows) are schematically illustrated as red curves. The TDEC is calculated by estimating the maximum noise power $\sigma_{add}$ of the electronic AWGN at the Rx (blue curves) that can be mathematically added to the signal within its bandwidth for a reference worst-case optical channel such that the received waveform still reaches the same target BER as in Subfigure (b).

feasible. Instead, the so-called transmitter-and-dispersion eye-closure (TDEC) [161, 294] is commonly used as a system-level predictor of the Tx performance for NRZ-OOK[3]. The conceptional idea behind the TDEC is to estimate the maximum noise power that can be mathematically added to the signal within its bandwidth for a reference worst-case optical channel such that the received waveform still reaches a defined target BER. Effects such as ISI, laser frequency-noise and RIN are directly included in the measurement, whereas link impairments and effects of the MMF such as mode partition noise and modal noise are mathematically estimated from established IEEE link models and consequently taken into account in the TDEC calculation [296, 297]. Hereby, it is assumed that all noise sources in the link are Gaussian and additive. This tolerable noise power is then compared to the noise power associated with the reception of a simulated ideal Tx waveform and identical BER [161, 296–298], assuming that the Rx features an ideally placed decision threshold and is subject to level-independent electronic AWGN[4]. Thereby, the TDEC represents a power penalty for achieving the same eye opening as an ideal Tx for a specified worst-case optical link. Importantly, the TDEC can be extracted from simple eye diagram measurements of the actual Tx waveform using a sampling oscilloscope, and the associated evaluation procedures can be straightforwardly automated, making it very cost-effective.

As a first step, we estimate the noise power associated with the reception of a simulated ideal Tx waveform. We denote the probability density functions (PDF) of the received "ones" and "zeroes" as $f_{\mathrm{r}1}(y)$ and $f_{\mathrm{r}0}(y)$, respectively, and we assume an equal distribution of "ones" and "zeroes", each occurring with probability $1/2$. The BER can then be calculated by integrating the respective tails of the two PDF associated with an erroneous detection of a "1" or "0" as [299]

$$\mathrm{BER} = \frac{1}{2}\int_{-\infty}^{y_{\mathrm{th}}} f_{\mathrm{r}1}(y)\,\mathrm{d}y + \frac{1}{2}\int_{y_{\mathrm{th}}}^{+\infty} f_{\mathrm{r}0}(y)\,\mathrm{d}y, \tag{C.1}$$

[3] Similarly, the so-called transmitter-and-dispersion eye-closure quaternary (TDECQ) can be defined for PAM4 signaling [295], which is, e.g., used in 400G Ethernet industry standards [162].

[4] This can be safely assumed, as electronic receiver noise dominates for direct-detection links without optical amplifiers in most cases of practical interest [299].

where $y_{\mathrm{th}}$ marks the decision threshold. It can then be shown [299], that for unimodal PDF $f_{\mathrm{r1}}(y)$ and $f_{\mathrm{r0}}(y)$, the minimum BER is reached if the decision threshold $y_{\mathrm{th}}$ is placed at the intersection of the two PDF, i.e., for $f_{\mathrm{r1}}(y_{\mathrm{th}}) = f_{\mathrm{r0}}(y_{\mathrm{th}})$. If electronic AWGN dominates, the statistics of the received "ones" and "zeroes" can be well approximated by two Gaussian PDF with associated mean values $y_1$ and $y_0$ and standard deviations $\sigma_1$ and $\sigma_0$, respectively, see Fig. C.1(b). The complementary error function $\mathrm{erfc}(x) = \frac{2}{\sqrt{\pi}} \int_x^{+\infty} \mathrm{e}^{-y^2}\, \mathrm{d}y$ can then be used to formulate a simple analytic expression for the optimum BER [298, 299],

$$\begin{aligned} \mathrm{BER} &= \frac{1}{4}\,\mathrm{erfc}\left(\frac{y_1 - y_{\mathrm{th}}}{\sqrt{2}\,\sigma_1}\right) + \frac{1}{4}\,\mathrm{erfc}\left(\frac{y_{\mathrm{th}} - y_0}{\sqrt{2}\,\sigma_0}\right) \\ &= \frac{1}{2}\,\mathrm{erfc}\left(\frac{Q}{\sqrt{2}}\right) \quad \text{with} \quad Q = \frac{y_1 - y_0}{\sigma_1 + \sigma_0}, \end{aligned} \tag{C.2}$$

where the last step follows from the assumption of level-independent noise ($\sigma_1 \approx \sigma_0$), i.e., $(y_1 - y_{\mathrm{th}})/\sigma_1 = (y_{\mathrm{th}} - y_0)/\sigma_0 = (y_1 - y_0)/(\sigma_1 + \sigma_0)$ must apply. The so-called $Q$-factor in Eq. C.2 is a quality metric and can be re-written in terms of the Tx $\mathrm{OMA} = y_1 - y_0$ as $Q = \mathrm{OMA}/(2\,\sigma_{\mathrm{Tx,ideal}})$ with $\sigma_{\mathrm{Tx,ideal}} = \sigma_1 = \sigma_0$. Thus, for a given target BER and Tx OMA, the standard deviation $\sigma_{\mathrm{Tx,ideal}}$ represents a measure of the noise power that could be added at the Rx for the reception of an ideal Tx waveform. For a BER of, e.g., $5 \times 10^{-5}$ as specified in the IEEE 802.3 industry standard [161], we find $Q = 3.8906$ and the associated standard deviation is given by $\sigma_{\mathrm{Tx,ideal}} = \mathrm{OMA}/7.7812$.

As a next step of the TDEC calculation, an eye diagram of the actual Tx waveform is recorded using a sampling oscilloscope, and the noise power that could be added to the detected Tx waveform by an optical channel and a Rx for achieving the same target BER as in Eq. C.2 is estimated, see Fig. C.1(c). To account for any eye distortion during BER evaluation, the procedure calculates two separate noise standard deviations $\sigma_{\mathrm{L,add}}$ and $\sigma_{\mathrm{R,add}}$, which are associated with positions that are offset to the left and to the right side from the eye's center position, respectively. Therefore, a total of four vertical histograms are extracted from the eye, one of the logical "zero" and one for the logical "one", each taken at $0.4$ UI and $0.6$ UI, i.e., at a position corresponding to a time of approximately $16$ ps and $23$ ps within the

39 ps-wide unit interval[5]. The temporal width is chosen as $0.04$ UI, corresponding to a time window of approximately $1.6$ ps. Importantly, the upper and lower limits of the histograms must be chosen such that no samples remain uncaptured. The four histogram acquisition windows are illustrated in Fig. C.1(c). From the pairs of histograms describing the distribution of "ones" and "zeroes" received from the real imperfect Tx, the PDF $f_{\mathrm{s1}}(y)$ and $f_{\mathrm{s0}}(y)$ are extracted. The two PDF captured at the right side of the eye ($0.6$ UI, red-shaded acquisition windows) are schematically illustrated in Fig. C.1(c) by the two red curves. Each histogram is normalized to $1$ and then convolved with a Gaussian distribution representing the added noise $\sigma_{\mathrm{add}}$, giving histograms that might be seen in a noisy receiver. The integral of the tail of each histogram that falls on the wrong side of the decision level $\overline{P}_{\mathrm{Tx}}$ gives the BER of that histogram for the respective added noise. We can thus determine the allowed noise standard deviation $\sigma_{\mathrm{add}}$ of the electronic AWGN at the Rx (blue curves in Fig. C.1(c)), such that the same target

$$\begin{aligned}\mathrm{BER} = &\frac{1}{4}\int f_{\mathrm{s1}}(y)\,\mathrm{erfc}\left(\frac{y-\overline{P}_{\mathrm{Tx}}}{\sqrt{2}\,\sigma_{\mathrm{add}}}\right)\mathrm{d}y \\ &+\frac{1}{4}\int f_{\mathrm{s0}}(y)\,\mathrm{erfc}\left(\frac{\overline{P}_{\mathrm{Tx}}-y}{\sqrt{2}\,\sigma_{\mathrm{add}}}\right)\mathrm{d}y\end{aligned} \tag{C.3}$$

is reached [161, 296, 297]. In Eq. C.3, the complementary error functions $\mathrm{erfc}(y)$ effectively act as a weighting function, which is large for samples near to the decision level $\overline{P}_{\mathrm{Tx}}$ and small for samples further away from the eye's center. For the special case of an ideal Tx as treated previously, the PDF can be expressed in terms of Dirac delta functions $\delta(y)$, defined as $\int_{-\infty}^{+\infty}\delta(y)h(y)\,\mathrm{d}y = h(0)$ for a test function $h(y)$. We thus find $f_{\mathrm{s1}}(y) = \delta(y-y_1)$ and $f_{\mathrm{s0}}(y) = \delta(y-y_0)$ with the respective on- and off-state Tx power levels $y_1$ and $y_0$, and Eq. C.3 hence simplifies to Eq. C.2. Equation C.3 is

[5] Note that the depicted positions and widths of the histogram acquisition windows are chosen according to the IEEE 802.3 [161] in Fig. C.1(c). However, the specific values might differ depending on the standardization organization and associated industry standard. For example, the International Telecommunication Union (ITU) defines the positions $0.425$ UI and $0.575$ UI within the unit interval for 50G passive optical networks [294].

separately evaluated for the pairs of PDF associated with the left and right side of the eye, and the value $\sigma_{\mathrm{add}}$ is consequently named $\sigma_{\mathrm{L,add}}$ and $\sigma_{\mathrm{R,add}}$. For estimating the worst-case performance, the smaller of the two values must be considered, i.e., $\sigma_{\mathrm{add}} = \min(\sigma_{\mathrm{L,add}}, \sigma_{\mathrm{R,add}})$.

We finally estimate the noise power $\sigma_{\mathrm{Tx}}$ that the Rx would be allowed to add to the Tx waveform when transmitted through a specified worst-case optical link. This includes mode partition noise, leading to phase jitter as a result of mode-hopping in the VCSEL and modal noise of the MMF as represented by the associated noise standard deviation $\sigma_{\mathrm{M}}$. Both contributions are mathematically estimated for a worst-case Tx and channel spectral properties using established IEEE link models [300]. We thus find [161, 300]

$$\begin{aligned} \sigma_{\mathrm{Tx}} &= \sqrt{\sigma_{\mathrm{add}}^2 + \sigma_{\mathrm{osc}}^2 - \sigma_{\mathrm{M}}^2} \\ &\approx (1 - M_1)\sqrt{\sigma_{\mathrm{add}}^2 + \sigma_{\mathrm{osc}}^2 - M_2^2}, \end{aligned} \tag{C.4}$$

where the last step follows from an empirical correction of $\sigma_{\mathrm{Tx}}$ by replacing $\sigma_{\mathrm{M}}^2$ through the terms $M_1 = 0.04$ and $M_2 = 0.0175\,\overline{P}_{\mathrm{Tx}}$ to correct for discrepancies that have been found between the power penalty as predicted by the TDEC compared to IEEE link models which are rooted in the estimation of the link impairments [300]. Since mode partition noise and modal noise are not yet included when finding $\sigma_{\mathrm{add}}$ according to the procedure described in Eq. C.3, the amount of tolerable noise $\sigma_{\mathrm{Tx}}$ at the Rx is reduced, leading to a negative sign for $\sigma_{\mathrm{M}}^2$ in the first line of Eq. C.4. On the other hand, finding the term $\sigma_{\mathrm{add}}$ implicitly included a noise term with standard deviation $\sigma_{\mathrm{osc}}$ associated with the oscilloscope used for taking the TDEC measurement. Therefore, the amount of tolerable noise $\sigma_{\mathrm{Tx}}$ at the Rx is increased by this amount, leading to a positive sign for $\sigma_{\mathrm{osc}}^2$ in the first line of Eq. C.4. The TDEC is then defined by relating $\sigma_{\mathrm{Tx,ideal}}$ to $\sigma_{\mathrm{Tx}}$ as calculated from Eq. C.4 in decibels,

$$\mathrm{TDEC} = 10\log_{10}(\sigma_{\mathrm{Tx,ideal}}/\sigma_{\mathrm{Tx}}). \tag{C.5}$$

In Eq. C.5, $\sigma_{\mathrm{Tx}} \leq \sigma_{\mathrm{Tx,ideal}}$ must hold true, which leads to TDEC values bigger than $0\,\mathrm{dB}$. Generally speaking, the lower the TDEC the better. The TDEC can also be interpreted as the increase in optical power required for the Tx to achieve the same eye oping as an ideal Tx for a given minimum reference BER as specified in the respective industry standard. By defining an upper bound for the TDEC, the difference to this value represents a margin for the impairments that could be tolerated on top of the mathematically considered worst-case optical link and reference Rx while still achieving the target BER. Therefore, the TDEC represents a direct figure of merit describing the quality of a Tx which can be straightforwardly utilized for ensuring compatibility among various vendors.

# D Freeform terahertz structures fabricated by multi-photon lithography and metal coating

This chapter has been published as Supplementary Information of [J4]. The material from the publication has been adapted to comply with the layout and the structure of this thesis.

*[Beginning of Supplementary Information of paper [J4]]*

## D.1 Dielectric response of the photoresist

For precise simulation and design of the THz structures, knowledge about the frequency-dependent dielectric response of the photoresist used for the 3D-printed support structures (VanCore B, Vanguard Automation GmbH, Karlsruhe, Germany) is required. We therefore measured the complex-valued relative permittivity $\underline{\epsilon}_\mathrm{r} = \epsilon' - \mathrm{j}\epsilon''$ of a photoresist sample in the frequency range between $0.220\,\mathrm{THz}$ and $0.325\,\mathrm{THz}$ using a commercially available material-characterization kit (MCK, Swissto12 SE, Renens, Switzerland).

The measurement setup is shown in Fig. D.1(a). A pair of WR-3 frequency-extension modules (V03VNA2-T/R-A, OML Inc., Morgan Hill, USA) are connected to a vector network analyzer (VNA, N5242B PNA-X, Keysight Technologies Inc., Santa Rosa, USA) via a millimeter-wave controller (N5292A, Keysight Technologies Inc.). In conjunction with the frequency-extension modules, the VNA enables $S$-parameter measurements in a frequency range from $0.220\,\mathrm{THz}$

and $0.325\,\mathrm{THz}$. The VNA is set to measure at $1001$ frequency points with an intermediate-frequency (IF) bandwidth of $500\,\mathrm{Hz}$. The MCK is directly connected to the frequency-extension modules via UG-387/UM waveguide flanges. The MCK itself consists of two corrugated horn antennas [301], effectively converting the input $\mathrm{TE}_{10}$ mode of the rectangular waveguides into a highly pure $\mathrm{HE}_{11}$ mode of the circular horn-antenna aperture. This allows for a plane-wave-like irradiation of the dielectric sample, which is placed in the gap between the two antennas. Prior to the actual measurement, the setup is calibrated using the gated-reflect-line (GRL) calibration technique [302]. Time-domain gating with a manufacturer-recommended window size of $400\,\mathrm{ps}$ is employed to isolate the characteristics of the MCK setup. The "Through" standard is then realized by closing the gap between the pair of corrugated antennas without any sample inserted, thereby normalizing $\underline{S}_{21}$. Finally, the "Reflect" standard is realized by inserting a $1\,\mathrm{mm}$-thick metal shim into the gap, effectively acting as a perfect metal reflector for normalizing $\underline{S}_{11}$.

As a sample, we use a $380\,\mu\mathrm{m}$-thick plate of photoresist which was fabricated via spin coating, followed by UV curing at a wavelength of $365\,\mathrm{nm}$ and subsequent heat curing at $85\,^{\circ}\mathrm{C}$ for one hour. The maximum thickness variation across the plate with roughly $11\,\mathrm{mm}$ diameter was measured to be of the order of $\pm 10\,\mu\mathrm{m}$. A picture of the photoresist sample is shown in the zoom-in in Fig. D.1(a). After clamping the sample between the two corrugated horn antennas, $S$-parameter measurements are taken. With the knowledge of the sample thickness, the real and imaginary parts of the permittivity, $\Re\{\underline{\epsilon}_\mathrm{r}\} = \epsilon'$ and $-\Im\{\underline{\epsilon}_\mathrm{r}\} = \epsilon''$, can be extracted from the acquired $\underline{S}_{21}$ and $\underline{S}_{11}$ data using the manufacturer-provided evaluation software [303]. Note that the results of this approach have been shown to lead to excellent agreement [304] with quasi-standard permittivity-measurement procedures developed by the National Institute of Standards and Technology (NIST) [305, 306]. The measured frequency-dependent real and imaginary parts of the permittivity of our sample are shown in Fig. D.1(b), see left panel for $\Re\{\underline{\epsilon}_\mathrm{r}\} = \epsilon'$ and right panel for $-\Im\{\underline{\epsilon}_\mathrm{r}\} = \epsilon''$. The solid blue lines represent the results obtained when evaluating the measured data for the mean sample thickness of $380\,\mu\mathrm{m}$, whereas the dashed lines correspond to the

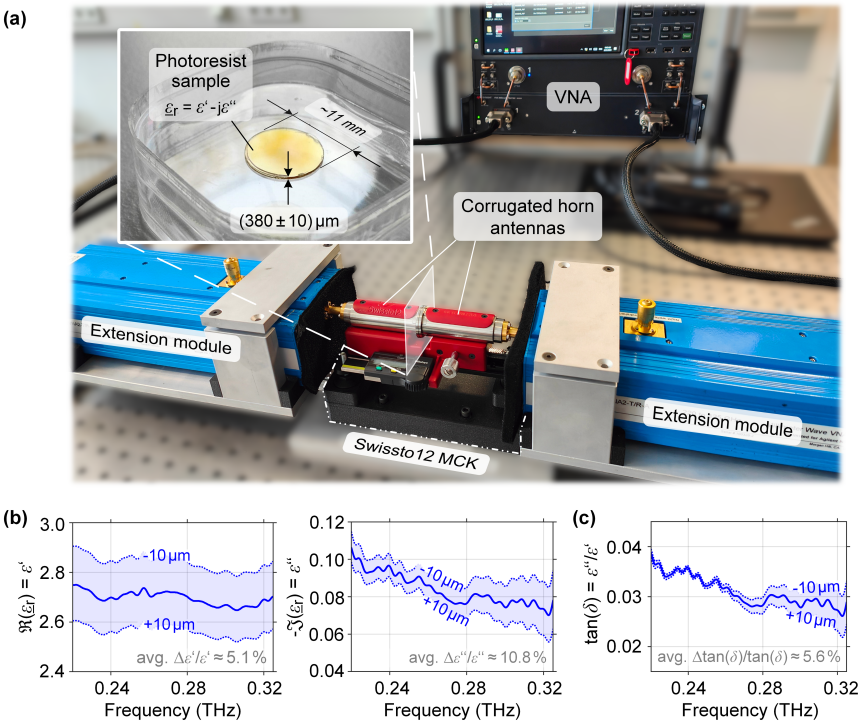


**Fig. D.1:** Permittivity measurement of multi-photon lithography photoresist. **(a)** Measurement setup, comprising a pair of frequency-extension modules connected to a vector network analyzer (VNA) to enable $S$-parameter measurements in a frequency range from $0.220$ THz and $0.325$ THz. A commercially available material-characterization kit (Swissto12 MCK) is directly connected to the frequency-extension modules. The MCK consists of two corrugated horn antennas providing a plane-wave-like irradiation of the $380\,\mu$m-thick photoresist sample with complex permittivity $\underline{\epsilon}_r = \epsilon' - j\epsilon''$, see zoom-in, which is placed in the gap between the two antennas. **(b)** Measured frequency-dependent real part $\Re\{\underline{\epsilon}_r\} = \epsilon'$ (left panel) and imaginary part $-\Im\{\underline{\epsilon}_r\} = \epsilon''$ (right panel) of the permittivity. The solid blue lines represent the results as evaluated using the mean sample thickness of $380\,\mu$m, whereas the dashed lines correspond to the respective estimated upper and lower limits as given by the uncertainty of the sample thickness of $\pm 10\,\mu$m. From the extracted data, we find an average relative uncertainty of $\Delta\epsilon'/\epsilon' \approx 5.1\,\%$ and $\Delta\epsilon''/\epsilon'' \approx 10.8\,\%$ for the real and imaginary parts, respectively. **(c)** Measured frequency-dependent loss tangent $\tan(\delta) = \epsilon''/\epsilon'$ calculated from the real and imaginary parts of the permittivity as given in Subfigure (b). Again, the solid blue line represets the result for the mean sample thickness whereas the dashed lines correspond to the respective estimated upper and lower limits. We find an average relative uncertainty of $\Delta\tan(\delta)/\tan(\delta) \approx 5.6\,\%$.

respective estimated upper and lower limits as given by the uncertainty of the sample thickness ($\pm 10\,\mu\mathrm{m}$). From the extracted data, we find an average relative uncertainty of $\Delta\epsilon'/\epsilon' \approx 5.1\,\%$ and $\Delta\epsilon''/\epsilon'' \approx 10.8\,\%$ for the real and imaginary parts, respectively. Figure D.1(c) shows the frequency-dependent loss tangent $\tan(\delta) = \epsilon''/\epsilon'$ calculated from the real and imaginary parts of the permittivity as given in Fig. D.1(b). Again, the solid blue line represents the result for the mean sample thickness, whereas the dashed lines correspond to the respective estimated upper and lower limit. We find an average relative uncertainty of $\Delta\tan(\delta)/\tan(\delta) \approx 5.6\,\%$. The measured values for the real part of the permittivity of the order of $\epsilon' \approx 2.5 - 2.9$ and for the loss tangent of the order of $\tan(\delta) \approx 0.02 - 0.04$ are in good agreement to reported characteristics of other multi-photon printable photoresists, e.g., SU-8 [173]. Note also that the reported uncertainties are in good agreement with previously reported measurement uncertainties using the same MCK measurement system [307]. The material characteristics of the 3D-printed support structures are subsequently modeled using the depicted results of the dielectric response measurement. To this end, the measured values for the permittivity $\epsilon'$ and loss tangent $\tan(\delta)$ in the frequency range from $0.220\,\mathrm{THz}$ to $0.325\,\mathrm{THz}$ were imported into CST Microwave Studio and fitted using a dispersion model of first order.

## D.2 Design of MCFS-based THz structures

For adapting the electrical characteristics and avoiding short circuits of the MCFS-based THz structures, we exploit the flexibility offered in the design and fabrication of the 3D-printed polymeric support structures to include appropriate isolation trenches with undercut sidewalls, see Section 5.2 and Fig. 5.2. A cross-sectional view of a typical MCFS is shown in Fig. D.2(a), where the indicated dimensions refer to TIC II, connecting an associated pair of CPW feeds, see Sections 5.3.1 and 5.5. The MCFS consists of the 3D-printed polymeric support ($\epsilon' = 2.66$, $\tan(\delta) = 0.033$) on an alumina substrate ($\epsilon' = 9.9$, $\tan(\delta) = 0.0001$) that is locally coated through highly directive metal evaporation along a direction perpendicular to the substrate, i.e., from top along the negative $z$-direction in Fig. D.2(a).

The metal layer of thickness $h_{\mathrm{m}} = 0.64\,\mu\mathrm{m}$ is thus deposited on all surfaces with direct line of sight to the evaporation source, thereby forming the three isolated metal strips in GSG configuration, Fig. 5.2(d). For a robust design, the depth $d_{\mathrm{it}}$ of the isolation trenches should be chosen large enough to avoid any influence of the metal residues that remain at the ground of the trenches on the electrical characteristics of the TIC, in particular the line impedance. This aspect is investigated in more detail in Fig. D.2(b), which depicts the simulated line impedance $Z_{\mathrm{L}}$ as a function of the gap width $w_{\mathrm{gap}}$ and the isolation-trench depth $d_{\mathrm{it}}$. In these simulations, the support height was chosen to be $h = 100\,\mu\mathrm{m}$ — large enough to avoid any influence of the high-permittivity substrate on the results. Contour lines in Fig. D.2(b) indicate the set of parameters for constant line impedances of $Z_{\mathrm{L}} = (50 \ldots 80)\,\Omega$. As expected, the line impedance can be effectively controlled by adapting the gap width $w_{\mathrm{gap}}$, whereas the influence of the isolation-trench depth $d_{\mathrm{it}}$ is rather small once $d_{\mathrm{it}}$ exceeds twice the gap width $w_{\mathrm{gap}}$, $d_{\mathrm{it}} > 2w_{\mathrm{gap}}$, i.e., to the right of the dashed white line in Fig. 5.2(b). In our experiments, all fabricated support structures were thus designed with isolation-trench depths $d_{\mathrm{it}}$ of $20\,\mu\mathrm{m}$ or more, and we rely on the gap width $w_{\mathrm{gap}}$ to control the line impedance $Z_{\mathrm{L}}$. Still, the transition section between the CPW and the MCFS requires special consideration, since the height $h$ of the support structure is continuously tapered down from an initial value of typically $50\,\mu\mathrm{m}$ or more to approximately $3\,\mu\mathrm{m}$ to ensure a smooth connection to the approximately $3\,\mu\mathrm{m}$-thick CPW strips on the substrate, see Fig. 5.2. At the same time, the isolation-trench depth $d_{\mathrm{it}}$ cannot exceed the support height $h$ and must hence be down-tapered as well — from the initial $20\,\mu\mathrm{m}$ or more to approximately $3\,\mu\mathrm{m}$. To avoid formation of shortcuts, deposition of metal in the tapered region of the isolation trench is avoided by dedicated shadowing structures that take the form of multiple arm-like roofs, see Inset Ⓣ of Fig. 5.2. For correct choice of the gap width in this transition region, we simulate again the line impedance $Z_{\mathrm{L}}$ as a function of that gap width $w_{\mathrm{gap}}$ and the support height $h$, see Fig. D.2(c). We subdivide the simulation in two distinct regions, labeled ① and ②: For large support heights $h > 20\,\mu\mathrm{m}$, the isolation-trench depth $d_{\mathrm{it}}$ is fixed to $20\,\mu\mathrm{m}$, and metal residues are present at the ground of the isolation trenches, see Region ② in Fig. D.2(c). In the transition region between the CPW and the MCFS, the isolation-trench depth is equal to the

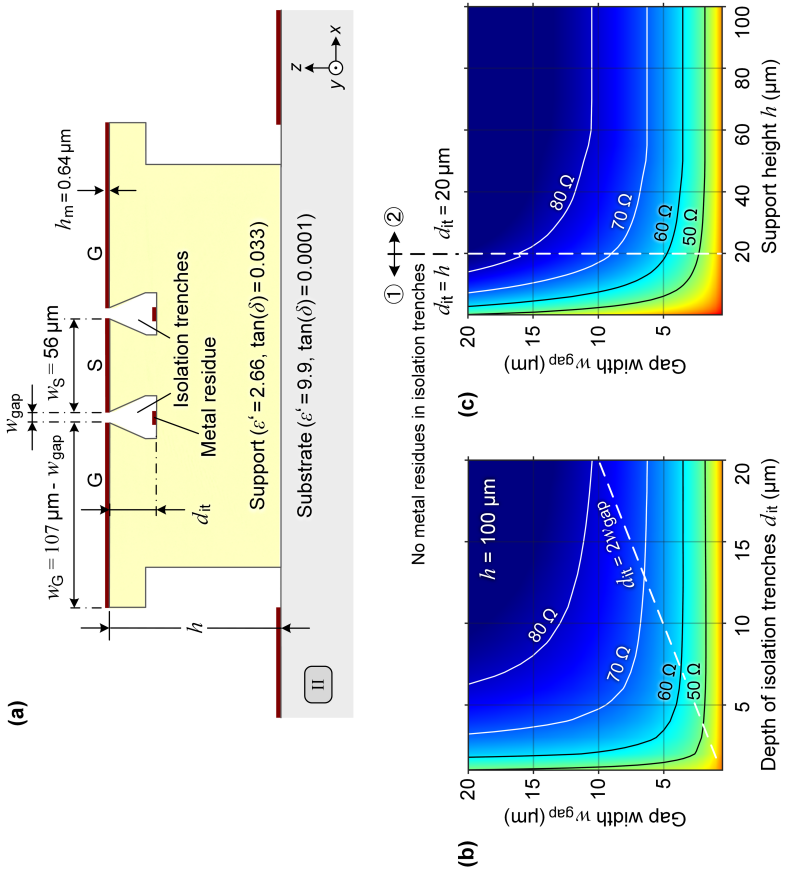


**Fig. D.2:** (Caption next page.)

**Fig. D.2:** Simulation of characteristic line impedance for MCFS-based THz structures and design of the transition to an on-chip CPW. **(a)** Cross-sectional view of a transmission line on a typical MCFS. The MCFS consists of the 3D-printed polymeric support on an alumina substrate and is locally coated through highly directive metal evaporation along a direction perpendicular to the substrate, i.e., from top along the negative $z$-direction. The metal layer is thus deposited on all surfaces with direct line of sight to the evaporation source, thereby forming the three isolated metal strips in ground-signal-ground (GSG) configuration. For a robust design, the depth $d_{\mathrm{it}}$ of the isolation trenches should be chosen large enough to avoid any influence of the metal residues at the ground of the trenches on the electrical characteristics such as the line impedance of the TIC. Still, the transition section between the CPW and the MCFS requires special consideration, since the height $h$ of the support structure is continuously tapered to ensure a smooth connection to the approximately 3 µm-thick CPW strips on the substrate and since the isolation-trench depth $d_{\mathrm{it}}$ cannot exceed the support height $h$. To avoid formation of shortcuts, deposition of metal in the tapered region of the isolation trenches is avoided by dedicated shadowing structures that take the form of multiple arm-like roofs, see Inset Ⓣ of Fig. 5.2. **(b)** Simulated line impedance $Z_{\mathrm{L}}$ as a function of the gap width $w_{\mathrm{gap}}$ and the isolation-trench depth $d_{\mathrm{it}}$. The support height was chosen to be $h = 100\,\mu\mathrm{m}$ — large enough to avoid any influence of the high-permittivity substrate on the results. Contour lines indicate the set of parameters for constant line impedances of $Z_{\mathrm{L}} = (50 \ldots 80)\,\Omega$. As expected, the line impedance can be effectively controlled by adapting the gap width $w_{\mathrm{gap}}$, whereas the influence of the isolation-trench depth $d_{\mathrm{it}}$ is rather small once $d_{\mathrm{it}}$ exceeds twice the gap width $w_{\mathrm{gap}}$, $d_{\mathrm{it}} > 2w_{\mathrm{gap}}$, i.e., to the right of the dashed white line. In our experiments, all fabricated support structures were thus designed with $d_{\mathrm{it}} \geq 20\,\mu\mathrm{m}$, and we rely on the gap width $w_{\mathrm{gap}}$ to control the line impedance. **(c)** For correct choice of the gap width in the transition region, we simulate again the line impedance $Z_{\mathrm{L}}$ as a function of the gap width $w_{\mathrm{gap}}$ and the support height $h$. We subdivide the simulation in two distinct regions, labeled ① and ②: For large support heights $h > 20\,\mu\mathrm{m}$, the isolation-trench depth $d_{\mathrm{it}}$ is fixed to 20 µm, and metal residues are present at the ground of the isolation trenches (Region ②). In the transition region between the CPW and the MCFS, the support height $h$ is smaller than 20 µm, the isolation-trench depth is equal to the support height, $d_{\mathrm{it}} = h$, and the trenches do not contain any metal residues (Region ①) due to the above-mentioned shadowing structures. In all simulations, we kept the signal-conductor width $w_{\mathrm{S}}$ fixed and varied the ground-conductor width $w_{\mathrm{G}}$ such that the overall structure width is maintained at a constant total width of $w_{\mathrm{S}} + 2w_{\mathrm{G}} + 2w_{\mathrm{gap}} = 270\,\mu\mathrm{m}$. This allows for geometrically smooth and electrically well-matched transitions to the fabricated CPW feeds, which also feature a total width of $w_{\mathrm{S}} + 2w_{\mathrm{G}} + 2d_{\mathrm{SG}} = 270\,\mu\mathrm{m}$ for TIC II. Contour lines again indicate constant line impedances of $Z_{\mathrm{L}} = (50 \ldots 80)\,\Omega$. For the 80 Ωcontour line, we observe a small discontinuity at the transition between Region ① and Region ②. We attribute this to the fact that, due to the associated rather large gap width of the order of 15 µm, the abrupt stop of the metal residues on the ground of the isolation trenches still has a slight influence on the resulting line impedance.

support height, $d_{\mathrm{it}} = h$, and the trenches do not contain any metal residues, see Region ① in Fig. D.2(c). In all simulations, we kept the signal-conductor width $w_{\mathrm{S}}$ fixed and varied the ground-conductor width $w_{\mathrm{G}}$ such that the overall structure width is maintained at a constant total width of $w_{\mathrm{S}} + 2w_{\mathrm{G}} + 2w_{\mathrm{gap}} = 270\,\mu\mathrm{m}$. This allows for geometrically smooth and electrically well-matched transitions to the fabricated CPW feeds, which also feature a total width of $w_{\mathrm{S}} + 2w_{\mathrm{G}} + 2d_{\mathrm{SG}} = 270\,\mu\mathrm{m}$ for TIC II, see Fig. 5.2(a) and Table 5.1 along with the associated explanation in Section 5.5. Contour lines in Fig. D.2(c) again indicate constant line impedances of $Z_{\mathrm{L}} = (50 \ldots 80)\,\Omega$. For the $80\,\Omega$ contour line, we observe a small discontinuity at the transition between Region ① and Region ②. We attribute this to the fact that, due to the associated rather large gap width of the order of $15\,\mu\mathrm{m}$, the abrupt stop of the metal residues on the ground of the $20\,\mu\mathrm{m}$-deep isolation trenches still has a slight influence on the resulting line impedance. Note that for some of the structures discussed in Chapter 5, the adjustment of the gap width $w_{\mathrm{gap}}$ was not yet implemented to provide a perfectly smooth transition, see, e.g., Fig. 5.3(b). This leaves room for further optimization and improvement of the overall device performance.

## D.3 Surface roughness measurements

The surface roughness of the various fabricated MCFS and of the feed CPW was measured using a white-light interferometer (ContourX-100, Bruker Inc., Billerica, USA) equipped with a $100\times$ / $0.8$ objective (WLI100XMRTC, Olympus K.K., Tokio, Japan). The results are shown in Fig. D.3. All measurements are performed in $(40 \times 40)\,\mu\mathrm{m}^2$ fields, each time averaging over ten recordings to reduce noise, and we apply a software-based tilt correction followed by a background subtraction to compensate for the waviness of the sampled areas. Final roughness extraction consisted of separating the areal image in a series of single-line profiles for which the mean root-mean-square (RMS) roughness $R_{\mathrm{q}}$ is computed [308]. Moreover, different fields on multiple positions have been measured for each sample to reliably determine the RMS surface roughness and its typical range of variation across the sample.

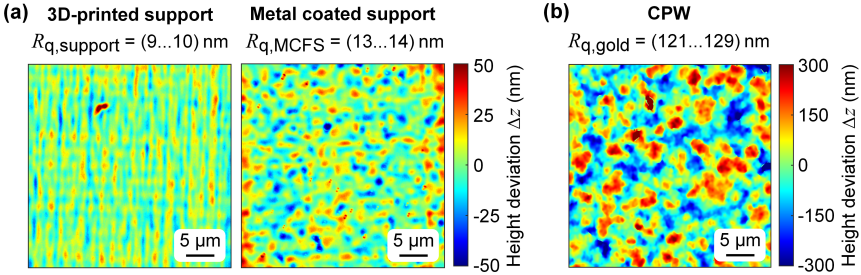


**Fig. D.3:** Surface topographies and associated surface roughness extracted from white-light interferometer measurements. **(a)** Height deviations $\Delta z$ from the mean surface profile for an exemplary bare 3D-printed support structure (left panel) and for the same structure after the metal coating process (right panel). A root-mean-square (RMS) surface roughness of $R_{\mathrm{q,MCFS}} = (13 \ldots 14)$ nm is found after metal deposition, slightly larger than the roughness of the underlying 3D-printed support of $R_{\mathrm{q,support}} = (9 \ldots 10)$ nm. **(b)** Height deviations $\Delta z$ measured for the gold metallization on the alumina substrates used for fabrication of the CPW transmission lines in our experiments. We found a rather large RMS surface roughness of $R_{\mathrm{q,gold}} = (121 \ldots 129)$ nm.

In Fig. D.3(a), the height deviations $\Delta z$ from the mean surface profile are shown for an exemplary bare 3D-printed support structure (left panel) and for the same structure after the metal coating process (right panel). The various measurements reveal an RMS surface roughness of $R_{\mathrm{q,MCFS}} = (13 \ldots 14)$ nm upon metal deposition, which is slightly larger than the roughness of the underlying 3D-printed support of $R_{\mathrm{q,support}} = (9 \ldots 10)$ nm. We also evaluated the surface roughness of the gold metallization on the alumina substrates used for fabrication of the CPW transmission lines in our experiments, Fig. D.3(b). We found a rather large RMS surface roughness of $R_{\mathrm{q,gold}} = (121 \ldots 129)$ nm, which was subsequently included in the simulations of the transmission lines, see Section 5.5.

## D.4 Characterization of THz interconnects

The THz interconnects (TIC) were measured on a semi-automated probing station (Summit 12000B-S, Cascade Microtech Inc., Beaverton, USA), enabling repeatable and consistent contacting of the samples under test. For $S$-parameter measurement in the different frequency ranges, a VNA (N5247B PNA-X, Keysight Technologies Inc.) is used in conjunction with a pair of frequency extending transmit / receive modules connected via a millimeter-wave controller (N5262A, Keysight Technologies Inc.). The VNA is set to measure at $801$ frequency points with an IF bandwidth of $100$ Hz for all recordings.

For the measurements shown in Fig. 5.3(c) and (d), a total of three frequency ranges ($10$ MHz $\ldots 0.110$ THz; $0.110$ THz $\ldots 0.170$ THz; $0.200$ THz $\ldots 0.330$ THz) are addressed by selecting the associated extension modules and probes, and a line-reflect-reflect-match (LRRM) calibration [309] was carried out using the manufacturer-recommended impedance standard substrate (ISS) to shift the reference planes to the probe tips. All measurements are done on a microwave-absorbing ISS holder (116-344, FormFactor GmbH, Thiendorf, Germany) to reduce unwanted substrate modes. For the frequency range from $10$ MHz to $0.110$ THz, we use a first pair of frequency extension modules (N5260-60003, Keysight Technologies Inc.) and coaxial probes (Infinity Probe i110-A-GSG-100, FormFactor GmbH), and the LRRM calibration is performed on the associated ISS (104-783, FormFactor GmbH). The second frequency range from $0.110$ THz to $0.170$ THz is measured with a second pair of frequency extension modules (V06VNA2-T/R-A, OML Inc.) and waveguide probes (Infinity Probe i170-T-GSG-100-BT, FormFactor GmbH). Lastly, measurements in the third frequency range from $0.200$ THz to $0.330$ THz are carried out with a third pair of frequency extension modules (V03VNA2-T/R-A, OML Inc.) and waveguide probes (Infinity Probe i325-T-GSG-100-BT, FormFactor GmbH). The LRRM calibrations for the measurements in the latter two frequency ranges are performed on a second ISS (138-357, FormFactor GmbH).

The measured $S$-parameter matrices $\underline{\mathbf{S}}_{\mathrm{meas}}$ between Plane $1'$ and Plane $2'$ (blue lines in Fig. 5.3(a)) comprise the compound characteristics of the respective TIC (TIC I, II, and III) as well as of the two associated 4 mm-long CPW feeds on the alumina substrates. The measured frequency-dependent loss is thus largely dominated by the loss of the two CPW feeds, and we need to mathematically remove their influence via dedicated de-embedding procedures [178]. To this end, the compound $S$-parameter matrices $\underline{\mathbf{S}}_{\mathrm{meas}}$ are first transformed into transfer matrices ($T$-matrices [163], see Section D.7), and the $T$-matrix $\underline{\mathbf{T}}_{\mathrm{meas}}$ of the network is subsequently represented by cascading the $T$-matrices of the individual elements,

$$\underline{\mathbf{T}}_{\mathrm{meas}} = \underline{\mathbf{T}}_{\mathrm{feed}}\underline{\mathbf{T}}_{\mathrm{TIC}}\underline{\mathbf{T}}_{\mathrm{feed}}. \tag{D.1}$$

In this relation $\underline{\mathbf{T}}_{\mathrm{feed}}$ and $\underline{\mathbf{T}}_{\mathrm{TIC}}$ represent the $T$-matrices of the two identical CPW feeds and the corresponding TIC, respectively. We then measured the $S$-parameter matrix $\underline{\mathbf{S}}_{\mathrm{feed,ref}}$ of an identical reference CPW with the length $L_{\mathrm{feed}}$ and calculated the corresponding $T$-matrix $\underline{\mathbf{T}}_{\mathrm{feed,ref}}$. Equation D.1 can then be multiplied from both sides by the inverse matrix $\underline{\mathbf{T}}^{-1}_{\mathrm{feed,ref}}$, leading to

$$\underline{\mathbf{T}}^{-1}_{\mathrm{feed,ref}}\underline{\mathbf{T}}_{\mathrm{meas}}\underline{\mathbf{T}}^{-1}_{\mathrm{feed,ref}} = \underline{\mathbf{T}}^{-1}_{\mathrm{feed,ref}}\underline{\mathbf{T}}_{\mathrm{feed}}\underline{\mathbf{T}}_{\mathrm{TIC}}\underline{\mathbf{T}}_{\mathrm{feed}}\underline{\mathbf{T}}^{-1}_{\mathrm{feed,ref}} = \underline{\mathbf{T}}_{\mathrm{TIC}}. \tag{D.2}$$

In this relation, we have made the assumption that the $T$-matrix of the CPW embedded in the measurement $\underline{\mathbf{T}}_{\mathrm{feed}}$ and of the separately measured reference CPW $\underline{\mathbf{T}}_{\mathrm{feed,ref}}$ are identical, i.e., $\underline{\mathbf{T}}^{-1}_{\mathrm{feed,ref}}\underline{\mathbf{T}}_{\mathrm{feed}} = \underline{\mathbf{T}}_{\mathrm{feed}}\underline{\mathbf{T}}^{-1}_{\mathrm{feed,ref}} = \mathbf{I}$, where $\mathbf{I}$ denotes the unity matrix. The extracted $T$-matrix $\underline{\mathbf{T}}_{\mathrm{TIC}}$ can then be converted back to the $S$-parameter matrix $\underline{\mathbf{S}}_{\mathrm{TIC}}$ with its complex transmission and reflection coefficients $\underline{S}_{21}$ and $\underline{S}_{11}$, respectively. Figure D.4 shows the resulting transmission factor $S_{21,\mathrm{dB}} = 10\log_{10}(|\underline{S}_{21}|^2)$ of TIC I (left), II (middle), and III (right), extracted via the $T$-matrix de-embedding approach described in Eq. D.2, as red curves in the frequency range up to $0.170$ THz. For frequencies beyond $0.200$ THz, we find increasingly strong ripples in the de-embedded data, that are caused by error multiplication arising from slight discrepancies between the "true" $T$-matrix $\underline{\mathbf{T}}_{\mathrm{feed}}$ of the CPW feed lines and its experimentally measured counterpart $\underline{\mathbf{T}}_{\mathrm{feed,ref}}$ — a known effect in mmW device characterization [177]. This leads to a high

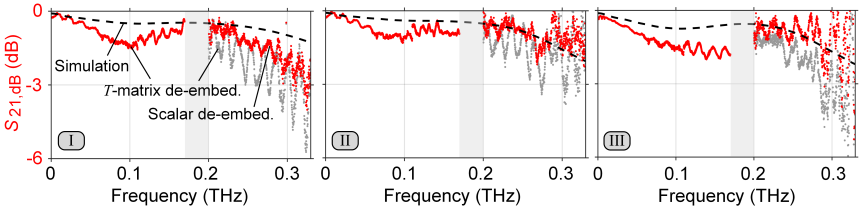


**Fig. D.4:** De-embedding of THz interconnects (TIC) using the $T$-matrix and the scalar de-embedding approach. In our measurements, the $S$-parameter matrices do not only comprise the characteristics of the TIC, but also the two $4$ mm-long CPW feeds on the two alumina substrates which largely dominate the overall transmission characteristics. For frequencies below $0.170$ THz, the feed lines feature low transmission losses and are well matched such that a mathematically rigorous $T$-matrix de-embedding technique according to Eq. D.2 can be used. In this frequency range, the associated transmission $S_{21,\mathrm{dB}} = 10\log_{10}(|\underline{S}_{21}|^2)$ is indicated by red curves for TIC I (left), II (middle), and III (right). For frequencies beyond $0.200$ THz, the feed lines become lossy and poorly matched, rendering the results of the $T$-matrix de-embedding technique unreliable and leading to strong oscillations of the associated curves, which are indicated in grey. We therefore resort to a simpler and more robust scalar correction approach as given in Eq. D.4 for estimating the TIC transmission in the frequency range from $0.200$ THz to $0.330$ THz. The results are again indicated by red curves in this frequency range, exhibiting less fluctuations than the results obtained from the $T$-matrix approach. Note that the measured $S$-parameters had to be acquired separately in different frequency ranges using dedicated signal sources, waveguides, and probes as described above, thereby leaving a gap between $0.170$ THz and $0.200$ THz, where no adequate signal sources were available.

sensitivity of the de-embedding procedure with respect to the insertion and return loss of the reference CPW and renders the results unreliable for frequencies beyond $0.200$ THz, see next paragraph for a more detailed explanation. As mentioned in Section 5.3, we therefore rely on a more robust scalar correction rather than on a mathematically rigorous but experimentally sensitive $T$-matrix de-embedding. For comparison of both approaches, we still display the results of the $T$-matrix de-embedding beyond $0.200$ THz in Fig. D.4, see grey curves. Note that the measured $S$-parameters had to be acquired separately in different frequency ranges using dedicated signal sources, waveguides, and probes as described above, thereby leaving a gap between $0.170$ THz and $0.200$ THz, where no adequate signal sources were available.

In the following, we aim at obtaining a better understanding of the effects of error multiplication in the $T$-matrix de-embedding approach. To this end, we distinguish between the "true" T-matrix $\underline{\mathbf{T}}_{\mathrm{feed}}$ of the CPW as contained in the

measured compound $T$-matrix $\underline{\mathbf{T}}_{\mathrm{meas}}$ and of the separately measured reference CPW $\underline{\mathbf{T}}_{\mathrm{feed,ref}}$, which differ from one another due to measurement inaccuracies, $\underline{\mathbf{T}}_{\mathrm{feed}} \neq \underline{\mathbf{T}}_{\mathrm{feed,ref}}$. The matrix multiplications $\underline{\mathbf{T}}_{\mathrm{feed,ref}}^{-1}\underline{\mathbf{T}}_{\mathrm{feed}}$ and $\underline{\mathbf{T}}_{\mathrm{feed}}\underline{\mathbf{T}}_{\mathrm{feed,ref}}^{-1}$ in Eq. D.2 are therefore no longer given by the unity matrix $\mathbf{I}$ and thus introduce errors during the de-embedding procedure. As an example, the first matrix multiplication in Eq. D.2 can be written in terms of the underlying $S$-parameters as

$$\underline{\mathbf{T}}_{\mathrm{B}}^{-1}\underline{\mathbf{T}}_{\mathrm{A}} = \begin{pmatrix} \frac{1}{\underline{S}_{21}^{\mathrm{B}}} & -\frac{\underline{S}_{22}^{\mathrm{B}}}{\underline{S}_{21}^{\mathrm{B}}} \\ \frac{\underline{S}_{11}^{\mathrm{B}}}{\underline{S}_{21}^{\mathrm{B}}} & \frac{(\underline{S}_{21}^{\mathrm{B}})^2 - \underline{S}_{11}^{\mathrm{B}}\underline{S}_{22}^{\mathrm{B}}}{\underline{S}_{21}^{\mathrm{B}}} \end{pmatrix}^{-1} \begin{pmatrix} \frac{1}{\underline{S}_{21}^{\mathrm{A}}} & -\frac{\underline{S}_{22}^{\mathrm{A}}}{\underline{S}_{21}^{\mathrm{A}}} \\ \frac{\underline{S}_{11}^{\mathrm{A}}}{\underline{S}_{21}^{\mathrm{A}}} & \frac{(\underline{S}_{21}^{\mathrm{A}})^2 - \underline{S}_{11}^{\mathrm{A}}\underline{S}_{22}^{\mathrm{A}}}{\underline{S}_{21}^{\mathrm{A}}} \end{pmatrix} \tag{D.3}$$

$$= \begin{pmatrix} \frac{\underline{S}_{21}^{\mathrm{B}}}{\underline{S}_{21}^{\mathrm{A}}} + \frac{\underline{S}_{22}^{\mathrm{B}}}{\underline{S}_{21}^{\mathrm{A}}\underline{S}_{21}^{\mathrm{B}}}\Delta\underline{S}_{11} & (\frac{\underline{S}_{21}^{\mathrm{A}}\underline{S}_{22}^{\mathrm{B}}}{\underline{S}_{21}^{\mathrm{B}}} - \frac{\underline{S}_{21}^{\mathrm{B}}\underline{S}_{22}^{\mathrm{A}}}{\underline{S}_{21}^{\mathrm{A}}}) - \frac{\underline{S}_{22}^{\mathrm{A}}\underline{S}_{22}^{\mathrm{B}}}{\underline{S}_{21}^{\mathrm{A}}\underline{S}_{21}^{\mathrm{B}}}\Delta\underline{S}_{11} \\ \frac{1}{\underline{S}_{21}^{\mathrm{A}}\underline{S}_{21}^{\mathrm{B}}}\Delta\underline{S}_{11} & \frac{\underline{S}_{21}^{\mathrm{A}}}{\underline{S}_{21}^{\mathrm{B}}} - \frac{\underline{S}_{22}^{\mathrm{A}}}{\underline{S}_{21}^{\mathrm{A}}\underline{S}_{21}^{\mathrm{B}}}\Delta\underline{S}_{11} \end{pmatrix},$$

where $\Delta\underline{S}_{11} = \underline{S}_{11}^{\mathrm{A}} - \underline{S}_{11}^{\mathrm{B}}$. In this relation, we denote the various $S$-parameters of the "true" embedded CPW and the separately measured reference CPW by the superscripts $\mathrm{A} \mathrel{\widehat{=}}$ "feed" and $\mathrm{B} \mathrel{\widehat{=}}$ "feed, ref", respectively, and we assumed all systems to reciprocal, i.e., $\underline{S}_{21}^{\mathrm{A}} = \underline{S}_{12}^{\mathrm{A}}$ and $\underline{S}_{21}^{\mathrm{B}} = \underline{S}_{12}^{\mathrm{B}}$. For an ideal measurement without noise, the underlying scattering parameters of $\underline{\mathbf{T}}_{\mathrm{feed}} = \underline{\mathbf{T}}_{\mathrm{A}}$ and $\underline{\mathbf{T}}_{\mathrm{feed,ref}} = \underline{\mathbf{T}}_{\mathrm{B}}$ are identical, i.e. $\underline{S}_{lm}^{\mathrm{A}} = \underline{S}_{lm}^{\mathrm{B}}$ with $l, m \in \{1, 2\}$, and the multiplication of the associated $T$-matrices in Eq. D.3 leads to the unity matrix $\mathbf{I}$ as assumed for deriving the de-embedding procedure in Eq. D.2. For noisy measurements, however, the expressions indicated in blue in Eq. D.3 can become very big, given the fact that, for large frequencies, the feed lines become increasingly lossy and reflective. As a consequence, the products $\underline{S}_{21}^{\mathrm{A}}\underline{S}_{21}^{\mathrm{B}}$ in the denominator of the highlighted expressions become small, while the numerators are either unity or increase with the reflection coefficients $\underline{S}_{22}^{\mathrm{A}}$, $\underline{S}_{22}^{\mathrm{B}}$ and $\underline{S}_{22}^{\mathrm{A}}\underline{S}_{22}^{\mathrm{B}}$. This leads to large values of the overall fraction which strongly "amplifies" any noise- or distortion-induced deviations [177] between the reflection $\underline{S}_{11}^{\mathrm{A}}$ of the "true" feed

line and its measured counterpart $\underline{S}_{11}^{\mathrm{B}}$. In our measurements, these effects are particularly detrimental for frequencies above $0.200\,\mathrm{THz}$, indicated by the strong oscillations of the grey traces in Fig. D.4.

To mitigate this problem, we use a more robust scalar correction technique to estimate the loss of the TIC for frequencies above $0.200\,\mathrm{THz}$, effectively removing only the attenuation of the CPW feeds from the recorded measurements between Plane $1'$ and Plane $2'$. More specifically, we first extract the transmission of the full arrangement $S_{2'1',\mathrm{meas,dB}} = 10\log_{10}(|\,\underline{S}_{2'1',\mathrm{meas}}|^2)$ from the measured compound $S$-parameter matrix $\underline{\mathbf{S}}_{\mathrm{meas}}$, and we extract the transmission of one $4\,\mathrm{mm}$-long CPW feed $S_{2'1',\mathrm{ref,dB}} = 10\log_{10}(|\,\underline{S}_{2'1',\mathrm{ref}}|^2)$ from the separately measured $S$-parameter matrix $\underline{\mathbf{S}}_{\mathrm{feed,ref}}$. Finally, the loss of the two feed lines is removed from the compound measurement by subtracting the associated dB-values,

$$S_{21,\mathrm{dB}} = S_{2'1',\mathrm{meas,dB}} - 2S_{2'1',\mathrm{ref,dB}}. \tag{D.4}$$

The transmission factor $S_{21,\mathrm{dB}}$ of TIC I (left), II (middle), and III (right) extracted via the scalar correction according to Eq. D.4 was calculated for frequencies between $0.200\,\mathrm{THz}$ and $0.330\,\mathrm{THz}$, see red curves in Fig. D.4. As expected, the data appears to fluctuate less than the results obtained from the $T$-matrix approach and indicated by the grey traces above $0.200\,\mathrm{THz}$. Notably, the results of both techniques are reasonably consistent at lower frequencies close to $0.200\,\mathrm{THz}$, supporting the validity of the approach.

## D.5 Characterization of THz probes

The THz probes (TP) were measured on a manual probing station (Cascade PM8, FormFactor GmbH), using a custom vacuum chuck attached to a manual actuator (RPP210, FormFactor GmbH) for alignment and contacting. The experimental setup, which is schematically illustrated in Fig. 5.4(a), is shown in more detail in Fig. D.5, with the zoom-in providing a closer look at the samples under test. First, the probed contacting chip with the two CPW feeds ($L_{\mathrm{feed}} = 1.5\,\mathrm{mm}$) is

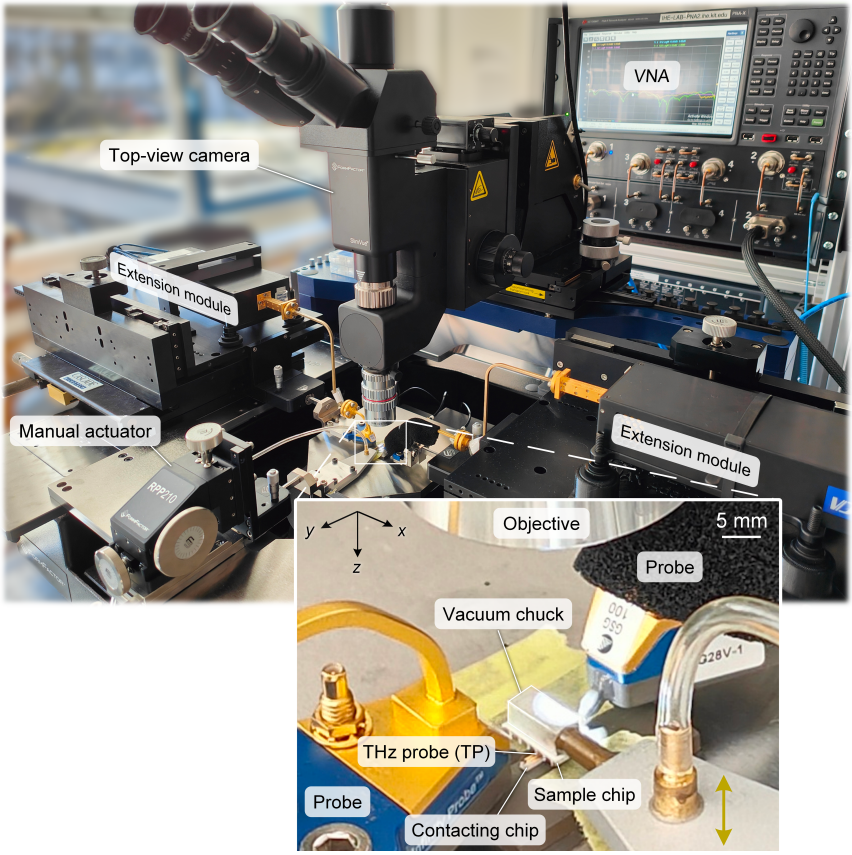


**Fig. D.5:** Experimental setup for characterization of THz probes (TP). The TP were measured on a manual probing station using a custom vacuum chuck attached to a manual actuator for alignment and contacting. The zoom-in provides a closer look at the samples under test. First, the contacting chip, see Fig. 5.4(a), is placed on a microwave-absorbing ISS holder, mounted on the sample stage of the probing station, and the CPW feed lines are electrically contacted using commercially available conventional probes. The sample chip containing the TP is then picked up by the custom vacuum chuck and moved towards the contacting chip using the manual actuator. The TP protrude beyond the contour of the chip such that they are visible in the top-view camera of the probing station. This arrangement allows for simultaneous monitoring of the TP and of the conventional probes contacting the CPW feeds on the contacting chip. After concurrent alignment of the three 100 µm-spaced tips of the TP with respect to the signal and ground conductors of the CPW feeds on each side, the TP are carefully moved down onto the contacting chip using the $z$-stage of the manual actuator. For $S$-parameter measurements in the different frequency ranges from 10 MHz to 0.330 THz, a vector network analyzer (VNA) is used in conjunction with different pairs of frequency-extending transmit / receive modules connected via a millimeter-wave controller.

placed on a microwave-absorbing ISS holder (116-344, FormFactor GmbH) and mounted on the sample stage of the probing station. The sample chip containing the TP is then picked up by the custom vacuum chuck and moved towards the contacting chip using the manual actuator. As mentioned in Chapter 5, the TP protrude beyond the contour of the chip such that they are visible in the top-view camera of the probing station, having its observation direction along the positive $z$-direction in the zoom-in of Fig. D.5. This arrangement allows for concurrent monitoring of the TP and of the conventional probes required for contacting of the CPW feeds on the contacting chip. For alignment of the two TP, the sample chip is first rotated around the $x$- and $y$-axis using goniometers attached to the manual actuator until it is oriented in parallel to the underlying contacting chip. Due to the comparatively large distance of $2L_{\mathrm{TP}} + L_{\mathrm{conn}} = 4.63\,\mathrm{mm}$ between the opposing tips of the two TP, special care must be taken for the rotation about the $x$-axis to avoid damaging the tips during contacting. Then, the sample chip is moved in the $(x, y)$-plane for concurrent alignment of the three $100\,\mu\mathrm{m}$-spaced tips with respect to the signal and ground conductors of the CPW feeds on both sides. Finally, the TP are carefully moved down on the CPW feeds below using the $z$-stage of the manual actuator.

For $S$-parameter measurements in the different frequency ranges from $10\,\mathrm{MHz}$ to $0.330\,\mathrm{THz}$, a VNA (N5242B PNA-X, Keysight Technologies Inc.) is used in conjunction with a pair of frequency-extending transmit / receive modules connected via a millimeter-wave controller (N5292A, Keysight Technologies Inc.), see Fig. D.5. For all recordings, the VNA is again set to measure at $801$ frequency points with an IF bandwidth of $100\,\mathrm{Hz}$. For the measurements shown in Fig. 5.4(b), a total of three frequency ranges ($10\,\mathrm{MHz} \ldots 0.130\,\mathrm{THz}$; $0.130\,\mathrm{THz} \ldots 0.220\,\mathrm{THz}$; $0.220\,\mathrm{THz} \ldots 0.330\,\mathrm{THz}$) are addressed by selecting corresponding extension modules and probes. For each of these frequency ranges, an LRRM calibration [309] is carried out using the manufacturer-recommended ISS (138-357, FormFactor GmbH). We use a broadband VNA system [310], comprising probes with integrated diplexers (T-Wave Dual Band Probe, T220-UBBT-GSG-100, FormFactor GmbH) to enable single-sweep measurements over the first two frequency ranges

from 10 MHz to 0.220 THz. To this end, the system combines a pair of frequency-extension modules from 10 MHz to 0.130 THz (N5295AX02, Keysight Technologies Inc.) with a second pair of frequency-extenders operating from 0.130 THz to 0.220 THz (WR5.1-VNAX, Virginia Diodes Inc., Charlottesville, USA) in the same probe. Lastly, measurements in the frequency range from 0.220 THz to 0.330 THz are carried out with a third pair of frequency-extension modules (WR3.4-VNAX, Virginia Diodes Inc.) and a corresponding set of waveguide probes (Infinity Probe i325-T-GSG-100-BT, FormFactor GmbH).

With the setup depicted in Fig. D.5, the measurements do not only comprise the characteristics of the two TP but also the two short CPW on the contacting chip leading from the measurement probes to the TP on each side as well as the connecting CPW on the sample chip. Therefore, the measured $S$-parameter matrices $\underline{\mathbf{S}}_{\mathrm{meas}}$ between Plane $1''$ and Plane $2''$ (brown lines in Fig. 5.4(a)) are converted to transfer matrices ($T$-matrices [163], see Section D.7), and the $T$-matrix $\underline{\mathbf{T}}_{\mathrm{meas}}$ of the network can again be represented by cascading the $T$-matrices of the individual elements, leading to

$$\underline{\mathbf{T}}_{\mathrm{meas}} = \underline{\mathbf{T}}_{\mathrm{feed}}\underline{\mathbf{T}}_{\mathrm{TP}}\underline{\mathbf{T}}_{\mathrm{conn}}\underline{\mathbf{T}}_{\mathrm{TP}}\underline{\mathbf{T}}_{\mathrm{feed}}. \tag{D.5}$$

In this relation $\underline{\mathbf{T}}_{\mathrm{feed}}$, $\underline{\mathbf{T}}_{\mathrm{TP}}$ and $\underline{\mathbf{T}}_{\mathrm{conn}}$ represent the $T$-matrices of the CPW feed, the TP, and the connecting CPW, respectively. In our measurement setup, the two $T$-matrices of the two TP are assumed to be identical and are labelled $\underline{\mathbf{T}}_{\mathrm{TP}}$ in the following. Similarly, the $T$-matrices of the two CPW feeds are assumed to be identical and denoted as $\underline{\mathbf{T}}_{\mathrm{feed}}$. The reference planes can then be moved to Plane $1'$ and Plane $2'$ (blue lines in Fig. 5.4(a)), thereby removing the influence of the two 1.5 mm-long CPW feeds. To this end, we measured the $S$-parameter matrix $\underline{\mathbf{S}}_{\mathrm{feed,ref}}$ of an identical CPW with the length $L_{\mathrm{feed}}$ and calculated the corresponding $T$-matrix $\underline{\mathbf{T}}_{\mathrm{feed,ref}}$. Equation D.5 can then be multiplied from both sides by the inverse matrix $\underline{\mathbf{T}}^{-1}_{\mathrm{feed,ref}}$ which leads to

$$\begin{aligned}\underline{\mathbf{T}}^{-1}_{\mathrm{feed,ref}}\underline{\mathbf{T}}_{\mathrm{meas}}\underline{\mathbf{T}}^{-1}_{\mathrm{feed,ref}} &= \underline{\mathbf{T}}^{-1}_{\mathrm{feed,ref}}\underline{\mathbf{T}}_{\mathrm{feed}}\underline{\mathbf{T}}_{\mathrm{TP}}\underline{\mathbf{T}}_{\mathrm{conn}}\underline{\mathbf{T}}_{\mathrm{TP}}\underline{\mathbf{T}}_{\mathrm{feed}}\underline{\mathbf{T}}^{-1}_{\mathrm{feed,ref}} \\ &= \underline{\mathbf{T}}_{\mathrm{TP}}\underline{\mathbf{T}}_{\mathrm{conn}}\underline{\mathbf{T}}_{\mathrm{TP}} = \underline{\mathbf{T}}_{\mathrm{TP-conn-TP}}\end{aligned} \tag{D.6}$$

under the assumption that the measured reference CPW and the embedded CPW feeds are identical, i.e., $\underline{\mathbf{T}}_{\mathrm{feed,ref}}^{-1}\underline{\mathbf{T}}_{\mathrm{feed}} = \underline{\mathbf{T}}_{\mathrm{feed}}\underline{\mathbf{T}}_{\mathrm{feed,ref}}^{-1} = \mathbf{I}$. The extracted $T$-matrix $\underline{\mathbf{T}}_{\mathrm{TP-conn-TP}}$ can then be converted back to the $S$-parameter matrix $\underline{\mathbf{S}}_{\mathrm{TP-conn-TP}}$ with its complex-valued transmission and reflection coefficients $\underline{S}_{2'1'}$ and $\underline{S}_{1'1'}$, respectively. Figure D.6 shows the associated transmission and reflection parameters $S_{2'1',\mathrm{dB}} = 10\log_{10}(|\underline{S}_{2'1'}|^2)$ (blue curve) and $S_{1'1',\mathrm{dB}} = 10\log_{10}(|\underline{S}_{1'1'}|^2)$ (green curve), which are in good agreement with the associated simulation (dashed black lines).

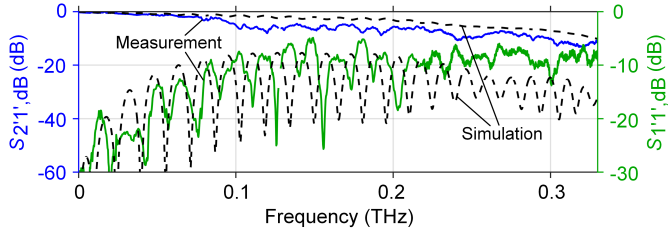


**Fig. D.6:** De-embedded measurements between reference Plane $1'$ and Plane $2'$ comprising the pair of TP and the connecting CPW. The raw measurements taken between Plane $1''$ and Plane $2''$ with the setup depicted in Fig. D.5 (brown lines in Fig. 5.4(a)), do not only comprise the characteristics of the two TP but also the two short CPW on the contacting chip leading from the measurement probes to the TP on each side as well as the connecting CPW on the sample chip. Using Eq. D.6, the reference planes can be moved to Plane $1'$ and Plane $2'$ (blue lines in Fig. 5.4(a)), thereby removing the influence of the two 1.5 mm-long CPW feeds. The associated transmission and reflection parameters $S_{2'1',\mathrm{dB}} = 10\log_{10}(|\underline{S}_{2'1'}|^2)$ (blue curve) and $S_{1'1',\mathrm{dB}} = 10\log_{10}(|\underline{S}_{1'1'}|^2)$ (green curve) are in good agreement with the associated simulation (dashed black lines). Note that the loss of the 3.8 mm-long connecting CPW still contributes significantly to the overall loss. This contribution is removed by using a scalar correction technique, leading to the loss of a single TP.

While the previously extracted parameters $S_{2'1',\mathrm{dB}}$ and $S_{1'1',\mathrm{dB}}$ already give an indication about the performance of the pair of TP, the loss of the 3.8 mm-long connecting CPW as contained in $\underline{\mathbf{S}}_{\mathrm{TP-conn-TP}}$ still contributes significantly to the overall loss. We therefore estimate the insertion loss of a single TP (Fig. 5.4(b)) by using a scalar correction to compensate for the losses caused by all concatenated CPW ($L_{\mathrm{feed}} + L_{\mathrm{conn}} + L_{\mathrm{feed}} = 6.8\,\mathrm{mm}$) in the arrangement between Plane $1''$ and Plane $2''$. To this end, we start from the measured transmission of the

full arrangement $S_{2''1'',\mathrm{meas,dB}} = 10\log_{10}(|\underline{S}_{2''1'',\mathrm{meas}}|^2)$ and we use a 6.8 mm-long reference CPW on the contacting chip to obtain the transmission of the connecting line and both feed lines given as $S_{2''1'',\mathrm{ref,dB}} = 10\log_{10}(|\underline{S}_{2''1'',\mathrm{ref}}|^2)$. The transmission of each of the two TP is then estimated by taking the difference of the two dB-values and dividing the result by two,

$$S_{21,\mathrm{dB}} = (S_{2''1'',\mathrm{meas,dB}} - S_{2''1'',\mathrm{ref,dB}})/2. \tag{D.7}$$

For evaluating the contacting repeatability of the TP, we performed the measurements in the frequency range from 0.220 THz to 0.330 THz for a total of $N = 50$ contacting cycles, see Fig. 5.4(c). The $z$-stage of the manual actuator repeatedly lifted the sample chip up and lowered it back down without intermediate re-alignment. For all measurements, we calculated the estimated transmission through a single TP using Eq. D.7 and extracted the corresponding linear magnitudes $|\underline{S}_{21}|_N = 10^{S_{21,\mathrm{dB}_N}/20}$. With the average transmission magnitude $\overline{|\underline{S}_{21}|} = (\sum_N |\underline{S}_{21}|_N)/N$, we can then express the measurement deviation $\Delta|\underline{S}_{21}|_N$ for the $N$-th measurement as the difference to the mean transmission,

$$\Delta|\underline{S}_{21}|_N = |\underline{S}_{21}|_N - \overline{|\underline{S}_{21}|}. \tag{D.8}$$

For the $N = 50$ contacting cycles, a maximum magnitude deviation of $\Delta|\underline{S}_{21}|_{\max} \approx 5 \times 10^{-3}$ was measured, corresponding to a maximum relative error of 0.6 %. Figure 5.4(c) shows the standard deviation of the transmission magnitude

$$\sigma(|\underline{S}_{21}|) = \sqrt{\frac{1}{N-1}\sum_N (\Delta|\underline{S}_{21}|_N)^2} \tag{D.9}$$

over the measured frequency range. We found a remarkably low maximum standard deviation of $\sigma(|\underline{S}_{21}|)_{\max} \approx 2 \times 10^{-3}$ (corresponding to $-55$ dB) near 0.32 THz.

## D.6 Characterization of THz antennas

The THz antennas (TA) were measured on a probe-based free-space antenna measurement setup [311, 312], which allows to move a receive antenna around a contacted antenna under test (AUT) to record a radiation pattern. The receive antenna and AUT are oriented such that both antennas are co-polarized. A picture of the experimental setup is shown in Fig. D.7, and in-detail explanations of the setup and the calibration steps summarized in the following can be found in the associated publications [311, 312]. For measurement in the frequency range from $0.220\,\mathrm{THz}$ to $0.325\,\mathrm{THz}$, a VNA (N5242A PNA-X, Keysight Technologies Inc.) is used in conjunction with a frequency-extension module (V03VNA2-T/R-A, OML Inc.) connected via a millimeter-wave controller (N5261A, Keysight Technologies Inc.). The VNA is again set to measure at $801$ frequency points with an IF bandwidth of $100\,\mathrm{Hz}$.

The calibration of the setup was carried out in multiple steps: First, a scalar gain calibration is performed using a standard horn antenna (QWH-3PRR00, QuinStar Technology Inc., Torrance, USA) with known gain $G_{\mathrm{horn}}$ connected to the extension module as the transmitter. From the measured transmission $\underline{S}_{21,\mathrm{horn}}$ the system characteristics including the free-space loss and the gain of the receive antenna can thereby be determined as

$$G_{\mathrm{sys}} = \left|\underline{S}_{21,\mathrm{horn}}\right|^2 / G_{\mathrm{horn}}. \tag{D.10}$$

Next, the known transmitter antenna is removed, and a waveguide probe (Infinity Probes i325-T-GSG-100-BT, FormFactor GmbH) is instead connected to the extension module. To remove the influence of the probe, an additional one-port short-open-load (SOL) calibration [312, 313] is carried out using an ISS (138-357, FormFactor GmbH). This calibration allows to determine the three elements of a one-port SOL error-adapter matrix $\underline{\mathbf{E}} = \left(\begin{smallmatrix} \underline{e}_{00} & \underline{e}_{01} \\ \underline{e}_{10} & \underline{e}_{11} \end{smallmatrix}\right)$, where the elements $\underline{e}_{00}$, $\underline{e}_{11}$, and $\underline{e}_{10}\underline{e}_{01}$ are related to the directivity, the source match and the reflection tracking, respectively. Assuming a reciprocal error network ($\underline{e}_{10} = \underline{e}_{01}$), the transmission of the probe is given by $G_{\mathrm{probe}} = |\underline{e}_{10}\underline{e}_{01}|$. With the probe transmission $G_{\mathrm{probe}}$

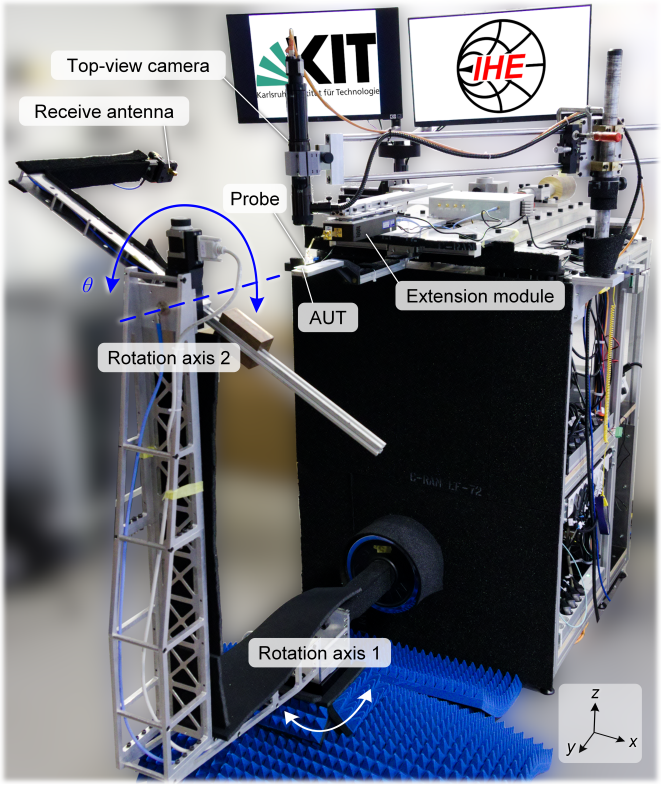


**Fig. D.7:** Experimental setup for characterization of THz antennas (TA). The TA were measured on a probe-based free-space antenna measurement setup, which allows to move a receive antenna around a contacted antenna under test (AUT) to record the direction-dependent radiation pattern of the latter. For measurement in the frequency range from 0.220 THz to 0.325 THz, a vector network analyzer is used in conjunction with a frequency-extension module connected via a millimeter-wave controller. A top-view camera helps in contacting the AUT and is swiveled to the side once the sample is contacted to not influence the measurement. The radiation pattern can be recorded by moving the receive antenna around the AUT at a constant distance of roughly 38 cm using a two-axis rotational system. For the antenna pattern shown in Fig. 5.5(b), the motor controlling the first rotation axis was set to a fixed position corresponding to an azimuth of $\varphi = 0\,^\circ$, while the stepping motor of the second stage was used to move the receive antenna around the AUT by sweeping the elevation angle $\theta$ — the corresponding trajectory is illustrated by a blue half-circle in Fig. 5.5(a). For each elevation angle $\theta$ we extract the realized gain $G_{\mathrm{R,TA}}(\varphi = 0\,^\circ, \theta)$ from the corresponding $S$-parameter measurement $\underline{S}_{21,\mathrm{TA}}(\varphi = 0\,^\circ, \theta)$ after performing a dedicated gain and SOL calibration.

at hand, the AUT can be contacted, and the direction-dependent realized gain can be calculated from the measured direction-dependent transmission $\underline{S}_{21,\mathrm{TA}}(\varphi,\theta)$,

$$G_{\mathrm{R,TA}}(\varphi,\theta) = |\underline{S}_{21,\mathrm{TA}}(\varphi,\theta)|^2/(G_{\mathrm{sys}}G_{\mathrm{probe}}). \tag{D.11}$$

In these relations, the direction is defined by the azimuth $\varphi$ and elevation $\theta$.

The measured TA was manufactured directly at the end of a transmission line in the center of a chip, thereby allowing easy handling and contacting of the CPW feed during measurement. A top-view camera helps in contacting the AUT and is swiveled to the side once the sample is contacted to not influence the measurement, see Fig. D.7. The direction-dependent radiation pattern is recorded by moving the receive antenna around the AUT at a constant distance of roughly $38\,\mathrm{cm}$ using a two-axis rotational system. For the antenna pattern shown in Fig. 5.5(b), the motor controlling the first rotation axis was set to a fixed position corresponding to an azimuth of $\varphi = 0^\circ$, while the stepping motor of the second stage was used to move the receive antenna around the AUT by sweeping the elevation angle $\theta$ from $\theta_{\mathrm{min}} = -90^\circ$ to $\theta_{\mathrm{max}} = +90^\circ$ in steps of $2^\circ$ for a total of $91$ measurements. The trajectory of the receive antenna is indicated by a blue half-circle in Fig. 5.5(a). For each elevation angle $\theta$, we extracted the realized gain $G_{\mathrm{R,TA}}(\varphi = 0^\circ,\theta)$ from the corresponding calibrated $S$-parameter measurement $\underline{S}_{21,\mathrm{TA}}(\varphi = 0^\circ,\theta)$ using Eq. (D.11). The gain can finally be expressed in decibels with respect to an isotropic radiator as $G_{\mathrm{R,TA,dBi}}(\varphi = 0^\circ,\theta) = 10\log_{10} G_{\mathrm{R,TA}}(\varphi = 0^\circ,\theta)$. The radiation pattern ($H$-plane) was recorded for a frequency of $0.274\,\mathrm{THz}$, where a maximum realized gain of $5.5\,\mathrm{dBi}$ was measured in the direction perpendicular to the substrate, i.e., for an elevation angle of $\theta = 0^\circ$.

## D.7 Conversion between $S$-parameters and $T$-matrix parameters

For conversion between $S$-parameters and $T$-matrix parameters, we use the following relations [163, 176]:

$$\underline{\mathbf{T}} = \begin{pmatrix} \underline{T}_{11} & \underline{T}_{12} \\ \underline{T}_{21} & \underline{T}_{22} \end{pmatrix} = \begin{pmatrix} 1/\underline{S}_{21} & -\underline{S}_{22}/\underline{S}_{21} \\ \underline{S}_{11}/\underline{S}_{21} & -\det(\underline{\mathbf{S}})/\underline{S}_{21} \end{pmatrix}, \tag{D.12}$$

$$\underline{\mathbf{S}} = \begin{pmatrix} \underline{S}_{11} & \underline{S}_{12} \\ \underline{S}_{21} & \underline{S}_{22} \end{pmatrix} = \begin{pmatrix} \underline{T}_{21}/\underline{T}_{11} & \det(\underline{\mathbf{T}})/\underline{T}_{11} \\ 1/\underline{T}_{11} & -\underline{T}_{12}/\underline{T}_{11} \end{pmatrix}. \tag{D.13}$$

In these relations, $\det(\underline{\mathbf{S}}) = \underline{S}_{11}\underline{S}_{22} - \underline{S}_{12}\underline{S}_{21}$ and $\det(\underline{\mathbf{T}}) = \underline{T}_{11}\underline{T}_{22} - \underline{T}_{12}\underline{T}_{21}$ are the determinant of the $S$-parameter matrix $\underline{\mathbf{S}}$ and $T$-parameter matrix $\underline{\mathbf{T}}$, respectively.

*[End of Supplementary Information of paper [J4]]*

# Bibliography


[1] Y. Xu, "Hybrid photonic assemblies based on 3D-printed coupling structures", Ph.D. Dissertation, Karlsruher Institut für Technologie (KIT), 2022. DOI: 10.5445/KSP/1000154744.

[2] M. Blaicher, "Photonic packaging enabled by three-dimensional microprinting", Ph.D. Dissertation, Karlsruher Institut für Technologie (KIT), 2021. DOI: 10.5445/IR/1000148073.

[3] P.-I. Dietrich, M. Blaicher, I. Reuter, M. Billah, T. Hoose, A. Hofmann, C. Caer, R. Dangel, B. Offrein, U. Troppenz, M. Möhrle, W. Freude, and C. Koos, "*In situ* 3D nanoprinting of free-form coupling elements for hybrid photonic integration", *Nature Photonics* **12**(4), pp. 241–247 (2018). DOI: 10.1038/S41566-018-0133-4.

[4] J. Orton, *Semiconductors and the Information Revolution*. Elsevier, 2009. DOI: 10.1016/B978-0-444-53240-4.X0001-3.

[5] N. Margalit, C. Xiang, S. M. Bowers, A. Bjorlin, R. Blum, and J. E. Bowers, "Perspective on the future of silicon photonics and electronics", *Applied Physics Letters* **118**(22), 220501 (2021). DOI: 10.1063/5.0050117.

[6] Cisco Systems Inc. "Cisco visual networking index: Forecast and trends, 2017–2022". (2019), [Online]. Available: https://twiki.cern.ch/twiki/pub/HEPIX/TechwatchNetwork/HtwNetworkDocuments/white-paper-c11-741490.pdf.

[7] Research and Markets. "Mobile data traffic - Global strategic business report". (2023), [Online]. Available: https://www.researchandmarkets.com/reports/2228047/mobile_data_traffic_global_strategic_business.

[8] S. Y. Siew, B. Li, F. Gao, H. Y. Zheng, W. Zhang, P. Guo, S. W. Xie, A. Song, B. Dong, L. W. Luo, C. Li, X. Luo, and G.-Q. Lo, "Review of silicon photonics technology and platform development", *Journal of Lightwave Technology* **39**(13), pp. 4374–4389 (2021). DOI: 10.1109/JLT.2021.3066203.

[9] K. K. Lee, D. R. Lim, L. C. Kimerling, J. Shin, and F. Cerrina, "Fabrication of ultralow-loss $Si/SiO_2$ waveguides by roughness reduction", *Optics Letters* **26**(23), pp. 1888–1890 (2001). DOI: 10.1364/OL.26.001888.

[10] P. Trinh, B. Jalali, and S. Yegnanarayanan, "Integrated optical directional couplers in silicon-on-insulator", *Electronics Letters* **31**(24), pp. 2097–2098 (1995). DOI: 10.1049/EL:19951453.

[11] K. Liu, N. Jin, H. Cheng, N. Chauhan, M. W. Puckett, K. D. Nelson, R. O. Behunin, P. T. Rakich, and D. J. Blumenthal, "Ultralow 0.034 dB/m loss wafer-scale integrated photonics realizing 720 million $Q$ and 380 µW threshold Brillouin lasing", *Optics Letters* **47**(7), pp. 1855–1858 (2022). DOI: 10.1364/OL.454392.

[12] P. Trinh, S. Yegnanarayanan, F. Coppinger, and B. Jalali, "Silicon-on-insulator (SOI) phased-array wavelength multi/demultiplexer with extremely low-polarization sensitivity", *IEEE Photonics Technology Letters* **9**(7), pp. 940–942 (1997). DOI: 10.1109/68.593358.

[13] A. Liu, R. Jones, L. Liao, D. Samara-Rubio, D. Rubin, O. Cohen, R. Nicolaescu, and M. Paniccia, "A high-speed silicon optical modulator based on a metal–oxide–semiconductor capacitor", *Nature* **427**(6975), pp. 615–618 (2004). DOI: 10.1038/NATURE02310.

[14] S. Lischke, A. Peczek, J. S. Morgan, K. Sun, D. Steckler, Y. Yamamoto, F. Korndörfer, C. Mai, S. Marschmeyer, M. Fraschke, A. Krüger, A. Beling, and L. Zimmermann, "Ultra-fast germanium photodiode with 3-dB bandwidth of 265 GHz", *Nature Photonics* **15**(12), pp. 925–931 (2021). DOI: 10.1038/S41566-021-00893-W.

[15] M. Smit, K. Williams, and J. van der Tol, "Past, present, and future of InP-based photonic integration", *APL Photonics* **4**(5), 050901 (2019). DOI: 10.1063/1.5087862.

[16] J. Liu, G. Huang, R. N. Wang, J. He, A. S. Raja, T. Liu, N. J. Engelsen, and T. J. Kippenberg, "High-yield, wafer-scale fabrication of ultralow-loss, dispersion-engineered silicon nitride photonic circuits", *Nature Communications* **12**(1), 2236 (2021). DOI: 10.1038/S41467-021-21973-Z.

[17] C. G. H. Roeloffzen, M. Hoekman, E. J. Klein, L. S. Wevers, R. B. Timens, D. Marchenko, D. Geskus, R. Dekker, A. Alippi, R. Grootjans, A. van Rees, R. M. Oldenbeuving, J. P. Epping, R. G. Heideman, K. Worhoff, A. Leinse, D. Geuzebroek, E. Schreuder, P. W. L. van Dijk, I. Visscher, C. Taddei, Y. Fan, C. Taballione, Y. Liu, D. Marpaung, L. Zhuang, M. Benelajla, and K.-J. Boller, "Low-loss $Si_3N_4$ TriPleX optical waveguides: Technology and applications overview", *IEEE Journal of Selected Topics in Quantum Electronics* **24**(4), pp. 1–21 (2018). DOI: 10.1109/JSTQE.2018.2793945.

[18] B. Kuyken, F. Leo, S. Clemmen, U. Dave, R. V. Laer, T. Ideguchi, H. Zhao, X. Liu, J. Safioui, S. Coen, S. Gorza, S. K. Selvaraja, S. Massar, R. M. Osgood, P. Verheyen, J. V. Campenhout, R. Baets, W. J. Green, and G. Roelkens, "Nonlinear optical interactions in silicon waveguides", *Nanophotonics* **6**(2), pp. 377–392 (2017). DOI: 10.1515/NANOPH-2016-0001.

[19] C. Xiang, W. Jin, and J. E. Bowers, "Silicon nitride passive and active photonic integrated circuits: Trends and prospects", *Photonics Research* **10**(6), A82–A96 (2022). DOI: 10.1364/PRJ.452936.

[20] K.-J. Boller, A. van Rees, Y. Fan, J. Mak, R. Lammerink, C. Franken, P. van der Slot, D. Marpaung, C. Fallnich, J. Epping, R. Oldenbeuving, D. Geskus, R. Dekker, I. Visscher, R. Grootjans, C. Roeloffzen, M. Hoekman, E. Klein, A. Leinse, and R. Heideman, "Hybrid integrated semiconductor lasers with silicon nitride feedback circuits", *Photonics* **7**(1), 4 (2019). DOI: 10.3390/PHOTONICS7010004.

[21] Y. Vilenchik, C. T. Santis, S. T. Steger, N. Satyan, and A. Yariv, "Theory and observation on non-linear effects limiting the coherence properties of high-$Q$ hybrid Si/III-V lasers", in *Proc. SPIE* 9382, *Novel In-Plane Semiconductor Lasers XIV* (2015), paper 93820N. DOI: 10.1117/12.2078067.

[22] M. H. P. Pfeiffer, A. Kordts, V. Brasch, M. Zervas, M. Geiselmann, J. D. Jost, and T. J. Kippenberg, "Photonic Damascene process for integrated high-$Q$ microresonator based nonlinear photonics", *Optica* **3**(1), pp. 20–25 (2016). DOI: 10.1364/OPTICA.3.000020.

[23] B. Stern, X. Ji, Y. Okawachi, A. L. Gaeta, and M. Lipson, "Battery-operated integrated frequency comb generator", *Nature* **562**(7727), pp. 401–405 (2018). DOI: 10.1038/S41586-018-0598-9.

[24] B. Shen, L. Chang, J. Liu, H. Wang, Q.-F. Yang, C. Xiang, R. N. Wang, J. He, T. Liu, W. Xie, J. Guo, D. Kinghorn, L. Wu, Q.-X. Ji, T. J. Kippenberg, K. Vahala, and J. E. Bowers, "Integrated turnkey soliton microcombs", *Nature* **582**(7812), pp. 365–369 (2020). DOI: 10.1038/S41586-020-2358-X.

[25] T. C. Briles, S.-P. Yu, L. Chang, C. Xiang, J. Guo, D. Kinghorn, G. Moille, K. Srinivasan, J. E. Bowers, and S. B. Papp, "Hybrid InP and SiN integration of an octave-spanning frequency comb", *APL Photonics* **6**(2), 026102 (2021). DOI: 10.1063/5.0035452.

[26] W. Jin, Q.-F. Yang, L. Chang, B. Shen, H. Wang, M. A. Leal, L. Wu, M. Gao, A. Feshali, M. Paniccia, K. J. Vahala, and J. E. Bowers, "Hertz-linewidth semiconductor lasers using CMOS-ready ultra-high-$Q$ microresonators", *Nature Photonics* **15**(5), pp. 346–353 (2021). DOI: 10.1038/S41566-021-00761-7.

[27] C. O. de Beeck, B. Haq, L. Elsinger, A. Gocalinska, E. Pelucchi, B. Corbett, G. Roelkens, and B. Kuyken, "Heterogeneous III-V on silicon nitride amplifiers and lasers via microtransfer printing", *Optica* **7**(5), pp. 386–393 (2020). DOI: 10.1364/OPTICA.382989.

[28] C. Xiang, W. Jin, O. Terra, B. Dong, H. Wang, L. Wu, J. Guo, T. J. Morin, E. Hughes, J. Peters, Q.-X. Ji, A. Feshali, M. Paniccia, K. J. Vahala, and J. E. Bowers, "3D integration enables ultralow-noise isolator-free lasers in silicon photonics", *Nature* **620**(7972), pp. 78–85 (2023). DOI: 10.1038/S41586-023-06251-W.

[29] M. A. Tran, C. Zhang, T. J. Morin, L. Chang, S. Barik, Z. Yuan, W. Lee, G. Kim, A. Malik, Z. Zhang, J. Guo, H. Wang, B. Shen, L. Wu, K. Vahala, J. E. Bowers, H. Park, and T. Komljenovic, "Extending the spectrum of fully integrated photonics to submicrometre wavelengths", *Nature* **610**(7930), pp. 54–60 (2022). DOI: 10.1038/S41586-022-05119-9.

[30] D. Liang, A. W. Fang, H. Park, T. E. Reynolds, K. Warner, D. C. Oakley, and J. E. Bowers, "Low-temperature, strong $SiO_2$-$SiO_2$ covalent wafer bonding for III-V compound semiconductors-to-silicon photonic integrated circuits", *Journal of Electronic Materials* **37**(10), pp. 1552–1559 (2008). DOI: 10.1007/S11664-008-0489-1.

[31] Y. Gao, J.-C. Lo, S. Lee, R. Patel, L. Zhu, J. Nee, D. Tsou, R. Carney, and J. Sun, "High-power, narrow-linewidth, miniaturized silicon photonic tunable laser with accurate frequency control", *Journal of Lightwave Technology* **38**(2), pp. 265–271 (2020). DOI: 10.1109/JLT.2019.2940589.

[32] H. Guan, A. Novack, T. Galfsky, Y. Ma, S. Fathololoumi, A. Horth, T. N. Huynh, J. Roman, R. Shi, M. Caverley, Y. Liu, T. Baehr-Jones, K. Bergman, and M. Hochberg, "Widely-tunable, narrow-linewidth III-V/silicon hybrid external-cavity laser for coherent communication", *Optics Express* **26**(7), pp. 7920–7933 (2018). DOI: 10.1364/OE.26.007920.

[33] N. Kobayashi, K. Sato, M. Namiwaka, K. Yamamoto, S. Watanabe, T. Kita, H. Yamada, and H. Yamazaki, "Silicon photonic hybrid ring-filter external cavity wavelength tunable lasers", *Journal of Lightwave Technology* **33**(6), pp. 1241–1246 (2015). DOI: 10.1109/JLT.2014.2385106.

[34] S. Watanabe, M. Takahashi, K. Suzuki, T. Takeuchi, Y. Deki, T. Hatanaka, N. Sakuma, A. Kawauchi, S. Takaesu, M. Horie, T. Miyazaki, M. Kurihara,

M. Kanemoto, T. Kaneko, I. Tomita, M. Namiwaka, M. Nido, and H. Yamazaki, "High power tunable resonated-ring-reflector laser using passive alignment technology", in *European Conference on Optical Communications* (ECOC 2006), pp. 1–2. DOI: 10.1109/ECOC.2006.4801077.

[35] J. S. Lee, L. Carroll, C. Scarcella, N. Pavarelli, S. Menezo, S. Bernabe, E. Temporiti, and P. O'Brien, "Meeting the electrical, optical, and thermal design challenges of photonic-packaging", *IEEE Journal of Selected Topics in Quantum Electronics* **22**(6), pp. 409–417 (2016). DOI: 10.1109/JSTQE.2016.2543150.

[36] E. R. H. Fuchs, E. J. Bruce, R. J. Ram, and R. E. Kirchain, "Process-based cost modeling of photonics manufacture: The cost competitiveness of monolithic integration of a 1550-nm DFB laser and an electroabsorptive modulator on an InP platform", *Journal of Lightwave Technology* **24**(8), pp. 3175–3186 (2006). DOI: 10.1109/JLT.2006.875961.

[37] S. Latkowski, D. Pustakhod, M. Chatzimichailidis, W. Yao, and X. J. M. Leijtens, "Open standards for automation of testing of photonic integrated circuits", *IEEE Journal of Selected Topics in Quantum Electronics* **25**(5), pp. 1–8 (2019). DOI: 10.1109/JSTQE.2019.2921401.

[38] T. Baldacchini, Ed., *Three-Dimensional Microfabrication Using Two-Photon Polymerization*. William Andrew, 2016. DOI: 10.1016/C2014-0-01016-7.

[39] H. Wang, W. Zhang, D. Ladika, H. Yu, D. Gailevičius, H. Wang, C.-F. Pan, P. N. S. Nair, Y. Ke, T. Mori, J. Y. E. Chan, Q. Ruan, M. Farsari, M. Malinauskas, S. Juodkazis, M. Gu, and J. K. W. Yang, "Two-photon polymerization lithography for optics and photonics: Fundamentals, materials, technologies, and applications", *Advanced Functional Materials* **33**(39), 2214211 (2023). DOI: 10.1002/ADFM.202214211.

[40] M. Blaicher, M. R. Billah, J. Kemal, T. Hoose, P. Marin-Palomo, A. Hofmann, Y. Kutuvantavida, C. Kieninger, P.-I. Dietrich, M. Lauermann, S. Wolf, U. Troppenz, M. Möhrle, F. Merget, S. Skacel, J. Witzens, S. Randel, W. Freude, and C. Koos, "Hybrid multi-chip assembly of optical

communication engines by *in situ* 3D nano-lithography", *Light: Science & Applications* **9**(1), 71 (2020). DOI: 10.1038/S41377-020-0272-5.

[41] A. Nesic, M. Blaicher, P. Marin-Palomo, C. Füllner, S. Randel, W. Freude, and C. Koos, "Ultra-broadband polarisation beam splitters and rotators based on 3D-printed waveguides", *Light: Advanced Manufacturing* **4**(3), 22 (2023). DOI: 10.37188/LAM.2023.022.

[42] M. R. Billah, M. Blaicher, T. Hoose, P.-I. Dietrich, P. Marin-Palomo, N. Lindenmann, A. Nesic, A. Hofmann, U. Troppenz, M. Möhrle, S. Randel, W. Freude, and C. Koos, "Hybrid integration of silicon photonics circuits and InP lasers by photonic wire bonding", *Optica* **5**(7), pp. 876–883 (2018). DOI: 10.1364/OPTICA.5.000876.

[43] Y. Xu, A. Kuzmin, E. Knehr, M. Blaicher, K. Ilin, P.-I. Dietrich, W. Freude, M. Siegel, and C. Koos, "Superconducting nanowire single-photon detector with 3D-printed free-form microlenses", *Optics Express* **29**(17), pp. 27 708–27 731 (2021). DOI: 10.1364/OE.427639.

[44] A. Shafie, N. Yang, C. Han, J. M. Jornet, M. Juntti, and T. Kürner, "Terahertz communications for 6G and beyond wireless networks: Challenges, key advancements, and opportunities", *IEEE Network* **37**(3), pp. 162–169 (2023). DOI: 10.1109/MNET.118.2200057.

[45] T. Harter, "Wireless terahertz communications: Optoelectronic devices and signal processing", Ph.D. Dissertation, Karlsruher Institut für Technologie (KIT), 2021. DOI: 10.5445/KSP/1000128941.

[46] P. Sen, J. V. Siles, N. Thawdar, and J. M. Jornet, "Multi-kilometre and multi-gigabit-per-second sub-terahertz communications for wireless backhaul applications", *Nature Electronics* **6**(2), pp. 164–175 (2022). DOI: 10.1038/S41928-022-00897-6.

[47] I. G. de Arrieta, "Beyond the infrared: A centenary of Heinrich Rubens's death", *The European Physical Journal H* **47**(1), 11 (2022). DOI: 10.1140/EPJH/S13129-022-00044-X.

[48] S. Makhlouf, O. Cojocari, M. Hofmann, T. Nagatsuma, S. Preu, N. Weimann, H.-W. Hübers, and A. Stöhr, "Terahertz sources and receivers: From the past to the future", *IEEE Journal of Microwaves* **3**(3), pp. 894–912 (2023). DOI: 10.1109/JMW.2023.3282875.

[49] H.-J. Song, "Packages for terahertz electronics", *Proceedings of the IEEE* **105**(6), pp. 1121–1138 (2017). DOI: 10.1109/JPROC.2016.2633547.

[50] M. Grzeslo, S. Dülme, S. Clochiatti, T. Neerfeld, T. Haddad, P. Lu, J. Tebart, S. Makhlouf, C. Biurrun-Quel, J. L. F. Estévez, J. Lackmann, N. Weimann, and A. Stöhr, "High saturation photocurrent THz waveguide-type MUTC-photodiodes reaching mW output power within the WR3.4 band", *Optics Express* **31**(4), pp. 6484–6498 (2023). DOI: 10.1364/OE.475987.

[51] T. Harter, S. Ummethala, M. Blaicher, S. Muehlbrandt, S. Wolf, M. Weber, M. M. H. Adib, J. N. Kemal, M. Merboldt, F. Boes, S. Nellen, A. Tessmann, M. Walther, B. Globisch, T. Zwick, W. Freude, S. Randel, and C. Koos, "Wireless THz link with optoelectronic transmitter and receiver", *Optica* **6**(8), pp. 1063–1070 (2019). DOI: 10.1364/OPTICA.6.001063.

[52] S. Ummethala, T. Harter, K. Koehnle, Z. Li, S. Muehlbrandt, Y. Kutuvantavida, J. Kemal, P. Marin-Palomo, J. Schaefer, A. Tessmann, S. K. Garlapati, A. Bacher, L. Hahn, M. Walther, T. Zwick, S. Randel, W. Freude, and C. Koos, "THz-to-optical conversion in wireless communications using an ultra-broadband plasmonic modulator", *Nature Photonics* **13**(8), pp. 519–524 (2019). DOI: 10.1038/S41566-019-0475-6.

[53] T. Harter, S. Muehlbrandt, S. Ummethala, A. Schmid, S. Nellen, L. Hahn, W. Freude, and C. Koos, "Silicon–plasmonic integrated circuits for terahertz signal generation and coherent detection", *Nature Photonics* **12**(10), pp. 625–633 (2018). DOI: 10.1038/S41566-018-0237-X.

[54] F. Thome and A. Leuther, "A 75–305-GHz power amplifier MMIC with 10–14.9-dBm $P_{\mathrm{out}}$ in a 35-nm InGaAs mHEMT technology", *IEEE*

*Microwave and Wireless Components Letters* **31**(6), pp. 741–743 (2021). DOI: 10.1109/LMWC.2021.3058101.

[55] H.-Y. Lee, "Wideband characterization of a typical bonding wire for microwave and millimeter-wave integrated circuits", *IEEE Transactions on Microwave Theory and Techniques* **43**(1), pp. 63–68 (1995). DOI: 10.1109/22.363006.

[56] A. Jentzsch and W. Heinrich, "Theory and measurements of flip-chip interconnects for frequencies up to 100 GHz", *IEEE Transactions on Microwave Theory and Techniques* **49**(5), pp. 871–878 (2001). DOI: 10.1109/22.920143.

[57] S. Kawata, H.-B. Sun, T. Tanaka, and K. Takada, "Finer features for functional microdevices", *Nature* **412**(6848), pp. 697–698 (2001). DOI: 10.1038/35089130.

[58] Y. Song, R. M. Panas, S. Chizari, L. A. Shaw, J. A. Jackson, J. B. Hopkins, and A. J. Pascall, "Additively manufacturable micro-mechanical logic gates", *Nature Communications* **10**(1), 882 (2019). DOI: 10.1038/S41467-019-08678-0.

[59] T. Frenzel, M. Kadic, and M. Wegener, "Three-dimensional mechanical metamaterials with a twist", *Science* **358**(6366), pp. 1072–1074 (2017). DOI: 10.1126/SCIENCE.AAO4640.

[60] S. Grebenyuk, A. R. A. Fattah, M. Kumar, B. Toprakhisar, G. Rustandi, A. Vananroye, I. Salmon, C. Verfaillie, M. Grillo, and A. Ranga, "Large-scale perfused tissues via synthetic 3D soft microfluidics", *Nature Communications* **14**(1), 193 (2023). DOI: 10.1038/S41467-022-35619-1.

[61] M. Hippler, E. D. Lemma, S. Bertels, E. Blasco, C. Barner-Kowollik, M. Wegener, and M. Bastmeyer, "3D scaffolds to study basic cell biology", *Advanced Materials* **31**(26), 1808110 (2019). DOI: 10.1002/ADMA.201808110.

[62] L. Yang, H. Hu, A. Scholz, F. Feist, G. C. Marques, S. Kraus, N. M. Bojanowski, E. Blasco, C. Barner-Kowollik, J. Aghassi-Hagmann, and M. Wegener, "Laser printed microelectronics", *Nature Communications* **14**(1), 1103 (2023). DOI: 10.1038/S41467-023-36722-7.

[63] T. Gissibl, S. Thiele, A. Herkommer, and H. Giessen, "Two-photon direct laser writing of ultracompact multi-lens objectives", *Nature Photonics* **10**(8), pp. 554–560 (2016). DOI: 10.1038/NPHOTON.2016.121.

[64] M. Göppert-Mayer, "Über Elementarakte mit zwei Quantensprüngen", *Annalen der Physik* **401**(3), pp. 273–294 (1931). DOI: 10.1002/ANDP.19314010303.

[65] W. Kaiser and C. G. B. Garrett, "Two-photon excitation in $CaF_2$:$Eu^{2+}$", *Physical Review Letters* **7**(6), pp. 229–231 (1961). DOI: 10.1103/PHYSREVLETT.7.229.

[66] W. R. Zipfel, R. M. Williams, and W. W. Webb, "Nonlinear magic: Multiphoton microscopy in the biosciences", *Nature Biotechnology* **21**(11), pp. 1369–1377 (2003). DOI: 10.1038/NBT899.

[67] S. Maruo, O. Nakamura, and S. Kawata, "Three-dimensional microfabrication with two-photon-absorbed photopolymerization", *Optics Letters* **22**(2), pp. 132–134 (1997). DOI: 10.1364/OL.22.000132.

[68] M. Malinauskas, A. Žukauskas, S. Hasegawa, Y. Hayasaki, V. Mizeikis, R. Buividas, and S. Juodkazis, "Ultrafast laser processing of materials: From science to industry", *Light: Science & Applications* **5**(8), e16133 (2016). DOI: 10.1038/LSA.2016.133.

[69] W. H. Teh, U. Dürig, U. Drechsler, C. G. Smith, and H.-J. Güntherodt, "Effect of low numerical-aperture femtosecond two-photon absorption on (SU-8) resist for ultrahigh-aspect-ratio microstereolithography", *Journal of Applied Physics* **97**(5), 054907 (2005). DOI: 10.1063/1.1856214.

[70] A. S. Quick, J. Fischer, B. Richter, T. Pauloehrl, V. Trouillet, M. Wegener, and C. Barner-Kowollik, "Preparation of reactive three-dimensional microstructures via direct laser writing and thiol-ene chemistry", *Macromolecular Rapid Communications* **34**(4), pp. 335–340 (2013). DOI: 10.1002/MARC.201200796.

[71] J. Fischer, J. B. Mueller, J. Kaschke, T. J. A. Wolf, A.-N. Unterreiner, and M. Wegener, "Three-dimensional multi-photon direct laser writing with variable repetition rate", *Optics Express* **21**(22), pp. 26 244–26 260 (2013). DOI: 10.1364/OE.21.026244.

[72] J. B. Mueller, J. Fischer, F. Mayer, M. Kadic, and M. Wegener, "Polymerization kinetics in three-dimensional direct laser writing", *Advanced Materials* **26**(38), pp. 6566–6571 (2014). DOI: 10.1002/ADMA.201402366.

[73] K. Takada, H.-B. Sun, and S. Kawata, "Improved spatial resolution and surface roughness in photopolymerization-based laser nanowriting", *Applied Physics Letters* **86**(7), 071122 (2005). DOI: 10.1063/1.1864249.

[74] H.-B. Sun, K. Takada, M.-S. Kim, K.-S. Lee, and S. Kawata, "Scaling laws of voxels in two-photon photopolymerization nanofabrication", *Applied Physics Letters* **83**(6), pp. 1104–1106 (2003). DOI: 10.1063/1.1599968.

[75] J. Fischer and M. Wegener, "Three-dimensional optical laser lithography beyond the diffraction limit", *Laser & Photonics Reviews* **7**(1), pp. 22–44 (2012). DOI: 10.1002/LPOR.201100046.

[76] P. Kiefer, V. Hahn, M. Nardi, L. Yang, E. Blasco, C. Barner-Kowollik, and M. Wegener, "Sensitive photoresists for rapid multiphoton 3D laser micro- and nanoprinting", *Advanced Optical Materials* **8**(19), 2000895 (2020). DOI: 10.1002/ADOM.202000895.

[77] L. Yang, A. Münchinger, M. Kadic, V. Hahn, F. Mayer, E. Blasco, C. Barner-Kowollik, and M. Wegener, "On the Schwarzschild effect in 3D two-photon laser lithography", *Advanced Optical Materials* **7**(22), 1901040 (2019). DOI: 10.1002/ADOM.201901040.

[78] B. Richards and E. Wolf, "Electromagnetic diffraction in optical systems, II. Structure of the image field in an aplanatic system", *Proceedings of the Royal Society of London. Series A. Mathematical and Physical Sciences* **253**(1274), pp. 358–379 (1959). DOI: 10.1098/RSPA.1959.0200.

[79] J. Mertz, "3d imaging", in *Introduction to Optical Microscopy*. Cambridge University Press, 2019, pp. 70–91. DOI: 10.1017/9781108552660.007.

[80] J. Fischer, J. B. Mueller, A. S. Quick, J. Kaschke, C. Barner-Kowollik, and M. Wegener, "Exploring the mechanisms in STED-enhanced direct laser writing", *Advanced Optical Materials* **3**(2), pp. 221–232 (2014). DOI: 10.1002/ADOM.201400413.

[81] B. J. Jiao, F. Chen, Y. Liu, X. Fan, S. Zeng, Q. Dong, L. Deng, H. Gao, and W. Xiong, "Acousto-optic scanning spatial-switching multiphoton lithography", *International Journal of Extreme Manufacturing* **5**(3), 035008 (2023). DOI: 10.1088/2631-7990/ACE0A7.

[82] V. Hahn, T. Messer, N. M. Bojanowski, E. R. Curticean, I. Wacker, R. R. Schröder, E. Blasco, and M. Wegener, "Two-step absorption instead of two-photon absorption in 3D nanoprinting", *Nature Photonics* **15**(12), pp. 932–938 (2021). DOI: 10.1038/S41566-021-00906-8.

[83] V. Hahn, P. Rietz, F. Hermann, P. Müller, C. Barner-Kowollik, T. Schlöder, W. Wenzel, E. Blasco, and M. Wegener, "Light-sheet 3D microprinting via two-colour two-step absorption", *Nature Photonics* **16**(11), pp. 784–791 (2022). DOI: 10.1038/S41566-022-01081-0.

[84] X. Liu, C. Ding, X. Gao, X. Shen, M. Tang, Z. Yang, L. Xu, C. Kuang, and X. Liu, "High-resolution 3D nanoprinting based on two-step absorption via an integrated fiber-coupled laser diode", *Optics Letters* **48**(16), pp. 4300–4303 (2023). DOI: 10.1364/OL.495286.

[85] S. A. Diddams, K. Vahala, and T. Udem, "Optical frequency combs: Coherently uniting the electromagnetic spectrum", *Science* **369**(6501), eaay3676 (2020). DOI: 10.1126/SCIENCE.AAY3676.

[86] P. Trocha, M. Karpov, D. Ganin, M. H. P. Pfeiffer, A. Kordts, S. Wolf, J. Krockenberger, P. Marin-Palomo, C. Weimann, S. Randel, W. Freude, T. J. Kippenberg, and C. Koos, "Ultrafast optical ranging using microresonator soliton frequency combs", *Science* **359**(6378), pp. 887–891 (2018). DOI: 10.1126/SCIENCE.AAO3924.

[87] L. Li, T. Wang, X. Li, P. Huang, Y. Guo, L. Lu, L. Zhou, and G. Zeng, "Continuous-variable quantum key distribution with on-chip light sources", *Photonics Research* **11**(4), pp. 504–516 (2023). DOI: 10.1364/PRJ.473328.

[88] K. Kikuchi, "Characterization of semiconductor-laser phase noise and estimation of bit-error rate performance with low-speed offline digital coherent receivers", *Optics Express* **20**(5), pp. 5291–5302 (2012). DOI: 10.1364/OE.20.005291.

[89] N. V. Bandel, M. Myara, M. Sellahi, T. Souici, R. Dardaillon, and P. Signoret, "Time-dependent laser linewidth: Beat-note digital acquisition and numerical analysis", *Optics Express* **24**(24), pp. 27 961–27 978 (2016). DOI: 10.1364/OE.24.027961.

[90] Z. Zhang and A. Yariv, "A general relation between frequency noise and lineshape of laser light", *IEEE Journal of Quantum Electronics* **56**(3), pp. 1–5 (2020). DOI: 10.1109/JQE.2020.2980011.

[91] N. Wiener, "Generalized harmonic analysis", *Acta Mathematica* **55**, pp. 117–258 (1930). DOI: 10.1007/bf02546511.

[92] A. Khintchine, "Korrelationstheorie der stationären stochastischen Prozesse", *Mathematische Annalen* **109**(1), pp. 604–615 (1934). DOI: 10.1007/BF01449156.

[93] G. M. Stéphan, T. T. Tam, S. Blin, P. Besnard, and M. Têtu, "Laser line shape and spectral density of frequency noise", *Physical Review A* **71**(4), 043809 (2005). DOI: 10.1103/PHYSREVA.71.043809.

[94] L. Mercer, "1/*f* frequency noise effects on self-heterodyne linewidth measurements", *Journal of Lightwave Technology* **9**(4), pp. 485–493 (1991). DOI: 10.1109/50.76663.

[95] G. D. Domenico, S. Schilt, and P. Thomann, "Simple approach to the relation between laser frequency noise and laser line shape", *Applied Optics* **49**(25), pp. 4801–4807 (2010). DOI: 10.1364/AO.49.004801.

[96] A. L. Schawlow and C. H. Townes, "Infrared and optical masers", *Physical Review* **112**(6), pp. 1940–1949 (1958). DOI: 10.1103/PHYSREV.112.1940.

[97] M. Lax, "Classical noise. V. Noise in self-sustained oscillators", *Physical Review* **160**(2), pp. 290–307 (1967). DOI: 10.1103/PHYSREV.160.290.

[98] C. Henry, "Theory of the linewidth of semiconductor lasers", *IEEE Journal of Quantum Electronics* **18**(2), pp. 259–264 (1982). DOI: 10.1109/JQE.1982.1071522.

[99] L. A. Coldren, S. W. Corzine, and M. L. Mašanović, *Diode Lasers and Photonic Integrated Circuits*. John Wiley & Sons, 2012. DOI: 10.1002/9781118148167.

[100] M. Osinski and J. Buus, "Linewidth broadening factor in semiconductor lasers – An overview", *IEEE Journal of Quantum Electronics* **23**(1), pp. 9–29 (1987). DOI: 10.1109/JQE.1987.1073204.

[101] M. Chen, Z. Meng, J. Wang, and W. Chen, "Ultra-narrow linewidth measurement based on Voigt profile fitting", *Optics Express* **23**(5), pp. 6803–6808 (2015). DOI: 10.1364/OE.23.006803.

[102] T. Pfau, S. Hoffmann, and R. Noe, "Hardware-efficient coherent digital receiver concept with feedforward carrier recovery for *M*-QAM constellations", *Journal of Lightwave Technology* **27**(8), pp. 989–999 (2009). DOI: 10.1109/JLT.2008.2010511.

[103] J. N. Kemal, P. Marin-Palomo, M. Karpov, M. H. Anderson, W. Freude, T. J. Kippenberg, and C. Koos, "Chapter 2 - Chip-based frequency combs for wavelength-division multiplexing applications", in *Optical Fiber Telecommunications VII*, A. E. Willner, Ed. Academic Press, 2020, pp. 51–102. DOI: 10.1016/b978-0-12-816502-7.00002-6.

[104] M. A. Tran, D. Huang, and J. E. Bowers, "Tutorial on narrow linewidth tunable semiconductor lasers using Si/III-V heterogeneous integration", *APL Photonics* **4**(11), 111101 (2019). DOI: 10.1063/1.5124254.

[105] H. R. T. R. Paschotta and U. Keller, "Noise of solid state lasers", in *Solid-State Lasers and Applications*, A. Sennaroglu, Ed. CRC Press, 2007, pp. 473–510. DOI: 10.1201/9781420005295-12.

[106] Q. Cui, Y. Lei, Y. Chen, C. Qiu, Y. Wang, D. Zhang, L. Fan, Y. Song, P. Jia, L. Liang, Y. Wang, L. Qin, Y. Ning, and L. Wang, "Advances in wide-tuning and narrow-linewidth external-cavity diode lasers", *Science China Information Sciences* **65**(8), 181401 (2022). DOI: 10.1007/S11432-021-3454-7.

[107] C. Xiang, P. A. Morton, and J. E. Bowers, "Ultra-narrow linewidth laser based on a semiconductor gain chip and extended $Si_3N_4$ Bragg grating", *Optics Letters* **44**(15), pp. 3825–3828 (2019). DOI: 10.1364/OL.44.003825.

[108] P. A. Morton, C. Xiang, J. B. Khurgin, C. D. Morton, M. Tran, J. Peters, J. Guo, M. J. Morton, and J. E. Bowers, "Integrated coherent tunable laser (ICTL) with ultra-wideband wavelength tuning and sub-100 Hz Lorentzian linewidth", *Journal of Lightwave Technology* **40**(6), pp. 1802–1809 (2022). DOI: 10.1109/JLT.2021.3127155.

[109] E. Patzak, A. Sugimura, S. Saito, T. Mukai, and H. Olesen, "Semiconductor laser linewidth in optical feedback configurations", *Electronics Letters* **19**(24), pp. 1026–1027 (1983). DOI: 10.1049/EL:19830695.

[110] K. Vahala and A. Yariv, "Detuned loading in coupled cavity semiconductor lasers – effect on quantum noise and dynamics", *Applied Physics Letters* **45**(5), pp. 501–503 (1984). DOI: 10.1063/1.95316.

[111] R. Kazarinov and C. Henry, "The relation of line narrowing and chirp reduction resulting from the coupling of a semiconductor laser to passive resonator", *IEEE Journal of Quantum Electronics* **23**(9), pp. 1401–1409 (1987). DOI: 10.1109/JQE.1987.1073531.

[112] D. G. Rabus, "Ring resonators: Theory and modeling", in *Integrated Ring Resonators*. Springer, 2007, pp. 3–40. DOI: 10.1007/978-3-540-68788-7_2.

[113] R. Soref and B. Bennett, "Electrooptical effects in silicon", *IEEE Journal of Quantum Electronics* **23**(1), pp. 123–129 (1987). DOI: 10.1109/JQE.1987.1073206.

[114] A. van Rees, Y. Fan, D. Geskus, E. J. Klein, R. M. Oldenbeuving, P. J. M. van der Slot, and K.-J. Boller, "Ring resonator enhanced mode-hop-free wavelength tuning of an integrated extended-cavity laser", *Optics Express* **28**(4), pp. 5669–5683 (2020). DOI: 10.1364/OE.386356.

[115] K. Wörhoff, R. G. Heideman, A. Leinse, and M. Hoekman, "TriPleX: A versatile dielectric photonic platform", *Advanced Optical Technologies* **4**(2), pp. 189–207 (2015). DOI: 10.1515/AOT-2015-0016.

[116] H. Bao, A. Cooper, M. Rowley, L. D. Lauro, J. S. T. Gongora, S. T. Chu, B. E. Little, G.-L. Oppo, R. Morandotti, D. J. Moss, B. Wetzel, M. Peccianti, and A. Pasquazi, "Laser cavity-soliton microcombs", *Nature Photonics* **13**(6), pp. 384–389 (2019). DOI: 10.1038/S41566-019-0379-5.

[117] A. R. Johnson, Y. Okawachi, M. R. E. Lamont, J. S. Levy, M. Lipson, and A. L. Gaeta, "Microresonator-based comb generation without an external laser source", *Optics Express* **22**(2), pp. 1394–1401 (2014). DOI: 10.1364/OE.22.001394.

[118] H. Guo, M. Karpov, E. Lucas, A. Kordts, M. H. P. Pfeiffer, V. Brasch, G. Lihachev, V. E. Lobanov, M. L. Gorodetsky, and T. J. Kippenberg, "Universal dynamics and deterministic switching of dissipative Kerr solitons in optical microresonators", *Nature Physics* **13**(1), pp. 94–102 (2016). DOI: 10.1038/NPHYS3893.

[119] T. Herr, V. Brasch, J. D. Jost, C. Y. Wang, N. M. Kondratiev, M. L. Gorodetsky, and T. J. Kippenberg, "Temporal solitons in optical microresonators", *Nature Photonics* **8**(2), pp. 145–152 (2013). DOI: 10.1038/NPHOTON.2013.343.

[120] X. Xue, M. Qi, and A. M. Weiner, "Normal-dispersion microresonator Kerr frequency combs", *Nanophotonics* **5**(2), pp. 244–262 (2016). DOI: 10.1515/NANOPH-2016-0016.

[121] C. Joshi, J. K. Jang, K. Luke, X. Ji, S. A. Miller, A. Klenner, Y. Okawachi, M. Lipson, and A. L. Gaeta, "Thermally controlled comb generation and soliton modelocking in microresonators", *Optics Letters* **41**(11), pp. 2565–2568 (2016). DOI: 10.1364/OL.41.002565.

[122] V. Brasch, M. Geiselmann, T. Herr, G. Lihachev, M. H. P. Pfeiffer, M. L. Gorodetsky, and T. J. Kippenberg, "Photonic chip-based optical frequency comb using soliton Cherenkov radiation", *Science* **351**(6271), pp. 357–360 (2016). DOI: 10.1126/SCIENCE.AAD4811.

[123] V. Torres-Company, J. Schroder, A. Fulop, M. Mazur, L. Lundberg, O. B. Helgason, M. Karlsson, and P. A. Andrekson, "Laser frequency combs for coherent optical communications", *Journal of Lightwave Technology* **37**(7), pp. 1663–1670 (2019). DOI: 10.1109/JLT.2019.2894170.

[124] J. R. Stone, T. C. Briles, T. E. Drake, D. T. Spencer, D. R. Carlson, S. A. Diddams, and S. B. Papp, "Thermal and nonlinear dissipative-soliton dynamics in Kerr-microresonator frequency combs", *Physical Review Letters* **121**(6) (2018). DOI: 10.1103/PHYSREVLETT.121.063902.

[125] T. Herr, K. Hartinger, J. Riemensberger, C. Y. Wang, E. Gavartin, R. Holzwarth, M. L. Gorodetsky, and T. J. Kippenberg, "Universal formation dynamics and noise of Kerr-frequency combs in microresonators", *Nature Photonics* **6**(7), pp. 480–487 (2012). DOI: 10.1038/NPHOTON.2012.127.

[126] P. Trocha, "Kerr-nonlinear microresonators and frequency combs: Modelling, design, and applications", Ph.D. Dissertation, Karlsruher Institut für Technologie (KIT), 2020. DOI: 10.5445/IR/1000142186.

[127] P. Del'Haye, A. Schliesser, O. Arcizet, T. Wilken, R. Holzwarth, and T. J. Kippenberg, "Optical frequency comb generation from a monolithic microresonator", *Nature* **450**(7173), pp. 1214–1217 (2007). DOI: 10.1038/NATURE06401.

[128] A. A. Savchenkov, A. B. Matsko, V. S. Ilchenko, I. Solomatine, D. Seidel, and L. Maleki, "Tunable optical frequency comb with a crystalline whispering gallery mode resonator", *Physical Review Letters* **101**(9) (2008). DOI: 10.1103/PHYSREVLETT.101.093902.

[129] A. S. Raja, A. S. Voloshin, H. Guo, S. E. Agafonova, J. Liu, A. S. Gorodnitskiy, M. Karpov, N. G. Pavlov, E. Lucas, R. R. Galiev, A. E. Shitikov, J. D. Jost, M. L. Gorodetsky, and T. J. Kippenberg, "Electrically pumped photonic integrated soliton microcomb", *Nature Communications* **10**(1), 680 (2019). DOI: 10.1038/S41467-019-08498-2.

[130] C. Xiang, J. Liu, J. Guo, L. Chang, R. N. Wang, W. Weng, J. Peters, W. Xie, Z. Zhang, J. Riemensberger, J. Selvidge, T. J. Kippenberg, and J. E. Bowers, "Laser soliton microcombs heterogeneously integrated on silicon", *Science* **373**(6550), pp. 99–103 (2021). DOI: 10.1126/SCIENCE.ABH2076.

[131] A. S. Voloshin, N. M. Kondratiev, G. V. Lihachev, J. Liu, V. E. Lobanov, N. Y. Dmitriev, W. Weng, T. J. Kippenberg, and I. A. Bilenko, "Dynamics of soliton self-injection locking in optical microresonators", *Nature Communications* **12**(1), 235 (2021). DOI: 10.1038/S41467-020-20196-Y.

[132] E. D. Hinkley and C. Freed, "Direct observation of the Lorentzian line shape as limited by quantum phase noise in a laser above threshold", *Physical Review Letters* **23**(6), pp. 277–280 (1969). DOI: 10.1103/PHYSREVLETT.23.277.

[133] T. N. Huynh, L. Nguyen, and L. P. Barry, "Phase noise characterization of SGDBR lasers using phase modulation detection method with delayed self-heterodyne measurements", *Journal of Lightwave Technology* **31**(8), pp. 1300–1308 (2013). DOI: 10.1109/JLT.2013.2247564.

[134] T. Okoshi, K. Kikuchi, and A. Nakayama, "Novel method for high resolution measurement of laser output spectrum", *Electronics Letters* **16**(16), pp. 630–631 (1980). DOI: 10.1049/EL:19800437.

[135] L. Richter, H. Mandelberg, M. Kruger, and P. McGrath, "Linewidth determination from self-heterodyne measurements with subcoherence delay times", *IEEE Journal of Quantum Electronics* **22**(11), pp. 2070–2074 (1986). DOI: 10.1109/JQE.1986.1072909.

[136] S. Camatel and V. Ferrero, "Narrow linewidth CW laser phase noise characterization methods for coherent transmission system applications", *Journal of Lightwave Technology* **26**(17), pp. 3048–3055 (2008). DOI: 10.1109/JLT.2008.925046.

[137] H. Tsuchida, "Simple technique for improving the resolution of the delayed self-heterodyne method", *Optics Letters* **15**(11), pp. 640–642 (1990). DOI: 10.1364/OL.15.000640.

[138] J. Dawson, N. Park, and K. Vahala, "An improved delayed self-heterodyne interferometer for linewidth measurements", *IEEE Photonics Technology Letters* **4**(9), pp. 1063–1066 (1992). DOI: 10.1109/68.157150.

[139] M. Xue and J. Zhao, "Laser linewidth measurement based on long and short delay fiber combination", *Optics Express* **29**(17), pp. 27 118–27 126 (2021). DOI: 10.1364/OE.428787.

[140] Z. Zhao, Z. Bai, D. Jin, Y. Qi, J. Ding, B. Yan, Y. Wang, Z. Lu, and R. P. Mildren, "Narrow laser-linewidth measurement using short delay self-heterodyne interferometry", *Optics Express* **30**(17), pp. 30 600–30 610 (2022). DOI: 10.1364/OE.455028.

[141] Z. Wang, C. Ke, Y. Zhong, C. Xing, H. Wang, K. Yang, S. Cui, and D. Liu, "Ultra-narrow-linewidth measurement utilizing dual-parameter acquisition through a partially coherent light interference", *Optics Express* **28**(6), pp. 8484–8493 (2020). DOI: 10.1364/OE.387398.

[142] S. Huang, T. Zhu, M. Liu, and W. Huang, "Precise measurement of ultra-narrow laser linewidths using the strong coherent envelope", *Scientific Reports* **7**(1), 41988 (2017). DOI: 10.1038/SREP41988.

[143] S. E. Harris, "Conversion of FM light to AM light using birefringent crystals", *Applied Physics Letters* **2**(3), pp. 47–49 (1963). DOI: 10.1063/1.1753768.

[144] B. Daino, P. Spano, M. Tamburrini, and S. Piazzolla, "Phase noise and spectral line shape in semiconductor lasers", *IEEE Journal of Quantum Electronics* **19**(3), pp. 266–270 (1983). DOI: 10.1109/JQE.1983.1071842.

[145] W. Sorin, K. Chang, G. Conrad, and P. Hernday, "Frequency domain analysis of an optical FM discriminator", *Journal of Lightwave Technology* **10**(6), pp. 787–793 (1992). DOI: 10.1109/50.143079.

[146] P. J. Winzer and D. T. Neilson, "From scaling disparities to integrated parallelism: A decathlon for a decade", *Journal of Lightwave Technology* **35**(5), pp. 1099–1115 (2017). DOI: 10.1109/JLT.2017.2662082.

[147] D. J. Richardson, "Filling the light pipe", *Science* **330**(6002), pp. 327–328 (2010). DOI: 10.1126/SCIENCE.1191708.

[148] P. J. Winzer, "Making spatial multiplexing a reality", *Nature Photonics* **8**(5), pp. 345–348 (2014). DOI: 10.1038/NPHOTON.2014.58.

[149] H.-G. Weber, R. Ludwig, S. Ferber, C. Schmidt-Langhorst, M. Kroh, V. Marembert, C. Boerner, and C. Schubert, "Ultrahigh-speed OTDM-transmission technology", *Journal of Lightwave Technology* **24**(12), pp. 4616–4627 (2006). DOI: 10.1109/JLT.2006.885784.

[150] K. Kikuchi, "Fundamentals of coherent optical fiber communications", *Journal of Lightwave Technology* **34**(1), pp. 157–179 (2016). DOI: 10.1109/JLT.2015.2463719.

[151] P. J. Winzer, "High-spectral-efficiency optical modulation formats", *Journal of Lightwave Technology* **30**(24), pp. 3824–3835 (2012). DOI: 10.1109/JLT.2012.2212180.

[152] E. Agrell, M. Karlsson, A. R. Chraplyvy, D. J. Richardson, P. M. Krummrich, P. Winzer, K. Roberts, J. K. Fischer, S. J. Savory, B. J. Eggleton, M. Secondini, F. R. Kschischang, A. Lord, J. Prat, I. Tomkos, J. E. Bowers, S. Srinivasan, M. Brandt-Pearce, and N. Gisin, "Roadmap of optical communications", *Journal of Optics* **18**(6), 063002 (2016). DOI: 10.1088/2040-8978/18/6/063002.

[153] C. Shannon, "Communication in the presence of noise", *Proceedings of the IRE* **37**(1), pp. 10–21 (1949). DOI: 10.1109/JRPROC.1949.232969.

[154] R.-J. Essiambre and R. W. Tkach, "Capacity trends and limits of optical communication networks", *Proceedings of the IEEE* **100**(5), pp. 1035–1055 (2012). DOI: 10.1109/JPROC.2012.2182970.

[155] J.-X. Cai, M. V. Mazurczyk, H. G. Batshon, M. Paskov, C. R. Davidson, Y. Hu, O. V. Sinkin, M. A. Bolshtyansky, D. G. Foursa, and A. N. Pilipetskii, "Performance comparison of probabilistically shaped QAM formats and hybrid shaped APSK formats with coded modulation", *Journal of Lightwave Technology* **38**(12), pp. 3280–3288 (2020). DOI: 10.1109/JLT.2020.2980449.

[156] Y. Han and G. Li, "Coherent optical communication using polarization multiple-input-multiple-output", *Optics Express* **13**(19), pp. 7527–7534 (2005). DOI: 10.1364/OPEX.13.007527.

[157] B. J. Puttnam, G. Rademacher, and R. S. Luís, "Space-division multiplexing for optical fiber communications", *Optica* **8**(9), pp. 1186–1203 (2021). DOI: 10.1364/OPTICA.427631.

[158] D. M. Kuchta, "Progress in VCSEL-based parallel links", in *VCSELs Fundamentals, Technology and Applications of Vertical Cavity Surface Emitting Lasers*, R. Michalzik, Ed. Springer, 2013, pp. 473–519. DOI: 10.1007/978-3-642-24986-0_16.

[159] R. Michalzik and K. J. Ebeling, "Operating principles of VCSELs", in *Vertical-Cavity Surface-Emitting Laser Devices*. Springer Berlin Heidelberg, 2003, pp. 53–98. DOI: 10.1007/978-3-662-05263-1_3.

[160] N. N. Ledentsov, O. Y. Makarov, V. A. Shchukin, V. P. Kalosha, N. Ledentsov, L. Chrochos, M. B. Sanayeh, and J. P. Turkiewicz, "High speed VCSEL technology and applications", *Journal of Lightwave Technology* **40**(6), pp. 1749–1763 (2022). DOI: 10.1109/JLT.2022.3149372.

[161] IEEE Standards Association. “802.3bm-2015 - IEEE standard for ethernet - Amendment 3: Physical layer specifications and management parameters for 40 Gb/s and 100 Gb/s operation over fiber optic cables”. (2015), [Online]. Available: https://doi.org/10.1109/IEEESTD.2015.7069180.

[162] IEEE Standards Association. “802.3bs-2017 - IEEE standard for ethernet - Amendment 10: Media access control parameters, physical layers, and management parameters for 200 Gb/s and 400 Gb/s operation”. (2017), [Online]. Available: https://doi.org/10.1109/IEEESTD.2017.8207825.

[163] D. M. Pozar, *Microwave Engineering, 4th ed.* John Wiley & Sons, 2012, ISBN: 978-0-4706-3155-3.

[164] C. P. Wen, “Coplanar waveguide: A surface strip transmission line suitable for nonreciprocal gyromagnetic device applications”, *IEEE Transactions on Microwave Theory and Techniques* **17**(12), pp. 1087–1090 (1969). DOI: 10.1109/TMTT.1969.1127105.

[165] I. Wolff, *Coplanar Microwave Integrated Circuits*. John Wiley & Sons, 2006. DOI: 10.1002/0470040882.

[166] M. Frankel, S. Gupta, J. Valdmanis, and G. Mourou, “Terahertz attenuation and dispersion characteristics of coplanar transmission lines”, *IEEE Transactions on Microwave Theory and Techniques* **39**(6), pp. 910–916 (1991). DOI: 10.1109/22.81658.

[167] G. Ghione, “A CAD-oriented analytical model for the losses of general asymmetric coplanar lines in hybrid and monolithic MICs”, *IEEE Transactions on Microwave Theory and Techniques* **41**(9), pp. 1499–1510 (1993). DOI: 10.1109/22.245668.

[168] J. Zhang and T. Hsiang, “Subterahertz attenuation in coplanar waveguides”, in *International Microwave Symposium* (MWSYM 2005), pp. 1905–1908. DOI: 10.1109/MWSYM.2005.1517108.

[169] E. Chen and S. Chou, "Characteristics of coplanar transmission lines on multilayer substrates: Modeling and experiments", *IEEE Transactions on Microwave Theory and Techniques* **45**(6), pp. 939–945 (1997). DOI: 10.1109/22.588606.

[170] E. Carlsson and S. Gevorgian, "Conformal mapping of the field and charge distributions in multilayered substrate CPWs", *IEEE Transactions on Microwave Theory and Techniques* **47**(8), pp. 1544–1552 (1999). DOI: 10.1109/22.780407.

[171] C. Veyres and V. F. Hanna, "Extension of the application of conformal mapping techniques to coplanar lines with finite dimensions", *International Journal of Electronics* **48**(1), pp. 47–56 (1980). DOI: 10.1080/00207218008901066.

[172] Dassault Systèmes SE. "CST Studio Suite® 2021, Release version 2021.00 - Sep 08 2020, User's handbook." (2020).

[173] S. Sahin, N. K. Nahar, and K. Sertel, "Dielectric properties of low-loss polymers for mmW and THz applications", *Journal of Infrared, Millimeter, and Terahertz Waves* **40**(5), pp. 557–573 (2019). DOI: 10.1007/S10762-019-00584-2.

[174] E. Mavrona, A. Theodosi, K. Mackosz, E. Perivolari, I. Utke, J. Michler, J. Schwiedrzik, M. Kafesaki, O. Tsilipakos, and A. Xomalis, "Refractive index measurement of IP-S and IP-Dip photoresists at THz frequencies and validation via 3D photonic metamaterials made by direct laser writing", *Optical Materials Express* **13**(11), pp. 3355–3364 (2023). DOI: 10.1364/OME.500287.

[175] K. Kurokawa, "Power waves and the scattering matrix", *IEEE Transactions on Microwave Theory and Techniques* **13**(2), pp. 194–202 (1965). DOI: 10.1109/TMTT.1965.1125964.

[176] D. Frickey, "Conversions between *S*, *Z*, *Y*, *H*, *ABCD*, and *T* parameters which are valid for complex source and load impedances", *IEEE Transactions on Microwave Theory and Techniques* **42**(2), pp. 205–211 (1994). DOI: 10.1109/22.275248.

[177] X. Ye, "De-embedding errors due to inaccurate test fixture characterization", *IEEE Electromagnetic Compatibility Magazine* **1**(4), pp. 75–78 (2012). DOI: 10.1109/MEMC.2012.6397064.

[178] Keysight Technologies Inc. "Application note 5980-2784EN: De-embedding and embedding *S*-parameter networks using a vector network analyzer". (2017), [Online]. Available: https://www.keysight.com/de/de/assets/7018-06806/application-notes/5980-2784.pdf.

[179] C. A. Balanis, *Antenna Theory: Analysis and Design, 4th ed.* John Wiley & Sons, 2016, ISBN: 978-1-1186-4206-1.

[180] J. D. Kraus and R. J. Marhefka, *Antennas, 3rd ed.* McGraw-Hill Science/Engineering/Math, 2001, ISBN: 978-0-0723-2103-6.

[181] F. Ohnimus, I. Ndip, S. Guttowski, and H. Reichl, "An efficient and broadband slot antenna for 60 GHz wireless applications", in *Electrical Design of Advanced Packaging and Systems Symposium* (EDAPS 2008), pp. 69–72. DOI: 10.1109/EDAPS.2008.4736001.

[182] M. Born, E. Wolf, A. B. Bhatia, P. C. Clemmow, D. Gabor, A. R. Stokes, A. M. Taylor, P. A. Wayman, and W. L. Wilcock, *Principles of Optics*. Cambridge University Press, 1999. DOI: 10.1017/CBO9781139644181.

[183] H. G. Booker, "Slot aerials and their relation to complementary wire aerials (Babinet's principle)", *Journal of the Institution of Electrical Engineers - Part IIIA: Radiolocation* **93**(4), pp. 620–626 (1946). DOI: 10.1049/JI-3A-1.1946.0150.

[184] S. Sierra-Garcia and J.-J. Laurin, "Study of a CPW inductively coupled slot antenna", *IEEE Transactions on Antennas and Propagation* **47**(1), pp. 58–64 (1999). DOI: 10.1109/8.752989.

[185] H.-C. Liu, T.-S. Horng, and N. Alexopoulos, "Radiation of printed antennas with a coplanar waveguide feed", *IEEE Transactions on Antennas and Propagation* **43**(10), pp. 1143–1148 (1995). DOI: 10.1109/8.467652.

[186] J. Schoenberg, T. Mader, B. Shaw, and Z. Popovic, "Quasi-optical antenna array amplifiers", in *International Microwave Symposium* (MWSYM 1995), pp. 605–608. DOI: 10.1109/MWSYM.1995.405933.

[187] E. Vourch, M. Drissi, and J. Citerne, "Slotline dipole fed by a coplanar waveguide", in *Antennas and Propagation Society International Symposium* (APS 1994), pp. 2208–2211. DOI: 10.1109/APS.1994.408045.

[188] K. F. Lee, *Principles of Antenna Theory*. John Wiley & Sons, 1984, ISBN: 978-0-4719-0167-9.

[189] D. Middleton and R. King, "The thin cylindrical antenna: A comparison of theories", *Journal of Applied Physics* **17**(4), pp. 273–284 (1946). DOI: 10.1063/1.1707714.

[190] M. A. Tran, D. Huang, J. Guo, T. Komljenovic, P. A. Morton, and J. E. Bowers, "Ring-resonator based widely-tunable narrow-linewidth Si/InP integrated lasers", *IEEE Journal of Selected Topics in Quantum Electronics* **26**(2), pp. 1–14 (2020). DOI: 10.1109/JSTQE.2019.2935274.

[191] P. Pintus, J. Guo, W. Jin, M. A. Tran, J. Peters, C. Xiang, J. Liang, O. J. Ohanian, and J. E. Bowers, "225 GHz mode-hop-free tuning with a narrow linewidth integrated InP/Si laser", in *Conference on Lasers and Electro-Optics* (CLEO 2022), paper SM2P.3. DOI: 10.1364/CLEO_SI.2022.SM2P.3.

[192] R. Tang, T. Kita, and H. Yamada, "Narrow-spectral-linewidth silicon photonic wavelength-tunable laser with highly asymmetric Mach-Zehnder interferometer", *Optics Letters* **40**(7), pp. 1504–1507 (2015). DOI: 10.1364/OL.40.001504.

[193] Y. Guo, R. Zhao, G. Zhou, L. Lu, A. Stroganov, M. Nisar, J. Chen, and L. Zhou, "Thermally tuned high-performance III-V/$Si_3N_4$ external cavity laser", *IEEE Photonics Journal* **13**(2), pp. 1–13 (2021). DOI: 10.1109/JPHOT.2021.3068529.

[194] X. Li, Y. Guo, C. Liu, X. Li, M. Jin, E. Siyu, W. Xu, L. Lu, J. Chen, and L. Zhou, "FMCW source based on a hybrid integrated III-V/Si-$Si_3N_4$ dual-layer external cavity laser", in *Conference on Lasers and Electro-Optics* (CLEO 2022), paper SM2P.7. DOI: 10.1364/CLEO_SI.2022.SM2P.7.

[195] I. Ghannam, B. Shen, F. Merget, and J. Witzens, "Silicon nitride external cavity laser with alignment tolerant multi-mode RSOA-to-PIC interface", *IEEE Journal of Selected Topics in Quantum Electronics* **28**(1: Semiconductor Lasers), pp. 1–10 (2022). DOI: 10.1109/JSTQE.2021.3117586.

[196] Y. Fan, A. van Rees, P. J. M. van der Slot, J. Mak, R. M. Oldenbeuving, M. Hoekman, D. Geskus, C. G. H. Roeloffzen, and K.-J. Boller, "Hybrid integrated InP-$Si_3N_4$ diode laser with a 40-Hz intrinsic linewidth", *Optics Express* **28**(15), pp. 21 713–21 728 (2020). DOI: 10.1364/OE.398906.

[197] Y. Fan, J. P. Epping, R. M. Oldenbeuving, C. G. H. Roeloffzen, M. Hoekman, R. Dekker, R. G. Heideman, P. J. M. van der Slot, and K.-J. Boller, "Optically integrated InP-$Si_3N_4$ hybrid laser", *IEEE Photonics Journal* **8**(6), pp. 1–11 (2016). DOI: 10.1109/JPHOT.2016.2633402.

[198] D. Kharas, J. J. Plant, W. Loh, R. B. Swint, S. Bramhavar, C. Heidelberger, S. Yegnanarayanan, and P. W. Juodawlkis, "High-power (>300 mW) on-chip laser with passively aligned silicon-nitride waveguide DBR cavity", *IEEE Photonics Journal* **12**(6), pp. 1–12 (2020). DOI: 10.1109/JPHOT.2020.3037834.

[199] J. Liu, H. Tian, E. Lucas, A. S. Raja, G. Lihachev, R. N. Wang, J. He, T. Liu, M. H. Anderson, W. Weng, S. A. Bhave, and T. J. Kippenberg, "Monolithic piezoelectric control of soliton microcombs", *Nature* **583**(7816), pp. 385–390 (2020). DOI: 10.1038/S41586-020-2465-8.

[200] J. Liu, A. S. Raja, M. Karpov, B. Ghadiani, M. H. P. Pfeiffer, B. Du, N. J. Engelsen, H. Guo, M. Zervas, and T. J. Kippenberg, "Ultralow-power chip-based soliton microcombs for photonic integration", *Optica* **5**(10), pp. 1347–1353 (2018). DOI: 10.1364/OPTICA.5.001347.

[201] R.-J. Essiambre, G. Kramer, P. J. Winzer, G. J. Foschini, and B. Göbel, "Capacity limits of optical fiber networks", *Journal of Lightwave Technology* **28**(4), pp. 662–701 (2010). DOI: 10.1109/JLT.2009.2039464.

[202] H. Nasu, K. Nagashima, T. Uemura, A. Izawa, and Y. Ishikawa, "1.3-Tb/s VCSEL-based on-board parallel-optical transceiver module for high-density optical interconnects", *Journal of Lightwave Technology* **36**(2), pp. 159–167 (2018). DOI: 10.1109/JLT.2017.2766081.

[203] T. Shiraishi, T. Yagisawa, T. Ikeuchi, S. Ide, and K. Tanaka, "Cost-effective low-loss flexible optical engine with microlens-imprinted film for high-speed on-board optical interconnection", in *Electronic Components and Technology Conference* (ECTC 2012), pp. 1505–1510. DOI: 10.1109/ECTC.2012.6249035.

[204] E. Mohammed and H. Au, "200 Gb/s 10-channel miniature optical interconnect transmitter module for high-performance computing (HPC)", in *Proc. SPIE* 7607, *Optoelectronic Interconnects and Component Integration IX* (2010), paper 760709. DOI: 10.1117/12.842229.

[205] B. Li, L. Wan, Y. Lv, W. Gao, C. Yang, Z. Li, and X. Zhang, "Low-cost high-efficiency optical coupling using through-silicon-hole in parallel optical transceiver module", *Applied Physics A* **95**(4), pp. 1123–1128 (2009). DOI: 10.1007/S00339-009-5127-0.

[206] J. Kim, D. Kim, B. Lee, and K. Oh, "Arrayed multimode fiber to VCSEL coupling for short reach communications using hybrid polymer-fiber lens", *IEEE Photonics Technology Letters* **19**(13), pp. 951–953 (2007). DOI: 10.1109/LPT.2007.898790.

[207] S. Chuang, D. Schoellner, A. Ugolini, J. Wakjira, G. Wolf, P. Gandhi, and A. Persaud, "Theoretical and empirical qualification of a mechanical-optical interface for parallel optics links", in *Proc. SPIE* 9368, *Optical Interconnects XV* (2015), paper 93680P. DOI: 10.1117/12.2077615.

[208] E. K. Kang, Y. W. Lee, S. Ravindran, J. K. Lee, H. J. Choi, G. W. Ju, J. W. Min, Y. M. Song, I.-B. Sohn, and Y. T. Lee, "4 channel × 10 Gb/s bidirectional optical subassembly using silicon optical bench with precise passive optical alignment", *Optics Express* **24**(10), pp. 10 777–10 785 (2016). DOI: 10.1364/OE.24.010777.

[209] C. L. Schow, F. E. Doany, A. V. Rylyakov, B. G. Lee, C. V. Jahnes, Y. H. Kwark, C. W. Baks, D. M. Kuchta, and J. A. Kash, "A 24-channel, 300 Gb/s, 8.2 pJ/bit, full-duplex fiber-coupled optical transceiver module based on a single "holey" CMOS IC", *Journal of Lightwave Technology* **29**(4), pp. 542–553 (2011). DOI: 10.1109/JLT.2010.2101580.

[210] H. He, F. Liu, H. Xue, P. Wu, M. Song, Y. Sun, and L. Cao, "Fabrication and performance analysis of a high-coupling-efficiency and convenient-integration optical transceiver", *Optoelectronics Letters* **13**(4), pp. 250–253 (2017). DOI: 10.1007/S11801-017-7072-Z.

[211] K. Shikama, Y. Abe, T. Kishi, K. Takeda, T. Fujii, H. Nishi, T. Matsui, A. Aratake, K. Nakajima, and S. Matsuo, "Multicore-fiber receptacle with compact fan-in/fan-out device for SDM transceiver applications", *Journal of Lightwave Technology* **36**(24), pp. 5815–5822 (2018). DOI: 10.1109/JLT.2018.2879100.

[212] D. L. Butler, M.-J. Li, S. Li, Y. Geng, R. R. Khrapko, R. A. Modavis, V. N. Nazarov, and A. V. Koklyushkin, "Space division multiplexing in short reach optical interconnects", *Journal of Lightwave Technology* **35**(4), pp. 677–682 (2017). DOI: 10.1109/JLT.2016.2619981.

[213] T. Gonda, K. Imamura, M. Tsukamoto, K. Kawasaki, S. Arai, R. Sugizaki, S. Beppu, D. Soma, H. Takahashi, and T. Tsuritani, "Design of multicore fiber having upgradability from standard single-mode fibers and its application", *Journal of Lightwave Technology* **37**(2), pp. 396–403 (2019). DOI: 10.1109/JLT.2019.2895903.

[214] M. Karppinen, A. Tanskanen, V. Heikkinen, P. Myöhänen, N. Salminen, J. Ollila, O. Tapaninen, P. Westbergh, J. Gustavsson, A. Larsson, R. Safaisini, R. King, M. Ko, D. Kissinger, A. Ç. Ulusoy, T. Taunay, L. Bansal, L. Grüner-Nielsen, E. Kehayas, J. Edmunds, and L. Stampoulidis, "Integration of 150 Gbps/fiber optical engines based on multicore fibers and 6-channel VCSELs and PDs", in *Proc. SPIE* 9753, *Optical Interconnects XVI* (2016), paper 97530S. DOI: 10.1117/12.2214555.

[215] F. E. Doany, D. M. Kuchta, A. V. Rylyakov, C. Baks, S. Tian, M. Schultz, F. Libsch, and C. L. Schow, "Multicore fiber 4 TX + 4 RX optical transceiver based on holey SiGe IC", in *Electronic Components and Technology Conference* (ECTC 2014), pp. 1016–1020. DOI: 10.1109/ECTC.2014.6897412.

[216] B. Rosinski, J. Chi, P. Grosso, and J. L. Bihan, "Multichannel transmission of a multicore fiber coupled with vertical-cavity surface-emitting lasers", *Journal of Lightwave Technology* **17**(5), pp. 807–810 (1999). DOI: 10.1109/50.762896.

[217] B. Zhu, T. F. Taunay, M. F. Yan, M. Fishteyn, G. Oulundsen, and D. Vaidya, "70-Gb/s multicore multimode fiber transmissions for optical data links", *IEEE Photonics Technology Letters* **22**(22), pp. 1647–1649 (2010). DOI: 10.1109/LPT.2010.2070490.

[218] B. G. Lee, D. M. Kuchta, F. E. Doany, C. L. Schow, P. Pepeljugoski, C. Baks, T. F. Taunay, B. Zhu, M. F. Yan, G. E. Oulundsen, D. S. Vaidya, W. Luo, and N. Li, "End-to-end multicore multimode fiber optic link operating up to 120 Gb/s", *Journal of Lightwave Technology* **30**(6), pp. 886–892 (2012). DOI: 10.1109/JLT.2012.2183853.

[219] P. D. Heyn, V. Kopp, S. A. Srinivasan, P. Verheyen, J. Park, M. Wlodawski, J. Singer, D. Neugroschl, B. Snyder, S. Balakrishnan, G. Lepage, M. Pantouvaki, P. Absil, and J. V. Campenhout, "Ultra-dense 16 × 56 Gb/s NRZ GeSi EAM-PD arrays coupled to multicore fiber for short-reach 896 Gb/s optical links", in *Optical Fiber Communication Conference* (OFC 2017), paper Th1B.7. DOI: 10.1364/OFC.2017.Th1B.7.

[220] P. Westbergh, J. S. Gustavsson, and A. Larsson, "VCSEL arrays for multicore fiber interconnects with an aggregate capacity of 240 Gb/s", *IEEE Photonics Technology Letters* **27**(3), pp. 296–299 (2015). DOI: 10.1109/LPT.2014.2369827.

[221] US Conec Ltd. "PRIZM® LightTurn® solutions". (2020), [Online]. Available: https://www.usconec.com/media/1398/prizm_lightturn_connector.pdf.

[222] US Conec Ltd. “FERRULE, 12F, PRIZM® LightTurn®”. (2012), [Online]. Available: https://www.usconec.com/umbraco/rhythm/protectedfilesapi/download?path=%5C%2ffiles%5C%2fdrawings%5C%2fC13950.pdf.

[223] V. I. Kopp, J. Park, M. Wlodawski, J. Singer, D. Neugroschl, and A. Z. Genack, “Pitch reducing optical fiber array and multicore fiber for space-division multiplexing”, in *IEEE Photonics Society Summer Topical Meeting Series* (2013), pp. 99–100. DOI: 10.1109/PHOSST.2013.6614505.

[224] S. Gross, N. Riesen, J. D. Love, and M. J. Withford, “Three-dimensional ultra-broadband integrated tapered mode multiplexers”, *Laser & Photonics Reviews* **8**(5), pp. L81–L85 (2014). DOI: 10.1002/LPOR.201400078.

[225] T. Hayashi, A. Mekis, T. Nakanishi, M. Peterson, S. Sahni, P. Sun, S. Freyling, G. Armijo, C. Sohn, D. Foltz, T. Pinguet, M. Mack, Y. Kaneuchi, O. Shimakawa, T. Morishima, T. Sasaki, and P. D. Dobbelaere, “End-to-end multi-core fibre transmission link enabled by silicon photonics transceiver with grating coupler array”, in *European Conference on Optical Communication* (ECOC 2017), pp. 1–3. DOI: 10.1109/ECOC.2017.8346057.

[226] N. Lindenmann, S. Dottermusch, M. L. Gödecke, T. Hoose, M. R. Billah, T. P. Onanuga, A. Hofmann, W. Freude, and C. Koos, “Connecting silicon photonic circuits to multicore fibers by photonic wire bonding”, *Journal of Lightwave Technology* **33**(4), pp. 755–760 (2015). DOI: 10.1109/JLT.2014.2373051.

[227] Broadcom Inc. “Datasheet AFCD-V64JZ: 28-Gb/s , 1×4 array oxide VCSEL”. (2017), [Online]. Available: https://www.broadcom.com/products/fiber-optic-modules-components/components-broadband/short-reach-gaas-die/lasers/afcd-v64jz.

[228] Broadcom Inc. “Datasheet SPD2025-4X: 28-Gb/s GaAs, 1×4 array PIN photodiode with 250 µm channel spacing”. (2017), [Online]. Available: https://www.broadcom.com/products/fiber-optic-modules-

components/components-broadband/short-reach-gaas-die/pin-photodiodes/spd2025-4x.

[229] S. Schmidt, T. Tiess, S. Schröter, R. Hambach, M. Jäger, H. Bartelt, A. Tünnermann, and H. Gross, "Wave-optical modeling beyond the thin-element-approximation", *Optics Express* **24**(26), pp. 30 188–30 200 (2016). DOI: 10.1364/OE.24.030188.

[230] M. Hackert, "Explanation of launch condition choice for GRIN multimode fiber attenuation and bandwidth measurements", *Journal of Lightwave Technology* **10**(2), pp. 125–129 (1992). DOI: 10.1109/50.120565.

[231] Precitec GmbH & Co. KG. "Optical sensor CHRocodile S". (2022), [Online]. Available: https://www.precitec.com/optical-3d-metrology/products/point-sensors/chrocodile-2s/.

[232] ficonTEC Service GmbH. "Verbundprojekt: printed freeform micro-optics for tailored photonic assemblies – PRIMA; Teilvorhaben: Entwicklung von Prozesstechnik für die Systemassemblierung (Abschlussbericht, Laufzeit des Vorhabens 01.09.2017 – 31.08.2020, verlängert bis 28.02.2021)". (2021), [Online]. Available: https://doi.org/10.2314/KXP:1780190670.

[233] The Fiber Optic Association Inc. "Modal effects on multimode fiber loss measurements". (2019), [Online]. Available: https://www.thefoa.org/tech/ref/testing/test/loss.html.

[234] A. H. Cherin, E. D. Head, C. R. Lovelace, and W. B. Gardner, "Selection of mandrel wrap mode filters for optical fiber loss measurements", *Fiber and Integrated Optics* **4**(1), pp. 49–66 (1982). DOI: 10.1080/01468038208203234.

[235] M. Trappen, M. Blaicher, P.-I. Dietrich, C. Dankwart, Y. Xu, T. Hoose, M. R. Billah, A. Abbasi, R. Baets, U. Troppenz, M. Theurer, K. Wörhoff, M. Seyfried, W. Freude, and C. Koos, "3D-printed optical probes for wafer-level testing of photonic integrated circuits", *Optics Express* **28**(25), pp. 37 996–38 007 (2020). DOI: 10.1364/OE.405139.

[236] E. Luan, S. Yu, M. Salmani, M. S. Nezami, B. J. Shastri, L. Chrostowski, and A. Eshaghi, "Towards a high-density photonic tensor core enabled by intensity-modulated microrings and photonic wire bonding", *Scientific Reports* **13**(1), 1260 (2023). DOI: 10.1038/s41598-023-27724-Y.

[237] Z.-C. Ma, Y.-L. Zhang, B. Han, Q.-D. Chen, and H.-B. Sun, "Femtosecond-laser direct writing of metallic micro/nanostructures: From fabrication strategies to future applications", *Small Methods* **2**(7), 1700413 (2018). DOI: 10.1002/SMTD.201700413.

[238] C. L. Lay, C. S. L. Koh, Y. H. Lee, G. C. Phan-Quang, H. Y. F. Sim, S. X. Leong, X. Han, I. Y. Phang, and X. Y. Ling, "Two-photon-assisted polymerization and reduction: Emerging formulations and applications", *ACS Applied Materials & Interfaces* **12**(9), pp. 10 061–10 079 (2020). DOI: 10.1021/ACSAMI.9B20911.

[239] L. Yang, F. Mayer, U. H. F. Bunz, E. Blasco, and M. Wegener, "Multi-material multi-photon 3D laser micro- and nanoprinting", *Light: Advanced Manufacturing* **2**, 17 (2021). DOI: 10.37188/LAM.2021.017.

[240] T. Tanaka, A. Ishikawa, and S. Kawata, "Two-photon-induced reduction of metal ions for fabricating three-dimensional electrically conductive metallic microstructure", *Applied Physics Letters* **88**(8), 081107 (2006). DOI: 10.1063/1.2177636.

[241] E. Blasco, J. Müller, P. Müller, V. Trouillet, M. Schön, T. Scherer, C. Barner-Kowollik, and M. Wegener, "Fabrication of conductive 3D gold-containing microstructures via direct laser writing", *Advanced Materials* **28**(18), pp. 3592–3595 (2016). DOI: 10.1002/ADMA.201506126.

[242] C. N. LaFratta, D. Lim, K. O'Malley, T. Baldacchini, and J. T. Fourkas, "Direct laser patterning of conductive wires on three-dimensional polymeric microstructures", *Chemistry of Materials* **18**(8), pp. 2038–2042 (2006). DOI: 10.1021/CM0525306.

[243] B.-B. Xu, H. Xia, L.-G. Niu, Y.-L. Zhang, K. Sun, Q.-D. Chen, Y. Xu, Z.-Q. Lv, Z.-H. Li, H. Misawa, and H.-B. Sun, "Flexible nanowiring of metal on

nonplanar substrates by femtosecond-laser-induced electroless plating", *Small* **6**(16), pp. 1762–1766 (2010). DOI: 10.1002/SMLL.201000511.

[244] S. K. Saha, B. Au, and J. S. Oakdale, "High-speed direct laser writing of silver nanostructures via two-photon reduction", *Advanced Engineering Materials* **21**(9), 1900583 (2019). DOI: 10.1002/ADEM.201900583.

[245] Q. Hu, X.-Z. Sun, C. D. J. Parmenter, M. W. Fay, E. F. Smith, G. A. Rance, Y. He, F. Zhang, Y. Liu, D. Irvine, C. Tuck, R. Hague, and R. Wildman, "Additive manufacture of complex 3D Au-containing nanocomposites by simultaneous two-photon polymerisation and photoreduction", *Scientific Reports* **7**(1), 17150 (2017). DOI: 10.1038/S41598-017-17391-1.

[246] F. Stellacci, C. Bauer, T. Meyer-Friedrichsen, W. Wenseleers, V. Alain, S. Kuebler, S. Pond, Y. Zhang, S. Marder, and J. Perry, "Laser and electron-beam induced growth of nanoparticles for 2D and 3D metal patterning", *Advanced Materials* **14**(3), pp. 194–198 (2002). DOI: 10.1002/1521-4095(20020205)14:3<194::AID-ADMA194>3.0.CO;2-W.

[247] S. Maruo and T. Saeki, "Femtosecond laser direct writing of metallic microstructures by photoreduction of silver nitrate in a polymer matrix", *Optics Express* **16**(2), pp. 1174–1179 (2008). DOI: 10.1364/OE.16.001174.

[248] S. Shukla, E. P. Furlani, X. Vidal, M. T. Swihart, and P. N. Prasad, "Two-photon lithography of sub-wavelength metallic structures in a polymer matrix", *Advanced Materials* **22**(33), pp. 3695–3699 (2010). DOI: 10.1002/ADMA.201000059.

[249] Z.-C. Ma, Y.-L. Zhang, B. Han, X.-Q. Liu, H.-Z. Zhang, Q.-D. Chen, and H.-B. Sun, "Femtosecond laser direct writing of plasmonic Ag/Pd alloy nanostructures enables flexible integration of robust SERS substrates", *Advanced Materials Technologies* **2**(6), 1600270 (2017). DOI: 10.1002/ADMT.201600270.

[250] L. Vurth, P. Baldeck, O. Stéphan, and G. Vitrant, "Two-photon induced fabrication of gold microstructures in polystyrene sulfonate thin films using a ruthenium(II) dye as photoinitiator", *Applied Physics Letters* **92**(17), 171103 (2008). DOI: 10.1063/1.2917810.

[251] W.-E. Lu, Y.-L. Zhang, M.-L. Zheng, Y.-P. Jia, J. Liu, X.-Z. Dong, Z.-S. Zhao, C.-B. Li, Y. Xia, T.-C. Ye, and X.-M. Duan, "Femtosecond direct laser writing of gold nanostructures by ionic liquid assisted multiphoton photoreduction", *Optical Materials Express* **3**(10), pp. 1660–1673 (2013). DOI: 10.1364/OME.3.001660.

[252] R. Nakamura, K. Kinashi, W. Sakai, and N. Tsutsumi, "Fabrication of gold microstructures using negative photoresists doped with gold ions through two-photon excitation", *Physical Chemistry Chemical Physics* **18**(25), pp. 17 024–17 028 (2016). DOI: 10.1039/C6CP02577C.

[253] M. R. Lee, H. K. Lee, Y. Yang, C. S. L. Koh, C. L. Lay, Y. H. Lee, I. Y. Phang, and X. Y. Ling, "Direct metal writing and precise positioning of gold nanoparticles within microfluidic channels for SERS sensing of gaseous analytes", *ACS Applied Materials & Interfaces* **9**(45), pp. 39 584–39 593 (2017). DOI: 10.1021/ACSAMI.7b11649.

[254] L. D. Zarzar, B. S. Swartzentruber, J. C. Harper, D. R. Dunphy, C. J. Brinker, J. Aizenberg, and B. Kaehr, "Multiphoton lithography of nanocrystalline platinum and palladium for site-specific catalysis in 3D microenvironments", *Journal of the American Chemical Society* **134**(9), pp. 4007–4010 (2012). DOI: 10.1021/JA211602T.

[255] S. Ren, Q. Wang, Y. Wang, and S. Qu, "Three distinct hydrogen sensing responses of palladium line patterns generated by femtosecond laser direct writing", *Journal of Physics D: Applied Physics* **45**(28), 285303 (2012). DOI: 10.1088/0022-3727/45/28/285303.

[256] B. Zhang, Y.-X. Guo, H. Zirath, and Y. P. Zhang, "Investigation on 3-D-printing technologies for millimeter-wave and terahertz applications", *Proceedings of the IEEE* **105**(4), pp. 723–736 (2017). DOI: 10.1109/JPROC.2016.2639520.

[257] A. Standaert, L. Brancato, B. Lips, F. Ceyssens, R. Puers, and P. Reynaert, "Three techniques for the fabrication of high precision, mm-sized metal components based on two-photon lithography, applied for manufacturing horn antennas for THz transceivers", *Journal of Micromechanics and Microengineering* **28**(3), 035008 (2018). DOI: 10.1088/1361-6439/AAA74B.

[258] R. Xu, S. Gao, B. S. Izquierdo, C. Gu, P. Reynaert, A. Standaert, G. J. Gibbons, W. Bosch, M. E. Gadringer, and D. Li, "A review of broadband low-cost and high-gain low-terahertz antennas for wireless communications applications", *IEEE Access* **8**, pp. 57 615–57 629 (2020). DOI: 10.1109/ACCESS.2020.2981393.

[259] F. Formanek, N. Takeyasu, T. Tanaka, K. Chiyoda, A. Ishikawa, and S. Kawata, "Three-dimensional fabrication of metallic nanostructures over large areas by two-photon polymerization", *Optics Express* **14**(2), pp. 800–809 (2006). DOI: 10.1364/OPEX.14.000800.

[260] N. Vasilantonakis, K. Terzaki, I. Sakellari, V. Purlys, D. Gray, C. M. Soukoulis, M. Vamvakaki, M. Kafesaki, and M. Farsari, "Three-dimensional metallic photonic crystals with optical bandgaps", *Advanced Materials* **24**(8), pp. 1101–1105 (2012). DOI: 10.1002/ADMA.201104778.

[261] T. Harter, C. Füllner, J. N. Kemal, S. Ummethala, J. L. Steinmann, M. Brosi, J. L. Hesler, E. Bründermann, A.-S. Müller, W. Freude, S. Randel, and C. Koos, "Generalized Kramers–Kronig receiver for coherent terahertz communications", *Nature Photonics* **14**(10), pp. 601–606 (2020). DOI: 10.1038/S41566-020-0675-0.

[262] N. Couture, W. Cui, M. Lippl, R. Ostic, D. J. J. Fandio, E. K. Yalavarthi, A. Vishnuradhan, A. Gamouras, N. Y. Joly, and J.-M. Ménard, "Single-pulse terahertz spectroscopy monitoring sub-millisecond time dynamics at a rate of 50 kHz", *Nature Communications* **14**(1), 2595 (2023). DOI: 10.1038/S41467-023-38354-3.

[263] B.-J. de Gans, P. Duineveld, and U. Schubert, "Inkjet printing of polymers: State of the art and future developments", *Advanced Materials* **16**(3), pp. 203–213 (2004). DOI: 10.1002/ADMA.200300385.

[264] Keysight Technologies Inc. "Application note 5992-1329EN: Sheet resistance/resistivity measurement using a source/measurement unit (SMU)". (2017), [Online]. Available: https://www.keysight.com/us/en/assets/7018-05102/application-notes/5992-1329.pdf.

[265] A. E. Yarimbiyik, H. A. Schafft, R. A. Allen, M. D. Vaudin, and M. E. Zaghloul, "Experimental and simulation studies of resistivity in nanoscale copper films", *Microelectronics Reliability* **49**(2), pp. 127–134 (2009). DOI: 10.1016/J.MICROREL.2008.11.003.

[266] S. Monayakul, S. Sinha, C.-T. Wang, N. Weimann, F. J. Schmuckle, M. Hrobak, V. Krozer, W. John, L. Weixelbaum, P. Wolter, O. Kruger, and W. Heinrich, "Flip-chip interconnects for 250 GHz modules", *IEEE Microwave and Wireless Components Letters* **25**(6), pp. 358–360 (2015). DOI: 10.1109/LMWC.2015.2424294.

[267] C.-H. Li and T.-Y. Chiu, "Low-loss single-band, dual-band, and broadband mm-wave and (sub-)THz interconnects for THz SoP heterogeneous system integration", *IEEE Transactions on Terahertz Science and Technology* **12**(2), pp. 130–143 (2022). DOI: 10.1109/TTHZ.2021.3128596.

[268] X. Konstantinou, J. D. Albrecht, P. Chahal, and J. Papapolymerou, "Flexible chip-first millimeter-wave packaging using multiple dielectrics", *IEEE Transactions on Components, Packaging and Manufacturing Technology* **12**(4), pp. 682–691 (2022). DOI: 10.1109/TCPMT.2022.3160626.

[269] M. T. Craton, X. Konstantinou, J. D. Albrecht, P. Chahal, and J. Papapolymerou, "Additive manufacturing of a W-band system-on-package", *IEEE Transactions on Microwave Theory and Techniques* **69**(9), pp. 4191–4198 (2021). DOI: 10.1109/TMTT.2021.3076066.

[270] M. M. Abdin, W. J. D. Johnson, J. Wang, and T. M. Weller, "W-band MMIC chip assembly using laser-enhanced direct print additive manufacturing", *IEEE Transactions on Microwave Theory and Techniques* **69**(12), pp. 5381–5392 (2021). DOI: 10.1109/TMTT.2021.3124237.

[271] M. Ihle, S. Ziesche, C. Zech, and B. Baumann, "Functional printing of MMIC-interconnects on LTCC packages for sub-THz applications", in *European Microelectronics and Packaging Conference & Exhibition* (EMPC 2019), pp. 1–4. DOI: 10.23919/EMPC44848.2019.8951799.

[272] C. Oakley, J. D. Albrecht, J. Papapolymerou, and P. Chahal, "Low-loss aerosol-jet printed wideband interconnects for embedded devices", *IEEE Transactions on Components, Packaging and Manufacturing Technology* **9**(11), pp. 2305–2313 (2019). DOI: 10.1109/TCPMT.2019.2933792.

[273] P. Fay, G. H. Bernstein, T. Lu, and J. M. Kulick, "Ultra-wide bandwidth inter-chip interconnects for heterogeneous millimeter-wave and THz circuits", *Journal of Infrared, Millimeter, and Terahertz Waves* **37**(9), pp. 874–880 (2016). DOI: 10.1007/S10762-016-0278-5.

[274] W. Wu, B. Liu, P. He, X. Wen, H. Yang, Y. Cao, Z. Wang, G. Shi, Q. Yang, A. Zhang, and C. Guo, "A W-band GSG probe fabricated by metal additive manufacturing", *IEEE Transactions on Instrumentation and Measurement* **71**, pp. 1–10 (2022). DOI: 10.1109/TIM.2022.3214278.

[275] R. Sakamaki and M. Horibe, "Long-term stability test on on-wafer measurement system in frequency ranges up to 325 GHz", *IEEE Transactions on Instrumentation and Measurement* **70**, 8002309, pp. 1–9 (2021). DOI: 10.1109/TIM.2020.3047486.

[276] T. Rahman, L. Renaud, D. Heo, M. Renn, and R. Panat, "Aerosol based direct-write micro-additive fabrication method for sub-mm 3D metal-dielectric structures", *Journal of Micromechanics and Microengineering* **25**(10), 107002 (2015). DOI: 10.1088/0960-1317/25/10/107002.

[277] D. Lohse, "Fundamental fluid dynamics challenges in inkjet printing", *Annual Review of Fluid Mechanics* **54**(1), pp. 349–382 (2022). DOI: 10.1146/ANNUREV-FLUID-022321-114001.

[278] W. Bogaerts, P. D. Heyn, T. V. Vaerenbergh, K. D. Vos, S. K. Selvaraja, T. Claes, P. Dumon, P. Bienstman, D. V. Thourhout, and R. Baets, "Silicon microring resonators", *Laser and Photonics Reviews* **6**(1), pp. 47–73 (2012). DOI: 10.1002/LPOR.201100017.

[279] Y. Lin, J. C. C. Mak, H. Chen, X. Mu, A. Stalmashonak, Y. Jung, X. Luo, P. G.-Q. Lo, W. D. Sacher, and J. K. S. Poon, "Low-loss broadband bi-layer edge couplers for visible light", *Optics Express* **29**(21), pp. 34 565–34 576 (2021). DOI: 10.1364/OE.435669.

[280] J. Liu, V. Brasch, M. H. P. Pfeiffer, A. Kordts, A. N. Kamel, H. Guo, M. Geiselmann, and T. J. Kippenberg, "Frequency-comb-assisted broadband precision spectroscopy with cascaded diode lasers", *Optics Letters* **41**(13), pp. 3134–3137 (2016). DOI: 10.1364/OL.41.003134.

[281] P. Del'Haye, O. Arcizet, M. L. Gorodetsky, R. Holzwarth, and T. J. Kippenberg, "Frequency comb assisted diode laser spectroscopy for measurement of microcavity dispersion", *Nature Photonics* **3**(9), pp. 529–533 (2009). DOI: 10.1038/NPHOTON.2009.138.

[282] T. J. Kippenberg, S. M. Spillane, and K. J. Vahala, "Modal coupling in traveling-wave resonators", *Optics Letters* **27**(19), pp. 1669–1671 (2002). DOI: 10.1364/OL.27.001669.

[283] M. L. Gorodetsky, A. D. Pryamikov, and V. S. Ilchenko, "Rayleigh scattering in high-$Q$ microspheres", *Journal of the Optical Society of America B* **17**(6), pp. 1051–1057 (2000). DOI: 10.1364/JOSAB.17.001051.

[284] D. Dragoman, "I: The Wigner distribution function in optics and optoelectronics", in *Progress in Optics*, E. Wolf, Ed. Elsevier, 1997, pp. 1–56. DOI: 10.1016/S0079-6638(08)70336-6.

[285] M. J. Bastiaans, "Wigner distribution function and its application to first-order optics", *Journal of the Optical Society of America* **69**(12), pp. 1710–1716 (1979). DOI: 10.1364/JOSA.69.001710.

[286] M. J. Bastiaans, "Use of the Wigner distribution function in optical problems", in *Proc. SPIE* 0492, *European Conference on Optics, Optical Systems and Applications* (1985), paper 251. DOI: 10.1117/12.943708.

[287] A. E. Siegman, "How to (maybe) measure laser beam quality", in *DPSS (Diode Pumped Solid State) Lasers: Applications and Issues* (DLAI 1998), paper MQ1. DOI: 10.1364/DLAI.1998.MQ1.

[288] G. Nemes and A. E. Siegman, "Measurement of all ten second-order moments of an astigmatic beam by the use of rotating simple astigmatic (anamorphic) optics", *Journal of the Optical Society of America A* **11**(8), pp. 2257–2264 (1994). DOI: 10.1364/JOSAA.11.002257.

[289] M. Eichhorn, "Optical resonators", in *Laser Physics*. Springer, 2014, pp. 49–74. DOI: 10.1007/978-3-319-05128-4_3.

[290] F. Gori, M. Santarsiero, and A. Sona, "The change of width for a partially coherent beam on paraxial propagation", *Optics Communications* **82**(3–4), pp. 197–203 (1991). DOI: 10.1016/0030-4018(91)90444-I.

[291] E. Wigner, "On the quantum correction for thermodynamic equilibrium", *Physical Review* **40**(5), pp. 749–759 (1932). DOI: 10.1103/PHYSREV.40.749.

[292] International Organization for Standardization. "ISO/IEC 11146-1: Lasers and laser-related equipment – Test methods for laser beam widths, divergence angles and beam propagation ratios – Part 1: Stigmatic and simple astigmatic beams". (2021), [Online]. Available: https://www.iso.org/obp/ui/#iso:std:iso:11146:-1:ed-2:v1:enl.

[293] S. Lavi, R. Prochaska, and E. Keren, "Generalized beam parameters and transformation laws for partially coherent light", *Applied Optics* **27**(17), pp. 3696–3703 (1988). DOI: 10.1364/AO.27.003696.

[294] International Telecommunication Union. “ITU-T G.9804.3 - 50-Gigabit-capable passive optical networks (50G-PON): Physical media dependent (PMD) layer specification”. (2021), [Online]. Available: https://www.itu.int/rec/T-REC-G.9804.3-202109-I.

[295] S. Echeverri-Chacon, J. J. Mohr, J. J. V. Olmos, P. Dawe, B. V. Pedersen, T. Franck, and S. B. Christensen, “Transmitter and dispersion eye closure quaternary (TDECQ) and its sensitivity to impairments in PAM4 waveforms”, *Journal of Lightwave Technology* **37**(3), pp. 852–860 (2019). DOI: 10.1109/JLT.2018.2881986.

[296] P. Dawe. “Improved 100GBASE-SR4 transmitter testing”. (2014), [Online]. Available: https://ieee802.org/3/bm/public/mmfadhoc/meetings/may15_14/Improved100GBASE-SR4txTestingV3.pdf.

[297] R. Johnson. “TDEC measurements update”. (2014), [Online]. Available: https://ieee802.org/3/bm/public/mmfadhoc/meetings/oct30_14/johnson_01_1014_mmf.pdf.

[298] M. Casasco, G. Caruso, I. N. Cano, D. Nesset, M. Valvo, V. Ferrero, and R. Gaudino, “TDEC metric in 50G-PON: Analytical and experimental investigation on several implementation aspects”, *Journal of Optical Communications and Networking* **15**(7), pp. 480–487 (2023). DOI: 10.1364/JOCN.489208.

[299] W. Freude, *Optical Transmitters and Receivers (OTR)*. Institute of Photonics and Quantum Electronics (IPQ), Karlsruhe Institute of Technology (KIT), 2023.

[300] P. Dawe. “Improvement to TDEC calculation for 100GBASE-SR4”. (2014), [Online]. Available: https://ieee802.org/3/bm/public/nov14/dawe_01a_1114_optx.pdf.

[301] R. Wylde, “Millimetre-wave Gaussian beam-mode optics and corrugated feed horns”, *IEE Proceedings H Microwaves, Optics and Antennas* **131**(4), pp. 258–262 (1984). DOI: 10.1049/IP-H-1.1984.0053.

[302] P. Bartley and S. Begley, “Improved free-space *S*-parameter calibration”, in *Instrumentation and Measurement Technology Conference Proceedings* (IMTC 2005), pp. 372–375. DOI: 10.1109/IMTC.2005.1604138.

[303] SWISSto12 SA. “webMCK - User guide, Rev: 1.3”. (2021).

[304] Y. Wang, X. Shang, N. M. Ridler, T. Huang, and W. Wu, “Characterization of dielectric materials at WR-15 band (50–75 GHz) using VNA-based technique”, *IEEE Transactions on Instrumentation and Measurement* **69**(7), pp. 4930–4939 (2020). DOI: 10.1109/TIM.2019.2954010.

[305] J. Baker-Jarvis, E. Vanzura, and W. Kissick, “Improved technique for determining complex permittivity with the transmission/reflection method”, *IEEE Transactions on Microwave Theory and Techniques* **38**(8), pp. 1096–1103 (1990). DOI: 10.1109/22.57336.

[306] J. Baker-Jarvis, M. D. Janezic, J. H. J. Grosvenor, and R. G. Geyer. “NIST technical note 1355: Transmission/reflection and short-circuit line methods for measuring permittivity and permeability”. (1992), [Online]. Available: https://nvlpubs.nist.gov/nistpubs/Legacy/TN/nbstechnicalnote1355r.pdf.

[307] A. Kazemipour, M. Wollensack, J. Hoffmann, M. Hudlička, S.-K. Yee, J. Rüfenacht, D. Stalder, G. Gäumann, and M. Zeier, “Analytical uncertainty evaluation of material parameter measurements at THz frequencies”, *Journal of Infrared, Millimeter, and Terahertz Waves* **41**(10), pp. 1199–1217 (2020). DOI: 10.1007/S10762-020-00723-0.

[308] S. Lesko. “Application note 575: Advantages of measuring surface roughness with white light interferometry”. (2020), [Online]. Available: https://www.photonics.com/White_Papers/Advantages_of_Measuring_Surface_Roughness_with/wpp1886.

[309] A. Davidson, K. Jones, and E. Strid, “LRM and LRRM calibrations with automatic determination of load inductance”, in *Automatic RF Techniques Group Conference Digest* (ARFTG 1990), pp. 57–63. DOI: 10.1109/ARFTG.1990.323996.

[310] Keysight Technologies Inc. “Technical overview 3121-1515EN: 170 GHz / 220 GHz broadband vector network analysis solution for on-wafer millimeter-wave component characterization”. (2022), [Online]. Available: https://www.keysight.com/de/de/assets/3121-1515/technical-overviews/170GHz-220GHz-Broadband-Vector-Network-Analysis-Solution.pdf.

[311] T. Zwick, C. Baks, U. Pfeiffer, D. Liu, and B. Gaucher, “Probe based MMW antenna measurement setup”, in *IEEE Antennas and Propagation Society Symposium* (APS 2004), pp. 747–750. DOI: 10.1109/APS.2004.1329778.

[312] S. Beer and T. Zwick, “Probe based radiation pattern measurements for highly integrated millimeter-wave antennas”, in *European Conference on Antennas and Propagation* (EuCAP 2010), pp. 1–5. [Online]. Available: https://ieeexplore.ieee.org/document/5505042.

[313] B. Bianco, A. Corana, S. Ridella, and C. Simicich, “Evaluation of errors in calibration procedures for measurements of reflection coefficient”, *IEEE Transactions on Instrumentation and Measurement* **27**(4), pp. 354–358 (1978). DOI: 10.1109/TIM.1978.4314711.

# Glossary

## List of abbreviations

| | |
|---|---|
| 2D | Two-dimensional |
| 3D | Three-dimensional |
| 3DMM2O | 3D Matter Made to Order |
| 6G | Sixth-generation |
| ADC | Analog-to-digital converter |
| Al(N) | Aluminum (nitride) |
| $Al_2O_3$ | Alumina |
| AOC | Active optical cables |
| AOM | Acousto-optic modulator |
| AR | Anti-reflection |
| ASA | Aligned simple astigmatic |
| AUT | Antenna under test |
| AWGN | Additive white Gaussian noise |
| BER(T) | Bit-error ratio (tester) |
| BMBF | Bundesministerium für Bildung und Forschung |
| BS | Beam splitter |
| BSOA | Booster semiconductor optical amplifier |
| CDR | Clock-and-data-recovery |
| CM | (Kerr) comb module |
| CMOS | Complementary metal-oxide-semiconductor |
| CPT | Cavity phase tuner |
| CPW | Coplanar waveguide |
| Cu | Copper |

| | |
|---|---|
| CW | Continuous-wave |
| DAC | Digital-to-analog converter |
| DBR | Distributed Bragg reflector |
| DD | Direct-detection |
| DFG | Deutsche Forschungsgemeinschaft |
| DKS | Dissipative Kerr soliton |
| DSP | Digital signal processing |
| EC | Edge coupler |
| ECL | External-cavity laser |
| EDFA | Erbium-doped fiber amplifier |
| EPFL | École Polytechnique Fédérale de Lausanne |
| ER | Extinction ratio |
| ESA | Electrical spectrum analyzer |
| FA | Fiber array |
| FaML | Facet-attached microlens |
| FM | Frequency modulation |
| FMCW | Frequency-modulated continuous-wave |
| FSR | Free spectral range |
| FWHM | Full-width at half maximum |
| FWM | Four-wave mixing |
| GC | Grating coupler |
| GDD | Group-delay dispersion |
| Ge | Germanium |
| GRL | Gated-reflect-line |
| GSG | Ground-signal-ground |
| GVD | Group-velocity dispersion |
| HBT | Heterojunction bipolar transistor |
| HEMT | High-electron-mobility transistor |
| HHI | Heinrich-Hertz-Institut |
| HR | High-reflectivity |
| IC | Integrated circuit |
| IEC | International Electrotechnical Commission |
| IEEE | Institute of Electrical and Electronics Engineers |

| | |
|---|---|
| IF | Intermediate-frequency |
| IHE | Institute of Radio Frequency Engineering and Electronics |
| IM | Intensity-modulated |
| IMT | Institute of Microstructure Technology |
| InGaAs(P) | Indium gallium arsenide (phosphide) |
| InP | Indium phosphide |
| IPQ | Institute of Photonics and Quantum Electronics |
| IS | Integrating sphere |
| ISI | Intersymbol interference |
| ISO | International Organization for Standardization |
| ISS | Impedance standard substrate |
| ITU | International Telecommunication Union |
| KIT | Karlsruhe Institute of Technology |
| LD | Laser diode |
| LIDAR | Light detection and ranging |
| LO | Local oscillator |
| LPS | Limited phase-space |
| LRRM | Line-reflect-reflect-match |
| LTI | Light Technology Institute |
| LUT | Laser under test |
| MCF | Multicore fiber |
| MCFS | Metal-coated freeform structure |
| MCK | Material characterization kit |
| MFD | Mode-field diameter |
| MM(F) | Multimode (fiber) |
| MMI | Multi-mode-interference |
| MMIC | Monolithic microwave integrated circuit |
| mmW | Millimeter-wave |
| MPL | Multi-photon lithography |
| MS | Multi-soliton |
| MT | Mechanical transfer |
| MZI | Mach-Zehnder interferometer |
| NA | Numerical aperture |

| | |
|---|---|
| (N)IR | (Near-)infrared |
| NIST | National Institute of Standards and Technology |
| NRZ | Non-return-to-zero |
| OCT | Optical coherence tomography |
| OMA | Optical modulation amplitude |
| OOK | On-off-keying |
| OSA | Optical spectrum analyzer |
| PAM | Pulse-amplitude modulation |
| PC | (Fiber optic) polarization controller |
| PCB | Printed circuit board |
| PD | Photodiode / photodetector |
| PDF | Probability density function |
| PDM | Polarization-division multiplexing |
| PGMEA | Propylene-glycol-methyl-ether-acetate |
| PIC | Photonic integrated circuit |
| PIPED | Plasmonic internal-photoemission detectors |
| PMMA | Poly(methyl methacrylate) |
| PMT | Photo multiplier tube |
| PNA | Phase-noise analyzer |
| PRBS | Pseudorandom binary sequence |
| PS | Phase shifter |
| PSD | Power spectral density |
| PSF | Point-spread function |
| PTFE | Polytetrafluoroethylene |
| PVD | Physical vapor deposition |
| PWB | Photonic wire bond |
| PZT | Lead zirconium titanate |
| QAM | Quadrature amplitude modulation |
| (Q)SFP | (Quad) small form-factor pluggable |
| RIN | Relative intensity noise |
| RMS | Root-mean-squared |
| RSOA | Reflective semiconductor optical amplifier |
| Rx | Receiver |

| | |
|---|---|
| SDM | Space-division multiplexing |
| SEM | Scanning electron microscopy |
| SI | International System of Units (*"Système international d'unités"*) |
| SIL | Self-injection locking |
| $Si_3N_4$ | Silicon nitride (integrated optical platform) |
| $SiO_2$ | Silicon dioxide |
| SiP | Silicon photonics |
| SM(F) | Single-mode (fiber) |
| SMSR | Side-mode suppression ratio |
| SNR | Signal-to-noise power ratio |
| SOL | Short-open-load |
| SPM | Self-phase modulation |
| SS | Single-soliton |
| SSC | Spot size converter |
| TA | THz antenna |
| TDEC(Q) | Transmitter-and-dispersion eye-closure (quaternary) |
| TDM | Time-division multiplexing |
| TE | Transverse electric |
| TEM | Transverse electromagnetic |
| THz | Terahertz |
| TIA | Transimpedance amplifier |
| TIC | THz (chip-chip) interconnect |
| TIR | Total-internal reflection |
| TP | THz probe (tips) |
| TPA | Two-photon absorption |
| Tx | Transmitter |
| UI | Unit (time) interval |
| UV | Ultraviolet |
| VCSEL | Vertical-cavity surface-emitting laser |
| VNA | Vector network analyzer |
| WDF | Wigner distribution function |
| WDM | Wavelength-division multiplexing |
| WG | Waveguide |

# List of mathematical symbols

## Uppercase Latin symbols

| | |
|---|---|
| $A_0, A_1$ | Illuminated area in a focal plane of the lithography beam |
| $A(\omega)$ | Term in $F(\omega)$ accounting for round-trip accumulated phase |
| $B$ | Channel bandwidth |
| $B(\omega)$ | Term in $F(\omega)$ accounting for frequency-dependent reflectivity |
| $C$ | Channel capacity, $C = B \log_2(1 + \mathrm{SNR})$ |
| $C'$ | Differential capacitance (in F/m) |
| $D$ | Lithographic dose, with polymerization threshold value $D_{\mathrm{th}}$ |
| $D_{\mathrm{int}}$ | Dispersion landscape of a resonator, represented as deviation of the resonance frequencies $\omega_n$ from an equidistant grid |
| $D_m$ | Dispersion term of $m$-th order, where $D_1$ represents the spacing of resonance frequencies $\omega_{\mathrm{n}}$ and $D_2$ represents the GVD |
| $D(\varphi, \theta)$ | Directivity of an antenna, relating the radiated power per solid angle $\xi(\varphi, \theta)$ to the radiated power per solid angle $\xi_{\mathrm{iso}}$ of an imaginary isotropic source with an equivalent radiated power $P_{\mathrm{rad}}$ |
| $\underline{E}$ | Complex electric field |
| $E_{\varphi/\theta}(\varphi, \theta)$ | Electric field components in $\varphi$/$\theta$-direction |
| $\underline{\mathbf{E}}$ | Error-adapter matrix $\underline{\mathbf{E}} = \left( \begin{smallmatrix} \underline{e}_{00} & \underline{e}_{01} \\ \underline{e}_{10} & \underline{e}_{11} \end{smallmatrix} \right)$, where the elements $\underline{e}_{00}$, $\underline{e}_{11}$, and $\underline{e}_{10}\underline{e}_{01}$ are related to the directivity, the source match and the reflection tracking, respectively |
| $F^2(\omega)$ | Linewidth reduction factor of ECL, $F^2(\omega) = \delta f_0 / \delta f_{\mathrm{ECL}}$ |
| $\mathcal{F}\{.\}$ | Fourier transform |
| $G$ | Unless specified differently: Optical gain |
| $G'$ | Differential conductance (in S/m) |
| $G(\varphi, \theta)$ | Gain of an antenna, $G(\varphi, \theta) = \eta_{\mathrm{rad}} D(\varphi, \theta)$ |
| $G_{\mathrm{R}}(\varphi, \theta)$ | Realized gain of an antenna, $G_{\mathrm{R}}(\varphi, \theta) = \eta_{\mathrm{in}} \eta_{\mathrm{rad}} D(\varphi, \theta)$ |
| $H_{\varphi/\theta}(\varphi, \theta)$ | Magnetic field components in $\varphi$/$\theta$-direction |
| $I$ | Chapter 2: Unless specified differently: Intensity \| Chapter 3 and Appendix A: Injection current |
| $I_i^+, I_i^-$ | Amplitude of incident and reflected current wave at Port $i$ |

| | |
|---|---|
| $I(x, y; z)$ | Spatial intensity distribution of a beam in the $(x, y)$-plane for a given position $z$ along the beam-axis ($z$-axis) |
| $\Delta I_{\mathrm{mod}}$ | Peak-to-peak swing of laser diode injection current |
| $\underline{\mathbf{I}}$ | Unity matrix, e.g., $\underline{\mathbf{I}}_1 = \begin{pmatrix}1\end{pmatrix}$, $\underline{\mathbf{I}}_2 = \begin{pmatrix}1 & 0\\ 0 & 1\end{pmatrix}$, etc. |
| $K$ | Number of passive sub-sections in extended laser cavity |
| $L$ | Unless specified differently: Geometrical length \| Chapter 3 and Appendix A: Perimeter of racetrack resonators |
| $L'$ | Differential inductance (in H/m) |
| $L_{\mathrm{eff}}$ | Effective optical cavity length (round-trip), $L_{\mathrm{eff}} = 2Ln_{\mathrm{g}}$ |
| $M^2$ | Beam quality factor |
| $N$ | Chapter 2: Order of nonlinearity \| Chapter 5 and Appendix D: Number of contacting cycles \| Appendix B: Number of $z$-positions along beam path |
| $P$ | (Optical) power |
| $P_{\mathrm{rad}}$ | Total radiated power of an antenna |
| $P_0, P_1$ | Points along lithography beam, separated by axial distance $\Delta z$ |
| $Q$ | Resonator quality factor \| Appendix C: OOK quality metric |
| $R$ | Line rate |
| $R'$ | Differential resistance (in $\Omega$/m) |
| $R_{\mathrm{q}}$ | Root-mean-squared surface roughness |
| $R_{\mathrm{S,MCFS}}$ | Effective sheet resistance of metal coating |
| $S$ | Responsivity of a photodiode |
| $\underline{\mathbf{S}}$ | Scattering ($S$-parameter) matrix, $\underline{\mathbf{S}} = \begin{pmatrix}\underline{S}_{11} & \underline{S}_{12}\\ \underline{S}_{21} & \underline{S}_{22}\end{pmatrix}$ |
| $S_{21,\mathrm{dB}}$ | Transmission from Port 1 to Port 2 in decibels, i.e., $S_{21,\mathrm{dB}} = 10\log_{10}(\lvert\underline{S}_{21}\rvert^2)$ |
| $S_{11,\mathrm{dB}}$ | Reflection at Port 1 in decibels, i.e., $S_{11,\mathrm{dB}} = 10\log_{10}(\lvert\underline{S}_{11}\rvert^2)$ |
| $\Delta\lvert\underline{S}_{21}\rvert_{\max}$ | Maximum deviation of transmission magnitude $\lvert\underline{S}_{21}\rvert$ |
| $S_\beta(f)$ | $\beta-$separation line, $S_\beta(f) = (8\ln(2)\, f)/\pi^2$ |
| $S_{\mathrm{E}}(\tilde{f})$ | Laser line shape |
| $S_{\mathrm{F}}(f)$ | Frequency-noise spectrum, modeled as $\sum_{\alpha=0}^{\alpha_{\max}} S_\alpha f^{-\alpha}$ |
| $T$ | Time slot width as defined by the line rate, $T = 1/R$ |
| $T_{\mathrm{drp}}(\omega)$ | Drop-port power transmission of a ring resonator |
| $T_{\mathrm{thrgh}}(\omega)$ | Through-port power transmission of a ring resonator |

| | |
|---|---|
| $\underline{\mathbf{T}}$ | Transfer matrix ($T$-matrix), $\underline{\mathbf{T}} = \left( \begin{smallmatrix} \underline{T}_{11} & \underline{T}_{12} \\ \underline{T}_{21} & \underline{T}_{22} \end{smallmatrix} \right)$ |
| $U$ | Voltage |
| $U_i^+, U_i^-$ | Amplitude of incident and reflected voltage wave at Port $i$ |
| $\tilde{W}(\vec{r}_\mathrm{t}, \vec{k}_\mathrm{t}; z)$ | WDF denoted in terms of the arguments $\vec{r}_\mathrm{t}$, $\vec{k}_\mathrm{t}$, and $z$ |
| $W(\vec{r}_\mathrm{t}, \vec{\Theta}_\mathrm{t}; z)$ | WDF denoted in terms of the arguments $\vec{r}_\mathrm{t}$, $\vec{\Theta}_\mathrm{t}$, and $z$ obtained by rewriting $\tilde{W}$ using $\vec{k}_\mathrm{t} = k\vec{\Theta}_\mathrm{t} = k(\theta_x, \theta_y)^\mathrm{T}$ |
| $\underline{Z}$ | (Complex) characteristic impedance |
| $Z_\mathrm{W}$ | Intrinsic wave impedance of free-space, $Z_\mathrm{W} \approx 120\pi\,\Omega$ |
| $Z_0$ | Real reference impedance, usually $Z_0 = 50\,\Omega$ |

## Lowercase Latin symbols

| | |
|---|---|
| $a$ | Unless specified differently: Real-valued amplitude transmission factor per round-trip \| Chapter 4: Core radius of a fiber |
| $a_\mathrm{PWB}$ | Insertion loss of PWB in decibels |
| $a_i, b_i$ | Incident and reflected wave amplitudes at Port $i$ (in units of $\sqrt{W}$) |
| $c$ | Vacuum speed of light, 299 792 458 m/s |
| $c_0, c_2, \ldots$ | Parameters for a rotational symmetric even-order polynomial representation of lens surfaces |
| $d$ | Unless specified differently: geometrical distance |
| $d_\mathrm{it}$ | Isolation-trench depth in 3D-printed support structure |
| e | Euler's number, $2.71828\ldots$ |
| $f$ | Frequency |
| $f_\mathrm{cut}$ | Cutoff-frequency obtained from intersection of $S_\mathrm{F}(f)$ with the $\beta-$separation line, $S_\mathrm{F}(f_\mathrm{cut}) = S_\beta(f_\mathrm{cut}) = (8\ln(2)\,f_\mathrm{cut})/\pi^2$ |
| $f_\mathrm{min}$ | Minimum Fourier frequency for observation time $\tau_0 = 1/f_\mathrm{min}$ |
| $\tilde{f}(t)$ | Instantaneous optical frequency, $\tilde{f}(t) = f_0 + \delta\tilde{f}(t)$ |
| $\delta\tilde{f}(t)$ | Fluctuation of instantaneous optical frequency linked to random phase fluctuations $\varphi(t)$, $\delta\tilde{f}(t) = \frac{d\varphi}{dt}/(2\pi)$ |
| $\delta f_\mathrm{(FWHM,L)}$ | Intrinsic (Lorentzian) linewidth (FWHM) |
| $\delta f_\mathrm{FWHM,G}$ | Effective (Gaussian) linewidth (FWHM) |
| $\delta f_\mathrm{FWHM,V}$ | Integrated (Voigt) linewidth (FWHM) |
| $\Delta f_\mathrm{cavity}$ | Bandwidth (FWHM) of passive laser resonator |

| | |
|---|---|
| $\Delta f_{\mathrm{FSR,R1/R2}}$ | Free spectral range of racetrack resonator R1 and R2, respectively |
| $\Delta f_{\mathrm{Vrnr}}$ | Vernier FSR, i.e., spectral spacing between the strong main reflection peak and the two most prominent side peaks |
| $f_{\mathrm{r}0/1}(y)$ | Probability density functions of received "zeroes" or "ones" |
| $f_{\mathrm{s}0/1}(y)$ | Probability density functions of send "zeroes" or "ones" |
| $f(x, y, \theta_x, \theta_y)$ | Function depending on the arguments $x$, $y$, $\theta_x$, and $\theta_y$ |
| $f_{1/2}(x/y, \theta_{x/y})$ | Functions separated from $W(\vec{r}_{\mathrm{t}}, \vec{\Theta}_{\mathrm{t}}; z)$ for ASA beams; depending only on the transverse direction $x/y$ and component $\theta_{x/y}$ of the direction vector $\vec{\Theta}_{\mathrm{t}}$, respectively |
| $\bar{f}(z)$ | Normalized average function of $f(x, y, \theta_x, \theta_y)$ weighted by the Wigner distribution function $W$ |
| $g$ | Distributed power gain coefficient |
| $\delta g$ | Gain fluctuation associated with frequency fluctuations $\delta\tilde{\omega}(t)$ |
| $h$ | Unless specified differently: Planck constant, $6.62607015 \times 10^{-34}$ Js \| Chapter 5 and Appendix D: Geometrical height |
| $h(x, y)$ | Lens surface height profile |
| $i(z, t)$ | Time- and position-dependent current on a transmission line |
| $\mathrm{j} = \sqrt{-1}$ | Imaginary unit |
| $k$ | Propagation constant, $k = \omega n/c$ |
| $\vec{k}_{\mathrm{t}}$ | Transverse spatial-frequency vector |
| $k_{\mathrm{t},x/y}$ | Components of transverse spatial-frequency vector $\vec{k}_{\mathrm{t}}$ along the $x$- and $y$-direction, respectively |
| $n$ | Refractive index |
| $n_{(\mathrm{e})\mathrm{g}}$ | (Effective) group refractive index, $n_{(\mathrm{e})\mathrm{g}} = n_{(\mathrm{e})}(\omega) + \omega \frac{\mathrm{d}n_{(\mathrm{e})}}{\mathrm{d}\omega}$ |
| $n_{\mathrm{sp}}$ | Spontaneous emission factor |
| $r$ | Radius |
| $r_1$ | Amplitude reflection coefficient of resonator back facet |
| $\underline{r}_{\mathrm{eff}}(\omega)$ | Frequency-dependent complex amplitude reflection coefficient |
| $\vec{r}_{\mathrm{t},1/2/\ldots}$ | Transverse position vector $1, 2, \ldots$ |
| $\vec{r}'_{\mathrm{t}}$ | Transverse offset vector |
| $s$ | Amount of non-overlapping point exposures |
| $t_{\mathrm{R}}$ | Pulse spacing, $t_{\mathrm{R}} = 2\pi/\Delta\omega_{\mathrm{FSR}}$ |

| | |
|---|---|
| $u(z,t)$ | Time- and position-dependent voltage on a transmission line |
| $v_\mathrm{g}$ | Group velocity, $v_\mathrm{g} = c/n_\mathrm{(e)g}$ |
| $v_\mathrm{scan}$ | Scanning speed of the laser focus in the MPL system |
| $w$ | Unless specified differently: Geometrical width \| Section 2.1 and Appendix B: Beam width |
| $x, y, z$ | Cartesian coordinate axes |
| $\Delta x, \Delta y$ | Deviation from optimal position along $x$- and $y$-direction, respectively, leading to a 1 dB excess loss |
| $\bar{x}, \bar{y}$ | Expected value (first moment) of the spatial intensity distribution $I(x, y; z)$ along the $x$- and $y$-direction, respectively |
| $y_\mathrm{th}$ | Decision threshold |
| $z_{0,x/y}$ | Beam waist positions for beam profiles lying in the $(x, z)$- and $(y, z)$-planes, respectively |
| $z_\mathrm{R}$ | Average Rayleigh length |
| $z_\mathrm{S}$ | VCSEL surface position |
| $\Delta z$ | Chapter 2: Infinitesimally short section of transmission line \| Appendix D: Height deviation from mean surface profile |

## Greek symbols

| | |
|---|---|
| $\alpha$ | Unless specified differently: Distributed power loss coefficient \| Section 2.2: Frequency noise order \| Chapter 4: Beam tilt angle |
| $\alpha_\mathrm{H}$ | Henry factor (linewidth enhancement factor) |
| $\beta(\omega)$ | Frequency-dependent propagation constant |
| $\beta_\mathrm{c}^{(1/2)}$ | First- and second-order derivative of the propagation constant $\beta(\omega)$ at $\omega_\mathrm{c}$, where $\beta_\mathrm{c}^{(1)} = n_\mathrm{(e)g}/c$ and $\beta_\mathrm{c}^{(2)}$ represents the GVD, respectively |
| $\beta'$ | Normalized cavity dispersion (unit-less), $\beta' \propto -\beta_\mathrm{c}^{(2)}$ |
| $\underline{\gamma}$ | (Complex) propagation parameter, $\underline{\gamma} = \sqrt{(R' + \mathrm{j}\omega L')(G' + \mathrm{j}\omega C')}$ |
| $\Gamma(.)$ | Coherence function (autocorrelation) |
| $\underline{\Gamma}_\mathrm{ref}$ | Complex amplitude reflection factor |
| $\tan(\delta)$ | Dissipation factor, $\tan(\delta) = \varepsilon''/\varepsilon'$ |
| $\Delta_\mathrm{T}$ | Thermally-induced resonance shift |

| | |
|---|---|
| $\varepsilon_0$ | Vacuum permittivity, $8.854187812813 \times 10^{-12}\ \frac{\mathrm{As}}{\mathrm{Vm}}$ |
| $\bar{\varepsilon}$ | Average ellipticity parameter (ISO/IEC 11146-1 standard) |
| $\underline{\varepsilon}_\mathrm{r}$ | Complex relative permittivity, $\underline{\varepsilon}_\mathrm{r} = \varepsilon' - \mathrm{j}\varepsilon''$ |
| $\zeta$ | Normalized pump laser detuning (unit-less), $\zeta \propto \delta\omega$ |
| $\eta$ | Unless specified differently: Power transmission factor |
| $\eta_\mathrm{rad}$ | Radiation efficiency of an antenna |
| $\eta_\mathrm{in}$ | Input-matching efficiency of an antenna |
| $\theta$ | Elevation angle |
| $\theta(\omega)$ | Frequency-dependent round-trip phase of racetrack resonator |
| $\theta_\mathrm{c}^{(0)}$ | Round-trip phase at $\omega_\mathrm{c}$ |
| $\theta_\mathrm{c}^{(1/2)}$ | First- and second-order derivative of the round-trip phase $\theta(\omega)$ at $\omega_\mathrm{c}$, where $\theta_\mathrm{c}^{(1)} = -\beta_\mathrm{c}^{(1)} L$ and $\theta_\mathrm{c}^{(2)} = -\beta_\mathrm{c}^{(2)} L$ correspond to the round-trip group delay and the GDD, respectively |
| $\theta_{x/y}$ | Components of $\vec{\Theta}_\mathrm{t}$ indicating the direction of $\vec{k}_\mathrm{t}$ along the $x$- and $y$-direction, respectively |
| $\tan\theta_{\mathrm{G},x/y}$ | Tangent of divergence angle of a Gaussian beam ($1/\mathrm{e}^2$ intensity contour) along the $x$- and $y$-direction, respectively, $\tan\theta_{\mathrm{G},x/y} = 2\tan\psi_{\mathrm{G},x/y}$ |
| $\vec{\Theta}_\mathrm{t}$ | Vector indicating the direction of $\vec{k}_\mathrm{t}$ |
| $\kappa$ | Real-valued amplitude transmission coefficient between racetrack resonator and bus waveguide |
| $\lambda$ | Wavelength |
| $\lambda_\mathrm{eff}$ | Effective wavelength of a virtual Gaussian beam leading to the same product of divergence parameter and corresponding variance of the intensity distribution for emulating multimode light propagation, $M_\mathrm{eff}^2 = \lambda_\mathrm{eff}/\lambda \geq 1$ |
| $\Delta\lambda_\mathrm{Vrnr}$ | Vernier FSR expressed in terms of a wavelength spacing |
| $\Lambda(\varphi)$ | Proportionality factor taking into account the $\varphi$-dependent change in field direction on opposing side of metal sheets |
| $\mu$ | (Finite) comb line index, $\mu \in \mathbb{Z}$ |
| $\mu_0$ | Vacuum permeability, $1.2566370621219 \times 10^{-6}\ \mathrm{N/A}^2$ |
| $\xi(\varphi, \theta)$ | Direction-dependent radiation pattern of an antenna |
| $\pi$ | Archimedes' constant, $3.14159\ldots$ |

| | |
|---|---|
| $\sigma$ | Unless specified differently: Standard deviation |
| $\sigma_{\mathrm{MCFS}}$ | Effective conductivity of metal coating |
| $\sigma^2$ | Variance (second central moment) |
| $\tau$ | Unless specified differently: Time difference \| Section 2.2.2 and Appendix A: Real-valued amplitude coupling coefficient between racetrack resonator and bus waveguide |
| $\tau_{\mathrm{c}}$ | Coherence time |
| $\tau_{\mathrm{d}}$ | Time delay in one path of an imbalanced MZI |
| $\tau_{\mathrm{exp}}$ | Exposure time |
| $\tau_{\mathrm{p}}$ | Photon lifetime |
| $\tau_{\mathrm{rt}}$ | Round-trip time of a resonator |
| $\tau_0$ | Observation time |
| $\phi$ | Photon flux |
| $\varphi$ | Chapter 4: Tilt angle with respect to optimum alignment \| Chapter 2 and Appendix D: Azimuth angle |
| $\varphi(t)$ | Random phase fluctuations |
| $\varphi_{\mathrm{bias}}$ | Phase shift for maintaining unbalanced MZI in quadrature |
| $\Delta\varphi(t)$ | Phase difference due to time delay $\tau_{\mathrm{d}}$ |
| $\Phi(\omega)$ | Frequency-dependent phase of external cavity |
| $\Phi_0$ | Constant phase offset |
| $\tan\psi_{\mathrm{G},x/y}$ | Tangent of divergence angle of a Gaussian beam (1/e intensity contour) along the $x$- and $y$-direction, respectively |
| $\Psi(\mu)$ | Spectral envelope of a single-soliton Kerr-comb |
| $\omega$ | Angular frequency, $\omega = 2\pi f$ |
| $\omega_{\mathrm{res},n}$ | Angular resonance frequencies of high-$Q$ ring resonator |
| $\omega_\mu$ | Spectrum of a frequency comb centered around $\omega_0$ with comb line spacing $\Delta\omega_{\mathrm{FSR}}$, i.e., $\omega_\mu = \omega_0 + \mu\,\Delta\omega_{\mathrm{FSR}}$ |
| $\delta\tilde{\omega}(t)$ | Fluctuation of instantaneous angular frequency, $\delta\tilde{\omega}(t) = 2\pi\,\delta\tilde{f}(t)$ |
| $\delta\omega$ | Absolute angular frequency detuning of a pump laser with respect to a resonance of a Kerr-nonlinear resonator, $\delta\omega = \omega_{\mathrm{res},0} - \omega_{\mathrm{p}}$ |
| $\delta\omega_{\mathrm{eff}}$ | Effective angular frequency detuning of a pump laser with respect to a resonance of a Kerr-nonlinear resonator, $\delta\omega_{\mathrm{eff}} = \delta\omega - \Delta_{\mathrm{T}}$ |
| $\Delta\omega$ | Angular free-spectral range |

# Danksagung

Die vorliegende Dissertation entstand während meiner Tätigkeit am Institut für Photonik und Quantenelektronik (IPQ) sowie am Institut für Mikrostrukturtechnik (IMT) innerhalb des Karlsruher Instituts für Technologie (KIT).

Die wissenschaftliche Arbeit war eingebettet in öffentlich geförderte Forschungsprojekte, allen voran dem Exzellenzcluster 3D Matter Made to Order (3DMM2O), gefördert von der Deutschen Forschungsgemeinschaft (DFG), sowie die Verbundprojekte PRIMA und Open6GHub, beide gefördert vom Bundesministerium für Bildung und Forschung (BMBF).

Eine Vielzahl an Personen hat mich in der Entstehung der vorliegenden Arbeit unterstützt und diese ermöglicht. Ihnen allen gilt mein herzlicher Dank. Einigen möchte ich an dieser Stelle meinen ganz besonderen Dank entgegenbringen.

Meinem Doktorvater Professor Christian Koos möchte ich besonders für das mir entgegengebrachte Vertrauen und das hohe Interesse an meiner Arbeit danken. Seine Ideen, Vorschläge und Ratschläge sowie die wissenschaftliche Freiheit, die er mir gab, haben wesentlich zur Entstehung dieser Arbeit beigetragen und diese erst ermöglicht.

Herrn Professor Wolfgang Freude gilt mein herzlichster Dank für die stets geduldige sowie überaus gründliche Durchsicht meiner Arbeiten, für die offenen und konstruktiven Diskussionen, und für die überaus wertvolle Kritik. Weiterhin möchte ich mich bei ihm für seine Tätigkeit als Fachstudienberater bedanken, durch welche er mich bereits während meines Master-Studiums grundlegend prägen und nachhaltig für die Photonik begeistern konnte.

Weiterhin gilt mein Dank Professor Thomas Zwick für die freundliche Betreuung als Korreferent, die Zurverfügungstellung diversen Messequipments, sowie die Unterstützung in Fragen rund um die Hochfrequenztechnik.

Mein ganz besonderer Dank gilt allen aktuellen sowie ehemaligen Bürokollegen in und um Raum 2.22, welche ich bereits seit meiner Bachelor-Arbeit im Jahr 2016 kennen und schätzen lernen durfte. Allen voran bedanke ich mich bei Yilin Xu für die Betreuung meiner Master-Arbeit, die enge und rückblickend überaus fruchtbare Zusammenarbeit, sowie für die immerwährende Unterstützung auch im weiteren Verlauf meiner Promotion. Matthias Blaicher danke ich für die Betreuung meiner Bachelor-Arbeit sowie für die hiermit verbundenen ersten Berührungspunkte mit der Multi-Photonen Lithographie. Darüber hinaus danke ich meinen beiden Vorgängern Matthias Blaicher und Yilin Xu für das üppige technologische Erbe — ohne dieses wäre die vorliegende Arbeit schlicht unmöglich umsetzbar gewesen. Yiyang Bao danke ich für die akribische Unterstützung bei der Automatisierung unseres Messplatzes zur Kalibrierung der integrierten ECL sowie für die Geduld, jeden noch so kleinen Änderungswunsch umzusetzen. Mareike Trappen möchte ich für die Dokumentation und geleisteten Vorarbeiten im Rahmen des Forschungsprojekts PRIMA danken, auf denen meine Arbeit aufbauen konnte. Philipp-Immanuel Dietrich danke ich für die Bereitstellung diverser Photoresists. Muhammad Rodlin ("Oding") Billah danke ich für die vielen hilfreichen Tipps und Tricks im Zusammenhang mit dem Aufbau von Multi-Chip-Modulen, die wesentlich zur Steigerung meiner feinmechanischen Fähigkeiten beitragen konnten.

Allen anderen aktuellen und ehemaligen wissenschaftlichen Wegbegleitern am IPQ und IMT möchte ich ebenfalls herzlich für die Zusammenarbeit danken — ihr alle habt die letzten Jahre unvergesslich gemacht. Ein ganz besonderer Dank gebührt Alexander Kotz, dessen umfangreiches Erbe an CST Simulationen sowie unermüdliche Unterstützung den Grundstein für die vorliegende Arbeit zu 3D-gedruckten mmW / THz Strukturen gelegt haben. In diesem Zusammenhang möchte ich auch Tobias Harter für die initialen Arbeiten danken. Bei Yung Chen und Huanfa Peng bedanke ich mich insbesondere für die Zurverfügungstellung der integrierten Ringresonatoren, sowie für die Hilfe im Rahmen meiner Publikation

zur Generation von Kerr-Frequenzkämmen. Pablo Marin-Palomo und Christoph Füllner möchte ich für die Unterstützung bei diversen Linienbreitenmessungen danken. Bei Christian Bremauer und Denis Ganin bedanke ich mich für die fortlaufende Zusammenarbeit im Bezug auf die Kalibrierung der integrierten ECL und die Unterstützung bei den hiermit verbundenen OCT-Messungen. Zu guter Letzt danke ich Alexander Kotz für die Aufnahme einer Vielzahl an REM-Bildern.

Ebenfalls möchte ich allen externen Doktoranden danken, die mit ihrer unermüdlichen Arbeit wesentlich zum Erfolg dieser Arbeit beigetragen haben. Joachim Hebeler (IHE, KIT) danke ich herzlichst für das wiederholte Charakterisieren meiner Bauteile sowie für die gemeinsamen Diskussionen und Auswertungen der Messdaten. Bei Qiaoshuang Zhang (LTI, KIT) möchte ich mich für die engagierte Zusammenarbeit beim Inkjet-Druck bedanken. Schließlich danke ich Alexander Quint (IHE, KIT) und Marius Kretschmann (IHE, KIT) für die Unterstützung bei der Charakterisierung diverser Photoresists sowie für die Einführung in die Laserstrukturierung von Keramiksubstraten.

Weiterhin möchte ich dem gesamten technischen und administrativen Personal für die hervorragende Zusammenarbeit und tatkräftige Unterstützung danken. Oswald Speck, Andreas Lipp, Steffen Pfeifer und Lisa Nolte danke ich für die Unterstützung bei der Faserpräparation und dem elektrischen Drahtbonden. Bei Steffen Herzog, Mirko Nonnenmacher, Andreas Gallego und Julian Jochum bedanke ich mich für die immer zügige und präzise Fertigstellung einer Vielzahl feinmechanischer Aufbauten. Anja Eberhardt und Birgit Hübner danke ich für diverse Arbeiten im IMT-Reinraum, insbesondere an der PVD-Beschichtungsanlage. Florian Rupp, Stefan Hengsbach und Samuel Bergdolt danke ich für die Unterstützung an der Wafersäge, für die Aufnahme der REM-Bilder sowie für das Einlernen in diverse Geräte. Dem CFN-Team um Bettina Uliczka danke ich für die Hilfe bei der Installation, Inbetriebnahme und Wartung unseres 3D-Druckers. Für die tatkräftige Unterstützung in Sachen Reiseplanung, Einkauf und für das allzeit offene Ohr möchte ich mich weiterhin bei Bernadette Lehmann, Maria-Luise ("Marlis") Koch, Tatiana Gassmann, Andrea Riemensperger, Alina Lauinger und Bettina Rasche bedanken. Zu guter Letzt gilt mein Dank auch David Guder, Volker Bös und Damian Wagner für den Support in allen Fragen rund um das Thema IT.

Den externen Kooperationspartnern Ute Troppenz und Martin Möhrle (Fraunhofer HHI), Dimitri Geskus und Ronald Dekker (LioniX International), Junqiu Liu und Tobias J. Kippenberg (EPFL), Achim Weber und Torben Kind (ficonTEC), Alexandra Henniger-Ludwig und Hermann Kapim (Rosenberger Hochfrequenztechnik), Clemens Wurster (Rosenberger OSI), sowie Matthias Lauermann (Vanguard Automation GmbH) möchte ich ebenfalls meinen besonderen Dank aussprechen.

Ich danke Christian Benz, Pirmin Adam, Carlos Eduardo Jimenez, David Karcher, Aaron Ensslin, Andrés Machado, Berk Ozkarali und Mustafa Emre Karaçar, deren Abschlussarbeiten ich direkt oder indirekt betreuen durfte, für ihre ausgezeichnete Arbeit. Ein großes Dankeschön gilt auch Yiyang Bao für ihre unermüdliche Arbeit als studentische Hilfskraft.

Huanfa Peng und Innokentiy Zhdanov danke ich für die wertvollen Hinweise und Diskussionen rund um das Phasenrauschen von Lasern. Bei Patrick Matalla und Jonas Krimmer möchte ich mich für ihre nützlichen Kommentare zum Thema Multiplexing bedanken. Alexander Kotz danke ich für seine Anmerkungen rund um das Thema Hochfrequenztechnik. Yiyang Bao und Joel Dittmer danke ich für das kritische Korrekturlesen.

Ein ganz besonderer Dank gilt meinen Eltern Martina und Thomas sowie meinem Bruder Lukas Maier. Danke, dass ihr mich stets in allem unterstützt und zu jeder Zeit mit Rat und Tat zur Seite steht. Ihr habt mir in meinem Leben Vieles ermöglicht, das ich mir nie erträumt hätte.

# List of publications

## Journal publications

[J1] Y. Xu[†], **P. Maier**[†], M. Blaicher, P.-I. Dietrich, P. Marin-Palomo, W. Hartmann, Y. Bao, H. Peng, M. R. Billah, S. Singer, U. Troppenz, M. Möhrle, S. Randel, W. Freude, and C. Koos, "Hybrid external-cavity lasers (ECL) using photonic wire bonds as coupling elements", *Scientific Reports* **11**(1), 16426 (2021). DOI: 10.1038/S41598-021-95981-W.
[†] **authors contributed equally to the work**.

[J2] **P. Maier**, Y. Chen, Y. Xu, Y. Bao, M. Blaicher, D. Geskus, R. Dekker, J. Liu, P.-I. Dietrich, H. Peng, S. Randel, W. Freude, T. J. Kippenberg, and C. Koos, "Sub-kHz-linewidth external-cavity laser (ECL) with $Si_3N_4$ resonator as a tunable pump for a Kerr frequency comb", *Journal of Lightwave Technology* **41**(11), pp. 3479–3490 (2023). DOI: 10.1109/JLT.2023.3243471.

[J3] **P. Maier**[†], Y. Xu[†], M. Trappen, M. Lauermann, A. Henniger-Ludwig, H. Kapim, T. Kind, A. Weber, M. Blaicher, P.-I. Dietrich, C. Wurster, S. Randel, W. Freude, and C. Koos, "3D-printed facet-attached optical elements for connecting VCSEL and photodiodes to fiber arrays and multi-core fibers", *Optics Express* **30**(26), pp. 46 602–46 625 (2022). DOI: 10.1364/OE.470676.
[†] **authors contributed equally to the work**.

[J4] **P. Maier**, A. Kotz, J. Hebeler, Q. Zhang, C. Benz, A. Quint, M. Kretschmann, T. Harter, S. Randel, U. Lemmer, W. Freude, T. Zwick, and C. Koos, "Freeform terahertz structures fabricated by multi-photon litho-

graphy and metal coating", *arXiv* **2401.03316** (2024). DOI: 10.48550/arXiv.2401.03316.

[J5] Y. Xu, **P. Maier**, M. Trappen, P.-I. Dietrich, M. Blaicher, R. Jutas, A. Weber, T. Kind, C. Dankwart, J. Stephan, A. Steffan, A. Abbasi, P. Morrissey, K. Gradkowski, B. Kelly, P. O'Brien, W. Freude, and C. Koos, "3D-printed facet-attached microlenses for advanced photonic system assembly", *Light: Advanced Manufacturing* **4**, 3 (2023). DOI: 10.37188/LAM.2023.003.

[J6] S. Singer, Y. Xu, S. T. Skacel, H. Zwickel, **P. Maier**, L. Freter, P.-I. Dietrich, M. Kaschel, C. Menzel, S. Randel, W. Freude, and C. Koos, "3D-printed facet-attached optical elements for beam shaping in optical phased arrays", *Optics Express* **30**(26), pp. 46 564–46 574 (2022). DOI: 10.1364/OE.456952.

[J7] S. Y. Haffert, R. J. Harris, A. Zanutta, F. A. Pike, A. Bianco, E. M. A. Redaelli, A. Benoît, D. G. MacLachlan, C. A. Ross, I. Gris-Sánchez, M. D. Trappen, Y. Xu, M. Blaicher, **P. Maier**, G. Riva, B. Sinquin, C. Kulcsár, N. A. Bharmal, É. Gendron, L. Staykov, T. J. Morris, S. Barboza, N. Münch, L. F. Bardou, L. Prengère, H.-F. G. Raynaud, P. Hottinger, T. Anagnos, J. Osborn, C. Koos, R. R. Thomson, T. A. Birks, I. A. G. Snellen, and C. U. Keller, "Diffraction-limited integral-field spectroscopy for extreme adaptive optics systems with the multicore fiber-fed integral-field unit", *Journal of Astronomical Telescopes, Instruments, and Systems* **6**(4), 045007 (2020). DOI: 10.1117/1.JATIS.6.4.045007.

## Conference publications

[C1] **P. Maier**, Y. Chen, Y. Xu, M. Blaicher, D. Geskus, R. Dekker, J. Liu, P.-I. Dietrich, H. Peng, S. Randel, W. Freude, T. J. Kippenberg, and C. Koos, "InP/$Si_3N_4$ hybrid external-cavity laser with sub-kHz linewidth acting as a pump source for Kerr frequency combs", in *European Conference on*

*Optical Communication* (ECOC 2022), paper We2E.4. [Online]. Available: https://opg.optica.org/abstract.cfm?uri=ECEOC-2022-We2E.4.

[C2] **P. Maier**†, Y. Xu†, M. Lauermann, A. Henniger-Ludwig, H. Kapim, M. Trappen, T. Kind, A. Weber, M. Blaicher, P.-I. Dietrich, C. Wurster, S. Randel, W. Freude, and C. Koos, "3D-printed optical elements for coupling of VCSEL and photodiode arrays to multi-core fibers in an SFP transceiver assembly", in *Optical Fiber Communication Conference* (OFC 2022), paper W2A.1. DOI: 10.1364/OFC.2022.W2A.1.
† **authors contributed equally to the work**.

[C3] **P. Maier**†, C. Bremauer†, Y. Bao, Y. Xu, D. Ganin, S. Randel, W. Freude, and C. Koos, "Swept-source optical coherence tomography (SS-OCT) using a hybrid silicon photonic external-cavity laser (ECL)", in *Conference on Lasers and Electro-Optics* (CLEO 2022), paper AM5I.4. DOI: 10.1364/CLEO_AT.2022.AM5I.4.
† **authors contributed equally to the work**.

[C4] **P. Maier**, A. Kotz, J. Hebeler, Q. Zhang, C. Benz, A. Quint, M. Kretschmann, T. Harter, S. Randel, U. Lemmer, W. Freude, T. Zwick, and C. Koos, "3D freeform millimeter-wave and THz structures based on multi-photon lithography", in *Optical Fiber Communication Conference* (OFC 2024), paper W2A.5. DOI: 10.1364/OFC.2024.W2A.5.

[C5] Y. Chen, G. Lihachev, H. Peng, H. Tian, D. Fang, A. Voloshin, J. Riemensberger, **P. Maier**, S. Skacel, M. Lauermann, A. Attanasio, S. Randel, W. Freude, S. Bhave, T. Kippenberg, and C. Koos, "Frequency-agile self-injection-locked lasers with sub-100 Hz linewidth based on in-package photonic wire bonds", in *Conference on Lasers and Electro-Optics* (CLEO 2023), paper STu4P.4. DOI: 10.1364/CLEO_SI.2023.STU4P.4.

[C6] H. Peng, Y. Chen, I. R. Lopez, G. Lihachev, H. Tian, A. Voloshin, J. Riemensberger, **P. Maier**, S. Skacel, M. Lauermann, A. Attanasio, S. Randel, W. Freude, S. Bhave, T. Kippenberg, and C. Koos, "Low-phase-noise frequency-agile hybrid integrated laser offering highly linear tuning

for FMCW LiDAR", in *Conference on Lasers and Electro-Optics* (CLEO 2024), paper SM2M.1.

[C7] P. Schwaab[†], **P. Maier**[†], Y. Bao, S. Singer, M. Worgull, W. Freude, and C. Koos, "Pluggable single-mode chip-chip connections using facet-attached microlenses and passive mechanical joints", in *Conference on Lasers and Electro-Optics* (CLEO 2024), paper SM1D.5.
[†] **authors contributed equally to the work**.

[C8] S. Singer, Y. Xu, S. T. Skacel, H. Zwickel, **P. Maier**, P.-I. Dietrich, M. Kaschel, C. Menzel, W. Freude, and C. Koos, "3D-printed facet-attached optical elements for beam shaping in solid-state phased arrays", in *Conference on Lasers and Electro-Optics* (CLEO 2022), paper SM4P.5. DOI: 10.1364/CLEO_SI.2022.SM4P.5.

[C9] E. Knehr, Y. Xu, Y. Bao, **P. Maier**, C. Jimenez, K. Ilin, M. Ziegler, H. Schmidt, S. Kempf, A. Kuzmin, C. Koos, and M. Siegel, "Optical packaging of SNSPDs with photonic wire bonds", in *European Conference on Applied Superconductivity* (EUCAS 2021), *invited*.

[C10] Y. Xu[†], **P. Maier**[†], M. Blaicher, P.-I. Dietrich, P. Marin-Palomo, W. Hartmann, M. R. Billah, U. Troppenz, M. Möhrle, S. Randel, W. Freude, and C. Koos, "InP/silicon hybrid external-cavity lasers (ECL) using photonic wirebonds as coupling elements", in *Optical Fiber Communication Conference* (OFC 2020), paper M4H.6. DOI: 10.1364/OFC.2020.M4H.6.
[†] **authors contributed equally to the work**.

[C11] T. Anagnos, **P. Maier**, P. Hottinger, C. H. Betters, T. Feger, S. G. Leon-Saval, I. Gris-Sánchez, S. Yerolatsitis, J. Lozi, T. A. Birks, S. Vievard, N. Jovanovic, A. D. Rains, M. J. Ireland, R. J. Harris, B. C. K. Tiong, O. Guyon, B. Norris, S. Y. Haffert, M. Blaicher, Y. Xu, M. Straub, J.-U. Pott, O. Sawodny, P. L. Neureuther, D. W. Coutts, C. Schwab, C. Koos, and A. Quirrenbach, "An innovative integral field unit upgrade with 3D-printed micro-lenses for the RHEA at Subaru", in *Proc. SPIE* 11451, *Advances in Optical and Mechanical Technologies for Telescopes and Instrumentation IV* (2020), paper 114516Y. DOI: 10.1117/12.2560626.

[C12] R. J. Harris, F. A. Pike, M. Trappen, S. Y. Haffert, Y. Xu, A. Benoît, C. Ross, D. G. MacLachlan, S. Barboza, N. Münch, I. Gris-Sánchez, M. Blaicher, **P. Maier**, C. Koos, T. A. Birks, and R. R. Thomson, "Multi-core fibre-fed integral field spectrograph (MCIFU) IV: The fiber link", in *Proc. SPIE* 11451, *Advances in Optical and Mechanical Technologies for Telescopes and Instrumentation IV* (2020), paper 1145124. DOI: 10.1117/12.2562689.

[C13] S. Y. Haffert, R. J. Harris, A. Zanutta, F. A. Pike, A. Bianco, E. Redaelli, A. Benoît, D. G. MacLachlan, C. A. Ross, I. Gris-Sánchez, M. D. Trappen, Y. Xu, M. Blaicher, **P. Maier**, G. Riva, B. Sinquin, C. Kulcsár, N. A. Bharmal, E. Gendron, L. Staykov, T. J. Morris, S. Barboza, N. Muench, L. Bardour, L. Prengère, H.-F. Raynaud, P. Hottinger, T. Anagnos, J. Osborn, C. Koos, R. R. Thompson, T. A. Birks, I. A. G. Snellen, C. U. Keller, L. Close, and J. R. Males, "Multi-core fibre-fed integral-field unit (MCIFU): Overview and first-light", in *Proc. SPIE* 11448, *Adaptive Optics Systems VII* (2020), paper 114484M. DOI: 10.1117/12.2562719.